# Search for new invisible particles in events with a Z boson at CMS

Von der Fakultät für Mathematik, Informatik und Naturwissenschaften der
RWTH Aachen University zur Erlangung des akademischen Grades eines
Doktors der Naturwissenschaften genehmigte Dissertation

vorgelegt von
Andreas Albert, M. Sc.
aus Bonn

Berichter: Professor Dr. Thomas Hebbeker
Professor Dr. Christopher Wiebusch

Tag der mündlichen Prüfung: 29.05.2019

# Abstract

This thesis documents a search for new particles at the Compact Muon Solenoid experiment (CMS) at the CERN Large Hadron Collider (LHC). Proton-proton collisions with reconstructed Z bosons are analyzed for evidence of the production of new unreconstructed ("invisible") particles. The search strategy is centered around the use of the missing transverse momentum $p_{\mathrm{T}}^{miss}$, which provides an indirect handle on the kinematic properties of particles that are not reconstructed directly in the detector. The production of invisible particles would be detected as an excess of events with large $p_{\mathrm{T}}^{miss}$ over the known background processes.

Analysis results are obtained based on the data sets collected by the CMS collaboration in the first half of the *Run-II* period of LHC operation in 2015 and 2016. The 2015 data set, corresponding to an integrated luminosity of 2.3 $\mathrm{fb}^{-1}$, provides a first, coarse-grained glimpse of physics at the world record center-of-mass energy of 13 TeV. Although relatively small in size, the high collision energy allows to rival the sensitivity achieved in previous, larger data sets at lower energies. In 2016, a larger data sample of 35.9 $\mathrm{fb}^{-1}$ could be recorded, providing additional statistical precision and sharpening the view of the high-energy landscape. The search for invisible particles is performed in both of these milestone data sets. After accounting for contributions from known backgrounds, no significant signal is observed in either sample.

A special focus is set on the interpretation of the experimental results in a number of models for the production of invisible particles. As part of this thesis, results from the Z+$p_{\mathrm{T}}^{miss}$ topology are for the first time interpreted in terms of *simplified models* of dark matter (DM) production, which are more robust than the previously used effective field theories. As a significant improvement over the interpretations provided in previous results, a stronger focus is put on simplified models with an extended scalar sector, for which the Z+$p_{\mathrm{T}}^{miss}$ signature provides competitive sensitivity. In a scenario with a second Higgs doublet and a pseudoscalar dark matter mediator, new portions of parameter space can be excluded for the first time. In addition to models of DM production, the analysis results are interpreted in terms of production of scalar unparticles, as well as gravitons in a scenario of large extra dimensions. In the case of unparticle production, significant errors have been discovered in the literature, leading to a revised view of the sensitivity of the Z+$p_{\mathrm{T}}^{miss}$ topology, which is smaller than previously thought. Nevertheless, the unparticle interpretation derived here provides leading sensitivity in parts of the parameter space.

Beyond the analysis of Run-II data, a study of the future analysis sensitivity at the high-luminosity LHC (HL-LHC) is performed. It is expected that the HL-LHC will provide a final proton-proton data set corresponding to 3 $\mathrm{ab}^{-1}$ with $\sqrt{s} = 14$ TeV over the next two decades. The effects of increased center-of-mass energy and integrated luminosity, as well as $p_{\mathrm{T}}^{miss}$ reconstruction performance are studied in detail. It is found that an analysis of this expected data set will result in a mass reach which is increased by approximately a factor of two compared to the present-day sensitivity. Notably, the large data set would enhance the sensitivity so significantly that a number of signals that are not probed today could reach discovery sensitivity at the end of the HL-LHC program.

# Zusammenfassung

Diese Dissertation beschäftigt sich mit der Suche nach neuen Teilchen mit dem Compact Muon Solenoid (CMS) Experiment am CERN Large Hadron Collider (LHC). Proton-Proton Kollisionsereignisse mit rekonstruierten Z-Bosonen werden auf Hinweise für die Produktion von neuen, nicht rekonstruierbaren ("unsichtbaren") Teilchen untersucht. Die Suchstrategie basiert auf der Auswertung der Verteilung des Fehlenden Transversalimpulses $p_{\mathrm{T}}^{miss}$, in der die Produktion solcher Teilchen einen charakteristischen Exzess gegenüber der erwarteten Verteilung in bekannten Prozessen hervorrufen würde.

Die Analyse basiert auf Datensätzen, die von der CMS-Kollaboration in der ersten Hälfte der *Run-II* Laufzeit des LHC in den Jahren 2015 und 2016 aufgezeichnet wurden. Der 2015er Datensatz mit einer integrierten Luminosität von 2.3 fb$^{-1}$ erlaubt erste Einblicke in die Physik bei der nie zuvor im Labor erreichten Schwerpunktsenergie von 13 TeV. Die hohe Kollisionsenergie ermöglicht eine kompetitive Sensitivität zu früheren Datensätzen, die größer sind, aber bei niedrigerer Energie aufgenommen wurden. Der zweite, im Jahr 2016 aufgenommene Datensatz, zeichnet sich durch eine größere integrierte Luminosität von 35.9 fb$^{-1}$ aus, und fügt der hohen Schwerpunktsenergie somit statistische Präzision hinzu. In keinem dieser beiden richtungsweisenden Datensätze kann ein Signal nachgewiesen werden.

Ein Schwerpunkt der Dissertation ist die Interpretation der experimentellen Ergebnisse in Modellen neuer Physik. Im Rahmen dieser Arbeit wurden Ergebnisse einer Z+$p_{\mathrm{T}}^{miss}$ Suche erstmals im Kontext von *simplified models*, also einfachen, aber vollständigen Modellen, der Produktion von Dunkle-Materie-Teilchen (DM) interpretiert. Diese erlauben robustere Schlussfolgerungen als die vormals verwendeten effektiven Feldtheorien. Erstmals wird auch ein Modell mit einem zweiten Higgs-Dublett und einem pseudoskalaren DM-Mediator betrachtet, das intrinsisch zur Z+$p_{\mathrm{T}}^{miss}$-Signatur führt. In diesem Modell kann ein neuer Teil des Parameterraums zum ersten Mal ausgeschlossen werden. Jenseits der Interpretationen im Zusammenhang mit DM werden die Analyse-Ergebnisse in Modellen für *Unparticle*- und Graviton-Produktion interpretiert. Im Kontext der Unparticles konnten Fehler in der vorhergehenden Literatur nachgewiesen werden, die zu überzogenen Sensitivitätseinschätzungen geführt hatten. Trotzdem sind die Ausschlussgrenzen, die in diesem Modell formuliert werden können, in Teilen des Parameterraums führend.

Als Ausblick in die Zukunft wird die Sensitivität der vorliegenden Suche am *high-luminosity* LHC (HL-LHC) untersucht. Der HL-LHC soll über die nächsten zwei Jahrzehnte einen Proton-Proton-Datensatz mit integrierter Luminosität von 3 ab$^{-1}$ bei $\sqrt{s} = 14$ TeV produzieren. Der Einfluss dieser hohen integrierten Luminosität, sowie der erhöhten Schwerpunktsenergie und der zu erwarteten experimentellen $p_{\mathrm{T}}^{miss}$-Rekonstruktion wird ausgewertet. Mit dem vollen HL-LHC Datensatz wird sich die Massensensitivität dieser Suche um einen Faktor von ca. zwei im Vergleich zu heute verbessern. Besonders ist hervorzuheben, dass der Sensitivitätszuwachs so groß ist, dass einige Signale, die heute noch unbemerkt geblieben sein könnten, im vergrößerten Datensatz zu einer statistisch signifikanten Entdeckung führen könnten.

# Contents

# 1. Preface

The task of particle physics is to understand what the universe looks like at very short distances. The discipline derives its name from the insight that matter, at the most basic level, seems to be made of particles. The complex behavior of macroscopic objects is then understood to be in some form derived from the microscopic particle interactions. With this reductionist view in mind, one may wonder if there are as-of-yet undiscovered particles and interactions to be found. This thesis is dedicated to a search for new *invisible* particles produced in proton-proton collisions. This preface is meant to introduce the target signatures, motivate the search, and outline principles used to conduct the search. Many of the initial points raised here will be handled in more detail in later sections, but this initial treatment should allow the reader to dive into the subsequent document more easily.

## 1.1. The search for new invisible particles

Calling a particle invisible is a useful colloquialism. In the context of particle colliders, one can define invisibility as the property of not being detected in the typical detector hardware used at colliders, which rely on ionization and electromagnetic or hadronic showering for particle detection. At the elementary level, invisibility then requires that a particle does not participate in the electromagnetic and strong interactions. A familiar example of invisible particles would be the known neutrinos, which already highlight that invisibility is a relative concept: Detection is possible with large, dedicated detectors (for examples, see Refs. [1, 2]), but the detection efficiency is so small that gigantic neutrino fluxes are necessary.

What is the motivation to search for new invisible particles? The example of neutrinos proves that very weakly interacting particles can exist in nature, and be produced in the laboratory. Beyond this very low motivational threshold, there are good reasons to look for them specifically rather than anything else that is simply “not prohibited”. The most convincing reasoning for the existence of additional invisible particles is rooted in our understanding of cosmology, which points to the existence of dark matter (DM).

## 1.2. The case for dark matter

The presence of large quantities of DM in the universe was first proposed in order to explain the redshifts of emission spectra observed in the Coma cluster [3]. If the mass density distribution in the cluster and the laws of gravity are known, it is possible to derive an estimate of the variance of redshifts of the constituent galaxies. For a cluster consisting only of the ordinary matter we know, one would expect the distribution of the gravitational mass to be related to the distribution of light emitted from it. However, it was found that the redshifts show a much greater variance than one would expect from an estimate of the luminous matter density present in the cluster. Decades later, a similarly surprising effect was observed in measurements of the rotational velocity of individual spiral galaxies [4, 5]. In this case, the radial dependence of the rotational velocity disagrees decisively with gravitational predictions based on density estimates for the luminous matter. Both of these phenomena point to one of two conclusions: Either the underlying theory of gravity is incorrect, or significant amounts of DM shape the behavior of galaxies (or both).

A further mismatch between luminous and gravitational matter was later also established in gravitational lensing, most prominently in the bullet cluster [6]. Here, the deflection of light traversing the cluster allows to infer the distribution of gravitational mass. When compared to the distribution of luminous matter, which is derived from the observation of X ray emission [6, 7], not only the radial dependence, but also the location of the center of mass is found to be inconsistent between the two. This is an important clue as it not only favors the existence of a non-luminous component, but is also not easily explained by a hypothetical modification of gravity.

Over the last decades, arguments for the existence of DM have moved from relying on these single, isolated phenomena toward a broader, more integrated view of cosmology. The standard model of modern cosmology is often referred to as “$\Lambda$CDM”, meaning that it can be summarized as general relativity with a finite cosmological constant $\Lambda$ and significant portions of *cold dark matter* in the universe [8]. The presence of dark matter is essential in this model to shape the way structures such as galaxies form during the evolution of the universe. *Cold* dark matter refers to DM particles that are sufficiently heavy to restrict their ability to move too efficiently through the universe, which would smooth out local density differences and hinder structure formation. It is known that the structure formation process cannot be driven by the known matter particles, which would have left the imprints of early structures in today’s cosmic microwave background (CMB), but no such imprints are observed [9]. The presence of large scale structure in the universe today can then only be understood as the result of early structure formation in the dark component of the matter in the universe [8, 10]. Beyond these qualitative arguments, many-body simulations based on the $\Lambda$CDM model can reproduce realistic cosmological structures (e.g. Ref. [11]). From the cosmological viewpoint, open questions revolve around the properties of DM, such as whether it is really all cold, or whether admixtures of *warm* or *hot* DM are necessary [12], and what DM candidate would yield optimal agreement.

The underlying nature of DM is unknown. One of the most widely studied possibilities is that of a *weakly interacting massive particle* (WIMP). WIMPs in the mass range of 1 GeV to 1 TeV, paired with interaction cross section similar to the weak interaction, have been seen as attractive candidates because they can account for many of the known astrophysical phenomena associated to DM (such as the relic density, cf. sec. 5). The perceived attractiveness of WIMPs as DM candidates was also bolstered by the fact that WIMPs can naturally arise in supersymmetry scenarios [13], which were widely believed to be realized in nature. Even though this prejudice has not been fulfilled, as evidenced by the absence of discoveries of supersymmetric particles, WIMPs remain the most sought-after DM candidates.

A wide-ranging experimental program has been dedicated to the search for WIMPs through *direct detection* (DD) experiments [14]. DD experiments build on the idea that that earth is constantly moving through a cloud of DM, leading to rare interactions of WIMPs with the earth’s matter. To search for such interactions, a sensitive volume of a target material is instrumented to detect the light emitted from nuclei after a WIMP-nucleon interaction. The experimental sensitivity is maximized by increasing the target size, nucleon number,

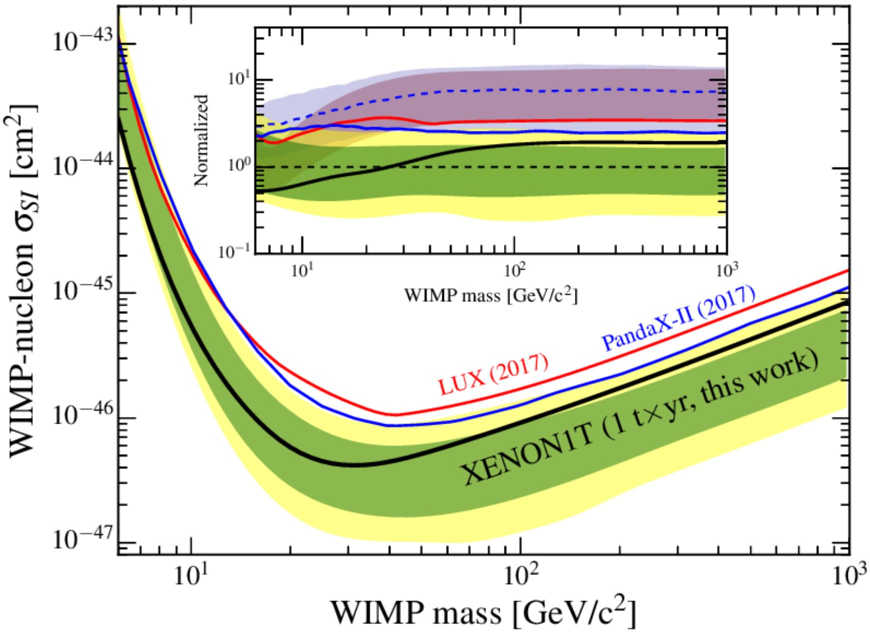

Figure 1.1.: The currently world-leading constraints on spin-independent WIMP-nucleon scattering cross-section from the XENON1T experiment [15]. The green (yellow) shaded regions show the one (two) standard deviation environment around the mean expected limit. The observed limit is shown as a black solid line. Also shown are competitive results from the independent LUX [18] and PandaX-II experiments [19] as solid coloured lines. The inset shows all curves divided by the expected limit from XENON1T to facilitate the comparison between the experiments. All exclusion limits are shown at a 90% confidence level. Image taken from Ref. [16].

and exposure time. While simple in principle, such a measurement poses extreme technical challenges, as various background contributions from natural radioactivity, cosmic radiation, and others need to be controlled with great precision, which becomes even more challenging as the target size increases. The currently leading DD sensitivity has been achieved by the XENON1T experiment, which uses a two-phase xenon-filled time projection chamber [15, 16]. Since no signal has been found to date, results are formulated as exclusion limits on the WIMP-nucleon cross section as a function of the WIMP mass, which is shown in Fig. 1.1. DD experiments are most sensitive for WIMP masses in the range of tens of GeV. At lower WIMP masses, the expected energy deposition per scattering is reduced, and the experimental sensitivity is limited by the energy threshold above which signals are detectable. The interplay between DD and collider searches for DM is further explored in sec. 7.

In this document, all DM related interpretations are derived for WIMP scenarios. However, the considered experimental signature is not specific to this case, but is model independent and covers other DM candidates, as long as they can be considered invisible. For a detailed review of DM, its history as a scientific concept, and especially possible other candidates, see Ref. [17] and references therein.

## 1.3. Detecting invisible particles at a collider

By definition, searches for invisible particles cannot rely on a direct detection of the particle in question, but an indirect way must be found. At colliders, the method of choice is to consider the momentum balance in a particle collisions. The incoming particle beams have their momenta aligned along a common axis. If conservation of momentum holds, the total momentum in the plane transverse to the beam axis must not change during the collision, and if it was zero before, must be zero after it. Using a detector that covers the full solid angle around the collision point, one could therefore be sure to always measure a total transverse momentum of zero if all final state particles are detectable. As soon as an invisible species of stable final state particles is created, that balance is thrown off, because the invisible particles carry away momentum. The value of the negative transverse momentum sum, referred to as *missing transverse momentum* or $p_{\mathrm{T}}^{miss}$, therefore serves as a measure of the momentum carried by invisible particles, and the recipe for a search is simple: Look for events with a large $p_{\mathrm{T}}^{miss}$. A schematic of the definition of $p_{\mathrm{T}}^{miss}$ is shown in Fig. 1.2. Unavoidable background contributions will be incurred from neutrino production, which needs to be estimated. Additionally, real particle detectors have limited geometrical acceptance, limited efficiency and measurement precision: Sometimes particles hit the cracks between two detector modules, escape close to the beam line, or are simply not reconstructed because the reconstruction algorithm is not perfect. These experimental issues also result in an artificial momentum imbalance ("fake" $p_{\mathrm{T}}^{miss}$), even if there are no invisible particles involved, but can be kept under control with good detector design and careful calibration.

The $p_{\mathrm{T}}^{miss}$-based detection scheme critically relies on the production of particles ("tags") beyond the sought-after invisible ones. If only invisible particles are produced, no $p_{\mathrm{T}}^{miss}$ can be defined, and the collision would not be recorded by the detector at all. The search topology is therefore defined by specializing on a given tag signature, such as a jet (*monojet* topology), a photon (*mono-photon*), or any other signature. In this thesis, the mono-Z topology is used, in which charged leptons from the decay of a Z boson are used as a tag signature. Since a Z boson be can radiated from incoming quarks, this choice of tag does not rely on the specifics of the production mechanism of the invisible particles, and can be used as a general signature. Example Feynman diagrams of this type of signature are shown in Fig. 1.3.

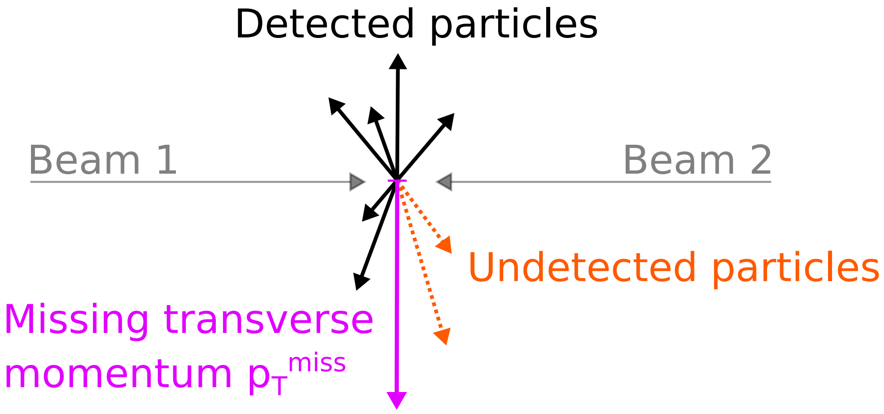

Figure 1.2.: Schematic definition of $p_{\mathrm{T}}^{miss}$. The momenta of incoming beam particles are aligned on a common axis. Due to conservation of momentum, the total momentum of outgoing particles transverse to that axis must sum to zero. If some of the outgoing particles are not detected, their transverse momentum can be inferred from the negative sum of the detected transverse momenta $p_{\mathrm{T}}^{miss}$.

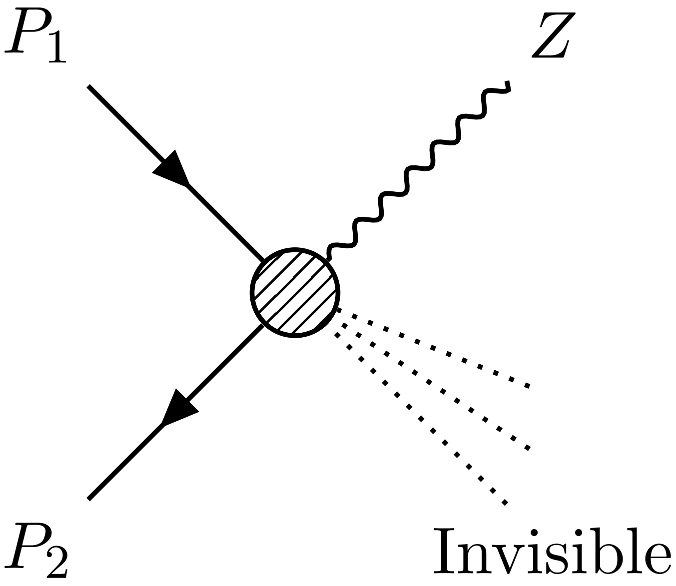

Figure 1.3.: Schematic Feynman diagram for the mono-Z topology. An incoming pair of partons $P_1$ and $P_2$ (indicated by fermion lines) interacts to produce any number of invisible particles (indicated by dotted lines) and a Z boson. The interaction is depicted here as an effective four-particle interaction, which is specified in more detail in sec. 4. Depending on each case of considered interaction, multiple combinations of incoming partons $P_{1/2}$ are possible, with the most common being a quark-anti-quark pair (shown here) or a pair of gluons (not pictured). All Feynman diagrams in this document have been prepared using the software from Ref. [20].

# Part I.

# Introduction

# 2. Experimental setup

The main topic of this thesis is the analysis of experimental data collected with the Compact Muon Solenoid (CMS) detector at the CERN Large Hadron Collider (LHC). In this section, the LHC and CMS machines are described with a focus on the aspects most relevant to the experimental analysis.

## 2.1. The Large Hadron Collider

The LHC [21] located at CERN near Geneva, Switzerland, is the highest-energy particle collider constructed by humans at the time of this writing. The LHC is a circular synchrotron built into the existing 27 km long tunnel previously used for the LEP accelerator. It was designed to explore particle interactions at and beyond the electroweak scale, probe the mechanism of electroweak symmetry breaking and allow for the discovery of new, possibly unexpected particles. In order to best serve these goals, the machine design was focused on a combination of high collision energy of up to $\sqrt{s} = 14$ TeV, as well as a large instantaneous luminosity of up to $1 \times 10^{34}$ $\mathrm{cm}^{-2}\mathrm{s}^{-1}$, both of which exceed the previously achieved record values in hadron collisions[1]. One of the technological innovations necessary to make these values possible, lies in the design of the dipole magnet system used to force the beams onto a circular orbit. The superconducting NbTi dipole magnets are operated at a temperature of 2 K, which is made possible by the use of superfluid helium as a coolant. This low temperature in turn allows for a high central magnetic field of up to 8.3 T, which drives the achievable beam energy. A key development was the efficient implementation of two separate beam pipes with independent dipole magnetic fields, as well as the iron yoke material and vacuum and cryogenic enclosures into a cylindrical structure with a diameter of approximately one meter. The cross section of the LHC dipole magnets is shown in Fig. 2.1.

The LHC hosts four large experiments situated at four beam crossing sites distributed along the ring, two of which are the general purpose experiments CMS [22] and ATLAS [23]. They are designed to provide measurements of standard model (SM) processes, and serve as a laboratory for the search of physics beyond the standard model (BSM).

Due to initial technical problems, the design performance values of the LHC were not reached immediately at the beginning of its physics program. In *Run-I* during the years 2010 to 2012, the machine was operated at $\sqrt{s} = 7$ and 8 TeV, delivering a total data set of approximately 30 $\mathrm{fb}^{-1}$, which allowed for the discovery of what seems to be the SM Higgs boson [24–26]. After a two-year shutdown, the LHC restarted data-taking in 2015 at a higher energy of $\sqrt{s} = 13$ TeV, delivering a first data set of $\approx 4.2$ $\mathrm{fb}^{-1}$, and went on to provide a large data set of $\approx 41.0$ $\mathrm{fb}^{-1}$ at the same energy in 2016 (of which CMS recorded $2.5\mathrm{fb}^{-1}$ and $36\mathrm{fb}^{-1}$, respectively). These two data sets, which form the beginning of the

---

[1] These values refer to proton-proton collisions. The LHC can also be used to generate heavy-ion collisions, which are not discussed here.

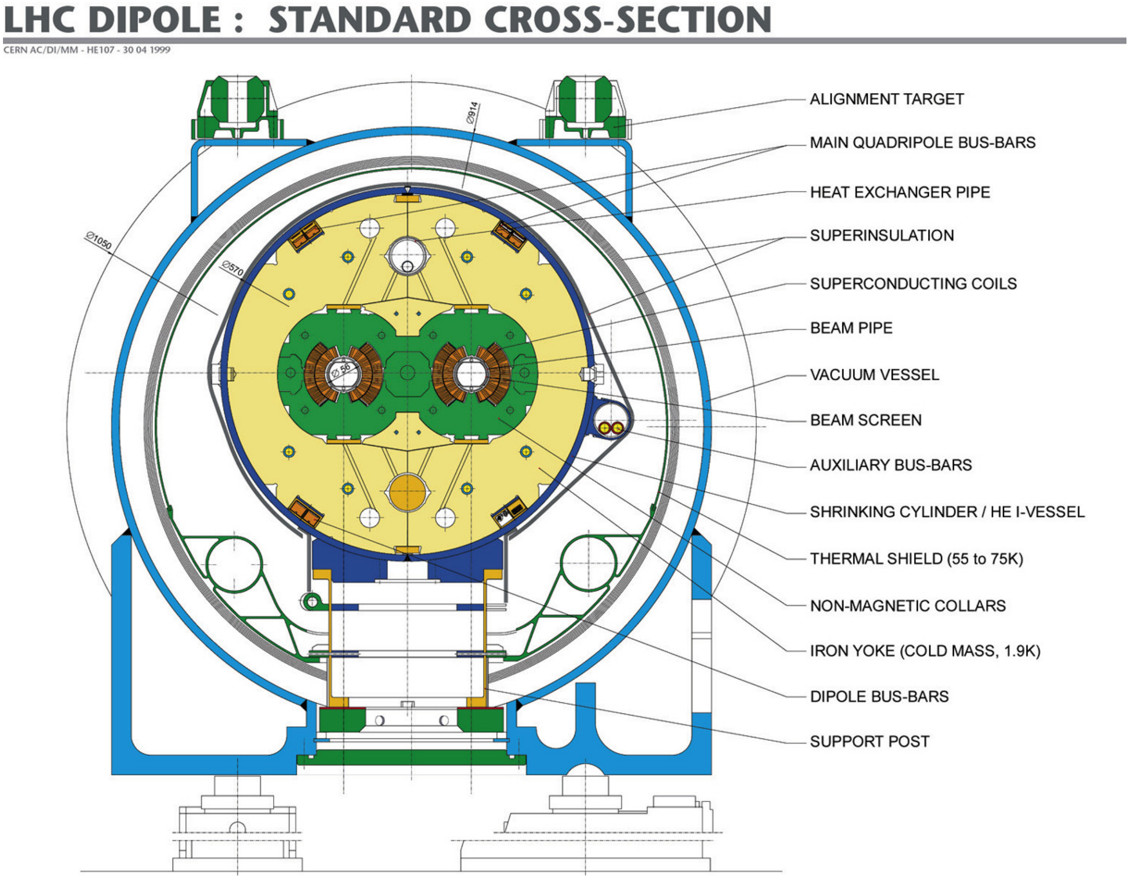

Figure 2.1.: Cross section of an LHC dipole magnet. All length scales are given in mm. Image taken from Ref. [27].

*Run-II* period, are the main focus of this thesis. Being the first data sets to ever be collected at $\sqrt{s} = 13$ TeV, they allow to probe a parameter space that was previously inaccessible, making them especially attractive for searches for new heavy particles. Fig. 2.2 summarizes the development of the integrated luminosity delivered by the LHC as measured with the CMS detector over time.

## 2.2. The CMS Detector

The CMS detector [22] is designed to allow for a reliable measurement of the energy and momenta of standard model particles originating from the particle collisions provided by the LHC. Its design was optimized with the search for the Higgs boson in mind, but has proven effective also for measurements of other SM processes, as well as searches for BSM particles. The key component for its physics performance is the large magnetic field of 3.8 T achieved by its central solenoid magnet. Measurements are performed using an array of subdetectors, which are housed within and around the solenoid coil. The subdetectors focus on four types of measurements: Tracking of charged particles close to the collision point, measurement of the energy of all charged particles, as well as neutral hadrons, and finally tracking of muons. Optimal performance is then achieved by combining the measurements from the independent

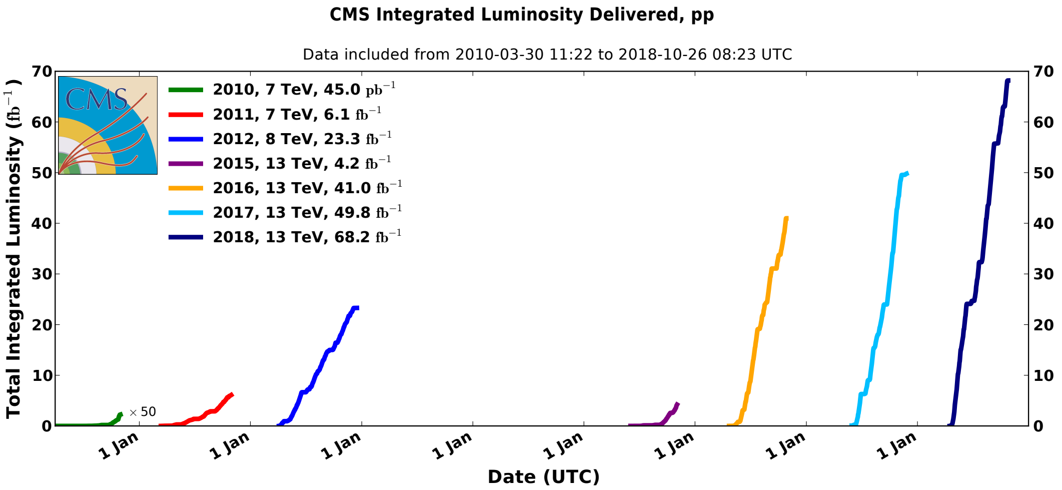

Figure 2.2.: Integrated luminosity delivered to the CMS experiment by the LHC between 2010 and 2018, as measured by CMS. Image taken from Ref. [28].

subdetectors to reconstruct the properties of individual particles. In this section, the detector layout and individual subdetectors are described. The exact components of the detector are subject to change and have evolved as upgrades to the initial detector hardware have been installed. Unless specifically noted, the descriptions in this section refer to the state of the detector during the running periods of 2015 and 2016, in which the data used analysis in subsequent chapters was taken.

## 2.2.1. Overall layout

The detector is approximately cylindrical, with the collision point in its center and its symmetry axis along the beam line. A cylindrical coordinate system is used with the z axis pointing along the beamline, the radial coordinate $r$ perpendicular to it, and the azimuth angle $\phi$ in the plane transverse to the beam axis. The geometric design of most detector components is split between the central *barrel* and forward *endcap* regions. The silicon tracking, as well as the electromagnetic and most of the hadronic calorimeters (ECAL and HCAL, respectively) are located within the free space $r < 3.2$ m inside the cylindrical solenoid coil, and each have different implementations for barrel and endcap. Detectors for muon tracking are located outside the solenoid and are embedded in an iron yoke, which serves to shape the magnetic field and provide structural support for the detector. The yoke consists of five cylindrical barrel *wheels* and two endcap *disks*, which can be moved independently and allow an opening of the detector for access to the modules within. A schematic view of the detector is shown in Fig. 2.3.

## 2.2.2. Magnet system

The active component of the CMS magnet [22, 30] is a superconducting solenoid coil. The current is conducted by a Rutherford cable made from niobium-titanium strands, which is embedded in an aluminum support structure. The support structure is essential to counter-

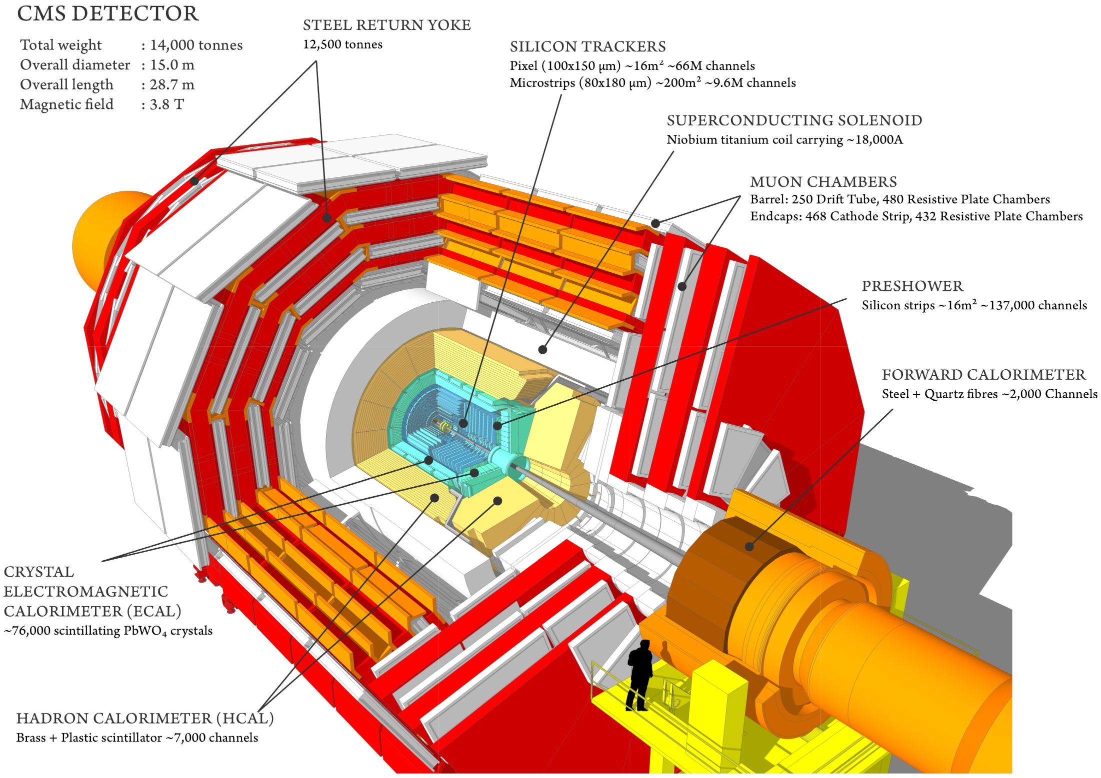

Figure 2.3.: Schematic cut-out view of the CMS detector. Image taken from Ref. [29].

act the mechanical forces induced by the magnetic field, and is thus a prerequisite for the relatively thin solenoid design. This design choice leaves maximal room for detector modules without compromising on the strength of the magnetic field. The coil is enclosed in an aluminum tank, which is cooled to an operating temperature of approximately 5 K using liquid helium. All included, the cooled magnet coil has an inner radius of 3.2 m, a thickness of 60 cm, and stores 2.6 GJ of energy at its nominal operating voltage of 19 kA. These parameters result in a homogeneous magnetic field of 3.8 T inside the coil, with magnetic field lines at the center of the detector oriented parallel to the beam axis. In this field configuration, the trajectories of charged particles are bent only in the transverse plane, allowing for a robust track-based measurement of their momenta.

### 2.2.3. Tracking system

The tracking system [22, 31] is the detector component mounted closest to the beam crossing point. Its outstanding precision gives it a central role in almost all aspects of particle reconstruction in CMS, and forms the basis for the particle flow reconstruction technique discussed in sec. 6.1. As the system is meant to allow track reconstruction close to the interaction point in the high-multiplicity LHC environment, its design is largely dictated by the occupancy aspect. Silicon detectors are chosen for their speed and the feasibility of highly granular module architectures. In all cases, the modules rely on a p-n junction as their sensitive area, in which traversing charged particles release ionization electrons and

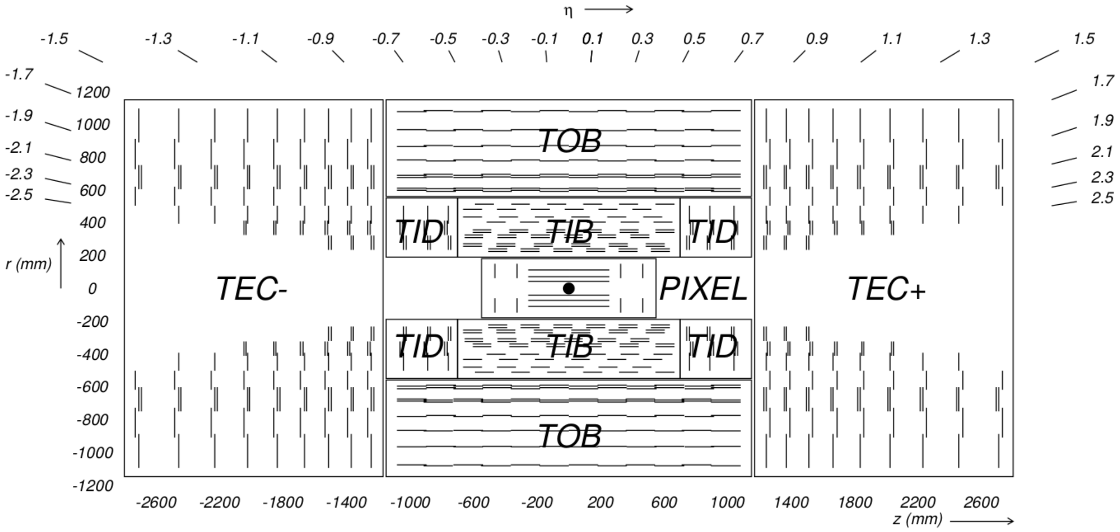

Figure 2.4.: Schematic showing the location and orientation of the CMS silicon tracking detector modules. The system is separated into the pixel part in the center, and surrounding strip detector, which in turn consists of an inner and outer component. The orthogonal module orientation in the barrel and endcap regions is designed to optimize the measurement for particles originating from the beamspot. The different parts of the system are referred to as *tracker inner barrel* (TIB), *tracker inner disks* (TID), *tracker outer barrel* (TOB) and *tracker endcap* (TEC±), with the plus or minus sign corresponding to the sign of the z coordinate. Image taken from Ref. [22].

holes, which can be detected. The subcomponents of the tracking system are separated into a barrel part with modules oriented parallel to the beamline, and an endcap part with modules oriented transverse to it. Very close to the interaction point, at $r < 20$ cm, the particle flux is very high, and a silicon pixel detector is used. By employing small pixel sizes of $150 \times 100\ \mu\text{m}^2$, it is possible to achieve sub-percent occupancies. Further away from the interaction point, the particle flux per area decreases and silicon strip detectors can be used. The strips have widths ranging from 80 to 180 μm and are mounted in multiple layers. A schematic view of the tracking detectors is shown in Fig. 2.4.

### 2.2.4. Electromagnetic calorimeter

The electromagnetic calorimeter [22, 32] is a homogeneous lead-tungstate calorimeter designed to measure the energies of electrons, photons, and charged hadrons. The ECAL is located around the inner tracking detectors, at a radius of 1.3 m from the beam line. In addition to the rate requirements imposed by the LHC bunch crossing frequency of 40 MHz, the calorimeter design is shaped by the space constraints inside the magnet coil. Lead tungstate is an ideal material to satisfy both of these requirements. With 85% of scintillation light being emitted within the bunch crossing time of 25 ns, there is little cross-contamination between adjacent bunch crossings. Additionally, at 0.89 cm, the radiation length of the material is short, allowing for a total of 25.8 radiation lengths in a compact crystal of 23 cm length. To provide similar coverage independent of $\eta$, each crystal is rotated so that it faces the beam crossing point. The sides of the crystals are polished so that scintillation light is focused towards the rear of the crystal, facing away from the beam line. The scintillation light is detected using avalanche photodiodes in the barrel, and vacuum phototriodes in the endcaps, both of which are well suited to an operation in a strong magnetic field. The exact device architectures for both readout types were specially developed for use with lead tungstate crystals: Their high quantum efficiency and intrinsic signal amplification compensate for the relatively low light yield of the crystals.

To provide improved granularity for the endcap system, an additional *preshower* detector is used. The preshower detector is a sampling calorimeter with lead absorbers and silicon strip readout. Two strip layers are placed orthogonally to each other, which allows for a precise, two-dimensional position measurement. Overall, the preshower has a thickness of three radiation lengths, which is thick enough to ensure that the majority of incident electrons and photons being showering, but thin enough so that showers are not contained within the preshower. The main measurement of the shower energy is still performed using the lead-tungstate devices, the preshower simply serves as a position monitor to improve the location measurement of incident particles, as well as a tool to resolve individual shower clusters. The latter task is especially important to distinguish the case of single incident photons from that of pions decaying to two nearby photons.

### 2.2.5. Hadron calorimeter

The hadron calorimeter [22, 33] consists of four parts: the barrel (HB), endcap (HE), outer (HO) and forward (HF) detectors.

#### 2.2.5.1. Barrel and endcap HCAL

The HB and HE detectors are sampling calorimeters located inside the magnet coil. Layers of 5 to 10 cm thick passive steel and brass absorber plates are interleaved with 5 mm thick active scintillator tiles. Upon interacting with the dense absorber material, incoming hadrons start forming showers, which then deposit energy in the scintillator tiles and thus induce light signals. The light from the scintillator tiles is extracted using wavelength shifting fibers, which are spliced to clear optical fibers outside the scintillator material. In the original HCAL design, the clear fibers transport the wavelength-shifted photons to hybrid photodiodes (HPDs), which are used for photon detection. Inside the HPDs, incoming photons strike a photo cathode, releasing an initial photo-electron, which is accelerated in a vacuum volume with a large electric field. The accelerated electron then hits a photodiode, releasing a large number of secondary electrons upon impact, as well as creating an avalanche inside the diode, which again releases further electrons. This method of utilizing two high-gain amplification steps rather than multiple lower gain steps results in a precisely known overall gain with small statistical fluctuations. As part of the *Phase-I* upgrade, the HPDs are being replaced by silicon photomultipliers (SiPMs) [34]. Each SiPM is approximately 2 mm$^2$ in size and consists of $\mathcal{O}(10^4)$ pixels, with each individual pixel being a Geiger-mode avalanche photodiode. The SiPMs require bias voltages of only $\approx 80$ V, compared to the HPDs, which are operated at voltages of $\mathcal{O}(\text{kV})$, but still deliver high gain, thus improving the operational stability of the devices. The upgrade was performed during in late 2016 /

early 2017 for the endcap detector, and will be performed during the LHC shutdown period from late 2018 to early 2020 (LS2) for the barrel.

#### 2.2.5.2. Outer HCAL

The HO detector covers the same pseudorapidity range as the HB, but is located just outside the magnet coil, before the first muon station. Light extraction is performed in the same way as for HE and HB, but no dedicated absorber is necessary, since incoming hadrons produce showers in the dense coil material. Detection of scintillation light is performed using SiPMs, as in the case of the upgrade HE/HB detectors. The HO serves to measure shower contributions not fully contained in the HB material, which appear more frequently at central pseudorapidities, as there is less material to traverse in this region. These contributions are increasingly relevant at higher hadron momenta and are especially important for a correct determination of $p_{\mathrm{T}}^{miss}$ in events with hard jets.

#### 2.2.5.3. Forward HCAL

The HF is the main component of the CMS detector covering the pseudorapidity range $|\eta| > 3.0$[2], which receives a much higher particle flux and corresponding radiation dose than any other. Consequently, the HO design is required to be as radiation hard as possible, while having reduced granularity requirements. A massive steel block is used as an absorber to achieve high stopping power. Since the scintillator tiles used in the other parts of the HCAL are not sufficiently radiation hard, the HF relies on quartz fibers to extract Cerenkov light emitted by charged shower constituents. As there is no dedicated ECAL in the very forward region, the HF serves to detect both electromagnetic and hadronic showers. The two are differentiated by the use of quartz fibers of different lengths. Long fibers, which cross the full absorber will obtain signals for all showers in the absorber, while shorter fibers starting further away from the interaction point are only sensitive to hadronic showers, which tend to have higher longitudinal extent. By comparing the light signal in long and short fibers, it is possible to distinguish whether the incident particle was a hadron or an electron/photon.

### 2.2.6. Muon system

The muon system [22, 37] consists of three types of detectors: Drift tubes (DTs), cathode strip chambers (CSCs), and resistive plate chambers (RPCs). As muons with $p_{\mathrm{T}} > 1$ GeV can effectively not be stopped at the length scales of the CMS detector, all three detector technologies rely on the detection of ionization electrons freed by muons passing through gas. The different detector architectures are employed to cover the different environments of the barrel and endcap regions, and allow for precise offline particle reconstruction as well as fast and accurate online triggering decisions. During LS2, gas electron multiplier (GEM) chambers will additionally be installed to provide redundant coverage in the region $1.6 < |\eta| < 2.2$ [38].

---

[2] At even larger absolute pseudorapidities, the CT-PPS [35] and CASTOR subdetectors [36] have been installed to allow for the study of very forward phenomena, such as the behavior of beam particle remnants. Due to their specialized nature, these components are not immediately relevant for the general-purpose detector operation.

### 2.2.6.1. Drift tubes

The barrel region of the detector is instrumented with DTs. At the heart of each DT module lies a large number of individual drift cells, which contain an anode wire, as well as the cathode strips and drift gas. The cells are approximately 2.4 m in length in the direction of the anode wire, with a width of approximately 42 mm between cathodes, which are mounted on the cell walls, and a height of 13 mm. In addition to the cathode strips, additional electrode strips are mounted to the unoccupied cell sides to shape the electric field and stabilize it against perturbations by the magnetic field. The design goal of the electric field shape is simple: The field should be strong close to the anode wire to allow for signal amplification, but weak further away from it, so that the initial ionization electrons travel unimpeded. This field configuration is matched with a gas mixture of 85% Ar and 15% $CO_2$, which provides sufficiently small ionization energies and drift times fast enough to suppress the probability of multiple overlapping drift periods. This working principle ensures that there is a linear relationship between the distance of the initial ionization from the wire, and the drift time needed to reach the wire. A measurement of the signal's detection time at the wire then allows for the reconstruction of the drift time using the known drift velocity. Because of the cell symmetry, the signal from individual cells alone cannot be used to measure arrival time and position at once. Additionally, there is an ambiguity in the position determination, as only the distance to the wire, but not the incident direction, is measured. Therefore, the individual cells are organized in layers, with four layers being combined into a "super-layer" (SL). By combining the timing measurement from the stacked cells, it is possible to obtain a simultaneous measurement of the muon arrival time, position and traversal direction. To allow for a measurement of both the $\phi$ and z coordinates of the path of a traversing muon, two or three SLs are rotated relative to each other and combined into one chamber. The chambers are placed in rings around the solenoid coil, with the first ring located between the coil and the iron yoke, two layers of chambers located in gaps inside the iron yoke, and a final layer outside the yoke. This placement outside the magnet and surrounded by the return yoke serves to greatly reduce the local magnetic field inside the chambers. Additionally, the substantial material budget constituted by the calorimeters, the magnet coil and iron yoke ensures a relatively low particle flux in the DTs, and avoids overly high occupancies that would prevent the detection of individual ionization events.

### 2.2.6.2. Cathode strip chambers

In the endcap region, drift tubes would not be an optimal choice, as the increased rate of incoming particles, as well as the partially strong and inhomogeneous magnetic field would spoil the drift-based measurement. Instead, CSCs are used. As in the case of DTs, CSCs use anode wires and cathode strips to generate electric fields and collect signal electrons from gas ionization. Rather than using independent measurement cells, CSCs rely on larger gas volumes instrumented with a number of wires and cathode strips, which are positioned so close together that primary electrons immediately trigger local avalanches. The strips are oriented radially outward from the beamline, with orthogonal wires in the azimuthal $\phi$ direction. By measuring voltage signals on both the wires and strips, a two-dimensional position measurement is obtained, and the resolution in the $\phi$ direction can additionally be improved by considering the charge distribution on adjacent strips. Based on the shape of this distribution, the most likely coordinate of the initial ionization can be estimated with a better precision than the physical strip spacing. Full CSC chambers are constructed as a prismatic stack of six instrumented gas volumes separated by cathode strip panels, which are combined into disks around the beamline, covering the full $\phi$ range. A total of four disks is placed parallel to each other in each of the endcaps.

#### 2.2.6.3. Resistive plate chambers

In addition to precise reconstruction of the position of muon hits, online event triggering requires an unambiguous association of each muon to an LHC bunch crossing. This timing information is obtained with RPCs, which can achieve a time resolution of a few ns. RPCs are gas-filled parallel plate capacitors with a small gas gap of 2 mm width, which are operated with a very high voltage of 8.5 to 9 kV, close to their breakthrough point. To prevent continuous breakdown, the capacitor plates are made of high-resistivity plastic, and a *double-gap* geometry is used, which simply means that there are gas gaps on both sides of the readout anode. This choice of geometry effectively doubles the signal size per incident particle and thus allows for a reduction in voltage, and therefore in breakdown probability, without loss of signal quality. Gas ionization from traversing muons immediately leads to avalanche creation, and causes an almost instantaneous mirror-charge signal on the anode. By segmenting the anode strips, a one-dimensional position measurement is possible. For this fast operation mode, it is imperative to avoid a spread of the ionization avalanche throughout the full sensitive gas volume, which gives a lower limit on the admissible ionization energy of the gas mixture. At the same time, the size of ionization clusters has to be so small that only a small number of neighbouring strips records the same ionization event, and other strips remain sensitive for further signals.

## 2.3. Data acquisition

Due to the large number of active channels in the full CMS detector, a single event, consisting of multiple simultaneous proton-proton collisions, produces $\mathcal{O}(1\text{ Mb})$ of data. As the LHC delivers proton-proton events at a rate of 40 MHz, a full recording of all events with CMS would imply a bandwidth of $\mathcal{O}(40\text{ Tb/s})$, which would quickly overwhelm any affordable readout and data storage system. Additionally, the dominant fraction of these events are low-$p_\mathrm{T}$ QCD scattering events, which are not very interesting for the study of the Higgs and gauge bosons, or searches for heavy new particles. To preferentially store events from the rare, interesting processes with large momentum transfer, and significantly reduce the necessary data storage capabilities, a two-stage triggering system is used [39]. Even with the rate reduction achieved through triggering, efficient handling of the selected events is necessary, and a multiple-stage computing architecture is used to perform this task [22, 40].

### 2.3.1. The Level-1 trigger

The Level-1 (L1) trigger is a fast, hardware-based selection system designed to quickly reduce the event rate from 40 MHz to $< 100$ kHz. It is based on a reduced readout of the calorimeter and muon systems, which allows for a coarse identification of all interesting types of physics objects. The silicon tracker is not read out at this stage as the track reconstruction algorithms necessary to make sense of its signals would require too much time to be run.

However, track reconstruction is performed in the muon system, which is possible due to the significantly lower hit multiplicities. The L1 trigger checks for a variety of individual signatures (such as “at least one electron with $p_{\mathrm{T}} > 100$ GeV”, or “at least two muons with $p_{\mathrm{T}} > 15$ GeV”) and accepts the event for further analysis if at least one of the pre-defined criteria is passed.

### 2.3.2. The High-Level trigger

The high-level trigger (HLT) is a software-based selection system. In contrast to the L1 trigger, the full detector information is read out and a more fine-grained reconstruction of objects is performed, including the time-consuming track reconstruction, which would not be possible without the significant rate reduction obtained in the L1 trigger. The read-out of the detector is a major task, as the information from hundreds of individual data sources needs to be read out in parallel and assembled into a consistent set of event data [41]. In a similar manner to before, the HLT tests a number of independent sets of selection criteria, which are matched to the corresponding less-refined L1 criteria. The combined set of L1 and HLT criteria for a given signature is referred to as a *trigger path*. Again, an event is kept if it is accepted by any of the trigger paths. The HLT reduces the rate of events from 100 kHz to $\approx 1$ kHz, which are then recorded for offline analysis.

### 2.3.3. Data processing and storage

If a collision event is selected by the HLT, the full detector information is read out and sent in real-time to the so-called CMS *Tier-0* (T0) computing center at CERN, where it is stored on tape and an initial reconstruction (“prompt reconstruction”) is performed. The T0 center serves as a buffer between CMS and computing centers across the world. The events are split into data sets depending on what type of trigger path was fired, with e.g. events passing a two-muon trigger path being sorted into the *DoubleMuon* data stream. The data sets are then replicated to the remote *Tier-1* (T1) centers, where the raw event data is once again archived on tape to provide redundant storage of the raw information. The T1 centers are also used to reconstruct the raw data again once all calibrations are available (“re-reconstruction”). Finally, a larger number of *Tier-2* (T2) centers hosted by CMS member groups provides the computing infrastructure for analysis users.

# 3. Theoretical background

## 3.1. The standard model of particle physics

The standard model of particle physics (SM) is a quantum field theory (QFT) that describes the interactions of leptons and quarks, as well as the gauge and Higgs bosons. The specific behaviors of the electroweak and strong interactions are encoded in the $SU(3)\times SU(2)\times U(1)$ group structure of the model. By assigning all matter fields to be part of singlets, doublets, or triplets of the respective groups, their participation or non-participation in a given type of interaction can be understood. The interactions are mediated by spin-1 gauge bosons, which arise as a result of the enforcement of local gauge symmetry in each of the groups. *Spontaneous symmetry breaking* of the local $SU(2)$ gauge symmetry generates the masses of the W and Z bosons, as well as those of the fermions. The scalar sector required for the minimal spontaneous symmetry breaking mechanism manifests itself in the physical Higgs boson, which is the only elementary spin-0 particle in the theory. For reviews of QFT in general, and the SM specifically, see Refs. [42–44].

### 3.1.1. Successes of the SM

The SM has been successful in describing a great number of particle physics phenomena over a large range of energy scales (for a nice summary of the theory and its experimental tests, see Ref. [45]). Especially the understanding of the electroweak interaction has been tested with a high degree of precision. Its main characteristic feature in the SM is the so-called V-A structure, which results in maximal parity violation in charged-current interactions: The W boson exclusively couples to left-handed particles and right-handed antiparticles. This feature has dramatic observable consequences, such as the angular distributions of electrons from $\beta$ decay [46], positron polarisation in $\mu^+$ decays [47], and the helicity suppression of charged pion decays to electrons $\pi^\pm \to \mathrm{e}^+\nu_\mathrm{e}/\mathrm{e}^-\bar{\nu}_\mathrm{e}$ [48]. Beyond being able to correctly describe these low-energy phenomena, measurements of the properties of the Z boson have shown remarkable agreement with SM predictions [49]. Through the study of $\mathrm{W}^+\mathrm{W}^-$ production in electron-positron collisions at LEP-II, it was further possible to probe the couplings of the gauge bosons with one another. The $\sqrt{s}$ dependence of the $\mathrm{e}^+\mathrm{e}^- \to \mathrm{W}^+\mathrm{W}^-$ process is critically sensitive to the $\gamma$WW and ZWW couplings, which were again found to precisely agree with SM predictions [50]. Finally, the Higgs boson, which is a direct consequence of the electroweak symmetry breaking mechanism in the SM, was observed directly at the LHC [24, 25], and its properties seem to be consistent with the SM prediction [26]. This non-exhaustive list showcases the sweeping success the SM can claim in describing the properties and interactions of the known particles.

### 3.1.2. Open questions

Open issues with the SM can be characterized as belonging to one of three groups: Theoretical issues, conflicting measurements, and incompleteness. The most frequently cited theoretical issue with the SM is the *hierarchy problem*, which denotes the apparent weakness of gravity relative to the electroweak and strong forces. This hierarchy of strengths translates into a hierarchy of characteristic energy scales, with the Planck mass $M_{Pl} \approx 10^{19}$ GeV being the characteristic scale of gravity. This becomes problematic due to radiative corrections to the mass of the SM Higgs boson: If there is no new physics below the Planck scale, radiative corrections would be of order $M_{Pl}$ [51]. The observed Higgs mass value of $m_h \approx 125$ GeV $\ll M_{Pl}$ then implies the existence of new physics below the Planck scale, or an immense *fine-tuning* of the parameters. While this issue warrants study, it is not clear that it requires a resolution via new physics. Some authors believe that apparent fine-tuning indicates a lack of fundamental understanding [52], while others argue that this argument is aesthetic rather than scientific, and should be discarded [53].

Stronger conclusions can be derived from measurements conflicting with SM predictions. The longest standing anomaly is that of the muon magnetic moment $g_\mu$, which is measured with an astounding precision of 0.6 ppm, and disagrees significantly from the expected theoretical value [54], while no deviation is observed for the electron. More recently, observations of B meson decays involving pairs of leptons have also shown deviations from the SM predictions. The SM implies lepton flavour universality, which means leptons of different flavours are expected to behave in the same way, with differences being only due to the non-identical masses. In measurements at LHCb, multiple search channels show apparent violations of lepton flavour universality, as evidenced by mismatched branching fractions for different lepton flavours [55, 56]. Additionally, the angular distributions in one of the relevant decay channels seem inconsistent with the SM prediction [57]. In both the $g_\mu$ and LHCb cases, the effects are significant, but not yet strong enough to rule out random coincidences. Additionally, the SM predictions for both effects rely on modeling of hadronic effects, which are not as well understood as purely electroweak calculations.

Finally, the SM is clearly incomplete in its coverage of nature. The most blatant omission is gravity, which has been observed on distances between a few centimeters and cosmological scales. It is unknown today how general relativity, which is successful in describing gravity at these large distance scales, relates to the SM. While irrelevant at low energies $E \ll M_{Pl}$, a quantum theory of gravity will be necessary to understand physics closer to the Planck scale. Beyond gravity, the SM also omits any treatment of finite neutrino masses, which have been detected experimentally through the observation of neutrino flavour oscillations [58]. The generation of neutrino mass terms would imply either the existence of right-handed neutrinos, which were previously not thought to exist, or a Majorana nature of the neutrinos (for an introduction, see Ref. [59]). Especially the case of Majorana neutrinos would have wide-ranging consequences, as lepton number violating processes such as neutrinoless double beta decay would be possible. Most relevent for this thesis, however, is the existence of DM, which has already been motivated in detail in sec. 1.2 and is one of the most pressing questions today. The observed properties of DM in the universe seem consistent with DM being composed of particles. While the SM contributes to DM through neutrinos, their masses are known to be much too small to be able to account for the full DM budget. Therefore, if DM is made of particles, these particles must be new particles, as-of-yet unknown to us.

Non-particle DM candidates exist, with one example being primordial black holes, although it is not clear how these would be produced in sufficient abundance to account for the observed DM related phenomena. In all of the cases discussed here, evidence seems to point towards the existence of some kind of new physics. However, taking into account possible alternative interpretations, no single "smoking gun" piece of evidence is known that would firmly establish the existence of physics beyond the SM.

## 3.2. Perturbation theory and renormalization

The calculation of scattering amplitudes in QFT is inherently complicated by the fact that there is no upper limit on the complexity of the interactions between two particles. While an electron-electron interaction, for example, can occur via a single exchange of a photon, it may also involve any other arbitrary number of photons, as shown in Fig. 3.1. Fortunately, this complication is resolved over most of the SM energy range by the fact that the relevant interactions are sufficiently weak, and particle interactions can be expressed as small corrections to the non-interacting theory (For detailed introductions to the topics of this section, refer again to Refs. [42–44]). Scattering amplitudes can then be written as infinite series terms with increasing powers of the coupling parameters, which can be understood to each represent an individual Feynman diagram. If the coupling parameter is sufficiently small, the series converges quickly and a calculation involving only the leading terms will already be a good approximation of the full result.

An additional complication arises from the existence of loop diagrams, which require the calculation of an integral over the momentum of the particle in the loop. The integration must in principle be executed up to infinite momenta, which can cause the integrals to diverge and provide nonsensical results. This phenomenon is understood to be the result of the incorrect assumption that the parameters of the theory are constants. The calculations are amended by *renormalization*, which is implemented by adding counter-terms to the integration that cancel the pathological divergences. The counter-terms can then be absorbed into a redefinition of the theoretical parameters, such as the strong coupling $\alpha_S$. This procedure results in a scale dependence of the parameter $\alpha_S \rightarrow \alpha_S(\mu_R)$ ("running coupling"), where $\mu_R$ is the renormalization scale. The dependence of the parameters on $\mu_R$ is calculable using the renormalization group equation, and cancels if all orders of the perturbative series are taken into account. However, in real applications of finite-order calculations, there is an ambiguity in the choice of $\mu_R$, which results in an effective uncertainty on the calculation results (cf. sec. 7.5.2).

## 3.3. Factorization and parton distribution functions

One of the fundamental aspects relevant to physics at the LHC is the fact that the beam protons are not fundamental, and the collision energy is sufficiently high to resolve their substructure. Naively, this aspect is of course daunting, as one could suspect that the non-perturbative interactions between the proton constituents could spoil any predictability of the outcome of proton-proton interactions. Fortunately, this is not the case, as *factorization* allows to separate the high-momentum "hard" interaction from the low-momentum dynamics inside the proton. In the parton picture, this feature can be understood as a consequence

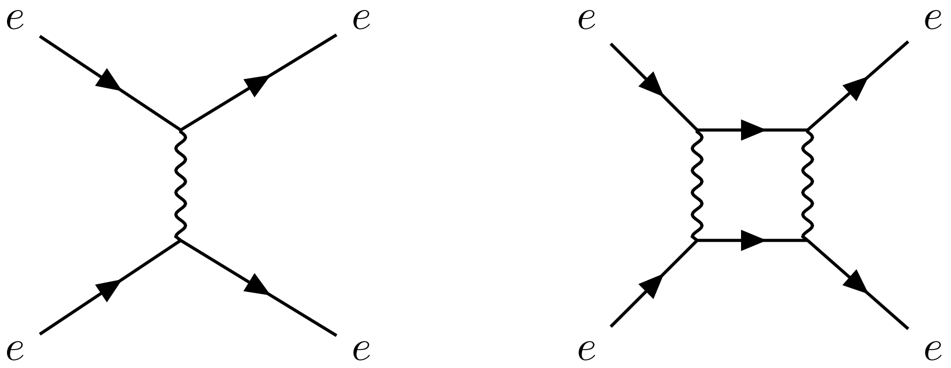

Figure 3.1.: Example Feynman diagrams for electron-electron scattering under exchange of one (left) or two photons (right). The straight solid lines indicate fermions, here electrons, and wavy lines indicate bosons, photons in this specific case. The time axis goes from left to right. By adding additional particle exchanges, particle interactions can become arbitrarily complicated. However, for weak interaction strengths, it is sufficient to consider low-multiplicity interactions to arrive at approximately correct results.

of the difference in time scales of the two interaction types [60]. While there are abundant parton-parton interactions happening within each individual proton, they are slowed down by the relativistic dilation of the passage of time inside the proton relative to the laboratory frame. As a result, the inner state of each proton can be approximated as constant over the time scale of a hard proton-proton interaction, which happens much faster. The description of the hard interaction itself is possible because of the running of the strong coupling $\alpha_S$: At high momentum transfers, the coupling is weak, interactions become perturbative and the partons can be treated as effectively free, individual particles ("asymptotic freedom"). The cross section of the full process can be written as a sum over individual parton process cross sections for the hard process convoluted with a parton distribution function (PDF) which encodes the probability to find a parton of a given type with a given momentum inside the proton [61]:

$$\sigma = \sum_{\text{Partons}} \int dx_1 \int dx_2 \; f_1(x_1,\, \mu_F^2)\; f_2(x_2,\, \mu_F^2)\; \hat{\sigma}(x_1\sqrt{s}/2,\, x_2\sqrt{s}/2\,, \mu_R) \tag{3.1}$$

Here, $\mu_F$ is the factorization scale, $x_i$ is the fraction of the total proton momentum carried by parton $i$, $f_i$ is the PDF associated to that parton, and $\hat{\sigma}$ is the parton-parton cross section for the hard process. The sum indicates that the total cross section is calculated as the combination of contributions for all possible incoming parton species. The formula given here is accurate only at the leading perturbative order. At higher orders, factorization still holds, but the mathematical implementation becomes more complicated and PDFs cannot be interpreted as straightforward probability densities. Like the renormalization scale, the factorization scale is an unphysical parameter and induces an uncertainty in calculation results, which is taken into account by varying it around a nominal value (cf. sec. 7.5.2).

In order to calculate the cross sections for any inelastic process at the LHC, one needs to obtain PDF values, which are unfortunately not calculable from first principles. While it is possible to derive the scale dependence of a PDF, its dependence on the Bjorken-x variables can only be obtained from measurements. Today's knowledge of the proton PDF is dominantly based on deep inelastic scattering data from HERA [62], but LHC-based measurements have begun to contribute in recent years [63]. Since PDFs are based on measurements, there are associated uncertainties, which have to be propagated to the final results of any computation. The calculation of PDF uncertainties is further discussed in sec. 7.5.2.

# 4. Signal models

A focus of this thesis is the interpretation of analysis results in specific models of new physics. In this section, the signal models are introduced, the terminology is defined, and preparatory studies are presented, which are a prerequisite for the final interpretations.

## 4.1. Dark matter mediators with couplings to quarks

One of the simplest scenarios for DM production at the LHC is that of a single bosonic mediator that couples to the SM quarks as well as the DM particle $\chi$. The mediator serves as a portal between the SM and the dark sector [1] and defines the way DM is produced. By considering different hypotheses for the properties of the mediator and its coupling structure to different particles, a large range of experimental signatures can be described. This type of model, where only the particles relevant to the specific interaction under study are included, and the interaction is described in an ultraviolet complete manner, is referred to as a *simplified model* [64].

While the ability to cover many collider searches with one model is attractive, care has to be taken in order not to violate constraints from well-established sectors of physics. Particularly, the introduction of new bosons can give rise to enhanced flavour-changing neutral currents, which are already strongly constrained by measurements of flavour observables such as $K^0 - \bar{K}^0$ mixing. To avoid the possibility of such violations entirely, the simplified models are designed to obey *Minimal flavour violation* (MFV) [65]. MFV simply requires that flavour and CP violation in the extended theory follow from terms containing the CKM or Yukawa matrices. MFV variation is implemented in different ways for the different scenarios described below.

In this search, scenarios with a single spin-0 or spin-1 mediator and a Dirac fermion DM candidate are considered. The implementation of Refs. [66–68] is used, and the topology is therefore referred to as DMSimp in the following. Formulas for the relevant Lagrangian terms, as well as those for the mediator widths are obtained from Ref. [69]. Example Feynman diagrams for associated production of DM particles and a Z boson in this model are shown in Fig. 4.1. Unless otherwise specified, the mediator is assumed decay with experimentally negligible decay length. The DM candidate is assumed to be stable, and a singlet under the SM gauge groups.

---

[1] *Dark sector* refers to the full set of particles that either make up the DM component of the universe, or interact only with this component, but not the SM particles.

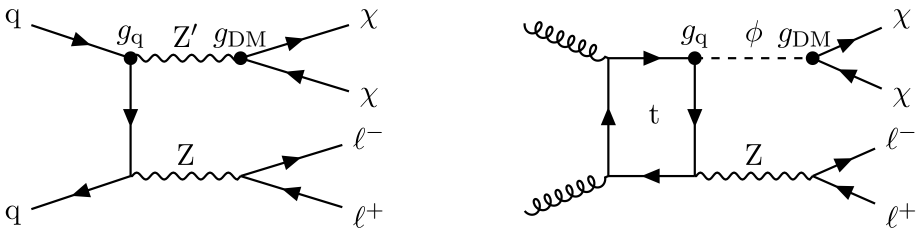

Figure 4.1.: Example Feynman graphs for the DMSimp model with a spin-1 mediator ($Z'$, left) and spin-0 mediator ($\phi$, right). DM particles are produced via a mediator that couples to SM quarks. The Z boson is produced by radiation from an SM quark line and is not immediately related to the DM production mechanism. Note that while all quark flavours could contribute to the loop on the right-hand side, only top quarks give a significant contribution.

### 4.1.1. Spin-1 mediators

In the spin-1 case, MFV is implemented by setting the quark couplings to flavour-independent values:

$$\mathcal{L} \subset \sum_{\mathrm{q}} Z'_\mu \bar{\mathrm{q}} \gamma^\mu (g_q^V - g_q^A \gamma_5) \mathrm{q} - Z'_\mu \bar{\chi} \gamma^\mu (g_{DM}^V - g_{DM}^A \gamma_5) \chi \,, \tag{4.1}$$

where $Z'_\mu$ is the DM mediator, $\chi$ is the DM candidate, and q/$\bar{\mathrm{q}}$ denote the SM quarks. The free parameters are the masses $m_{med}$ and $m_{DM}$ of mediator and DM candidate, as well as the four coupling parameters $g_q^V$, $g_q^A$, $g_{DM}^V$ and $g_{DM}^A$, which define the chiral properties of the mediator coupling to the SM quarks and DM candidate. This interaction structure is a generalized version of the SM Z boson, which couples to SM fermions with a mixture of axial-vector (A) and vector (V) couplings. In order to simplify the parameter space, only mediators with pure A couplings ($g_q^A \neq 0$, $g_{DM}^A \neq 0$, but $g_q^V = g_{DM}^V = 0$) or pure V couplings ($g_q^V \neq 0$, $g_{DM}^V \neq 0$, but $g_q^A = g_{DM}^A = 0$) are considered. Additionally the quark couplings are assumed to be identical for all quark flavours. The coupling shorthands $g_q$ and $g_{DM}$ are used to represent the A or V couplings in either case:

$$\mathcal{L}_V \subset g_q \sum_{\mathrm{q}} Z'_\mu \bar{\mathrm{q}} \gamma^\mu \mathrm{q} - g_{DM} Z'_\mu \bar{\chi} \gamma^\mu \chi \,, \tag{4.2}$$

and

$$\mathcal{L}_A \subset -g_q \sum_{\mathrm{q}} Z'_\mu \bar{\mathrm{q}} \gamma^\mu \gamma_5 \mathrm{q} + g_{DM} Z'_\mu \bar{\chi} \gamma^\mu \gamma_5 \chi \,. \tag{4.3}$$

This choice of couplings reduces the number of free parameters to four: $m_{DM}$, $m_{med}$, $g_q$ and $g_{DM}$. As soon as these parameters are specified, the width of the mediator can be calculated analytically by summing over the contributions from all fermions (SM quarks and DM particles, in this case, but an extension to leptons would be straightforward). The individual contributions depend on the color factor $N_f^c$ for a given fermion, as well as its mass, the dependence on which can be parameterized as a function of $z_f = \left(\frac{m_f}{m_{med}}\right)^2$ [69]:

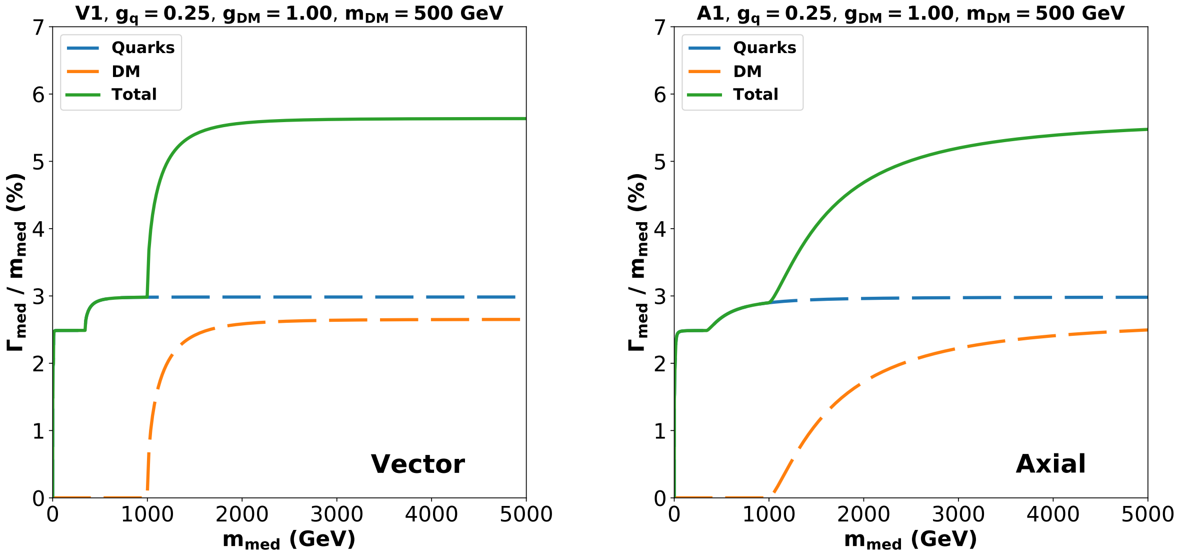

Figure 4.2.: Relative width of the mediator in the DMSimp models as a function of the mediator mass for a vector (left) and axial-vector mediator (right). The other free parameters of the model are set to constant values of $g_q = 0.25$, $g_{DM} = 1$ and $m_{DM} = 500$ GeV. The curves in both coupling scenarios converge to the same numerical values for $m_{med} \gg m_{DM}$, but do so at different rates. The "turn-on" behavior is significantly slower in the axial-vector case.

$$\frac{\Gamma_{A/V}}{m_{med}} = \sum_{f=\mathrm{q},\chi} \frac{g_f^2 N_f^c}{12\pi} \times (1-4z_f)^{\frac{3}{2}-n} \times (1+2z_f)^n, \text{ with } n = \begin{cases} 0, \text{axial-vector} \\ 1, \text{vector} \end{cases} \tag{4.4}$$

The contributions to the total width from quarks and DM couplings are shown in Fig. 4.2. The coupling values $g_q = 0.25$ and $g_{DM} = 1$ are chosen in accord with the "A1" and "V1" scenarios proposed by the LHC dark matter working group (DMWG) [70]. The width contributions from a given particle species $f$ is zero as long as $m_f > m_{med}/2$. As $m_{med}$ increases above this threshold, a width contribution appears and the decay of the mediator to that fermion species opens up. Note that in both the vector and axial-vector scenarios, the width terms converge towards the same values for $z_f \to 0$ (equivalently $m_{med}/m_{DM} \to \infty$), but do so with a different functional dependence on $z_f$. The "turn-on" is relatively sharp in the vector mediator case, and more drawn-out for an axial-vector coupling. The $p_{\mathrm{T}}^{miss}$ spectra for this model are shown in Fig. 4.3.

#### 4.1.1.1. Relationship between signal cross section and coupling parameters

The result of a search for a given signal of new physics is usually quantified by quoting the observed value of the signal strength $\mu$, which corresponds to the ratio of the observed and predicted signal cross sections. In the case where no significant signal is observed, the results are framed as an exclusion limit on the $\mu$ parameter. In both cases, it is interesting

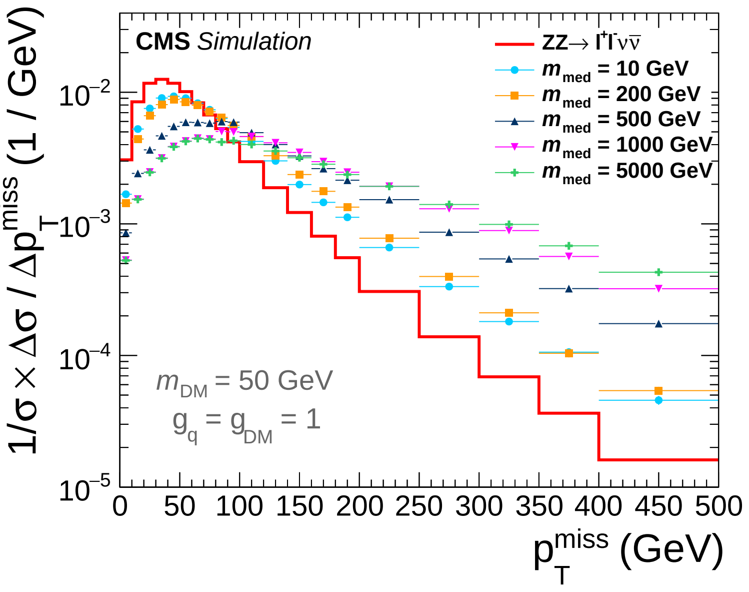

Figure 4.3.: Normalized generator-level $p_{\mathrm{T}}^{miss}$ distribution for the simplified model with a spin-1 vector mediator with $g_q = g_{DM} = 1.0$, $m_{DM} = 50$ GeV, and various values of $m_{med}$. The red solid line shows the $p_{\mathrm{T}}^{miss}$ spectrum of the SM ZZ process, which is the leading background. The $p_{\mathrm{T}}^{miss}$ spectrum becomes successively harder with increasing $m_{med}$.

to translate the observed signal strength into the space of the coupling parameters $g_q$ and $g_\chi$. In order to derive limits on the couplings $g_q$ and $g_\chi$, it is helpful to consider the analytical dependence of the signal cross section on the couplings. Since the mediator is always produced from a quark-antiquark-mediator vertex, its production cross section is necessarily proportional to $g_q^2$. An additional coupling dependence is incurred in the mediator decay, where the branching fraction to invisible particles is given by the ratio of the partial width $\Gamma_\chi$, which depends on $g_\chi$, and the total width $\Gamma_{tot}$, which depends on $g_\chi$ as well as $g_q$:

$$\sigma \times \mathrm{BR} \quad \propto \quad g_q^2 \times \frac{\Gamma_\chi(g_\chi)}{\Gamma_{tot}(g_\chi, g_q)} \ . \tag{4.5}$$

In a typical case, one would generate a signal sample for fixed values of $g_q^{gen}$ and $g_\chi^{gen}$ and process the sample through the experimental analysis to determine the exclusion limit on the signal strength $\mu$. The signal strength limit can then be translated into a coupling limit by expressing $\mu$ using the proportionality relation above:

$$\mu = \frac{(\sigma \times \mathrm{BR})_{obs}}{(\sigma \times \mathrm{BR})_{gen}} = \frac{\left(g_q^2 \frac{\Gamma_\chi(g_\chi)}{\Gamma_\mathrm{q}(g_q)+\Gamma_\chi(g_\chi)}\right)_{obs}}{\left(g_q^2 \frac{\Gamma_\chi(g_\chi)}{\Gamma_\mathrm{q}(g_q)+\Gamma_\chi(g_\chi)}\right)_{gen}} \ . \tag{4.6}$$

The labels *gen* and *obs* are short for *generated* and *observed*, respectively. Keeping one of the couplings $g_\chi$ and $g_q$ fixed, the analytical expressions for $\Gamma_{\chi/\mathrm{q}}$ from eq. 4.4 can be inserted and the equation can be solved algebraically for the excluded value of the other coupling.

To make the expression more readable, variables are understood to represent the generated values unless specified otherwise, and the "gen" label is dropped:

$$g_q^{obs} = \sqrt{\frac{\mu \times \Gamma_\chi}{C g_\chi^2 - \gamma_\mathrm{q} \times \mu}}, \quad g_\chi^{obs} = \sqrt{\frac{\mu \times \Gamma_\mathrm{q}}{C g_q^2 - \gamma_\chi \times \mu}}\,, \tag{4.7}$$

with

$$C = \frac{\Gamma_\chi + \Gamma_\mathrm{q}}{(g_q g_\chi)^2}, \quad \gamma_i = \frac{\Gamma_i}{g_i^2}\,.$$

Since the coupling is defined as a real number, this solution of course requires that the term under the root is positive. This requirement effectively creates a maximum signal strength value $\mu_{max}$ for which a coupling value can still be derived:

$$\mu_{max} = \begin{cases} 1 + \left(\frac{\Gamma_\chi}{\Gamma_q}\right)_{generated}, & \text{when deriving a } g_q \text{ value} \\ \\ 1 + \left(\frac{\Gamma_q}{\Gamma_\chi}\right)_{generated}, & \text{when deriving a } g_\chi \text{ value} \end{cases}\,. \tag{4.8}$$

In the parameter space with $m_{med} \gg m_{DM}$, where this analysis is most sensitive, the default choices of $g_q = 0.25$ and $g_\chi = 1.0$ imply $\Gamma_\chi \approx \Gamma_q$ and therefore $\mu_{max} \approx 2$. The reason for this boundary is that the expression for $\sigma \times \mathrm{BR}$ eventually saturates since the coupling dependence in the numerators and denominators of eq. 4.7 cancels in the limit of $g_q \to \infty$ or $g_\chi \to \infty$. This implies that no arbitrarily large signal strength values can be accommodated by varying only one coupling parameter, and it would be necessary to vary both parameters at the same time.

The exact behavior of the translation from the signal strength to the coupling values is shown in Fig. 4.4. For a signal strength of $\mu = 1$, the resulting coupling values are identical to the input coupling values. For $\mu \to \mu_{max}$, the translation function diverges and no coupling value can be deduced. Note that this divergence has a dependence on the mediator mass due to the top mass threshold: The ratio of the $\Gamma_\chi$ and $\Gamma_q$ terms is different below and above the threshold, which has opposite effects on the resulting $g_\chi$ and $g_q$ values (cf. eq. 4.8). In the limit of $\mu \to 0$, the behavior simplifies again and the observed coupling values scale as $\sqrt{\mu}$.

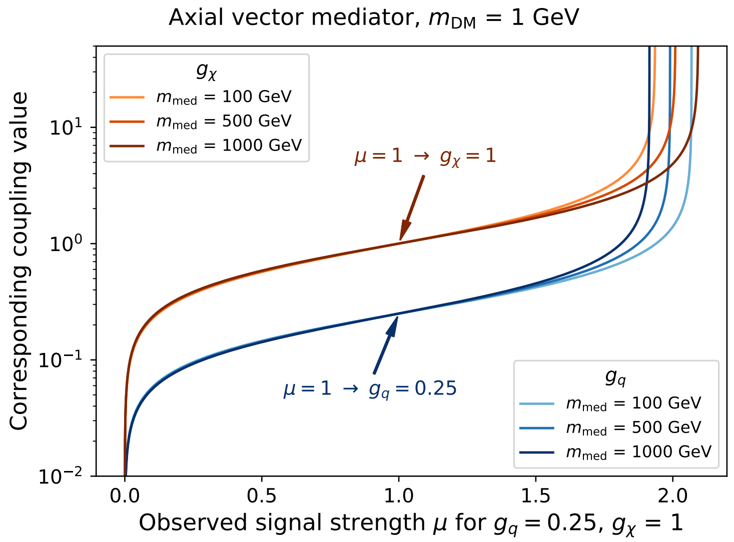

Figure 4.4.: Relation between the observed signal strength and the corresponding coupling values for the default set of couplings discussed in the text. Curves are shown separately for $g_\chi$ (red lines) and $g_q$ (blue lines), assuming that each coupling is varied independently, while the other one is kept constant at its starting value. The different color shadings indicate different choices for the mediator mass $m_{med}$. The couplings of the mediator to the fermions are assumed to be of axial vector type, and the DM mass is set to $m_{DM} = 1$ GeV. The two points indicated by the colored arrows represent the cases where the observed signal cross section coincides with the generated one, in which case the translation procedure simply reproduces the generated values of the couplings. For a vector mediator, the behavior is identical to the axial vector case in the limit of $m_{med} < m_{top}$ and $m_{med} \gg m_{top}$, but different for $m_{med} \approx m_{top}$, where the sharper turn-on behavior of the width function would lead to a more swift transition between the regimes (i. e. the line with $m_{med} = 500$ GeV would be much closer to that with $m_{med} = 1$ TeV).

### 4.1.2. Spin-0 mediators

In a similar manner to the separation of the vector and axial-vector components of the couplings of the spin-1 mediator, separate scalar (S) and pseudo-scalar (P) coupling scenarios are considered for the spin-0 mediator. The MFV assumption is implemented by requiring the couplings of the mediator to the quarks be proportional to $y_{\mathrm{q}} = \sqrt{2} m_{\mathrm{q}}/v$, where $v = 246$ GeV is the vacuum expectation value of the SM Higgs boson:

$$\mathcal{L}_S \subset -\frac{g_q}{\sqrt{2}} \sum_{\mathrm{q}} \Phi y_q \bar{\mathrm{q}} \mathrm{q} - g_{DM} \Phi \bar{\chi} \chi \, , \tag{4.9}$$

$$\mathcal{L}_P \subset -i \frac{g_q}{\sqrt{2}} \sum_{\mathrm{q}} \Phi y_q \bar{\mathrm{q}} \gamma_5 \mathrm{q} - i g_{DM} \Phi \bar{\chi} \gamma_5 \chi \, , \tag{4.10}$$

where $\Phi$ denotes the mediator. Like in the spin-1 case, this interaction is inspired by the familiar structure of the SM, in this case the Higgs interaction is a blueprint for the scalar mediator. Note that the coupling of the mediator to the DM particles does not depend on $m_{DM}$. This choice reflects an agnostic view of mass generation in the dark sector: no assumption is made as to how the DM candidate acquires a mass, and a full model of the dark sector physics would need to account for this question. The practical result of this choice is that the coupling of the mediator to DM is much larger than that of the SM fermions, with the exception of the top quark. A signal in this scenario would be faint, but detectable, whereas any further suppression (induced by e.g. the introduction of democratic fermion couplings) would reduce the expected signal yields below the threshold of detectability with the available data sets. This effect could partially be mitigated by increasing the coupling constants, but the coupling values are limited by the mediator width, which should not exceed $\approx 30\%$ of $m_{med}$ to ensure the perturbativity of the theory. The mediator width can be calculated as [69]:

$$\frac{\Gamma_{P/S}}{m_{med}} = \frac{g_{DM}^2}{8\pi}\left(1-4z_\chi^2\right)^{n/2} + \sum_q \frac{3g_q^2 y_q^2}{16\pi}\left(1-4z_q^2\right)^{n/2} \ , \tag{4.11}$$

with

$$n = \begin{cases} 1, \text{ pseudoscalar} \\ 3, \text{ scalar} \end{cases} , \tag{4.12}$$

and $z_f = \left(\frac{m_f}{m_{med}}\right)^2$ as defined above.

The composition of the total mediator width is shown as a function of $m_{med}$ for fixed $m_{DM}$ in Fig. 4.5. As with vector and axial-vector mediators, the widths of scalar and pseudoscalar mediators converge to identical values for $m_{med} \to \infty$ with different functional dependencies on the mass ratios $z_f$. Note that there is also a non-zero loop amplitude for mediator decays to two gluons, which is however phenomenologically irrelevant for $p_{\mathrm{T}}^{miss}$-based searches.

#### 4.1.2.1. Study of jet multiplicity merging

An important aspect of signal simulation is the treatment of parton radiation. In the simplest case, a matrix-element (ME) calculation for the basic hard process ($pp \to X$, where $X = \ell^+\ell^-\chi\bar{\chi}$ in this case) is performed without additional radiated partons (so $pp \to X + jets$ would explicitly not be included in the ME). The ME calculation is then complemented by the parton shower (PS), which adds parton radiation to the event. This method of signal sample generation is the de-facto standard among many analyses in CMS, as it is simple to implement, report, and reproduce. However, it is known that the approximations used in the PS application do not hold for large transverse jet momenta, and more refined methods should be used if either the jet momenta, or the accompanying recoil momentum of the colorless system under study are relevant to the analysis (for an example of data-simulation comparisons, see [71]). To achieve this, ME calculations are also performed for diagrams with additional outgoing partons. This is possible in the high-$p_{\mathrm{T}}$ regime since QCD behaves perturbatively at high scales. However, one is still unable to calculate analytically the behavior for low-$p_{\mathrm{T}}$ radiation. Additionally, the high-$p_{\mathrm{T}}$ calculations are only possible up to a certain multiplicity (Madgraph5_aMC@NLO can include up to four partons in a tree-level,

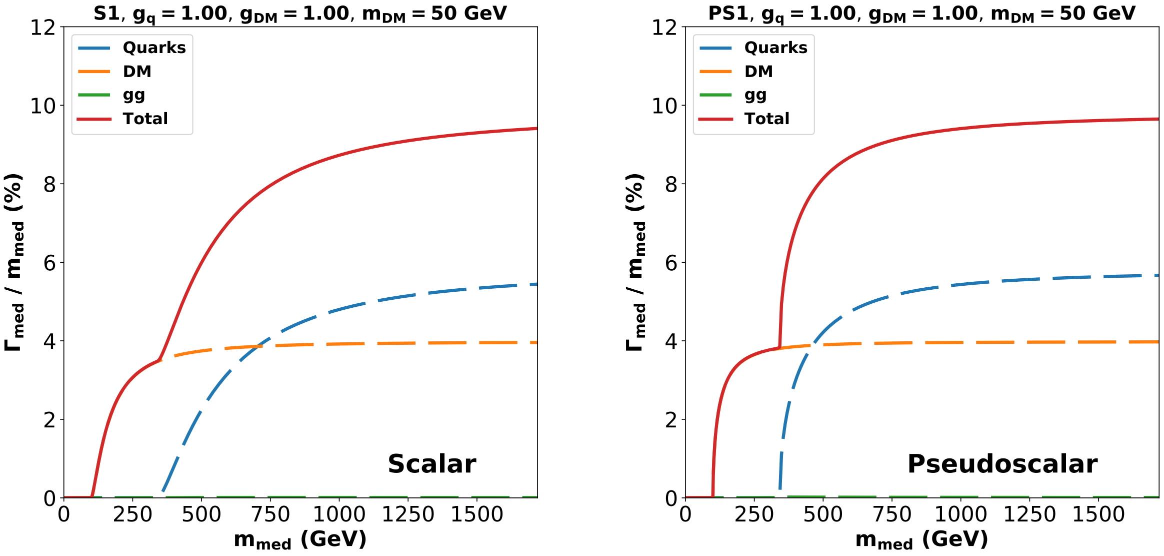

Figure 4.5.: Relative width of the mediator in the DMSimp models as a function of the mediator mass for a scalar (left) and pseudoscalar mediator (right). The other free parameters of the model are set to constant values of $g_q = g_{DM} = 1$ and $m_{DM} = 50$ GeV. The curves in both coupling scenarios converge to the same numerical values for $m_{med} \gg m_{DM}$, but do so at different rates. The "turn-on" behavior is significantly slower in the scalar case. Note that the width for a decay to two gluons is included in the plot, but so small as to be almost invisible in linear scaling, and as such only serves to illustrate its negligibility.

and up to two partons in a loop process), since the number of diagrams and therefore the computing effort scales exponentially with the desired parton multiplicity. Therefore, the PS is still necessary, and combinations of these multiple ME contributions with the PS yield results that are generally in better accord with measurements compared to single-multiplicity MEs (again, see Ref. [71]), and are therefore widely used in the modelling of SM processes at the LHC. In this section, the difference between the two modelling schemes for the signal samples with a spin-0 mediator is studied.

An intrinsic problem introduced by the combination of PS and multi-multiplicity ME predictions is double-counting. In the approach using only the 0-jet ME, there is no overlap: The ME ignores parton radiation, the PS takes care of it. In the approach with radiation at the ME level, a *merging* scheme has to be defined to ensure that the PS not will not produce additional jets that are already taken into account in the ME event. Here, the so-called MLM scheme is used [72–74], which is conveniently implemented in Madgraph5_aMC@NLO [75] and Pythia8 [76], allowing for an efficient chaining of the two programs. The basic idea of the MLM scheme is a separation of parton radiation into two regimes below and above an unphysical cut-off scale $q_{\text{cut}}$, which is evaluated as the $k_t$ distance associated to the clustering step that produces a given jet [77, 78]. Radiation with scales below $q_{\text{cut}}$ will be handled by the PS, while radiation above $q_{\text{cut}}$ is modelled by the ME. Since the ME only takes into account a finite number $N$ of final state partons, multiplicities above that number are generated by the PS in the same manner as before. To avoid double-counting, events generated at the ME level with radiation below the scale $q_{\text{cut}}$ are rejected by the algorithm.

In this section, the difference between the two modelling schemes for the signal samples with a spin-0 mediator is studied. Signal samples for the scalar and pseudoscalar mediator scenarios are generated once for both radiation modelling schemes described above. The samples are produced using Madgraph5_aMC@NLO, merging and showering is performed using PYTHIA8 with tune CUETP8M1 [79], and the full CMS detector simulation implementation in GEANT is used [80]. All generation parameters are kept identical with the exception of those related to the handling of jet radiation. The resulting reconstructed kinematic distributions are studied to understand the effect of the radiation handling. In both cases, a ME-level requirement of $p_{\text{T}}(\ell\ell) > 50$ GeV is applied to enrich the phase space relevant to the analysis. The success of the merging procedure is checked by considering the differential jet rates (DJRs) [73, 81]. During the process of jet clustering, the number of surviving objects is iteratively reduced down from the initial particle multiplicity. The DJR $d(n \rightarrow n-1)$ for a multiplicity transition $n \rightarrow n-1$ is defined as the value of the jet clustering scale at that clustering step. For example, if the second and third object in a three-object configuration are combined and the distance measure between the two objects has some value $\Delta$, then $d(3 \rightarrow 2) = \Delta$ (for a number of illustrative examples see Ref. [81]). The DJRs are physical observables, and their distribution among all events in a sample should therefore be smooth and unaffected by our choice of $q_{\text{cut}}$. The MLM procedure intrinsically reduces the event generation efficiency, as it will reject events only after the ME calculation is performed and the PS has been applied. Therefore, any computing time invested in these two steps is lost. To reduce the impact, Madgraph5_aMC@NLO supplies the user with a setting that allows to reject events already at the ME-level if they are likely to be rejected later. However, since the PS information for a given event is not available at the time of the ME calculation, the early-rejection method can only be applied with a safety margin that accounts for the impact of soft parton radiation in the shower. Practically, this means that if a cutoff value of around some nominal value $Q$ is desired, one would apply a more inclusive requirement at the ME-level, say at $Q/2$. The final $q_{\text{cut}}$ value applied after the parton shower is then found by scanning a range of values around $Q$, creating a small test sample of events, and considering the DJR distributions. If, for a given value of $q_{\text{cut}}$, the DJR distributions are smooth and show no cutoff-related features, that value is used [2]. For the spin-0 samples studied here, a ME-level requirement of 10 GeV was employed, and the final $q_{\text{cut}}$ value was optimized between 15 and 25 GeV in steps of 1 GeV, and a final value of $q_{\text{cut}} = 24$ GeV is chosen. The corresponding DJR distributions are shown in Fig. 4.7 for a scalar mediator sample with $m_{med} = 500$ GeV.

A comparison of the jet multiplicity and $p_{\text{T}}^{miss}$ distributions obtained through the two methods is shown in Fig. 4.6. The corresponding distributions for the pseudoscalar case exhibit very similar behavior and are omitted here. The merged signal samples are found to produce overall higher yields, with a difference between 10% and 40%, increasing with $m_{med}$. The effect is seen to increase with the value of $p_{\text{T}}^{miss}$, as well as with the jet multiplicity. The increase in radiative activity can be attributed to two factors: Madgraph5_aMC@NLO

---

[2] It is entirely possible to find multiple combinations of threshold values for which a similar performance is observed. In this case, all of the choices are valid and one can be picked at random.

is known to generate harder jets than Pythia8 [3], which is due to the aforementioned breakdown of the PS approximation at high $p_{\mathrm{T}}$. Additionally, the process under study here is loop-induced [4]. Information about the top quarks running in the loop is not propagated to the PS, which correspondingly has no way of generating gluons radiated from the top quarks. In the merged generation, radiation from top quark lines is included, leading to an overall harder $p_{\mathrm{T}}$ spectrum. While the increase in jet activity also induces a small decrease in acceptance for the final analysis selection, there is an overall increase in the final signal yield for the merged samples.

For the calculation of the final results, the merged method will be used. However, the final sensitivity is also determined using the 0-jet ME samples, and a comparison is included in sec. 8.2.2.

---

[3] This statement depends on the settings used for the parton shower, but generally holds for the optimized parameter sets used here [79].

[4] Note that the MLM scheme is appropriate for loop-induced processes since they are effectively LO, i.e. no simpler diagram is possible for the process. Processes simulated at NLO (i.e. including virtual corrections beyond the LO), would require a different merging scheme, as described in Ref. [82].

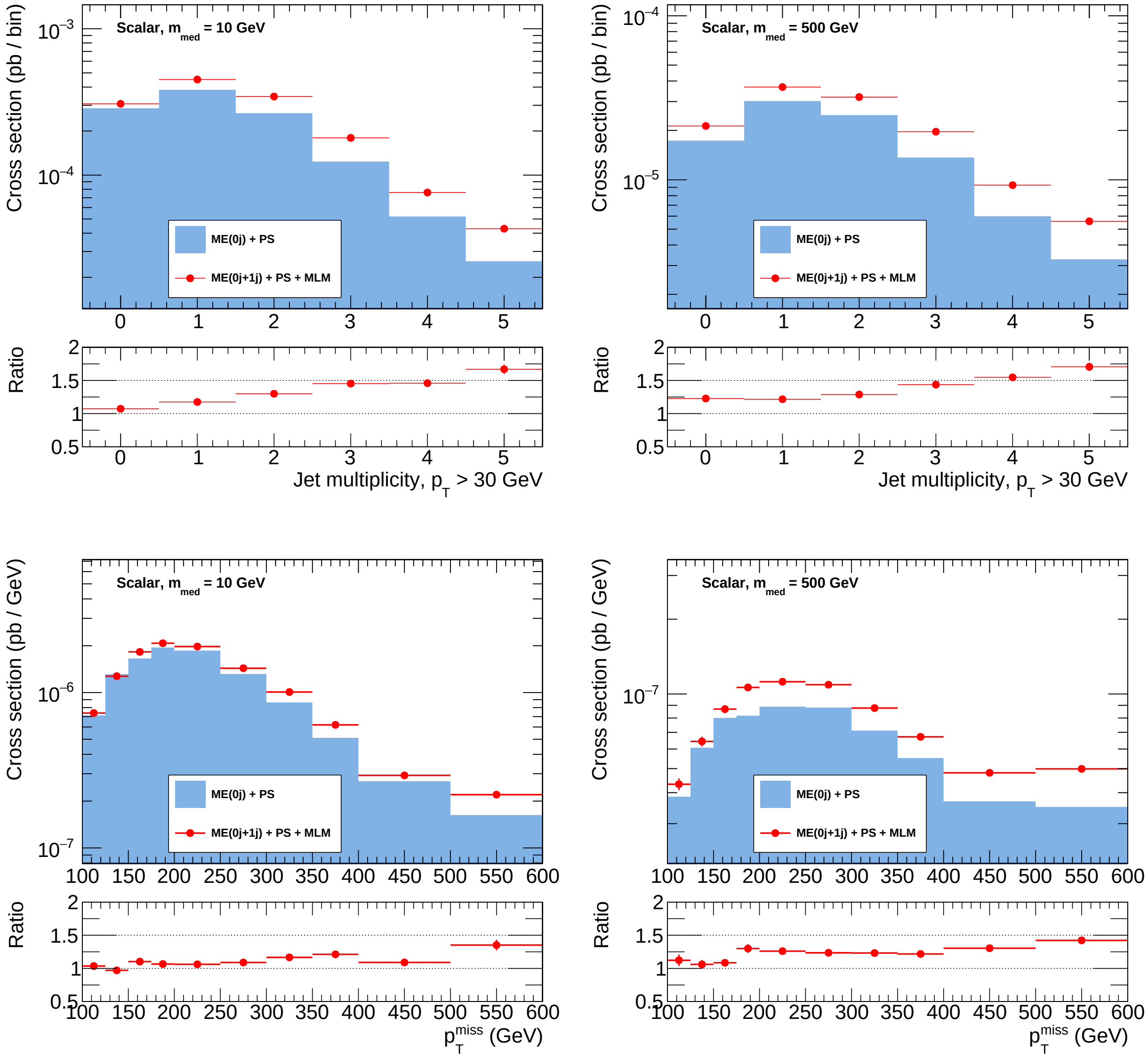

Figure 4.6.: Comparison of the kinematic properties of scalar mediator samples produced from the 0-jet ME, and 0+1-jet ME. The inclusive jet multiplicity (top) and final $p_{\mathrm{T}}^{miss}$ distributions (bottom) are shown for $m_{med} = 10$ GeV (left) and $m_{med} = 500$ GeV (right). The relationship between the two cases is similar for the pseudoscalar case. The samples are normalized to their respective cross sections as calculated by the event generator. The matching efficiency for the merged samples is taken into account.

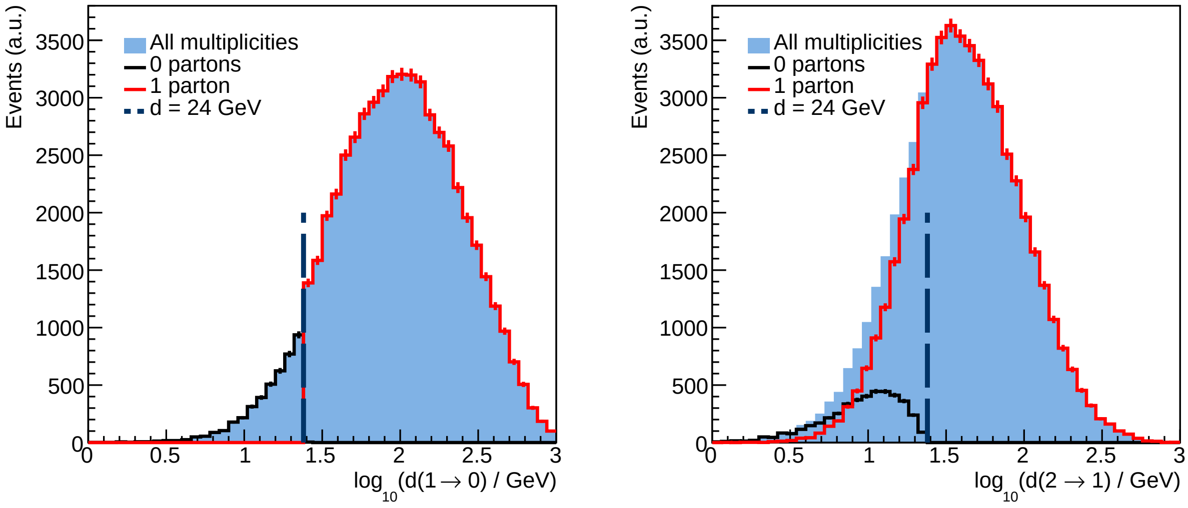

Figure 4.7.: Distribution of the differential jet rates for a signal sample with a scalar mediator with $m_{med} = 500$ GeV. The distributions are shown for the $1 \to 0$ (left) and $2 \to 1$ distributions (right). The samples contain ME-level events with zero or one outgoing parton, and the merging scale is set to $q_{\mathrm{cut}} = 24$ GeV. The distributions are shown split by the parton multiplicity at the ME-level (red, black solid lines), as well their sum (blue histogram). Error bars represent the statistical uncertainty due to the finite size of the generated event samples.

## 4.2. Dark matter mediators with couplings to SM bosons

The models described in the previous section are attractive due to their flexibility and simplicity. However, their focus on quark-coupled mediators fails to showcase the sensitivity of a search in the mono-Z topology. In cases where mediators only couple to the quark sector of the SM, the monojet signature will always provide superior sensitivity as the probability for the emission of a gluon jet is much larger than that for the emission of a Z boson. A different picture emerges once one considers mediators with couplings to SM bosons, such as the so-called a+2HDM model [83], which extends the SM by an additional Higgs doublet and a pseudoscalar DM mediator particle labeled “a”.

The addition of a second Higgs doublet results in the presence of two new neutral and charged scalars H and $H^{\pm}$, as well as an additional pseudoscalar A. The a and A bosons mix with a mixing angle $\theta$, resulting in the possibility of $H \to aZ$, as well as $A \to \chi\chi$ decays. This mixing acts as a portal between the SM and the dark sector: In the limiting case of $\theta \to 0$, the a mediator only interacts with the DM, and the A boson does not. For finite values of the mixing angle $\theta$, an a-Z boson pair can created from a H decay, and if the a boson subsequently decays to DM particles, an overall Z+$p_{\mathrm{T}}^{miss}$ signature is observed. A Feynman diagram for this dominant mode of DM particles in association with a Z boson is shown in Fig. 4.8. The DM candidate is again assumed to be a Dirac fermion.

Any change in the SM version of the gauge and Higgs sectors can easily affect many well-known physics processes. Therefore, it is important to understand what parts of the

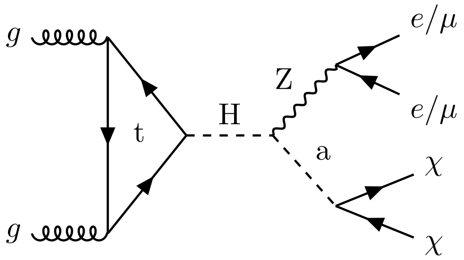

Figure 4.8.: Example Feynman graph for resonant production of a $Z + p_{\mathrm{T}}^{miss}$ signature in the a+2HDM model. DM particles are dominantly produced through the a mediator. The a mediator and the Z boson are produced from the decay of a heavy scalar H. Note that nonresonant diagrams like the ones shown in Fig. 4.1 also contribute, but are not significant compared to the resonant contribution.

a+2HDM parameter space are in conflict with already-made observations. The parameter choices adopted in this document follow the recommendations from the LHC DM working group [84] based on the work of Ref. [83], in which detailed studies are performed to formulate constraints based on existing measurement, and internal theoretical consistency.

To ensure compatibility with the measurements of the coupling strengths of the known h(125) boson, the coupling strength of the H boson to the SM gauge bosons $\cos(\beta - \alpha)$ is set to zero ("alignment limit"). This choice effectively separates the H and h bosons from each other, and results in the absence of H → hh or H → hA decays. Additional constraints arise from precision measurements of the properties of the W and Z bosons, which can be influenced by couplings of the SM gauge bosons to the new bosons in the theory. These constraints are evaded by setting the masses of the heavy bosons to be equal: $m_{\mathrm{H}} = m_{\mathrm{H}^{\pm}} = m_{\mathrm{A}}$. Finally, the widths of the new bosons receive contributions from purely bosonic interactions, which are controlled by the quartic couplings in the extended Higgs sector $\lambda_{P1}$, $\lambda_{P2}$, and $\lambda_3$. To prevent the widths from growing too large, which would prohibit a perturbative treatment of the model, these three couplings are chosen to have identical values, in this case $\lambda_{P1} = \lambda_{P2} = \lambda_3 = 3$. These choices leave a number of unconstrained parameters: The mass of the DM candidate $m_{DM}$, the ratio of the vacuum expectation values of the two Higgs doublets $\tan(\beta)$, the mixing angle of the a and A bosons $\theta$, as well as the new boson masses $m_{\mathrm{H}}$ and $m_{\mathrm{a}}$. As in the other simplified models of DM production, the exact value of the DM mass parameter is not relevant, as long as $m_{DM} < m_{\mathrm{a}}/2$, which is a prerequisite for direct DM production at the LHC. Therefore, $m_{DM} = 10$ GeV is fixed without any loss of generality. The $\tan(\beta)$ and $\theta$ parameters mostly affect the signal cross section, but not the kinematic properties of the signal [84], and are consequently also set to fixed values of $\tan(\beta) = 1$ and $\sin(\theta) = 0.35$. For this small value of $\sin(\theta)$, the a-A mixing is limited, and the a boson is the dominant DM mediator. Finally, the new boson masses $m_{\mathrm{a}}$ and $m_{\mathrm{H}}$ are varied, and any results are formulated in the $m_{\mathrm{a}}$-$m_{\mathrm{H}}$ plane. The kinematic properties of the signal, as well as the overall signal cross sections vary depending on the $m_{\mathrm{a}}$ and $m_{\mathrm{H}}$ parameters, which are studied in more detail in the next section.

### 4.2.1. Study of the parameter space

Signal samples are simulated using Madgraph5_aMC@NLO for the ME calculation, and Pythia8 for the PS. In the ME, all one-loop diagrams for the gg $\rightarrow \ell\ell\chi\chi$ process are taken into account.

The inclusive signal cross section in the $m_{\mathrm{a}}$-$m_{\mathrm{H}}$ plane is shown in Fig. 4.9. The highest cross section values can be achieved for low values of $m_{\mathrm{a}} < 300$ GeV and $m_{\mathrm{H}} > m_{\mathrm{a}}$, reaching up to $\approx 70$ fb. Cross sections in the order of a few femtobarns are observable in this central region up to maximal values of $m_{\mathrm{H}} \approx 1$ TeV and $m_{\mathrm{a}} \approx 400$ GeV. Along the diagonal $m_{\mathrm{H}} \approx m_{\mathrm{a}}$, the overall cross section is suppressed for two reasons: The diagram with a heavy scalar in the s-channel, as shown in Fig. 4.8, can only proceed with at least one off-shell boson, and the nonresonant contributions is suffering from destructive interference between the diagrams containing a and A bosons. Finally, below the diagonal, DM particles are produced predominantly from decays of the A boson, which in this case is lighter than the a. However, due to the choice of the mixing parameter, this process is significantly less likely.

The dependence of the signal properties on the free parameters $m_{\mathrm{H}}$ and $m_{\mathrm{a}}$ is studied in more detail. The parameter space separates into three independent subspaces as illustrated by the invariant mass distributions shown in Fig. 4.10. In the cases where $m_{\mathrm{H}} > m_{\mathrm{a}}$, the invariant mass of the $\chi\chi$ system $m_{\chi\chi}$ is sharply peaked at $m_{\mathrm{a}}$, indicating that the DM particles are predominantly produced via decays of on-shell a bosons. The total mass of the color-neutral system $m_{\chi\chi\ell\ell}$ peaks at $m_{\mathrm{H}}$, which shows that the resonant diagram with a H $\rightarrow$ aZ decay dominates the total cross section. In the “inverted” mass region, where $m_{\mathrm{a}} > m_{\mathrm{H}}$, the DM pairs are instead generated in decays of A bosons and the $m_{\chi\chi}$ distribution peaks at $m_{\mathrm{H}} = m_{\mathrm{A}}$. Additionally, there is a sub-leading non-resonant contribution from diagrams involving off-shell bosons. The opposite behavior then appears in the $m_{\chi\chi\ell\ell}$ distribution, which is resonant for events from the nonresonant part of the $m_{\chi\chi}$ distribution, and vice versa, as not all bosons in the diagram with an s-channel H boson can be on shell at the same time. The nonresonant contributions also appear in the $m_{\mathrm{H}} > m_{\mathrm{A}}$ region but are negligible compared to the resonant ones.

The different production contributions for the three mass regions also result in different behavior of the main kinematic quantities relevant for this analysis, which are shown in Fig. 4.11. Here, a consistent picture emerges: Points with $m_{\mathrm{H}} > m_{\mathrm{a}} + m_{\mathrm{Z}}$ result in events with largest boost and are consequently more favourably distributed in all four variables. For $m_{\mathrm{a}} > m_{\mathrm{H}}$, events are still boosted, but significantly less so than in the first region. Consequently, their acceptance will be reduced. Finally, for $m_{\mathrm{H}} \approx m_{\mathrm{a}} + m_{\mathrm{Z}}$, the a and Z bosons are produced almost at rest as their masses absorb most of the available energy. The events in this region have very little boost and score badly on all kinematic distributions, and are therefore much harder to differentiate from the low-boost SM backgrounds. In the distribution of the generator-level mediator $p_{\mathrm{T}}$, the two-body decay topology is evident: In the main sensitive parameter region, the $p_{\mathrm{T}}$ spectrum shows a Jacobian peak structure.

To illustrate the interplay between total cross section and acceptance effects, the cross section and acceptance after applying an signal region selection are shown in Fig. 4.12. The selection is identical to the reconstruction-level selection for the 2016 analysis (cf. sec. 8.1), except neglecting requirements on jets. Following the trends observed in the individual observables, the acceptance clearly favours the high-$m_{\mathrm{H}}$ region that is far away from the $m_{\mathrm{a}}$-$m_{\mathrm{H}}$ diagonal. After applying the selection, the $m_{\mathrm{H}} = m_{\mathrm{a}}$ diagonal and the kinematic

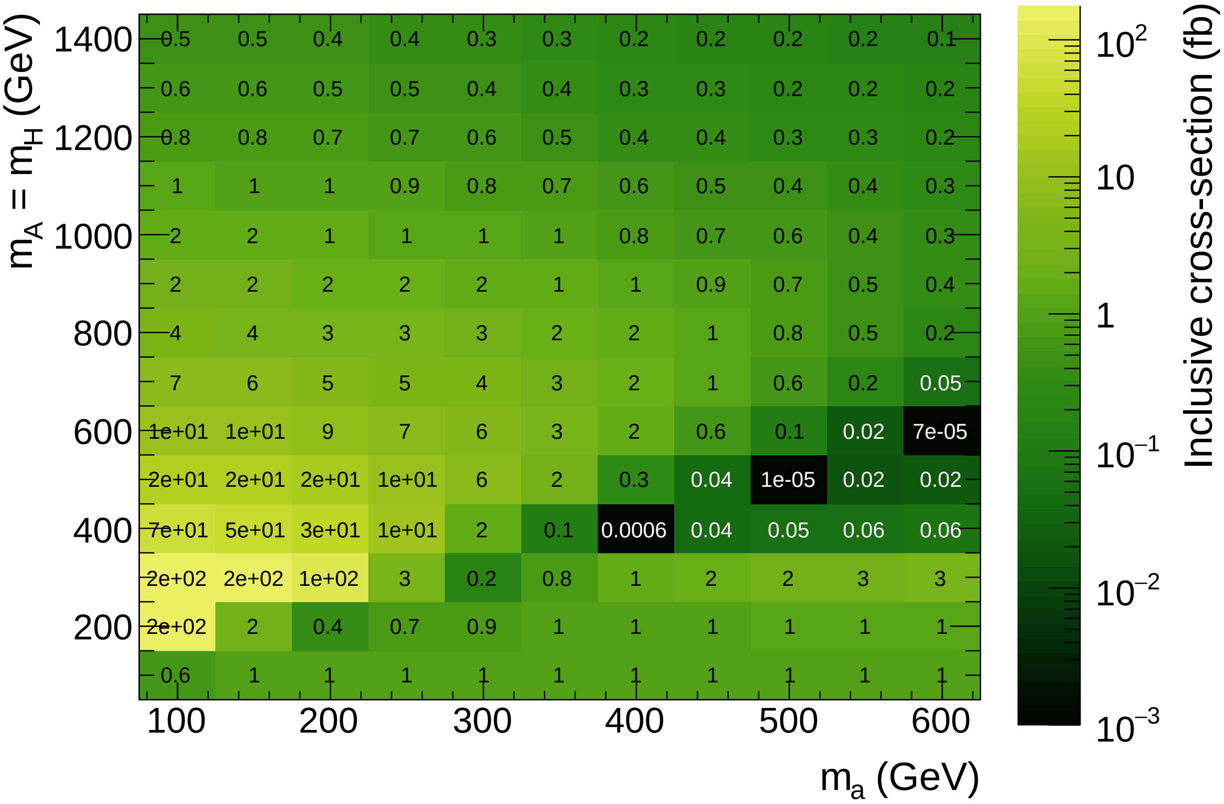

| | | | | | | | | | | |
|---|---|---|---|---|---|---|---|---|---|---|
| 0.5 | 0.5 | 0.4 | 0.4 | 0.3 | 0.3 | 0.2 | 0.2 | 0.2 | 0.2 | 0.1 |
| 0.6 | 0.6 | 0.5 | 0.5 | 0.4 | 0.4 | 0.3 | 0.3 | 0.2 | 0.2 | 0.2 |
| 0.8 | 0.8 | 0.7 | 0.7 | 0.6 | 0.5 | 0.4 | 0.4 | 0.3 | 0.3 | 0.2 |
| 1 | 1 | 1 | 0.9 | 0.8 | 0.7 | 0.6 | 0.5 | 0.4 | 0.4 | 0.3 |
| 2 | 2 | 1 | 1 | 1 | 1 | 0.8 | 0.7 | 0.6 | 0.4 | 0.3 |
| 2 | 2 | 2 | 2 | 2 | 1 | 1 | 0.9 | 0.7 | 0.5 | 0.4 |
| 4 | 4 | 3 | 3 | 3 | 2 | 2 | 1 | 0.8 | 0.5 | 0.2 |
| 7 | 6 | 5 | 5 | 4 | 3 | 2 | 1 | 0.6 | 0.2 | 0.05 |
| 1e+01 | 1e+01 | 9 | 7 | 6 | 3 | 2 | 0.6 | 0.1 | 0.02 | 7e-05 |
| 2e+01 | 2e+01 | 2e+01 | 1e+01 | 6 | 2 | 0.3 | 0.04 | 1e-05 | 0.02 | 0.02 |
| 7e+01 | 5e+01 | 3e+01 | 1e+01 | 2 | 0.1 | 0.0006 | 0.04 | 0.05 | 0.06 | 0.06 |
| 2e+02 | 2e+02 | 1e+02 | 3 | 0.2 | 0.8 | 1 | 2 | 2 | 3 | 3 |
| 2e+02 | 2 | 0.4 | 0.7 | 0.9 | 1 | 1 | 1 | 1 | 1 | 1 |
| 0.6 | 1 | 1 | 1 | 1 | 1 | 1 | 1 | 1 | 1 | 1 |

Figure 4.9.: The inclusive sample cross section for the mono-Z signal in the $m_a$-$m_H$ plane for the a+2HDM model. The SM branching fraction for the decay of the Z boson to a $\mu^+\mu^-$ or $e^+e^-$ pair of approximately 6.7% [85] is taken into account.

threshold $m_H = m_a + m_Z$ merge to a combined low-sensitivity region that is not probable in mono-Z events. The situation is slightly improved in the inverted mass region, where final cross sections of $\approx 0.3$ fb are found.

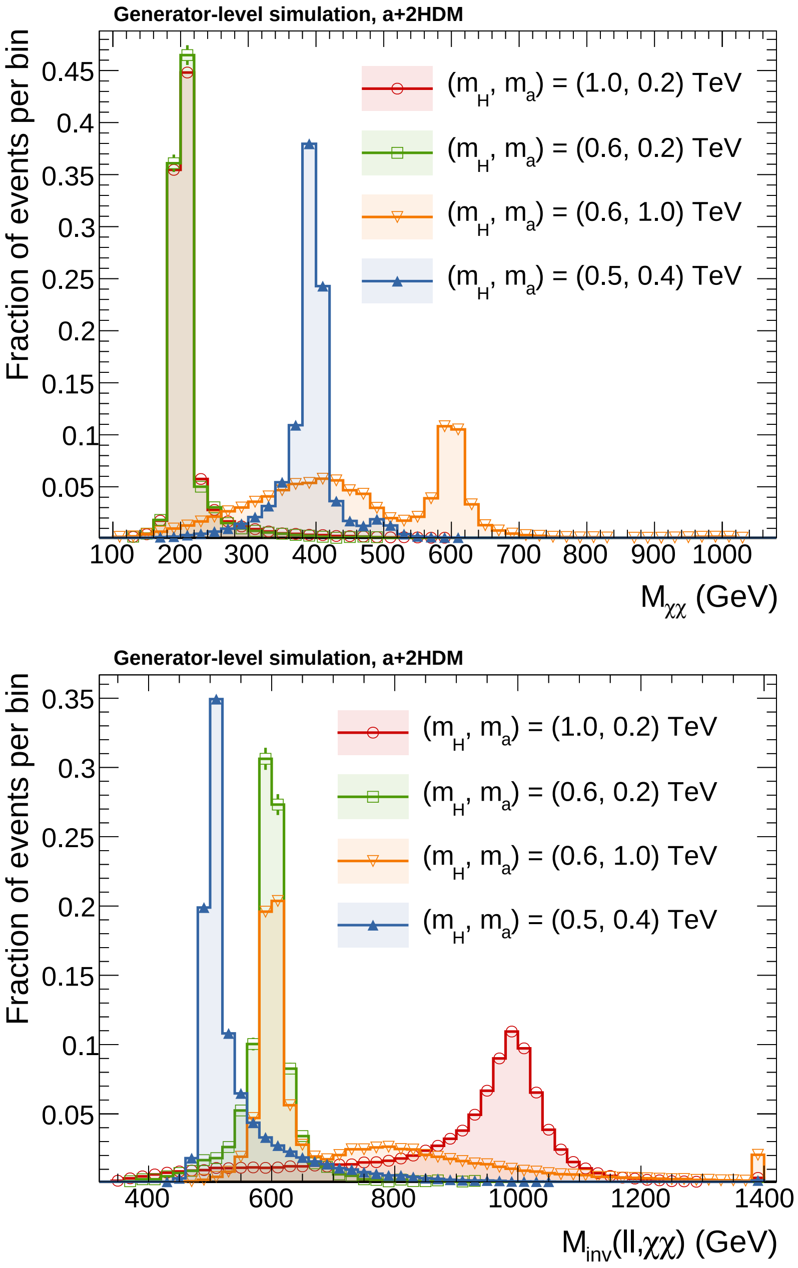

Figure 4.10.: Invariant mass distributions of the $\chi\chi$ system (top) and the $\ell\ell\chi\chi$ system (bottom) for the pp $\rightarrow$ Z($\ell\ell$)+$\chi\chi$ process in the a+2HDM model. The distributions are shown for different combinations of the light pseudoscalar mass $m_{\mathrm{a}}$ and the heavy scalar mass $m_{\mathrm{H}} = m_{\mathrm{A}}$. The red and green curves (circle and square markers) show the behavior for two parameter points with $m_{\mathrm{H}} > m_{\mathrm{a}} + m_{\mathrm{Z}}$, while the orange histogram corresponds to the inverted mass region $m_{\mathrm{H}} < m_{\mathrm{a}}$. The blue histogram shows a parameter point with $m_{\mathrm{H}} \approx m_{\mathrm{a}} + m_{\mathrm{Z}}$, which is close to the kinematic threshold for on-shell H $\rightarrow$ a + Z decays. Note that in all cases, the distributions are normalized to unit area. The error bars represent the statistical uncertainty related to the finite size of generated event samples.

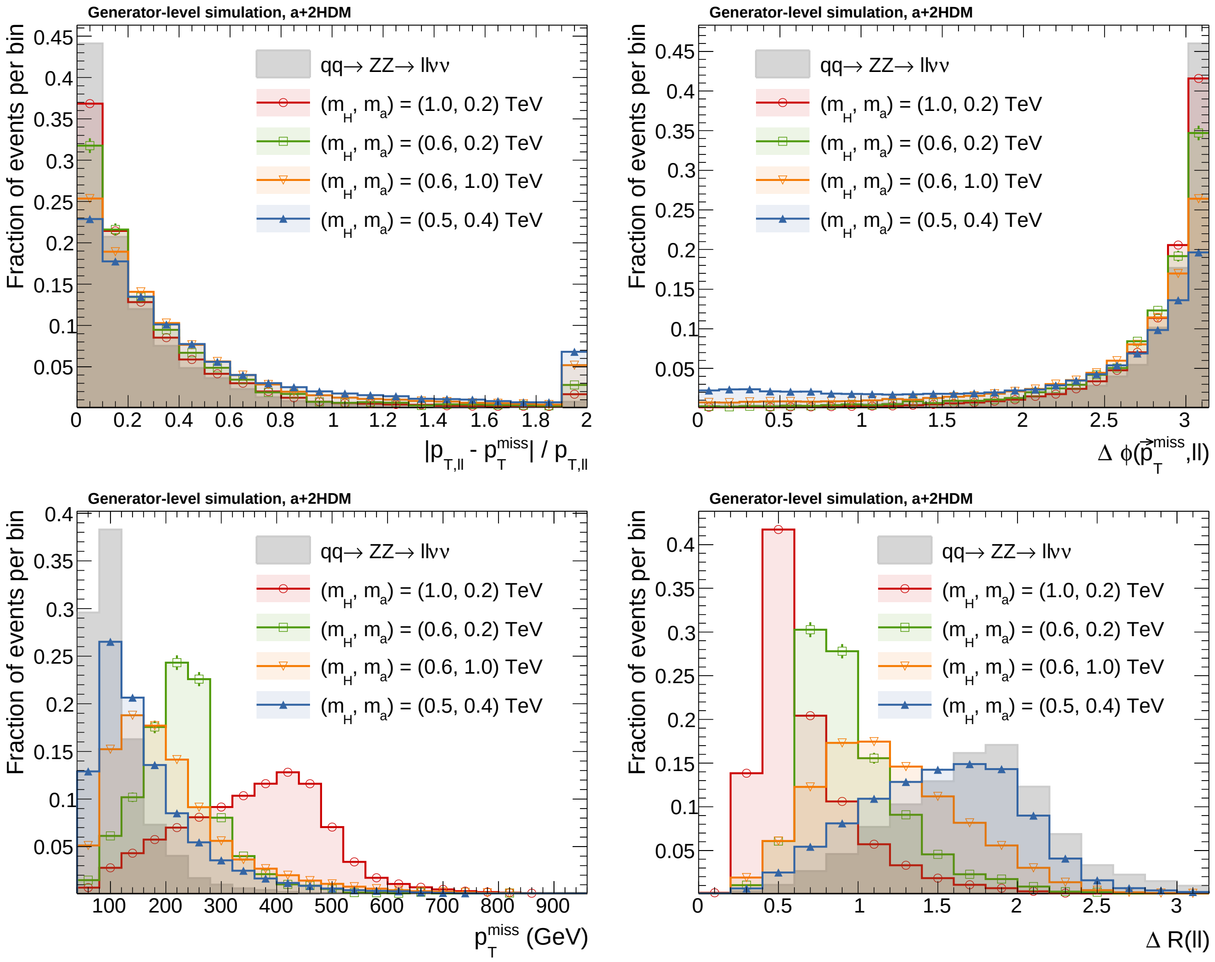

Figure 4.11.: The main kinematic distributions for the pp $\rightarrow$ Z($\ell\ell$) + $\chi\chi$ process in the a+2HDM model: $|p_{\mathrm{T}}^{miss}/p_{\mathrm{T}}(\ell\ell) - 1|$ (top left), $\Delta\phi(\ell\ell, \vec{p}_{\mathrm{T}}^{\,miss})$ (top right), $p_{\mathrm{T}}^{miss}$ (bottom left) and $\Delta R(\ell, \ell)$. Events with $p_{\mathrm{T}}(\ell\ell) > 60$ GeV, $p_{\mathrm{T}}^{miss} > 60$ GeV, and $76 < m(\ell\ell) < 106$ GeV are shown. The color coding and choice of parameter points is identical to Fig. 4.10, but the distributions are now also shown for the leading ZZ background (solid gray histogram). The signal curves are shown for multiple choices of $m_{\mathrm{a}}$ and $m_{\mathrm{H}} = m_{\mathrm{A}}$.

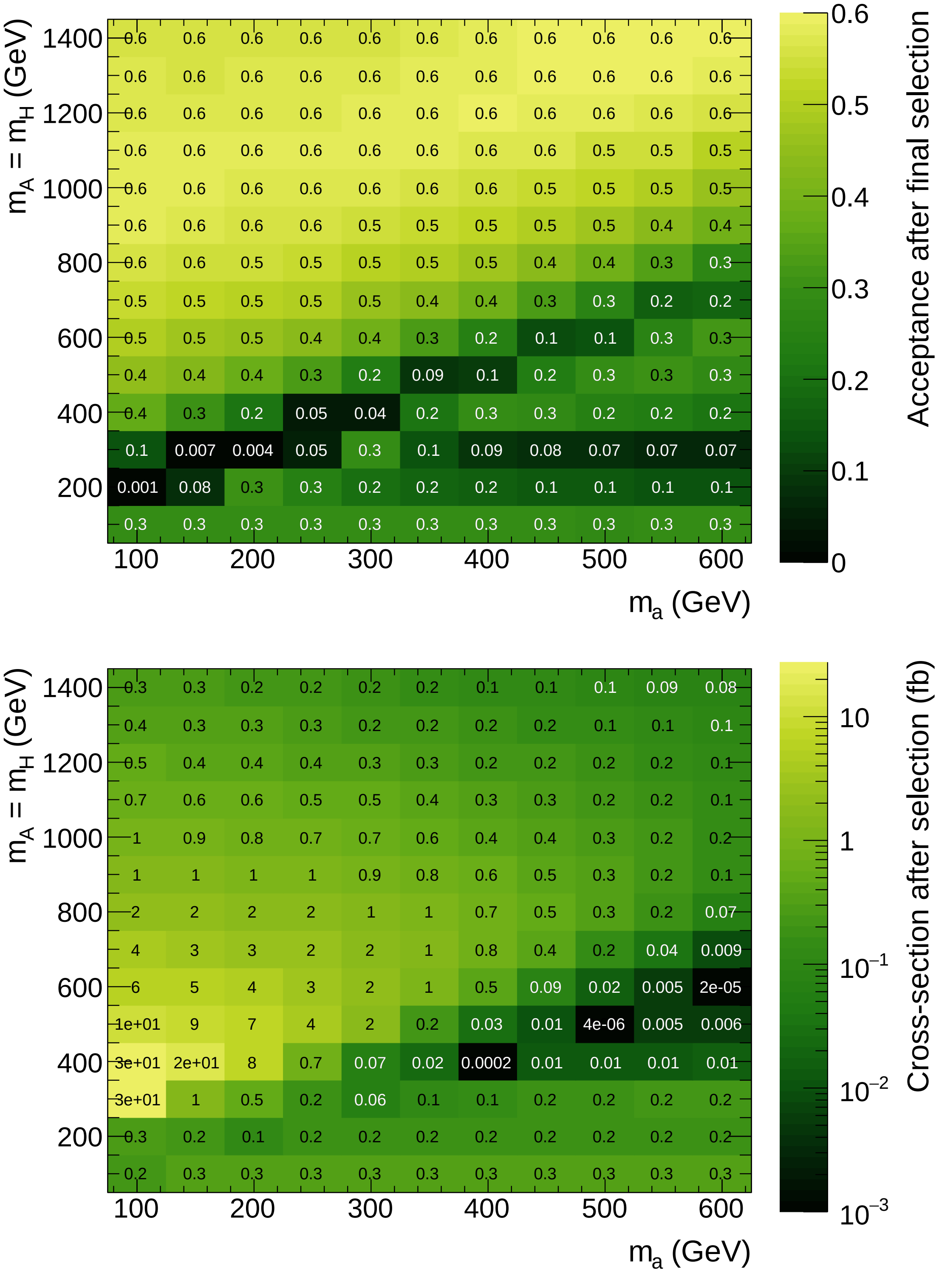

Figure 4.12.: The acceptance (top) and cross section (bottom) for the pp → $Z(\ell\ell) + \chi\chi$ process in the a+2HDM signal. The values are shown in the $m_a$-$m_H$ plane after applying the selection described in the text.

## 4.3. Unparticles

Unparticles are a mathematically motivated extension of the SM. Unlike many other proposed BSM theories, they were not designed to solve any particular problem of the SM, but were discovered as a phenomenologically intriguing theoretical possibility by Howard Georgi [86]. Georgi's initial publication prompted extensive theoretical studies to understand the consequences of the existence of unparticles on collider phenomenology [87–90], as well as cosmology (e.g. [91]) and solid state physics (e.g. [92]). The underlying premise of the theory is that the SM is extended at high energies by so-called Banks-Zaks (BZ) fields [93], which interact with the SM particles via the exchange of an unspecified set of heavy particles. The interesting aspect of the BZ fields is that while their high-energy behavior is complicated, their low-energy behavior is not. In the low-energy limit below an energy scale $\Lambda_U$, the BZ fields give rise to scale-invariant *unparticle* fields, which earn their name because they do not have a fixed mass, but exhibit a continuous mass spectrum, making them radically different from what is usually referred to as a particle. As a resulting peculiarity, the phase-space factor for the emission of a single unparticle has the same form as that for multiple usual particles, except that the number of particles is replaced with the non-integer scaling dimension parameter $d_U$. While unparticles are not immediately useful in solving a theoretical problem, their defining property of scale invariance raised significant interest, as it is a special case of conformal invariance, which in turn was a topic of interest at the time [94].

Unparticles can generally have spins of zero, one, or two. Here, only spin-0 unparticles are considered, as there are strong constraints on spin-1 unparticles from precision measurements [95], and the spin-2 case is phenomenologically covered by the extra dimensions scenario discussed in sec. 4.4. The corresponding interaction Lagrangian term is:

$$\mathcal{L}_U = \frac{\lambda_U}{\Lambda_U^{d_U-1}} \bar{q} q \mathcal{O}_U \, , \tag{4.13}$$

where $\lambda_U$ is the unparticle-SM coupling, which can be matched to the parameter of the high-energy theory, but is treated as an independent parameter here. $\Lambda_U$ is the energy

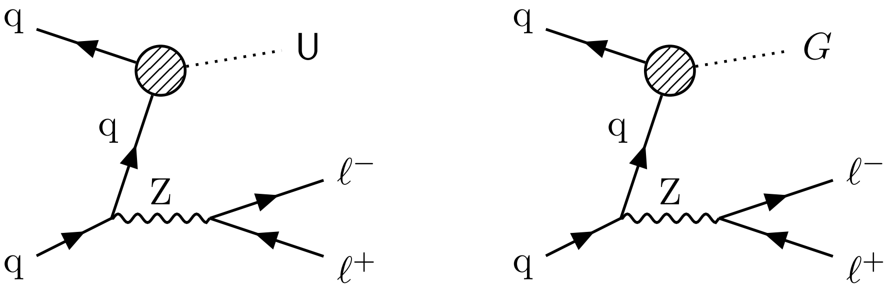

Figure 4.13.: Example Feynman diagrams for the associated production of a Z boson and an unparticle (left) or graviton (right). The production processes for these two particle types are identical except for any effects related to the spin of the outgoing particle, which is zero for the unparticle, and two for the graviton. In both cases, the new particles are assumed to be produced from an interaction with SM quarks.

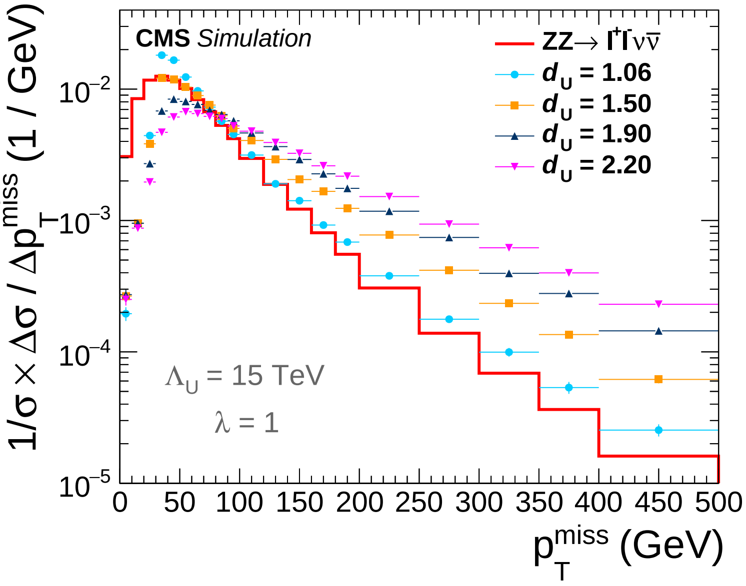

Figure 4.14.: Normalized generator-level $p_{\mathrm{T}}^{miss}$ distribution for the pp $\rightarrow$ Z($\ell\ell$) $+ U$ process for different values of $d_U$. The red solid line shows the $p_{\mathrm{T}}^{miss}$ spectrum of the SM ZZ process, which is the leading background. As the values of $\Lambda_U$ and $\lambda$ only have an effect on the overall signal cross section, they do not affect the shapes shown here.

scale up to which the EFT approximation remains valid and $d_U$ is the scaling dimension of the unparticle operator $\mathcal{O}_U$. The coupling structure is chosen to be purely scalar, but gives the same numerical results as a purely pseudoscalar coupling [96]. Note that previous publications [97, 98] have sometimes quoted this Lagrangian with an incorrect exponent of $\Lambda_U$. Using dimensional analysis it is easy to convince oneself that the exponent given here is correct: Fermion fields have mass dimension 3/2, and the unparticle operator has mass dimension $d_U$ by definition, giving a total mass dimension of $3 + d_U$ for the combined $q\bar{q}\mathcal{O}_U$ operator. In order for the full Lagrangian term to have the obligatory mass dimension value of 4, the only possibility is for $\Lambda_U$ to come with an exponent of $1 - d_U$.

The implementation of the unparticle and extra dimension processes of Refs. [96, 99] in the PYTHIA8 event generator is used. The corresponding Feynman diagram is shown in Fig. 4.13. Fig. 4.14 shows the inclusive generator-level $p_{\mathrm{T}}^{miss}$ distribution in $Z + U$ events for a number of values of $d_U$. The distribution of $p_{\mathrm{T}}^{miss}$ is found to generally be harder than in the SM ZZ background, making the high-$p_{\mathrm{T}}^{miss}$ region most sensitive to the signal. This effect becomes more pronounced with increasing $d_U$.

### 4.3.1. Previous constraints

A number of previous results has been reported on searches for the production of unparticles from events with jets+$p_{\mathrm{T}}^{miss}$ at CDF or photons+$p_{\mathrm{T}}^{miss}$ at LEP [100], as well as Z+$p_{\mathrm{T}}^{miss}$ events at CMS [97].

The previous version of this analysis performed on the data set recorded by CMS in 2012 [97], originally claimed to have obtained the most stringent bounds on $\Lambda_U$ to date over the full considered range of $d_U$, surpassing both the constraints from previous colliders as well as the CMS monojet result with $\sqrt{s} = 8$ TeV. This dominating role of the mono-Z signature was understood to be the result of the lower $p_{\mathrm{T}}^{miss}$ threshold of the mono-Z analysis compared to the monojet case, as it resulted in larger signal acceptance. While this effect exists, it is insufficient to make up for the relatively low mono-Z signal cross section. During the preparation of this thesis, it was realized that the apparent strength of the mono-Z constraints was the result of a subtle error in the PYTHIA8 software, which was used to generate the signal samples for both the 8 and 13 TeV versions of this analysis. To increase the efficiency of event generation, PYTHIA8 had been configured to only generate such events where the Z boson decays to a pair of electrons or muons. This behavior is controlled with the `onIfAny` syntax:

```
23:onIfAny = 11 -11 13 -13 .
```

In this case, the instruction only picks those decays of the Z boson (identification number 23) that produce any $e^{\pm}$ ($\pm11$) or $\mu^{\pm}$ ($\pm13$) leptons. While PYTHIA8 succeeded in producing physical events that were filtered in the desired way, the software neglected to account for the branching ratio (BR) of the selected decays when calculating the cross section for the generated sample, resulting in a mismatch of cross section and event sample. In Ref. [97], signal events in the electron and muon final states were generated in separate samples, resulting in an over-estimation of the total cross section by a factor of $1/\mathrm{BR}(Z \to \ell\ell) \approx 30$. For the analysis described in sec. 7 of this thesis, as well as Ref. [98], both final states were generated in the same samples, resulting in a mis-normalization factor of $1/(2 \times BR(Z \to \ell\ell)) \approx 15$. As part of this thesis, errata for both Refs. [97, 98] were prepared to correct this error, and all results shown in this document already take this change into account. The authors of the PYTHIA8 software were alerted to the mistake in the code and implemented a solution in version 8.226 [101].

## 4.4. Large extra dimensions

Large extra dimensions were introduced as a novel way of solving the hierarchy problem by Arkani-Hamed, Dvali and Dimopoulos in Ref. [102]. The model is commonly referred to as ADD after their initials. The hierarchy problem is the apparent mismatch of the strengths of the electroweak and gravitational interactions, which is equivalent to the mismatch of the electroweak and Planck scales by a factor of $\mathcal{O}(10^{15})$ (cf. sec. 3.1.2). The solution envisioned in the ADD model is simple: Gravity is not intrinsically weak, it just seems that way because its effect is diluted by a number of additional dimensions of space. The addition of $n$ dimensions with radius $R$ would result in an apparent shift of the real 4+n dimensional Planck mass $M_{Pl}$ up to the observed four-dimensional value:

$$(M_{Pl})^2_{4-d} \propto (M_{Pl})^2_{(4+n)-d} R^n \; . \tag{4.14}$$

The effect increases with the size and number of extra dimensions, but even for $n = 2$ and $R \approx 0.1$ mm, the Planck scale can be reduced to coincide with the electroweak scale of $\approx 1$ TeV. The SM fields are localized on a small region of the additional dimension, which prevents immediate and fundamental effects from appearing in day-to-day observations of matter around us. Phenomenologically, the new dimensions would still alter the distance dependence of gravitational forces at very short ranges $\lessapprox R$, which has never been measured for $R < 1$ mm. Additionally, they could result in the production of gravitons at the LHC. These gravitons could either contribute virtually, e.g. leading to distortions in the Drell-Yan invariant mass spectrum, or be emitted as real particles. Since gravity permeates the additional dimensions freely, the gravitons would likely escape into the extra dimensions and avoid detection, leading to a missing energy signature.

Interestingly, the phenomenology of graviton emission coincides with that of spin-2 unparticles with the simple replacements $\Lambda_U \to M_D$ and $d_U \to n/2 + 1$, as well as a simplified phase space factor. Therefore, the ADD graviton case can be considered to be a special case of the generalized unparticle framework. The corresponding Feynman diagram is identical to that of unparticle production, and shown in Fig. 4.13.

### 4.4.1. Truncation

The implementation of the unparticle and ADD models uses the framework of effective field theories (EFTs), which allow for a simplified view of processes where a heavy particle is exchanged. If the mass of the heavy particle is sufficiently large, the kinematics of the exchange process do not depend on the mass of the heavy particle anymore. A well-known example of this behavior is the Fermi theory of weak charged-current interactions, which correctly describes phenomena where a W boson is exchanged in the limit where the energy scale of the process Q is much smaller than the mass of the W boson: $Q \ll M_W$. While well-suited for low-energy phenomena, the EFT approximation may break down at colliders such as the LHC, where large interaction scales can be probed. To avoid over-optimistic results, *truncation* can be applied. Truncation simply means that in a given sample of simulated signal events, all events with a hard interaction scale higher than a certain threshold are either discarded or suppressed with a small weight. For the ADD case, a standard truncation method implemented in PYTHIA8 is used. All events with $\hat{s} > M_D^2$ are suppressed by a weight $w_{trunc.}$, where $\sqrt{\hat{s}}$ is the center-of-mass energy of the two incoming partons.

$$w_{trunc.} = \frac{M_D^4}{\hat{s}^2} \; . \tag{4.15}$$

The effect of this procedure is shown in Fig. 4.15 for one of the signal points. The $\hat{s}$ distribution is smoothly, but decidedly cut-off for $\hat{s} > M_D$. In the $p_{\mathrm{T}}^{miss}$ distribution, which is the main relevant quantity for this analysis, the effect of the truncation is spread out along the whole spectrum and does not show a steep, localized cut-off. Due to the correlation between $\hat{s}$ and $p_{\mathrm{T}}^{miss}$, the effect of the truncation increases with increasing $p_{\mathrm{T}}^{miss}$ from $-40\%$ at $p_{\mathrm{T}}^{miss} = 500$ GeV down to $-60\%$ at $p_{\mathrm{T}}^{miss} > 3$ TeV. The effect on the overall signal cross section is demonstrated in Fig. 4.16. The truncation method generally has a stronger effect for larger values of the number of extra dimensions $d$. This effect partially compensates the $d$-dependence of the untruncated cross sections and reduces the overall spread as a function of $d$.

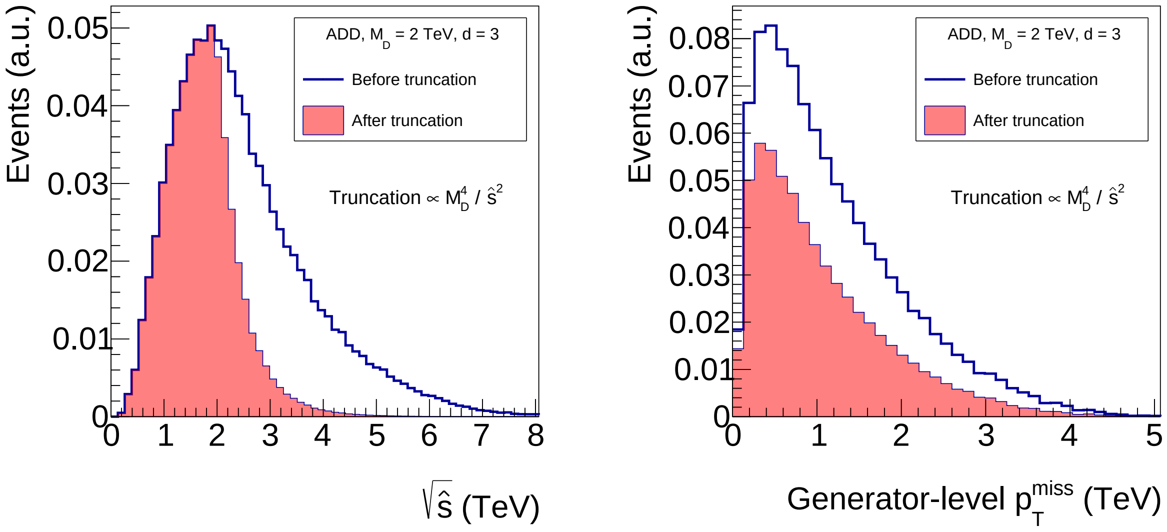

Figure 4.15.: Distributions of the $\hat{s}$ and generator-level $p_{\mathrm{T}}^{miss}$ variables for the ADD scenario with $M_D = 2$ TeV and $d = 3$. The distributions are shown before (blue solid lines) and after (red filled area) applying the truncation procedure described in the text.

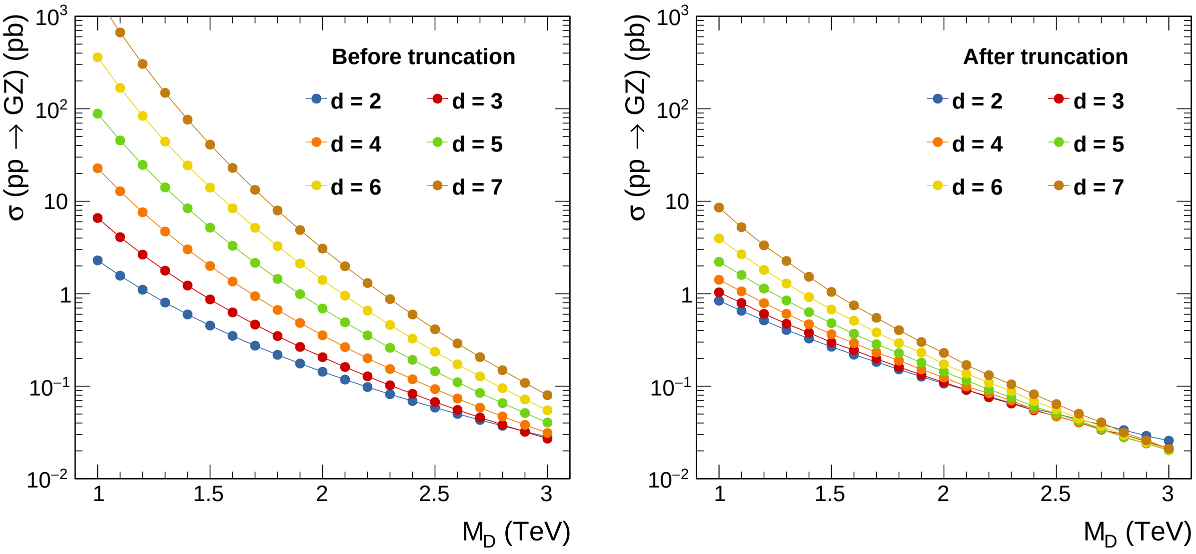

Figure 4.16.: Total signal cross sections for associated production of a graviton and Z boson in the ADD model. The cross sections require a minimum value of the graviton $p_{\mathrm{T}}$ of 50 GeV and are shown before (left) and after the application of the truncation procedure (right).

# 5. Dark matter relic density in simplified models

The simplified DM models discussed in the previous sections allow for the modelling of collider based signatures. However, to really qualify as models of *dark matter*, rather than just *any* new invisible particle, an important question is their compatibility with the known properties of DM, the most important of which is its abundance in the universe. Based on the Planck collaboration's observation of the cosmic microwave background, a global fit of the parameters of the ΛCDM model, allows for a precise determination of $\Omega h^2 = 0.12 \pm 0.001$ [9, 10], where $\Omega$ is the DM mass density in units of the critical density, and $h$ is the dimensionless Hubble parameter [85]. To understand the connection between the considered simplified models and the cosmological constraints, relic density results are derived for the parameter space considered in this analysis. In the following section, the calculation principles and technical setup are discussed, and results for the DMSimp and a+2HDM models are presented in subsequent sections. For reviews of the topic, see Refs. [103, 104].

The work presented here was inspired by discussions with the authors of Ref. [105], in which a similar study was performed for the DMSimp models using an older parameter choice recommendation, as well as an older version of the calculation software. Due to a programming mistake in that previous software version, the results presented in Ref. [105] are not correct for $m_{DM} > m_{med}$, as double s-channel annihilation is not taken into account (cf. Fig. 5.2). Previous versions of the studies shown here were included in Refs. [70, 84].

## 5.1. Thermal evolution and freeze-out

The abundance of a particle species in the universe is understood to be the result of the thermal evolution of the universe between the big bang and today. At sufficiently early times in the universe, and correspondingly at sufficiently high temperatures $T$, all particle species are in thermal equilibrium. Production and annihilation of particle pairs happens at identical rates and the equilibrium number density $n^{eq}$ of each massive particle species is determined by its mass $m$ and number of degrees of freedom $g$:

$$n^{eq} = g \left( \frac{mT}{2\pi} \right)^{3/2} \exp\left(-m/T\right) \ . \tag{5.1}$$

For particles with GeV-scale masses, thermal equilibrium would clearly imply a negligible number density in the low-temperature present-day universe. Fortunately, the expansion of the universe leads to a deviation from thermal equilibrium, which can be described using the Boltzmann equation:

$$\frac{dn}{dt} + 3Hn = -\langle \sigma v \rangle \left( n^2 - (n^{eq})^2 \right) \ . \tag{5.2}$$

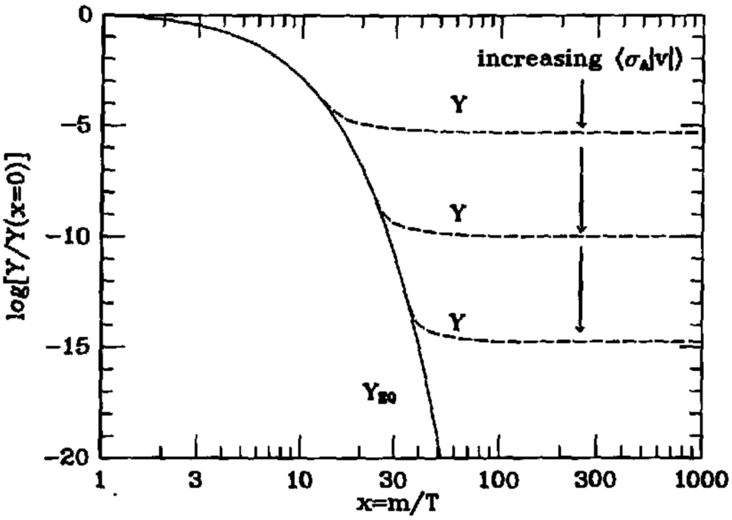

Figure 5.1.: Demonstration of thermal freeze-out. The variable Y on the vertical axis is proportional to the number of DM particles in the universe, while the horizontal axis shows the ratio of the DM particle mass $m$ and the temperature of the universe $T$. In thermal equilibrium (solid line), Y decreases with increasing $x$ as the universe cools and expands. Only the departure from the equilibrium value ("freeze-out") leads to non-zero present-day abundances at large $x$ (dashed lines). Depending on the interaction strength, as given by the annihilation cross section, freeze-out happens at different times, with larger annihilation cross sections leading to later freeze-out and smaller late-time abundances. Image taken from Ref. [103].

Here, $H$ is the Hubble constant, $\langle \sigma v \rangle$ is the thermal average of the product of particle velocity and annihilation cross section and $n$ is the current number density for the given particle species. The term proportional to $H$ represents the effect of the expansion of space, which reduces the particle number density even for a constant number of particles. The right-hand term encodes the effect of particle interactions, the strength of which is governed by the annihilation cross section. As the universe expands, it becomes increasingly unlikely for two DM particles to annihilate, as they become more and more separated. Finally, as the interaction rate becomes comparable to the expansion rate $\langle \sigma v \rangle n \approx H$, the particle interactions become negligible and the number of particles becomes constant. This process, which leads to non-zero present-day abundances, is called *freeze-out*. The resulting dependence of the particle number density on the temperature of the universe is illustrated in Fig. 5.1.

## 5.2. Technical setup

To compare the model predictions to this measurement, the relic density is calculated in the same parameter space that LHC analyses probe. The calculation is performed by the MadDM software with version 3.0 [106, 107]. MadDM is conveniently integrated into Madgraph5_aMC@NLO as a plugin that allows the user to directly calculate annihilation cross sections and relic densities for any model that is available in the *Universal FeynRules Out-*

*put* (UFO) format [108]. MadDM performs a *freeze-out* calculation. For a given parameter point, the velocity-averaged annihilation cross section is calculated, taking into account all tree-level DM-DM annihilation diagrams. The underlying assumption of this calculation is the completeness of the model: Additional DM candidates could enhance, additional annihilation mechanism could deplete the relic density compared to the values expected from the simplified model. Therefore, the relic density calculation is a qualitative guide as to what model assumptions are viable.

## 5.3. Results for DMSimp

For the DMSimp models, DM annihilation can proceed in two distinct ways: direct annihilation of a DM pair into a single mediator, as well as diagrams with a t-channel DM particle and two mediators. The corresponding diagrams are shown in Fig. 5.2. The resulting relic density values in the parameter space relevant to the LHC are shown in Fig. 5.3 for spin-1 mediators and in Fig. 5.4 for spin-0 mediators . While the exact shape of the allowed regions depends on the choice of scenario, there are some features that are common to all scenarios:

- Very light DM masses are vulnerable to overabundance. At the time of freeze-out, the DM particles are non-relativistic, and the center-of-mass energy of a DM-DM interaction is given as $\sqrt{s} = 2m_{DM} \times (1 + \mathcal{O}(v^2/c^2))$. If $m_{DM} \ll m_{med}$, the c.o.m. energy is too small to allow for annihilation, since the Breit-Wigner shape around the mediator mass acts as a bottleneck for the reaction.

- The resonance diagonal always causes underabundance. This can be understood from the same argument as before: When $\sqrt{s} \approx 2m_{DM} \approx m_{med}$, s-channel annihilation is very efficient. The transverse size of the underabundant region along the diagonal is defined by the mediator width and overall strength of s-channel annihilation. In the spin-1 case, the main difference between the axial and vector mediator scenarios is the $m_{DM}$-dependence of the width, which is much sharper for the vector case, resulting in increased annihilation and a larger underabundant region along the diagonal (cf. sec. 4.1 and Fig. 4.2). For the spin-0 case, the difference in coupling types leads to an overall different behavior: The s-channel annihilation cross section is proportional to the - very small - velocity and therefore suppressed, leading to a smaller underabundance region than in the pseudoscalar case.

- Between the over- and under-abundant regions, the relic density transitions continuously and thus must cross the desired value of 0.118.

- Above the diagonal $m_{DM} = m_{med}/2$, s-channel annihilation is penalized as the increasing c.o.m. energy would require an off-shell mediator to proceed. Annihilation is therefore dominated by the DM DM → Med. Med. process (cf. Fig. 5.2), which becomes efficient for $m_{DM} > m_{med}$ and leads to a new region of underabundance.

- Finally, for $m_{DM} \gg m_{med}$, the leading term for the double s-channel annihilation cross section falls as $1/m_{DM}^2$ [70], eventually leading back to an overabundance. The axial-vector scenario is an exception, as subleading terms contribute significantly.

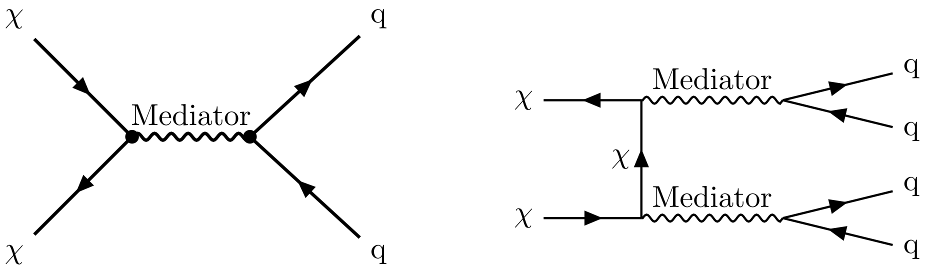

Figure 5.2.: Feynman diagrams contributing to the annihilation of DM pairs into SM particles for the DMSimp spin-1 scenarios. For a spin-0 mediator, the graphs are identical except for the mediator lines. The diagram with a single s-channel mediator (left) is dominant for $m_{DM} < m_{med}/2$, while the diagram with two s-channel mediators and a t-channel DM particle (right) is dominant for $m_{DM} > m_{med}$.

In summary, the parameter regions to which the LHC is sensitive can produce the observed value of the relic density even in a simplified model with only a single DM candidate. The allowed regions clearly motivate $p_{\mathrm{T}}^{miss}$-based searches, but also searches for decays of a mediator to SM fermions, which can cover the allowed regions with $m_{DM} > m_{med}/2$ [109, 110]. From the TeV-scale scan presented here, no clearly bounded allowed region is found. This raises the question of whether it will be possible to fully exclude a simplified model topology using collider constraints. Fig. 5.5 shows the relic density results for a larger range of $m_{DM}$ and $m_{med}$ up to 100 TeV, which is beyond the reach of the LHC, but could conceivably be probed by future accelerators. In all mediator scenarios, the underabundant trench close to the $m_{med}/2 = m_{DM}$ diagonal prevails up to large masses. However, it becomes narrower with larger masses and would thus require a delicate tuning of the $m_{DM}$ and $m_{med}$ parameters to achieve a sensible relic density in the higher mass regime. It will therefore not be possibly to fully exclude the allowed regions even with future accelerators, although the specific allowed solution may not be theoretically attractive due to the required tuning, which the TeV-scale solutions do not suffer from. The only relevant deviation can be observed in the axial vector case: Here, an underabundant region with $m_{med} \lessapprox 5$ TeV exists over the whole range of $m_{DM}$. Probing the full extent of this $m_{med}$ region would therefore be a very valuable constraint on the DMSimp scenarios. Current bounds from dijet searches [109] reach up to 2.5–3.0 TeV[1].

Beyond the scope of the LHC sensitivity, it is interesting to consider larger mass ranges for the DM and mediator particles.

## 5.4. Results for the a+2HDM

The a+2HDM scenario is similar to the pseudoscalar DMSimp scenario in its behavior relative to the SM fermion masses. However, an important difference arises due to the presence

---

[1] A search for very wide dijet resonances with $\Gamma/M \gtrapprox 0.3$ can exclude an axial vector mediator between 2 and 4.5 TeV [111]. However, due to the width requirement, it does not apply for the coupling choice $g_q = 0.25$ used here.

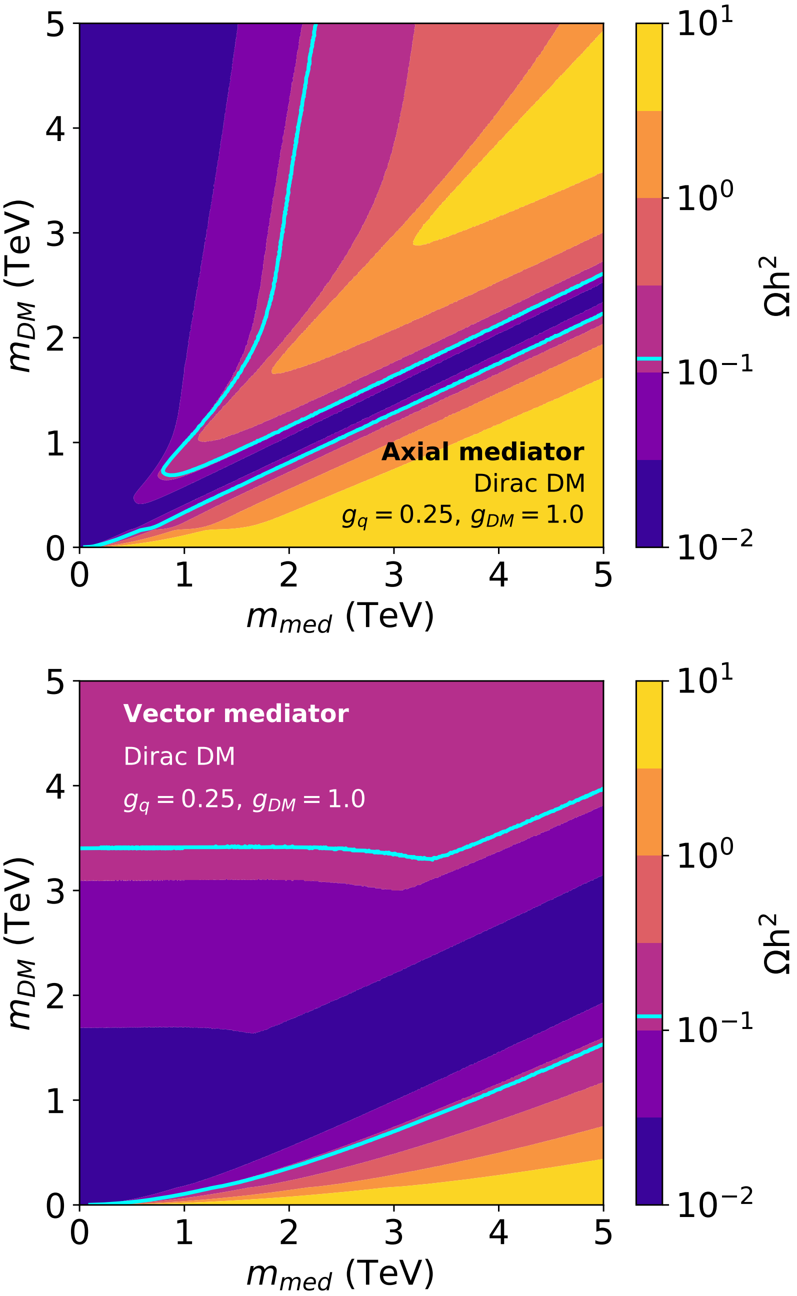

Figure 5.3.: Dark matter relic density as a function of the dark matter and mediator masses in the DMSimp scenarios with a spin-1 mediator: axial-vector (top), and vector (bottom). The mass range shown here reflects the approximate sensitivity range of the of the LHC searches. The teal line indicates the value $\Omega h^2 = 0.120 \pm 0.001$, which is the measurement obtained by the Planck collaboration [10]. The uncertainty in the measured value is so small as to not be relevant here. White auxiliary lines indicate relevant parameter values.

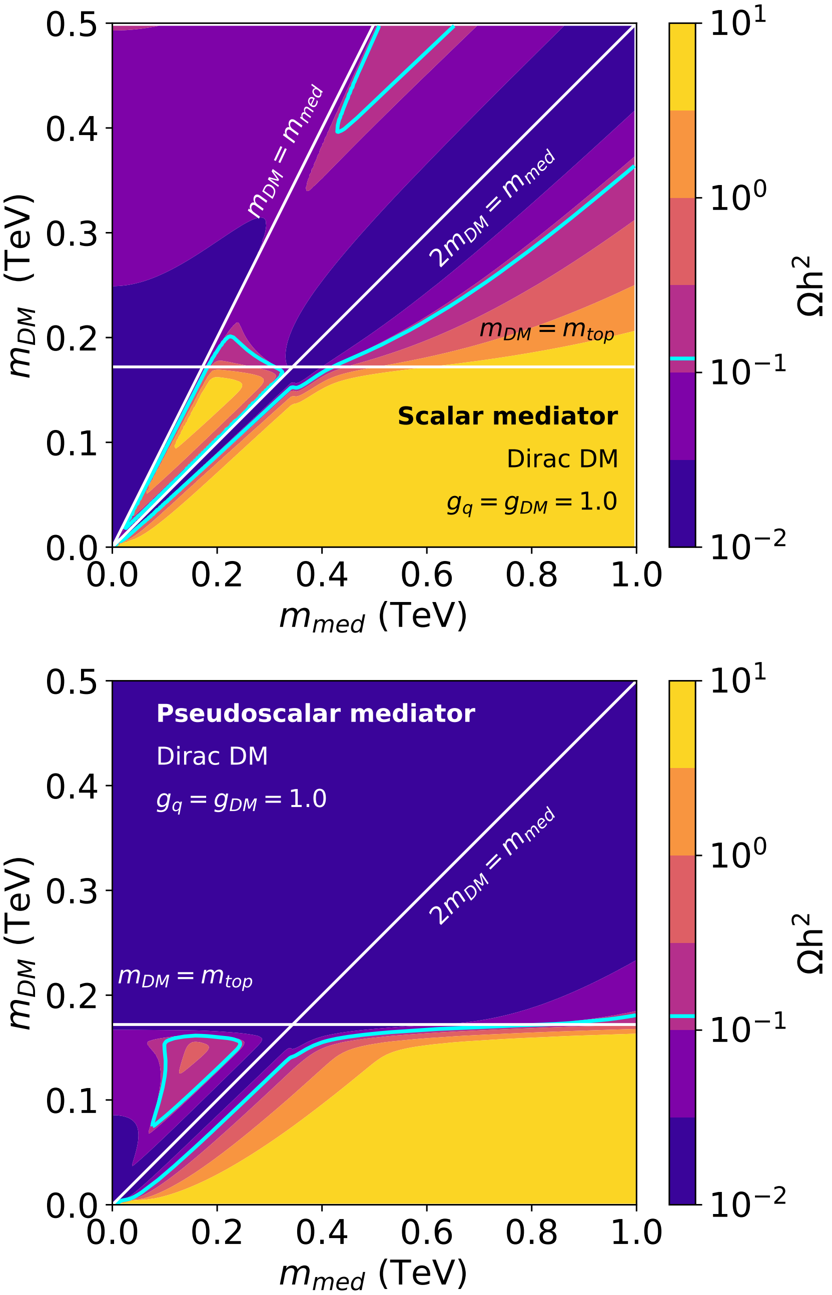

Figure 5.4.: Same as Fig. 5.3, but now for the DMSimp scenarios with spin-0 mediators: Scalar (top) and pseudoscalar (bottom).

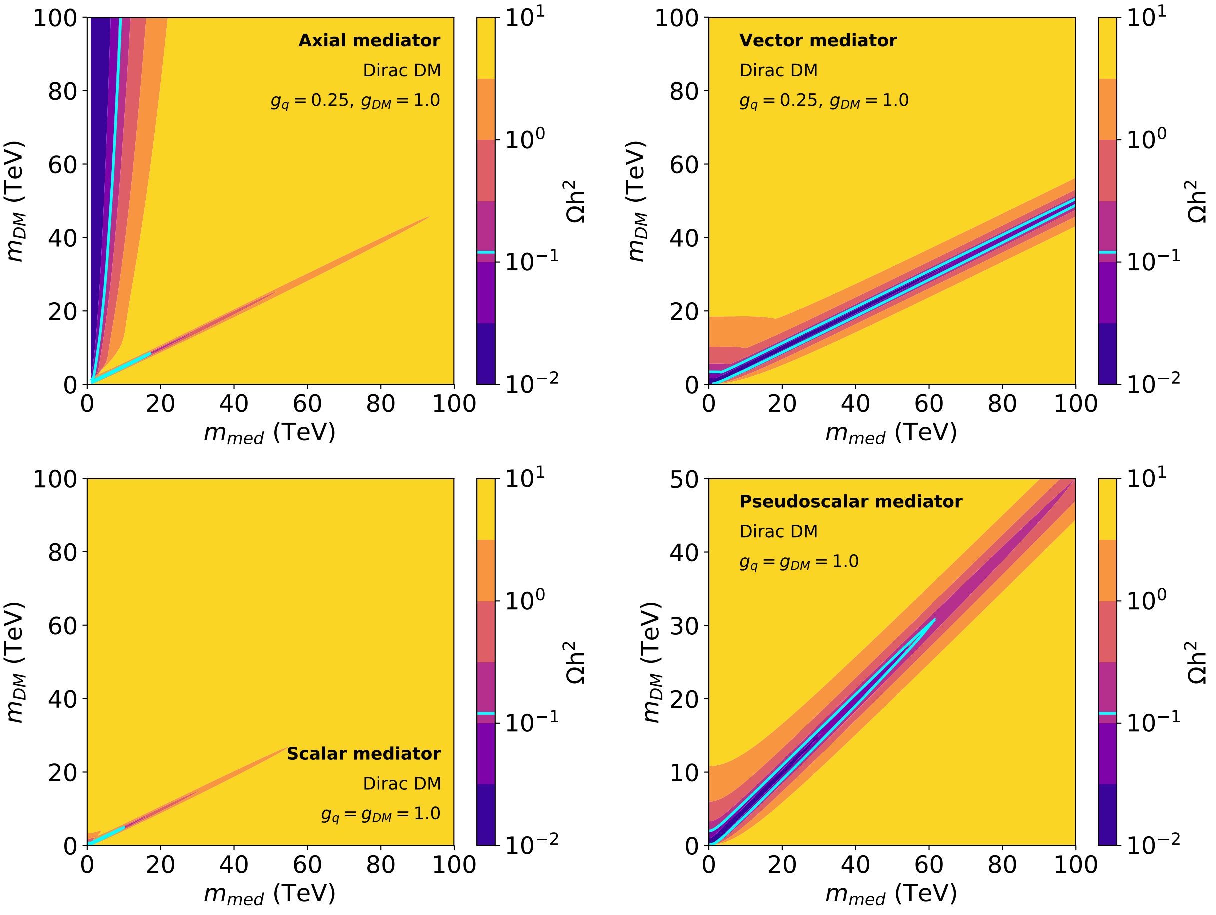

Figure 5.5.: Same as Figs. 5.3 and 5.4, but with increased axis ranges, now focusing on DM and mediator masses up to 100 TeV.

of additional bosons in the theory, which result in additional annihilation channels. The corresponding Feynman diagrams are shown in Fig. 5.6, and Fig. 5.7 shows the dependence of the relic density on the DM candidate mass, which is sculpted by the various kinematic thresholds for different annihilation channels. Although this behavior seems overly complicated at first, it is worth reminding oneself that the question at hand is whether or not the signal model can reproduce the observed relic density. Therefore, many of the features visible in Fig. 5.7 are not relevant because they appear at relic densities far larger or smaller than the observed value and therefore have no bearing on the qualitative answer to the question under study. Similarly to the spin-0 DMSimp scenarios, small values of $m_{DM}$ invariably lead to an overabundance, as only the Yukawa-suppressed annihilation into light quarks is possible.

The relic density is shown in the plane of the mediator and DM masses $m_\mathrm{a}$ and $m_{med}$ in Fig. 5.8. Here, the kinematic thresholds for the single and double s-channel processes (cf. Fig. 5.6) again shape the overall picture. The most relevant threshold is that of the top mass, as annihilation becomes very efficient for $m_{DM} > m_\mathrm{top}$. Overall, there is a number of independent allowed regions in the range up to $m_\mathrm{a}$, $m_{DM} \approx 1$ TeV. For larger values of $m_{DM}$ and $m_\mathrm{a}$ up to 10 TeV, allowed regions exist for $m_{DM} \approx m_{top}$, as well as $m_{DM} > m_\mathrm{a}$,

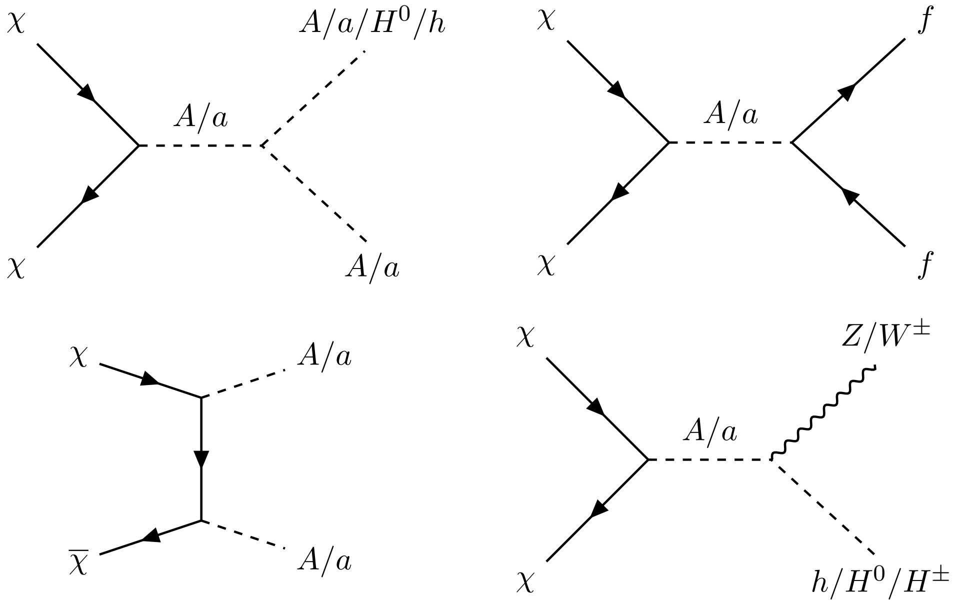

Figure 5.6.: Feynman diagrams contributing to the annihilation of DM pairs into SM particles for the a+2HDM. All tree-level annihilation diagrams are considered. Single (top left, top right, and bottom right), as well as double s-channel (bottom left) diagrams contribute. If multiple particles are given, they are interchangeable, as long as charge conservation in the full diagram is maintained (e.g. the bottom left diagram can result in $Zh$ and $W^+H^-$ final states, but not $W^+h$).

$m_{\mathrm{a}} < 5$ TeV. As in the axial-vector case above, it is questionable whether the fine-tuned $m_{DM} \approx m_{top}$ solution is to be considered attractive, but theoretical prejudice alone is surely not sufficient to rule out the possibility.

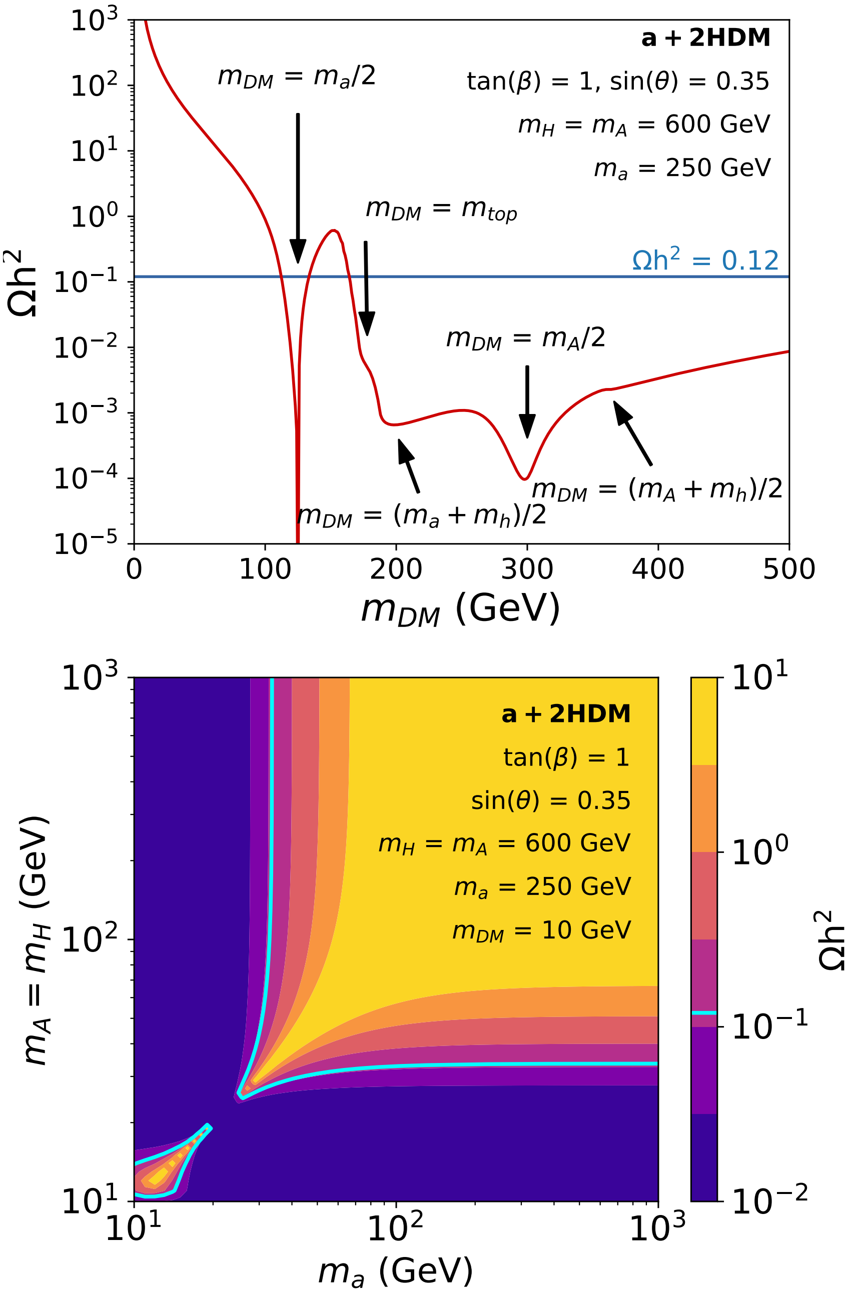

Figure 5.7.: Relic density for the a+2HDM model as a function of $m_{DM}$ (top) and as a function of $m_\mathrm{a}$ and $m_\mathrm{H} = m_\mathrm{A} = m_{\mathrm{H}^\pm}$ (bottom). The default parameter values are chosen, and $m_\mathrm{H} = m_\mathrm{A} = m_{\mathrm{H}^\pm} = 600$ GeV, as well as $m_\mathrm{a} = 250$ GeV (top), $m_{DM} = 10$ GeV (bottom). The graphical conventions are the same as used in Fig. 5.3.

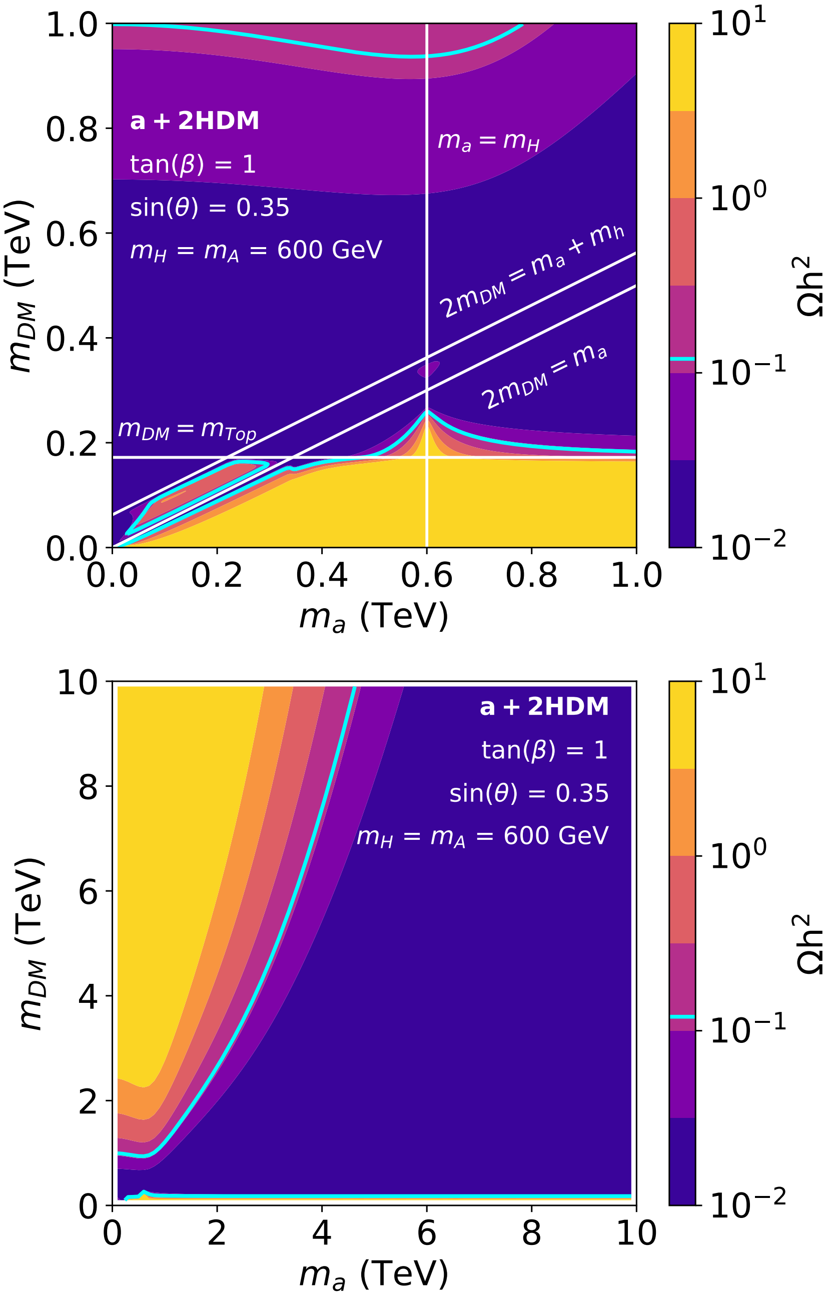

Figure 5.8.: Relic density for the a+2HDM model in the plane of $m_{DM}$ and $m_{\mathrm{a}}$. The default parameter choices described in the text are used and the heavy boson masses are set to $m_{\mathrm{H}} = m_{\mathrm{A}} = m_{\mathrm{H}^{\pm}} = 600$ GeV. The result is shown for the sensitivity range of the LHC (top), and beyond (bottom). The graphical conventions are the same as used in Fig. 5.3.

# Part II.

# Experimental analysis

# 6. Signature reconstruction and triggering

In this section, the methods used to reconstruct collision events are discussed. Events with a $Z + p_{\mathrm{T}}^{miss}$ topology are targeted, where the Z boson decays to a $e^{\pm}$ or $\mu^{+}\mu^{-}$ pair. The lifetime of the Z boson is sufficiently small to be neglected, which implies that both leptons are created without any displacement from the interaction point. For signal events, the $p_{\mathrm{T}}^{miss}$ component would be due to the production of new invisible particles, which are assumed to be produced at the same location as the leptons, and leave the detector without any decays or further interactions.

## 6.1. Object definition

Analyses aimed at probing the hard interaction rely on well-defined signatures for particles such as electrons and muons, but also more abstract objects such as $p_{\mathrm{T}}^{miss}$. Generally, CMS relies on the concept of *Particle Flow* (PF) reconstruction [112]. The goal of PF is to combine signatures from different parts of the detector to achieve optimal identification performance for a given particle. An intuitive example of this is jet reconstruction: It is possible to reconstruct jets by applying a clustering algorithm to all calorimeter deposits, which is a widely used method. The PF approach to this problem would instead be to first reconstruct individual particles, such as hadrons, electrons, etc. from the combined tracker and calorimeter information, and apply jet clustering using these particle candidates, rather than the underlying energy deposits, as inputs. This approach allows to harvest the strengths of multiple detector components, e.g. by being able to combine the good track position resolution with the superior ECAL energy resolution for highly energetic electrons. In this section, the reconstruction and identification methods used for all relevant objects are discussed. All descriptions in this section correspond to the official CMS performance publications cited in each subsection.

### 6.1.1. Track reconstruction

Track reconstruction is a central precursor to many more complex object definitions [113]. It is based on multiple applications of the *Kalman Filter* (KF) method. Starting from *seeds*, which are sets of a small number of hits, the KF method iteratively extrapolates tracks outwards from one tracker layer to the next. The extrapolation is performed using the current best estimate of a given track momentum and the associated bending in the magnetic field. If a hit in the next layers is found to be compatible with the extrapolated track, it is added to the track, the track parameters are updated, and the procedure is repeated. For each traversed layer of material, the track momentum is reduced according to the expected average energy loss as described by the Bethe-Bloch equation, and the expected distribution of scattering angles is applied as an uncertainty to the track direction. The full procedure is applied multiple times to identify prompt as well as displaced tracks and recover inefficiencies. After each iteration, hits corresponding to the identified tracks are removed, which reduces ambiguities and computational complexity for the following iterations.

## 6.1.2. Muons

A detailed account of muon reconstruction and identification in CMS is given in Ref. [114]. Here, a brief summary of the underlying principles is given, and the used identification criteria are defined.

### 6.1.2.1. Reconstruction

Muons are reconstructed using tracking information from silicon tracking systems and the gas-based muon system. Tracks for muon candidates are built either using only hits in the muon system (*standalone* tracks), or from a combination of the hits from both systems. *Tracker muon tracks* are extrapolated tracks from the silicon system, which are loosely compatible with a segment in the muon system [1]. The highest quality tracks are *Global muon tracks*, which are found by extrapolating tracks reconstructed in the muon system backwards, finding a matching tracker track, and performing a new track fit on the combined set of hits of both tracks. A single muon candidate can have tracks of multiple types associated it. The muon momentum is obtained using the *Tune-P* algorithm, which chooses from one of multiple available refitting schemes to obtain the optimal performance. The choice is made depending on the properties of each muon, and e.g. gives greater weight to the silicon track information for low muon momenta.

### 6.1.2.2. Identification

Two sets of selection criteria are used: A high-purity signal selection is used to identify muons for the construction of a Z-boson candidate. A lower-purity set of identification ("ID") requirements is applied to identify additional muons that are not part of the dilepton candidate. Muons passing this second set are used to reject ("veto") events with additional leptons, as the signals in this analysis do not predict additional leptons.

The signal muon selection is based on the so-called "medium" ID [114], which is designed to be efficient for both prompt muons and secondary muons from meson decays. To pass the medium ID, each muon is required to be categorized as a muon by the PF algorithm, as well as either a tracker or global muon. A degree of compatibility between the tracker track and track segments in the muon system is calculated based on the distance of track and each segment, as well as the agreement of their direction estimates. This segment compatibility rating ranges between zero and one, with one indicating good agreement [115]. If a muon is not reconstructed as a global muon, its segment compatibility rating is required to be larger than 0.451 to reject low-quality tracks, and no further criteria are applied. If the muon is reconstructed as a global muon, the segment compatibility requirement is relaxed to a threshold of at least 0.303, but additional track quality criteria are imposed. A good

---

[1] A *segment* is the set of reconstructed hits from a single multi-layer chamber.

overall track quality is enforced by requiring the $\chi^2/ndf$ value of the global track fit to be smaller than 3. Consistency of the tracker and standalone tracks is ensured by requiring their matching to result in a $\chi^2$ value of less than 12. Finally, the track is iteratively split into two parts in multiple places, and the at each iteration the two parts are required to match geometrically with $\chi^2 < 12$ ("kink-finding") [114].

In addition to the requirements of the medium ID, requirements are imposed on the impact parameters of muon tracks. As signal-like muons are produced as decay products of Z bosons, they are not expected to show significant displacement from the primary vertex. Therefore, the distance of closest approach between the muon track and the primary vertex in the beam direction is required to be smaller than 1 mm, while the distance in the transverse plane is required to be smaller than 0.2 mm. The transverse impact parameter is constrained more strictly because it can be measured with significantly better resolution [113].

To ensure that the selected muons indeed arise from the primary interaction rather than being produced from hadronic activity, an isolation criterion is applied. To select isolated muons, a cone with radius $R = 0.5$ in the $\eta - \phi$-plane centered on the muon direction is considered. An isolation variable $I$ is calculated as the sum of transverse momenta of all PF charged hadrons ($\mathrm{h}^{\pm}$), neutral hadrons ($\mathrm{h}^0$) and photons ($\gamma$) inside the cone divided by the muon momentum. In order to mitigate the influence of PU, charged particles are only considered if they originate from the PV. Since no originating vertex can be associated to the neutral hadrons, an average correction is applied by subtracting from the isolation sum half of the sum value for charged hadrons originating from PU vertices. This method follows the average charge-to-neutral ratio in hadronic jets [116]:

$$\begin{aligned} I_{\mu} = \frac{1}{p_{\mathrm{T}}(\mu)} \Bigg( & \sum_{\mathrm{h}^{\pm}\text{ from PV}} p_{\mathrm{T}}(\mathrm{h}^{\pm}) + \sum_{\mathrm{h}^0} p_{\mathrm{T}}(\mathrm{h}^0) \\ & + \sum_{\gamma} p_{\mathrm{T}}(\gamma) - \frac{1}{2} \sum_{\mathrm{h}^{\pm}\text{ not from PV}} p_{\mathrm{T}}(\mathrm{h}^{\pm}) \Bigg) . \end{aligned} \tag{6.1}$$

The relative isolation value is required to be smaller than 0.15 for signal muons.

Fur the purposes of rejecting events with additional muons beyond the two leptons belonging to the dilepton candidate, a more inclusive selection is applied. Veto muons are required to be PF muons and either tracker or global muons, have $p_{\mathrm{T}} > 10$ GeV and $I < 0.25$. To also reject events with muons created in meson decays, muons passing the "soft ID" with $p_{\mathrm{T}} > 3$ GeV are also considered as veto muons. Soft muons are required to have a high-quality tracker track that is consistent with at least one muon station, have tracker hits in at least 5 layers, at least one pixel hit. Very loose impact parameter maximal values of 0.3 cm (in the transverse plane) and 20 cm (in the beam direction) are applied.

### 6.1.3. Electrons

The methods used for the reconstruction and identification of electrons in CMS are detailed in [117], which is summarized here.

Table 6.1.: Summary of muon identification criteria used for signal selection, as well as background rejection (veto). The two veto selections given for 2015 are complementary, i. e. a muon needs to only pass one of the two sets of criteria in order to be used for the veto criterion.

| Year | Selection Type | ID | $d_{xy}$ / $d_z$ (cm) | Isolation | $p_T$ (GeV) |
|---|---|---|---|---|---|
| 2015 | Signal | Medium | 0.02 / 0.1 | 0.15 | 20 |
| | Veto 1 | Loose | - | 0.25 | 10 |
| | Veto 2 | Soft | - | - | 3 |
| 2016 | Signal | Tight | 0.02 / 0.1 | 0.15 | 20 |
| | Veto | Loose | - | 0.25 | 5 |

#### 6.1.3.1. Reconstruction

The reconstruction of electron candidates relies on information from the tracking and ECAL systems. The main challenge in electron reconstruction is posed by Bremsstrahlung, which causes electrons to radiate between 30% and 90% of their energy before reaching the ECAL. The energy loss affects both the determination of track parameters, and collection of ECAL energy deposits.

The collection of ECAL deposits focuses on the definition of so-called *super-clusters* (SCs), which can encompass several clusters arising from Bremsstrahlung photons radiated by the primary electron. SCs are found starting from crystals that contain locally maximal energy deposits. In an iterative procedure, adjacent sets of crystals are added if they contain energy deposits above a given threshold. Due to the bending of the electron trajectory in the magnetic field, Bremsstrahlung photons are spread out in $\phi$, and a larger range of $\phi$ is correspondingly used for crystal collection compared to the $\eta$ direction, where only a small spread is expected.

Based on the SCs and standard tracks found in the event, electron seeds are determined. A seed is a set of hits in the first three track layers, which defines an initial direction estimate and can thus be used as a starting point for full track reconstruction. For electrons with little radiated Bremsstrahlung, seeds are found starting from standard reconstructed tracks that are found to be pointing to an SC. For electrons with larger radiative losses, possible electron seeds are found by extrapolating possible trajectories backwards from the SC position. The results from both seeding methods are combined.

Using the set of seeds as an input, track reconstruction is performed using a Gaussian Sum Filter (GSF) [118]. The GSF method is a generalized form of the Kalman filter method used in the general track reconstruction. It differs from the standard version of the algorithm by modelling the energy loss in each material layer as a sum of multiple Gaussian functions, rather than a single Gaussian. For the highly radiative electrons, this results in a significant improvement in track parameter resolution.

The final electron momentum estimate is obtained from a weighted linear combination of the track momentum and SC energy. The weight is determined as a function of the values of the track and cluster properties, as well as their associated uncertainties. Compared to the energy information from the ECAL, this combination leads to a resolution improvement of up to 2% at low $p_\mathrm{T}$, but has a moderate effect for $p_\mathrm{T} \gtrapprox 20$ GeV, where the ECAL measurement dominates the combination.

#### 6.1.3.2. Identification

As for the case of the muons, a high-purity signal-like selection is applied to select electrons for the reconstruction of a dilepton candidate, while an inclusive veto selection is used to reject events with additional electrons.

Signal-like electrons are identified using requirements on the ECAL super cluster, track, as well as their compatibility. A first task of the identification procedure is to select ECAL super clusters that are likely to have been created by an incoming electron rather than a hadron. To this end, a lateral shower shape size $\sigma_{i\eta i\eta}$ is calculated by considering the $\eta$ coordinates of energy deposits in a five-by-five matrix of crystals around the highest energy deposit of the super cluster. The width $\sigma_{i\eta i\eta}$ is then calculated as the variance of the $\eta$ coordinate weighted by the logarithm of the energy deposited in each crystal. Practically speaking, $\sigma_{i\eta i\eta}$ will be small for showers that have their energy deposits focused in a small central area, whereas it will be larger for showers with more spread-out energy deposits. To further suppress hadronic contributions, the ratio $h/E$ is considered, where $E$ is the energy deposited in the super cluster, and $h$ is the energy deposited in the HCAL towers located directly outward of the super cluster location. While hadrons often create showers already in the ECAL, they typically deposit most of their energy in the HCAL, thus making $h/E$ a powerful variable to suppress hadron contributions. The second important aspect of the identification is the track reconstruction. For optimal reconstruction, a track should have hits in all pixel layers. A maximal number of missing hits is imposed to avoid badly reconstructed tracks. To ascertain that the track is compatible with the primary vertex, upper thresholds are set on the impact parameter in the z direction $d_z$ and the transverse plane $d_{xy}$. Since it is unlikely to find a signal-like Z boson candidate consisting of electrons from secondary vertices, the impact parameter requirements are not applied for the 2016 analysis. Beyond the separate criteria for the super cluster and track, the compatibility between the two is another handle for the rejection of combinatorial background. The $\eta$ ($\phi$) coordinate of the position information from tracker and ECAL are required to be consistent within a maximal absolute difference $\Delta\eta_\mathrm{in}$. Additionally, the momentum measurement provided by the track and the energy measurement from the super cluster are required to be consistent. Finally, electrons are required to be isolated. As in the case of the muons, isolation is evaluated by summing over the transverse momenta of PF candidates in a cone with radius $R = 0.4$ around the electron. One relevant difference to the muon case is the treatment of the PU correction. For electrons, an "effective area" $A_\mathrm{eff}$ is defined, which, when multiplied by the average PU energy density in an event $\rho$, estimates the PU contribution to the isolation sum. By subtracting this estimate $\rho \times A_\mathrm{eff}$, the impact of PU is suppressed.

$$I_\mathrm{e} = \frac{1}{p_\mathrm{T}(e)} \left( \sum_{\mathrm{h}^\pm} p_\mathrm{T}(\mathrm{h}^\pm) + \sum_{\mathrm{e}} p_\mathrm{T}(\mathrm{e}) + \max\left(0, \sum_{\gamma} p_\mathrm{T}(\gamma) + \sum_{\mathrm{h}^0} p_\mathrm{T}(\mathrm{h}^0) - \rho \times A_\mathrm{eff} \right) \right)$$

The exact parameters for the electron identification criteria are summarized in Tab. 6.2. Signal-like electrons are identified using the "Medium" criteria, whereas veto electrons are identified using the "Veto" working point. For both working points, optimization of the requirements has been performed separately for the barrel and endcap regions, owing to the differences in instrumentation as well as prevalence of hadron backgrounds.

Table 6.2.: Summary of electron identification criteria. The categorization into barrel and endcap regions is based on the super cluster pseudorapidity $\eta_{\mathrm{SC}}$, where $|\eta_{\mathrm{SC}}| < 1.479$ is counted towards the barrel and $1.479 < |\eta_{\mathrm{SC}}| < 2.5$ is counted towards the endcaps. All numerical values in the table are maximal values, i. e. the measured value is required to be smaller than the given value for the electron to pass the selection. Where two values are given, the first refers to the criteria used for the analysis of the 2015 data set, while the second refers to those used for the 2016 data set.

| | **Medium ID** | | **Veto ID** | |
|---|---|---|---|---|
| | Barrel | Endcap | Barrel | Endcap |
| Variable | | | | |
| $\sigma_{i\eta i\eta}$ | 0.0101 / 0.00998 | 0.0283 / 0.0298 | 0.0114 / 0.0115 | 0.0352 / 0.037 |
| $\lvert\Delta\eta_{\mathrm{in}}\rvert$ | 0.0103 / 0.00311 | 0.00733 / 0.00609 | 0.0152 / 0.00749 | 0.0113 / 0.00895 |
| $\lvert\Delta\phi_{\mathrm{in}}\rvert$ | 0.0336 / 0.103 | 0.114 / 0.045 | 0.216 / 0.228 | 0.237 / 0.213 |
| $h/E$ | 0.0876 / 0.253 | 0.0678 / 0.0878 | 0.181 / 0.356 | 0.116 / 0.211 |
| $I_{\mathrm{e}}$ | 0.0766 / 0.0695 | 0.0678 / 0.0821 | 0.126 / 0.175 | 0.144 / 0.159 |
| $1/E_{\mathrm{SC}} - 1/p_{\mathrm{track}}\,(\mathrm{GeV}^{-1})$ | 0.0174 / 0.134 | 0.0898 / 0.13 | 0.207 / 0.299 | 0.174 / 0.15 |
| $\lvert d_{xy}\rvert$(cm) | 0.0118 / – | 0.0739 / – | 0.0564 / – | 0.222 / – |
| $\lvert d_z\rvert$(cm) | 0.373 / – | 0.602 / – | 0.472 / – | 0.921 / – |
| Missing inner hits | 3 / 2 | 3 / 2 | 3 / 3 | 4 / 4 |
| Conversion veto | Yes | Yes | Yes | Yes |

### 6.1.4. Jets

Jets are identified using the `Anti-`$k_t$ algorithm with a distance parameter of $R = 0.4$ [119]. Clustering is performed by the FastJet package [120] using the PF candidates as inputs. To suppress energy contributions from particles originating from PU interactions, *charged-hadron subtraction* is applied, which means that charged hadrons with tracks not compatible with the primary vertex are removed from the list of candidates before clustering [121]. The clustering is performed without considering any categorization of the input candidates, which means that not only each hadronic shower, but also any other set of close-by particles, or even individual isolated particles will give rise to a jet. Jet quality can be monitored by considering the fractions of the total energy carried by particles in each of the PF candidate categories. Jets from real hadronic showers will always contain a mixture of reconstructed neutral and charged hadrons, charged leptons and photons. By requiring that no individual component be completely dominant or missing, jets from hadronic showers can be preferentially selected and backgrounds from instrumental noise or isolated leptons can be suppressed. The so-called "Loose PF ID" selection criteria are used. They are summarized in Tab. 6.3. Note that owing to the limited $|\eta|$ coverage of the tracking systems, no charge determination is possible for constituents with $|\eta| > 2.5$. Therefore, electrons (charged hadrons) are counted as photons (neutral hadrons), and requirements are only placed on their combined energy fractions. To reject residual contributions from jets that mostly represent a duplicate of an isolated lepton, all jets are removed that overlap within $\Delta R \leq 0.4$ with an isolated lepton passing the respective identification criteria.

#### 6.1.4.1. Tagging of $\tau$ and b jets

The jets defined in this section are practical constructions used to reign in in the complex phenomenology of hadronic showers. In their inclusive definition, they do not directly differentiate the cause or specific properties of a jet. However, this additional information can be useful in order to categorize events based on whether jets arise from initial gluons, quarks, or hadronically decaying $\tau$ leptons, which will often be reconstructed in a single jet. To identify the origin of a jet, *b tagging* and $\tau$ *tagging* are used. Events containing b or $\tau$ jets will later be rejected in order to reduce the background contributions from the $\mathrm{t\bar{t}}$ and and WZ processes.

For b tagging, the multivariate *CombinedSecondaryVertex* algorithm is trained to identify the specific decay signatures of B mesons. As its input, the details of the jet constituents, such as associated tracks, are used. The tagging is mainly based on the presence of displaced vertices formed by tracks inside a jet, which are caused by the significant lifetime of B mesons, as well as soft muons, which arise from B decays. The so-called "medium" working point of the algorithm is used [122].

For $\tau$ leptons, a limited number of decay topologies is available for direct reconstruction. Hadronic decays of $\tau$ leptons involve one or three charged hadrons, and a number of neutral pions. These topologies are reconstructed using the "hadrons-plus-strips" algorithm [123, 124], which relies on PF hadrons and ECAL energy deposits clustered into strip-like regions. The ECAL strips are used to reconstruct the energy of the neutral pions, which almost exclusively decay into pairs of photons, with possible subsequent photon conversions into $\mathrm{e^+e^-}$ pairs. To be identified as $\tau$ leptons, the jets are required to be isolated from other hadronic activity in the event.

Table 6.3.: Summary of the "Loose PF ID" jet identification criteria. The given $|\eta|$ regions are exclusive from left to right.

| | Requirements split by jet $\|\eta\|$ | | | |
|---|---|---|---|---|
| Variable | $< 2.4$ | $< 2.7$ | $< 3.0$ | $< 5.0$ |
| Max. neutral hadron fraction | 0.99 | 0.99 | - | - |
| Max. photon fraction | 0.99 | 0.99 | 0.9 | 0.9 |
| Min. number of constituents | 1 | 1 | 2 | 10 |
| Min. charged hadron fraction | $> 0$ | - | - | - |
| Min. charged multiplicity | $> 0$ | - | - | - |
| Max. electron fraction | 0.99 | - | - | - |

### 6.1.5. Missing transverse momentum

Missing transverse momentum $\vec{p}_{\mathrm{T}}^{\,miss}$ is reconstructed from the full set of PF candidates [125].

$$\vec{p}_{\mathrm{T}}^{\,miss} = - \sum_{\text{PF candidates}} \vec{p}_T$$

The magnitude of the $\vec{p}_{\mathrm{T}}^{\,miss}$ vector is referred to as $p_{\mathrm{T}}^{miss}$. Note that there is no special treatment attempting to remove charged hadrons associated with PU vertices. To account for the calibration of the jet energy scale, the $\vec{p}_{\mathrm{T}}^{\,miss}$ vector is corrected according to the vectorial sum of the shifts of the individual jet momenta.

$$\vec{p}_{\mathrm{T}}^{\,miss} \to \vec{p}_{\mathrm{T}}^{\,miss} - \sum_{i \in \text{jets}} \left( \vec{p}_i^{\,\text{corrected}} - \vec{p}_i^{\,\text{uncorrected}} \right)$$

This correction is referred to as "Type-1" correction.

Since the definition of $p_{\mathrm{T}}^{miss}$ needs to be as inclusive as possible in order not to miss any components of the event, it is vulnerable to contamination from energy deposits due to detector noise, beam background effects, failures of the event reconstruction algorithms, as well as PU contributions. To mitigate the effects of well-known sources of "fake" $p_{\mathrm{T}}^{miss}$, an event filtering method is used, where events affected by one of the known effects are rejected [125]. Known sources are HCAL noise (`HBHENoise(Iso)Filter`), beam halo muons (`CSCTightHalo2015Filter / globalSuperTightHalo2016Filter`), significant energy deposits in an ECAL crystal with inactive final readout (`EcalDeadCellTriggerPrimitiveFilter`), a lack of well-identified vertices (`goodVertices`), and badly reconstructed ECAL endcap SCs, charged hadrons, or muons (`eeBadScFilter`, `BadChargedCandidateFilter`, `BadPFMuonFilter`). The filtering procedures have evolved with time, and a summary of which filters are applied for the analysis of the data set of each year is given in Tab 6.4.

## 6.2. Triggers

In this section, the triggering criteria used to define a baseline data set are described.

Signal events are collected using single and double electron and muon triggers. As the expected trigger rates are the main driver for the choices of trigger requirements, double lepton triggers can have lower $p_{\mathrm{T}}$ thresholds and possibly more inclusive identification criteria

Table 6.4.: Summary of applied $p_{\mathrm{T}}^{miss}$ filters. A check-mark in the respective column indicates that the filter is applied in the analysis of a given year's data. Please refer to the text for a description of the individual filters.

| Technical filter name | Applied in 2015 | Applied in 2016 |
|---|---|---|
| HBHENoiseFilter | ✓ | ✓ |
| HBHENoiseIsoFilter | ✓ | ✓ |
| CSCTightHalo2015Filter | ✓ | ✗ |
| globalSuperTightHalo2016Filter | ✗ | ✓ |
| EcalDeadCellTriggerPrimitiveFilter | ✓ | ✓ |
| goodVertices | ✓ | ✓ |
| eeBadScFilter | ✓ | ✓ |
| BadChargedCandidateFilter | ✗ | ✓ |
| BadPFMuonFilter | ✗ | ✓ |

than single lepton triggers, because there are fewer double-lepton than single-lepton events. While the signal topology always contains two leptons, the single lepton triggers are still added in order to recover residual inefficiencies in the two-lepton triggers.

For the muon triggers, muons can either have a track based solely on the information from the inner tracking system, or a track with combined information from the inner tracker and outer muon system. The double muon triggers always require one higher-$p_{\mathrm{T}}$ muon ($p_{\mathrm{T}} > 17$ GeV) that is reconstructed with a track from both systems, as well as a second muon with $p_{\mathrm{T}} > 8$ GeV that can either be tracker based ("TkMu") or combined. In addition, loose track-based isolation criteria ("TrkIsoVVL") are applied to both muons. Track-based isolation is calculated by considering the momenta of all tracks in the proximity of the muon. Additionally, the two muons are required to be consistent with coming from the same vertex by imposing a requirement on the difference of the z coordinates or the point of closest approach between the track and the beam axis ("DZ"). The single muon trigger has a slightly higher $p_{\mathrm{T}}$ threshold of 20 GeV and a more PF based isolation requirement, which is more strict than in the case of the two-muon trigger.

In a very similar manner to the muons, the two-electron trigger requires two electrons with $p_{\mathrm{T}} > 17$ and 12 GeV, respectively. Loose criteria are applied on the calorimeter shower deposits ("CaloIdL"), the track quality ("TrackIdL") and isolation ("IsoVL"). Again, the two electrons are required to have similar $z$ coordinates. The single-electron trigger requires $p_{\mathrm{T}} > 23$ GeV and applies an inclusive selection criterion ("WPLoose").

Events for the opposite-flavour control region are collected using combined electron-muon triggers. The triggers require either a muon with $p_{\mathrm{T}} > 8$ GeV and an electron with $p_{\mathrm{T}} > 17$ GeV, or a muon with $p_{\mathrm{T}} > 17$ GeV and an electron with $p_{\mathrm{T}} > 12$ GeV. The requirements on the individual components are very similar to those of the same-flavour triggers discussed above.

In all cases, the identification and isolation criteria, as well as the $p_{\mathrm{T}}$ thresholds for the trigger objects are more inclusive than the selection criteria applied in the offline analysis, which are detailed above. The used trigger paths are summarized in Tab. 6.5.

Table 6.5.: Triggers paths used to select events at the online HLT stage. The `OR` of the given triggers is used, i. e. an event needs to pass at least one of the paths to be considered further. Reference triggers are used for the measurement of the efficiency of the signal triggers (cf. sec. 7.3.5).

| **Year** | **Target** | **Technical name** | **$p_T$ threshold (GeV)** |
|---|---|---|---|
| 2015 | Muons | Mu17_TrkIsoVVL_(Tk)Mu8_TrkIsoVVL_DZ | 17, 8 |
| | | Iso(Tk)Mu20 | 20 |
| | Electrons | Ele17_Ele12_CaloIdL_TrackIdL_IsoVL_DZ | 17, 12 |
| | | Ele23_WPLoose_Gsf | 23 |
| | Mixed | Mu8_TrkIsoVVL_Ele17_CaloIdL_TrackIdL_IsoVL | 8, 17 |
| | | Mu17_TrkIsoVVL_Ele12_CaloIdL_TrackIdL_IsoVL | 17, 12 |
| | Reference | Mu17_TrkIsoVVL | 17 |
| | | Ele12_CaloIdL_TrackIdL_IsoVVL | 12 |
| 2016 | Muons | Mu17_TrkIsoVVL_(Tk)Mu8_TrkIsoVVL_DZ | 17, 8 |
| | | Iso(Tk)Mu24 | 24 |
| | Electrons | Ele23_Ele12_CaloIdL_TrackIdL_IsoVL_DZ | 23, 12 |
| | | Ele25_eta2p1_WPTight_Gsf | 25 |
| | | Ele27_WPTight_Gsf | 27 |
| | | Ele115_CaloIdVT_GsfTrkIdT | 115 |
| | Mixed | HLT_Mu23_TrkIsoVVL_Ele12_CaloIdL_TrackIdL_IsoVL(_DZ) | 23, 12 |
| | | HLT_Mu8_TrkIsoVVL_Ele23_CaloIdL_TrackIdL_IsoVL(_DZ) | 8, 23 |

# 7. Analysis of the 2015 data set

In 2015, the CMS collaboration collected its first data set with $\sqrt{s} = 13$ TeV, and thus entered into a previously unprobed energy regime. In this section, a search for invisible particles, based on this data set is described. Events with a $Z + p_{\mathrm{T}}^{miss}$ topology are studied, where the Z boson decays into prompt $\mathrm{e}^{+}\mathrm{e}^{-}$ or $\mu^{+}\mu^{-}$ pairs.

It is organized as follows: The kinematic properties of $Z + p_{\mathrm{T}}^{miss}$ events and corresponding signal selection criteria are discussed in secs. 7.1 and 7.2. Subsequently, the background estimation techniques are discussed in sec. 7.3, and studies of the $p_{\mathrm{T}}^{miss}$ reconstruction performance are presented. Sections 7.4 and 7.5 are dedicated to the used statistical methods and treatment of uncertainties, respectively. Finally, the analysis results are discussed in sec. 7.6.

The analyzed data set has an integrated luminosity of 2.3 $\mathrm{fb}^{-1}$ and is analysed in the so-called `Feb08` reconstruction. The triggering and object selection criteria have been detailed in sec. 6. The results of this analysis have been published in Ref. [98].

## 7.1. Kinematic distributions

The invariant mass distribution of the dilepton pairs is shown in Fig. 7.1 for all events passing the trigger selection and containing an OSSF dilepton pair. At this loose selection stage, the spectrum is dominated by the Drell-Yan process. The second most significant contribution arises from the category of “nonresonant” processes, which in this analysis is defined as the collection of all processes that can give rise to same-flavour as well as opposite-flavour lepton pairs, such as $\mathrm{t\bar{t}}$ and WW. The nonresonant processes will later be estimated in a common, partially data-driven way. Finally, small contributions arise from the diboson processes WZ and ZZ, which are the most similar to the sought-after signal, but have small overall cross sections and are thus almost negligible at this very inclusive selection stage. Overall, the simulated prediction for the spectra agrees well with the behavior in data except for a small displacement of the Z peak: This is a result of residual differences in the lepton momentum scale. Outside the Z peak region, this effect also exists, but has a much smaller effect on the shape of the nonresonant part of the distribution.

The most important quantity for this analysis is missing transverse momentum $p_{\mathrm{T}}^{miss}$, which is closely related to the transverse momentum of the dilepton system $p_{\mathrm{T}}(\ell\ell)$. The distributions of both quantities are shown in Fig. 7.2 for events passing the requirement on the dilepton mass ($|m_{\ell\ell} - m_{\mathrm{Z}}| < 10$ GeV). In the distribution of the $p_{\mathrm{T}}(\ell\ell)$ variable, it is immediately apparent that this variable is not well suited to control the DY background by itself: Over the full available spectrum up to $p_{\mathrm{T}}(\ell\ell) \approx 500$ GeV, the DY process remains dominant. For the DY process, the shape of this distribution is completely controlled by the behavior of the ISR radiation: The only way for the Z boson to obtain large transverse momentum is the presence of hard recoiling jets. Accordingly, a slightly harder spectrum is observed in data compared to the LO simulation. A different picture emerges in the distribution of $p_{\mathrm{T}}^{miss}$: The DY contribution falls rapidly with $p_{\mathrm{T}}^{miss}$, which is a result of the production process for $p_{\mathrm{T}}^{miss}$ in DY events: As there is no intrinsic production of invisible particles, any measured $p_{\mathrm{T}}^{miss}$ can only be the result of mismeasurement, limited acceptance, and neutrino production in hadronic processes. All of these sources may generate moderate $p_{\mathrm{T}}^{miss}$ contributions, but will hardly contribute to signal-like topologies with $p_{\mathrm{T}}^{miss} > 80$ GeV. A dedicated study of the contamination from DY events in the signal region is discussed in sec. 7.3.2. At higher $p_{\mathrm{T}}^{miss}$ values, the spectrum is dominated by the nonresonant and diboson processes, which intrinsically produce neutrinos and are thus not reliant on misreconstruction. Notably, the agreement between data and simulation improved towards higher $p_{\mathrm{T}}^{miss}$, which is a simple result of the fact that the misreconstruction effects at low $p_{\mathrm{T}}^{miss}$ are harder to simulate than the real hard event kinematics, which are dominant in the upper parts of the spectrum.

## 7.2. Offline event selection

The selection of signal events follows a four-step strategy:

- Selection of candidate events with two opposite-sign same-flavour leptons. Single and double lepton triggers are combined to maximize the trigger efficiency.
- Reconstruction of a Z boson candidate: The dilepton system is required to be consistent in mass with the nominal Z boson mass, and have a minimum transverse momentum.
- Rejection of the reducible background by removing events with additional leptons, more than two identified jets, or at least one b jet. The selection up to this point is referred to as *preselection*.
- Amplification of the signal topology via application of requirements on the geometric relationship of $\vec{p}_{\mathrm{T}}^{miss}$ and $\vec{p}_{\mathrm{T}}$ (Z), aiming to extract events where these two vectors are back-to-back in the transverse plane and have similar magnitude. This last selection step is referred to as *final* selection.

The exact criteria are listed in Tab. 7.1. The distributions of the main discriminant variables after applying the preselection criteria are shown in Fig. 7.3. Good agreement is observed between data and simulated SM prediction. The quality of $p_{\mathrm{T}}^{miss}$ simulation can further be studied by considering the distribution of the components of $p_{\mathrm{T}}^{miss}$ parallel and orthogonal to the transverse component of the dilepton momentum. The distributions of these quantities are shown in Fig. 7.4. For events passing the preselection criteria, the distribution of the parallel $p_{\mathrm{T}}^{miss}$ component normalized to the total $p_{\mathrm{T}}^{miss}$ is strongly and equally peaked at $\pm 1$, indicating that it is equally likely to obtain $p_{\mathrm{T}}^{miss}$ contributions from over- and underestimation of the recoil jet momentum. After additionally requiring $p_{\mathrm{T}}^{miss} >$ 80 GeV, the peak of events at $-1$ is suppressed, and dominantly populated by DY events, while the ZZ, WZ and signal processes cluster towards sharper peaks at $+1$. The distribution of the orthogonal component is less peaked overall (the ratio of maximal to minimal bin content is approximately three, compared to five for the parallel case), and shows a peak at $+1$, which is due to events in which the hard jets and the Z boson are well measured, but soft jets from the underlying event and PU events cause mismeasured components. While these contributions are isotropically oriented, they are mostly observed in the orthogonal direction since their magnitude is small compared to the hard event momenta, leading to a suppression of the parallel component.

The "cutflow", i. e. a comparison of the total yields observed in data and simulation for each successive selection step is shown in Fig. 7.5. From the succession of steps, it is easily deducible which requirements are the most important: the boost of the dilepton system, as well as the topology requirements on the angles and balance of dilepton and $p_{\mathrm{T}}^{miss}$ have the largest effects on the event yields. Other requirements such as the dilepton mass, the rejection of events with additional leptons or b tagged jets, have little overall effect. As expected from the individual distributions discussed above, the step-by-step agreement in the selection efficiency between data and simulation is good.

Table 7.1.: Summary of the event selection criteria used in the analysis of the 2015 data set.

| | Variable | Requirement |
|---|---|---|
| **Preselection** | $p_{\mathrm{T}}^{\ell}$ | $> 20$ GeV |
| | $\lvert\eta(\mathrm{e})\rvert$ | $< 1.44$ or $> 1.57$ and $< 2.5$ |
| | $\lvert\eta(\mu)\rvert$ | $< 2.4$ |
| | $\lvert m_{\ell\ell} - m_{\mathrm{Z}}\rvert$ | $< 10$ GeV |
| | $p_{\mathrm{T}}^{\ell\ell}$ | $> 50$ GeV |
| | Jet counting | $\leq 1$ jet with $p_{\mathrm{T}}^{\mathrm{j}} > 30$ GeV |
| | 3<sup>rd</sup>-lepton veto | $p_{\mathrm{T}}(\mathrm{e}, \mu) > 10$, $p_{\mathrm{T}}(\tau) > 20$ |
| | Top quark veto | Veto on b jets and soft muons |
| **Final Selection** | $\Delta\phi(\ell\ell, \vec{p}_{\mathrm{T}}^{miss})$ | $> 2.7$ radians |
| | $\lvert p_{\mathrm{T}}^{miss} - p_{\mathrm{T}}(\ell\ell)\rvert / p_{\mathrm{T}}(\ell\ell)$ | $< 0.2$ |
| | $p_{\mathrm{T}}^{miss}$ | $> 80$ GeV |

## 7.3. Background estimation

The basis of the background estimation in this analysis are samples obtained from Monte Carlo (MC) simulation, which are described in the following section. Corrections to the MC behavior derived from external theoretical programs or data are described in the subsequent sections.

### 7.3.1. Simulated samples

Where possible, the highest available perturbative order is used for the matrix element calculation. For the VV backgrounds, the POWHEG generator is used, which provides predictions at NLO in QCD with up to one radiated parton taken into account in the matrix element calculation [126–130]. The gluon-induced ZZ component is simulated using MCFM [131]. For the DY process, a tree-level calculation from Madgraph5_aMC@NLO is used with up to four radiated partons in the matrix element [73, 74]. While a one-loop prediction would be available, it is imperative for this analysis to have a sufficient number of high-$p_{\mathrm{T}}(\ell\ell)$

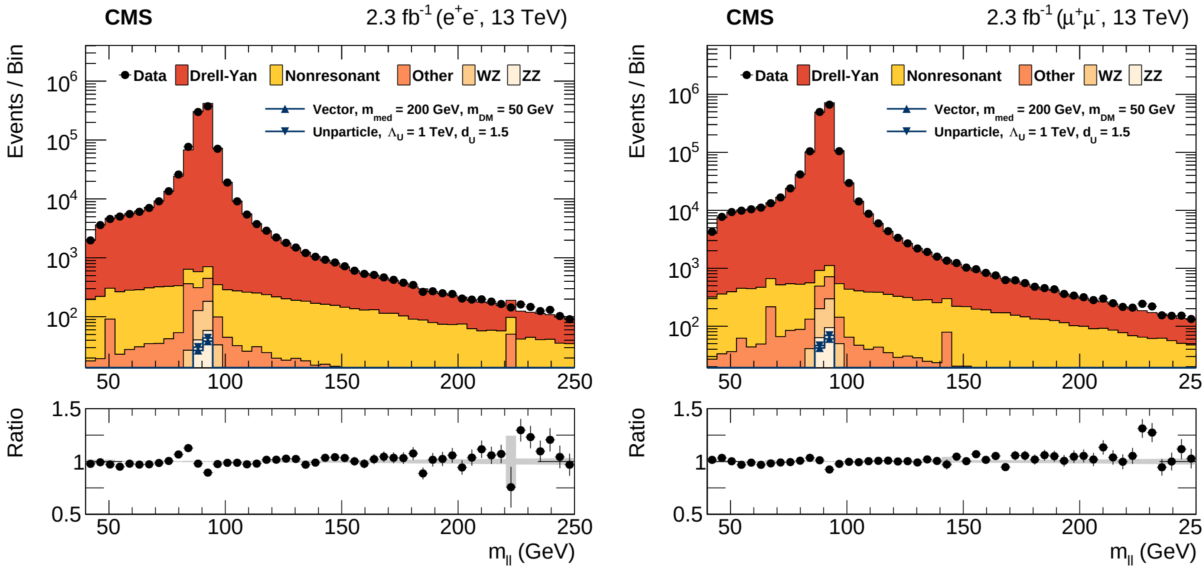

Figure 7.1.: Distribution of the invariant mass of the dilepton pair in electron pairs (left) and muon events (right). All events passing the trigger selection and containing an opposite-sign same-flavour dilepton pair are included. The distributions are shown for data (black points), background contributions estimated from simulation (stacked, solid histograms) and two benchmark signals (blue hollow histograms with solid markers). In the lower panel, the ratio of data over background is given, with the gray band representing the background uncertainty due to the finite size of generated event samples. The benchmark signals are for DM production through a vector mediator, with $m_{med}$ = 200 GeV, $m_{DM}$ = 50 GeV and $g_q = g_{DM}$ = 1.0, as well as unparticle production with EFT scale $\Lambda_U$ = 1 TeV, and scaling dimension $d_U$ = 1.5. These choices will be kept throughout this section.

events available, which is not the case for the available one-loop samples. Therefore, the tree-level calculation is preferred in this case. The $\mathrm{t\bar{t}}$ process, with or without an associated production of a Z or W boson, as well as the triboson VVV and t-channel single top quark production are simulated using Madgraph5_aMC@NLO at one-loop level with up to two radiated partons [82, 132, 133]. QCD multijet events are simulated using Pythia8 version 8.2 [76]. A summary of the used generators, perturbative orders and applied corrections is given in Tab. 7.2.

Signal samples of DM production are generated using Madgraph5_aMC@NLO at leading order (LO) in QCD. Samples for the unparticle scenario are generated using Pythia8, also at LO in QCD.

In all cases, parton showering is applied using Pythia8, and the implementation of the full CMS detector geometry in Geant [80] is used to model interactions between final state particles and the detector material.

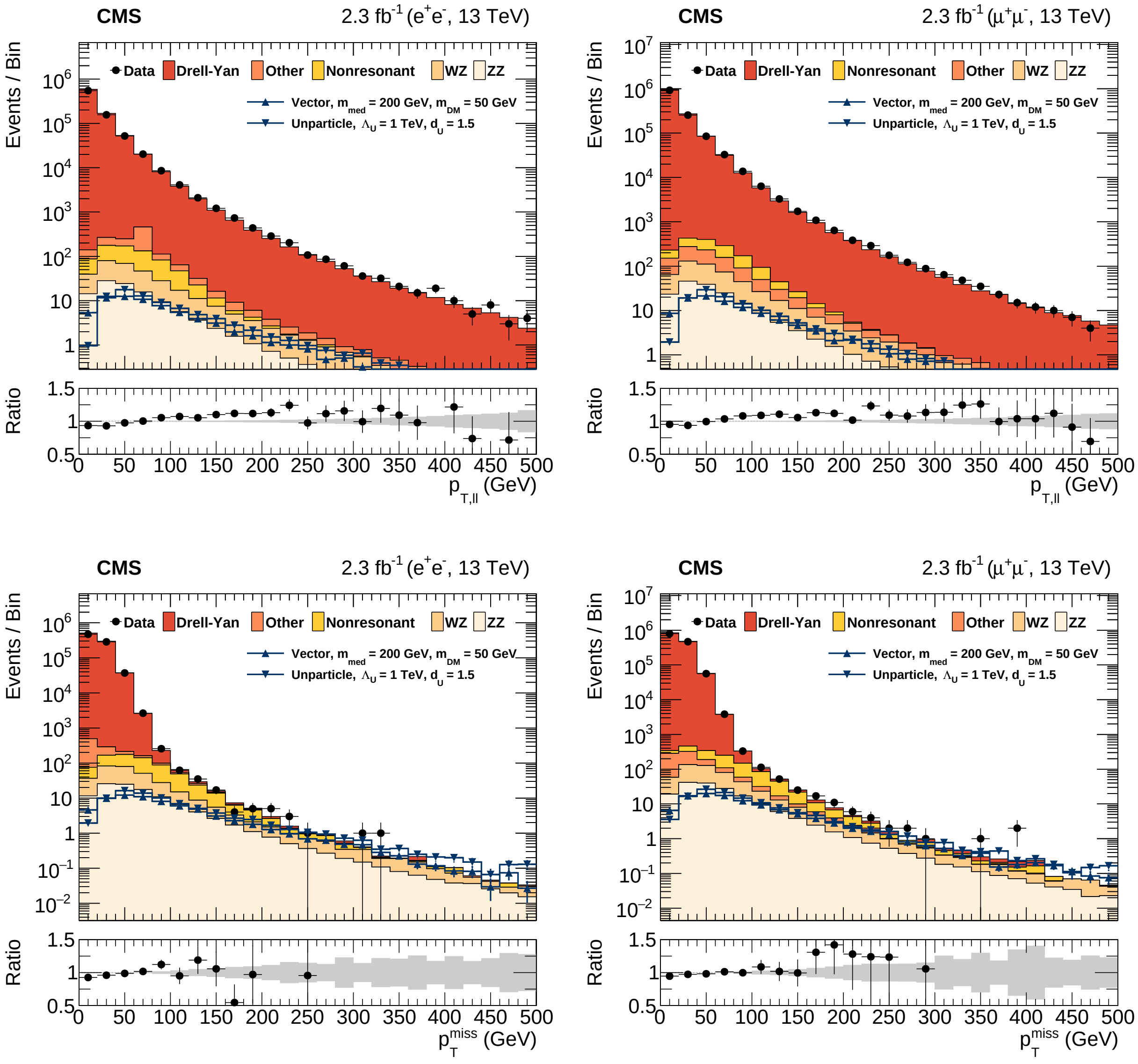

Figure 7.2.: Distribution of transverse momentum of the lepton pair (upper panels) and the missing transverse momentum (lower panels) for events with an OSSF lepton pair with $|m(\ell\ell) - m_Z| < 10$ GeV and up to one jet. The distributions are shown separately for events with electron (left) and muon pairs (right).

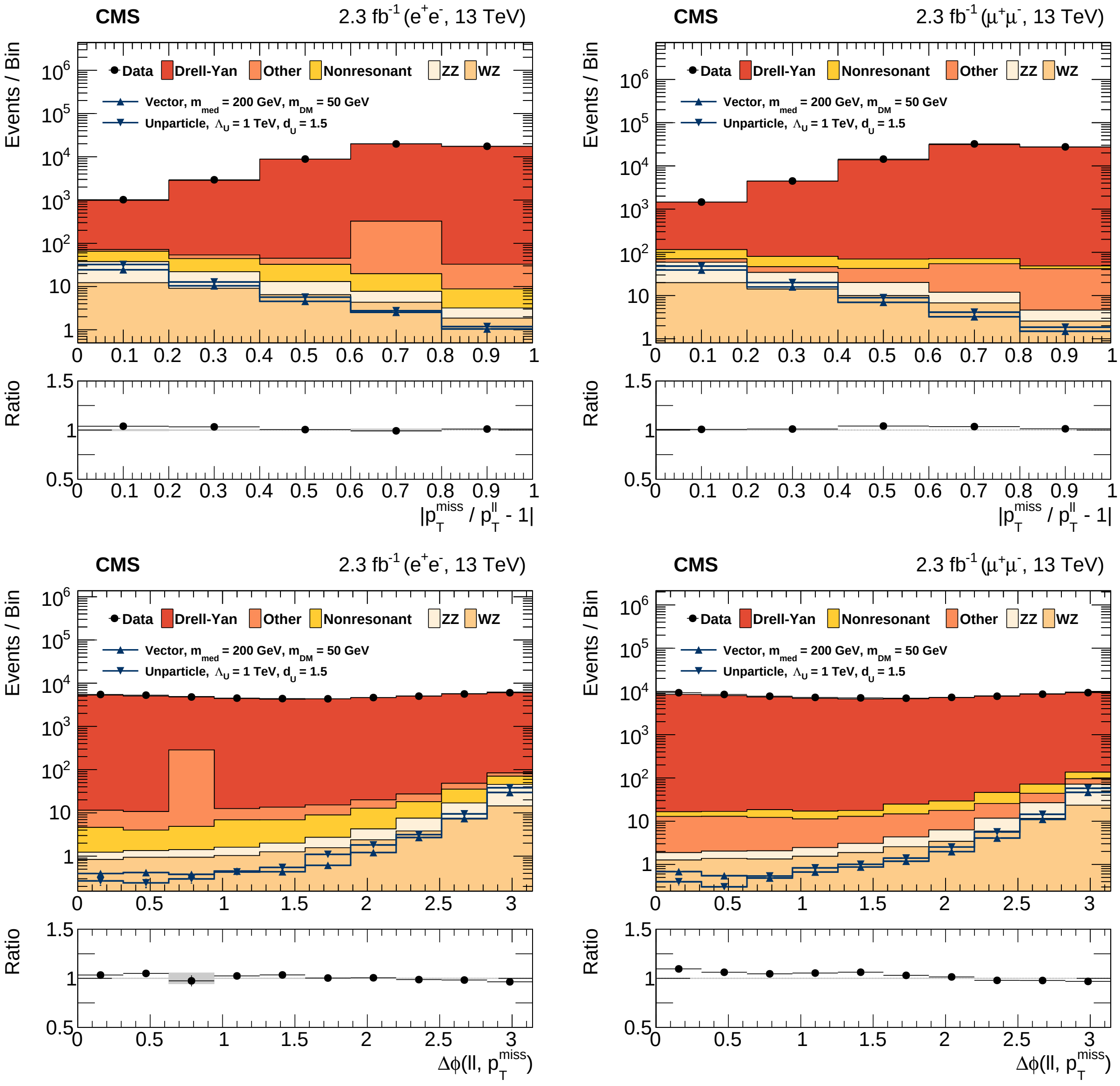

Figure 7.3.: Distribution of the balance variable $|p_{\mathrm{T}}^{miss}/p_{\mathrm{T}}(\ell\ell) - 1|$ (top) and the angular separation $\Delta\phi(\ell\ell, p_{\mathrm{T}}^{miss})$ between the $\vec{p}_{\mathrm{T}}^{\,miss}$ and $\vec{p}_{\mathrm{T}}(\ell\ell)$ vectors in the transverse plane after preselection for electron (left) and muon events (right).

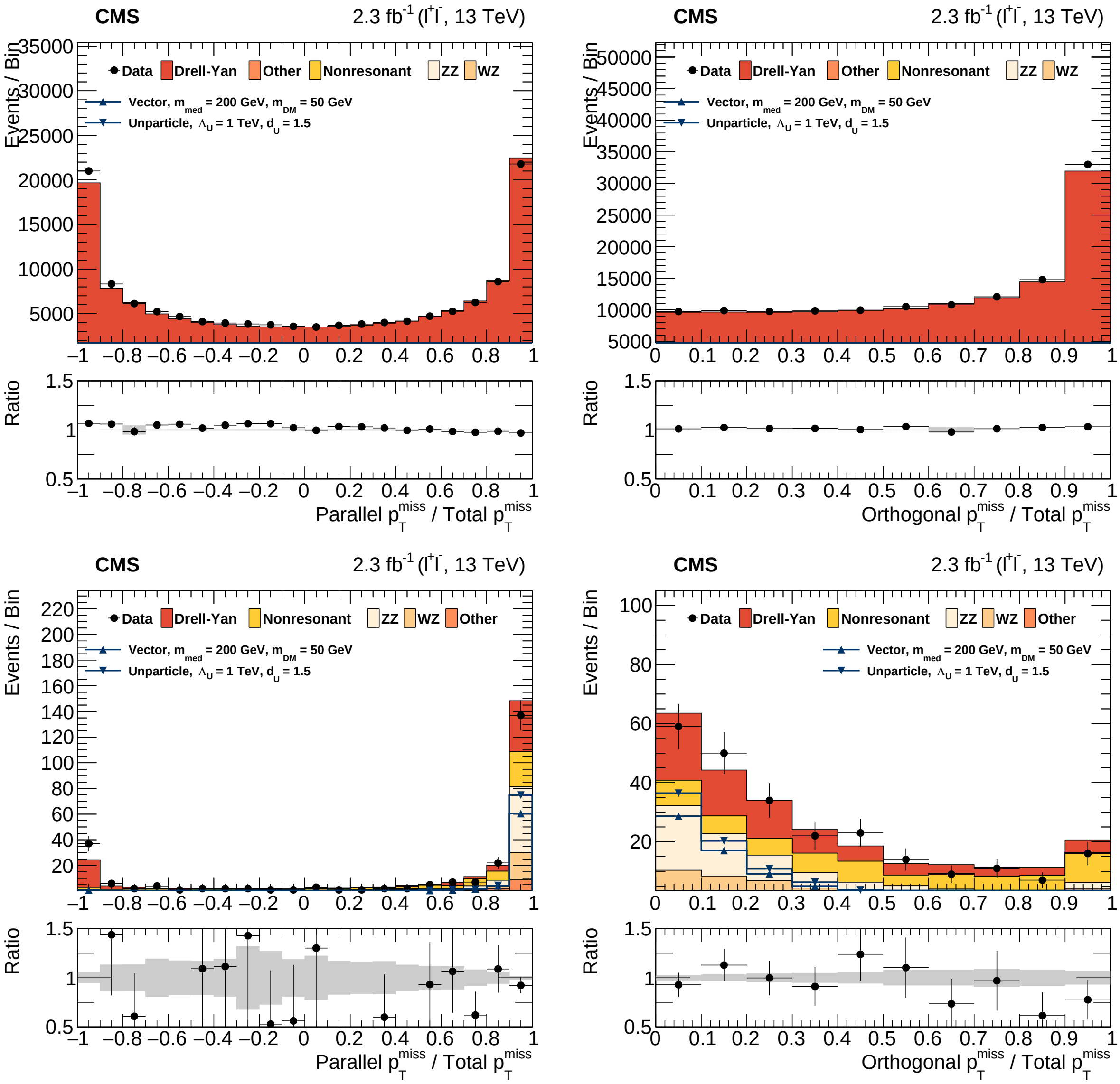

Figure 7.4.: Distribution of the components of $\vec{p}_{\mathrm{T}}^{miss}$ parallel (left) and orthogonal (right) to the transverse component of the dilepton momentum. The distributions are shown for the combined electron and muon channels after preselection (top), as well as with an additional requirement of $p_{\mathrm{T}}^{miss} > 80$ GeV applied.

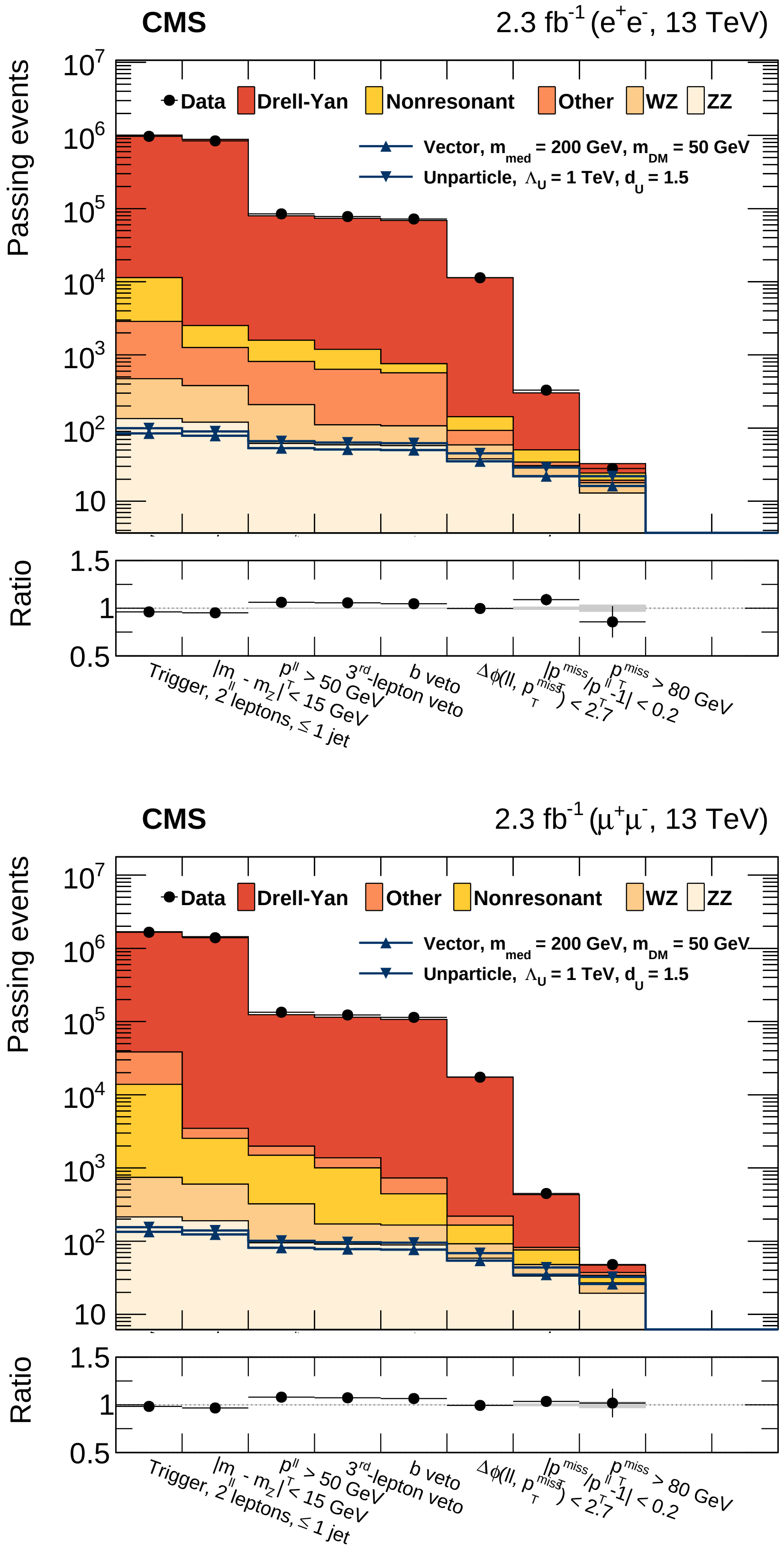

Figure 7.5.: Simulated and observed event yields after each cumulative selection step for electron (upper panel) and muon events (bottom panel). Each horizontal bin corresponds to one of the cumulative selection stages.

Table 7.2.: Overview of simulation samples used in the analysis of the 2015 data set. The generators are abbreviated as PH for Powheg, MG5 for Madgraph5_aMC@NLO and P8 for Pythia8. In the corrections column, "norm." means that only the total cross section of a process is corrected.

| Process | Generator | Pert. order | Corrections |
|---|---|---|---|
| $ZZ \to \ell\ell + \nu\nu/\ell\ell/\mathrm{qq}$<br>$WZ \to \ell\ell\ell\nu$<br>$WW \to \ell\ell\nu\nu$ | PH | NLO+PS | NNLO QCD, NLO EWK [134–137]<br>–<br>– |
| $Z/\gamma^* \to \ell\ell$ | MG5 | LO+PS | NNLO QCD (norm.) [138, 139] |
| $VVV$ | MG5 | NLO+PS | – |
| $\mathrm{t\bar{t}}$<br>$\mathrm{t\bar{t}} + W/Z$<br>Single top | MG5 | NLO+PS | NNLO QCD (norm.) [140–145]<br>–<br>– |
| QCD Multijets | P8 | NLL | – |

## 7.3.2. Drell-Yan

The shape of DY contributions to all distributions is estimated from simulation. Two measures are taken to ensure a sensible modeling of the DY background in the signal region: A normalization scale factor is obtained from a control region that has the same selection criteria as the signal region, except for an inverted requirement on the missing transverse momentum: $50 < p_{\mathrm{T}}^{miss} < 80$ GeV. The normalization of the DY process is increased so that the integral of the DY and other SM contributions fits the observed number of data events in the control region. This yields scale factors of 1.02 and 1.17 for the muon and electron channels, respectively. The uncertainty of the extrapolation from $p_{\mathrm{T}}^{miss} < 100$ GeV to $p_{\mathrm{T}}^{miss} > 100$ GeV is taken into account by applying a constant normalization uncertainty of 100% is applied to the DY prediction in the signal region. Effectively, when the maximum-likelihood fit is later applied to the signal region (cf. sec. 7.4), this allows the fit to determine the DY component from data. Since the DY contamination over most of the signal region is small, this has little impact on the sensitivity.

Note that the above correction is only applied for the final selection. For all other selection stages, distributions are shown with the DY component normalized to the inclusive cross section calculated at NNLO in QCD as computed by FEWZ version 3.1 [138, 139], which gives good overall agreement.

#### 7.3.2.1. Study of $p_{\mathrm{T}}^{miss}$ modeling in DY

To ensure that the estimate of the Drell-Yan contribution is sensible, additional tests are performed. Two dedicated variables are considered: The angular separation of jets and $p_{\mathrm{T}}^{miss}$, $\Delta\phi(jet, p_{\mathrm{T}}^{miss})$, and the ratio of $p_{\mathrm{T}}^{miss}$ as reconstructed by the PF algorithm and $p_{\mathrm{T}}^{miss}$ reconstructed only from calorimeter information and muon tracks ("calo" $p_{\mathrm{T}}^{miss}$). The first variable is sensitive to $p_{\mathrm{T}}^{miss}$ contributions induced by mismeasurement of jets, which would lead to events clustering around values of 0 and/or $\pi$. The second variable can be used to verify that the PF $p_{\mathrm{T}}^{miss}$ reconstruction algorithm performs well. Calo $p_{\mathrm{T}}^{miss}$ reconstruction is straightforward, and does not involve the reconstruction of real particle candidates. While this robustness is an advantage, the less refined reconstruction technique also leads to deteriorated resolution compared to PF-based $p_{\mathrm{T}}^{miss}$. Note that for the distribution of $\Delta\phi(\mathrm{jet}, p_{\mathrm{T}}^{miss})$, only events with one jet with $p_{\mathrm{T}} > 30$ GeV are used. Different regions are considered:

1. With preselection and $p_{\mathrm{T}}^{miss} > 80$ GeV (Fig. 7.6). At this loose selection stage, the general modeling quality of the considered variables is reasonable. The distribution of $\Delta\phi(\mathrm{jet}, p_{\mathrm{T}}^{miss})$ shows peaks at $\pi$ and 0, with the peak at 0 being made up almost entirely by DY events. The ratio of calorimeter and PF $p_{\mathrm{T}}^{miss}$ is centered between 1.0 and 1.2, indicating a slightly larger $p_{\mathrm{T}}^{miss}$ response in the calo-driven reconstruction.

2. With preselection, $p_{\mathrm{T}}^{miss} > 80$ GeV and $\Delta\phi(ll, p_{\mathrm{T}}^{miss}) > 2.7$ (Fig. 7.7). This region allows to study the effect of applying of the signal-like angular separation cut. For DY events, which acquire high dilepton momenta only from recoil jets, the requirement is correlated with the angular separation between jet and $p_{\mathrm{T}}^{miss}$. In comparing to region 1, the expected contribution of DY events at $\Delta\phi(jet, p_{\mathrm{T}}^{miss}) \approx \pi$ is suppressed. The requirement also constrains the PF/Calo variable closer to unity.

3. With preselection, $p_{\mathrm{T}}^{miss} > 80$ GeV, $|p_{\mathrm{T}}^{miss} - p_{\mathrm{T}}^{\ell\ell}|/p_{\mathrm{T}}^{\ell\ell} > 0.4$ and $|u_{\parallel}/p_{\mathrm{T}}^{\ell\ell}| > 1$ (Fig. 7.8). The topology requirements are inverted with respect to the signal region. This selection explicitly enriches fake-$p_{\mathrm{T}}^{miss}$ contributions and rejects real ones, yielding an estimate of the "worst case scenario". This region is dominated by DY events, especially in the case of events with a jet. In comparison to region 1, events with $\Delta\phi(\mathrm{jet}, p_{\mathrm{T}}^{miss}) \approx 0$ are suppressed, and the deviation between data and simulation around $\Delta\phi(\mathrm{jet}, p_{\mathrm{T}}^{miss}) \approx \pi$ is increased. Similarly, an overall excess is observed in the calo/PF ratio. In both cases, the distribution shape agrees between data and simulation, but a normalization difference of up to 80 % is observed.

4. With preselection, $p_{\mathrm{T}}^{miss} > 80$ GeV, $|p_{\mathrm{T}}^{miss} - p_{\mathrm{T}}^{\ell\ell}|/p_{\mathrm{T}}^{\ell\ell} > 0.4$ and $|u_{\parallel}/p_{\mathrm{T}}^{\ell\ell}| > 1$ and $\Delta\phi(ll, p_{\mathrm{T}}^{miss}) > 2.7$(Fig. 7.9). While still enriched in fake $p_{\mathrm{T}}^{miss}$, the effect of the $\Delta\phi(ll, p_{\mathrm{T}}^{miss})$ requirement is studied. The previously observed excess is removed, indicating that $\Delta\phi(ll, p_{\mathrm{T}}^{miss})$ is useful in suppressing fake-$p_{\mathrm{T}}^{miss}$ contributions from DY events.

5. After final selection (Fig. 7.10). With all selection requirements applied, no significant differences between data and simulation are observed.

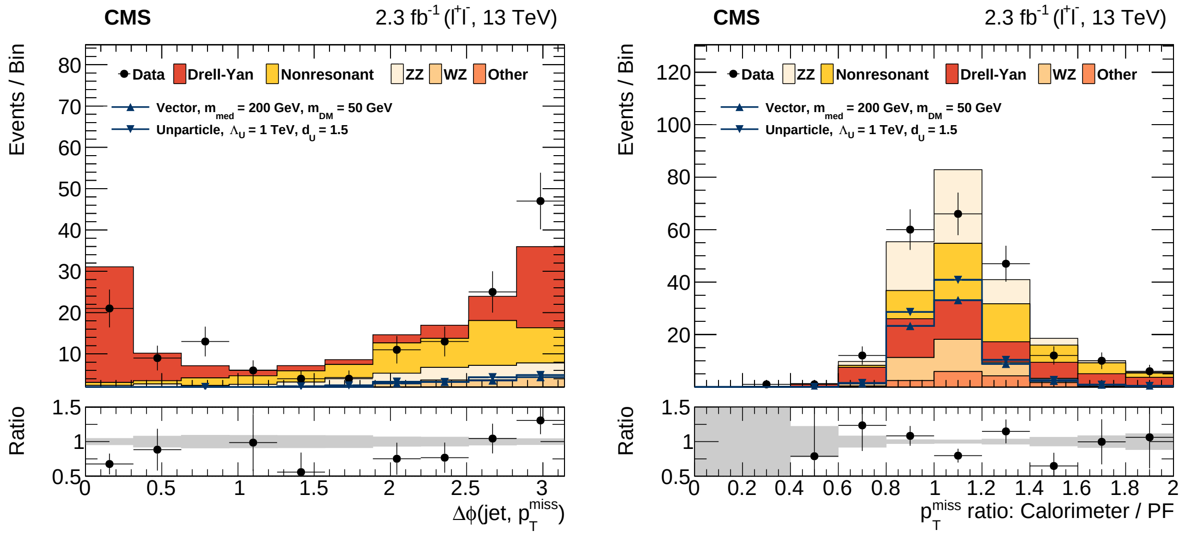

Figure 7.6.: Distributions of $\Delta\phi(jet, p_{\mathrm{T}}^{miss})$ (left) and $p_{\mathrm{T}}^{miss}$ (PF)/$p_{\mathrm{T}}^{miss}$ (Calo) (right) after requiring preselection and $p_{\mathrm{T}}^{miss} > 80$ GeV. This region is referred to as “region 1” in the text.

To understand the impact of possible fake $p_{\mathrm{T}}^{miss}$ on the shape of the $p_{\mathrm{T}}^{miss}$ distribution, the $p_{\mathrm{T}}^{miss}$ distributions for the right-most $\Delta\phi(jet, p_{\mathrm{T}}^{miss})$ bin of each region are shown in fig. 7.11. While there is a disagreement of the simulated normalization with respect to data, the shapes of the distributions are well modelled in all cases. Even in region 3, which is enriched in events with fake $p_{\mathrm{T}}^{miss}$, the difference between data and simulation is completely covered by the 100% uncertainty on the DY normalization. Sufficient numbers of simulated events are present in all bins.

In summary, the study of fake-$p_{\mathrm{T}}^{miss}$ related variables indicates that the simulation shape used for DY estimate in combination with a 100% normalization uncertainty is sensible.

### 7.3.3. Nonresonant backgrounds

Background processes where the lepton pair does not originate from a single resonance (e.g. $Z \to \ell\ell$) are designated as “nonresonant” backgrounds. This class of backgrounds is almost exclusively made up of the $\mathrm{t\bar{t}}$ and $WW$ processes, which have a favourable property: Since the decays generating the leptons are independent, they can produce different-flavour as well as same-flavour lepton pairs, i. e. they produce not only $\mathrm{e^+e^-}$ and $\mu^+\mu^-$, but also $\mathrm{e}^\pm\mu^\mp$ pairs. The rate of these processes in the same-flavour signal region can be estimated from a different-flavour control region, which is described in this section. The shape of the $p_{\mathrm{T}}^{miss}$ distribution of these processes is taken from simulation.

The control sample is selected in exactly the same way as the signal region, except requiring a $\mathrm{e}\mu$ pair instead of the nominal same-flavour pair. A transfer factor $k_{\mathrm{ee}/\mu\mu}$ from the control to the signal region is derived directly from the yields in the muon and electron signal regions $N_{\mathrm{ee}/\mu\mu}$. The ratio of the electron and muon yields encodes information about all efficiency and acceptance differences between the two processes, but is insensitive to signal contributions, as all signal hypotheses are flavour-symmetric:

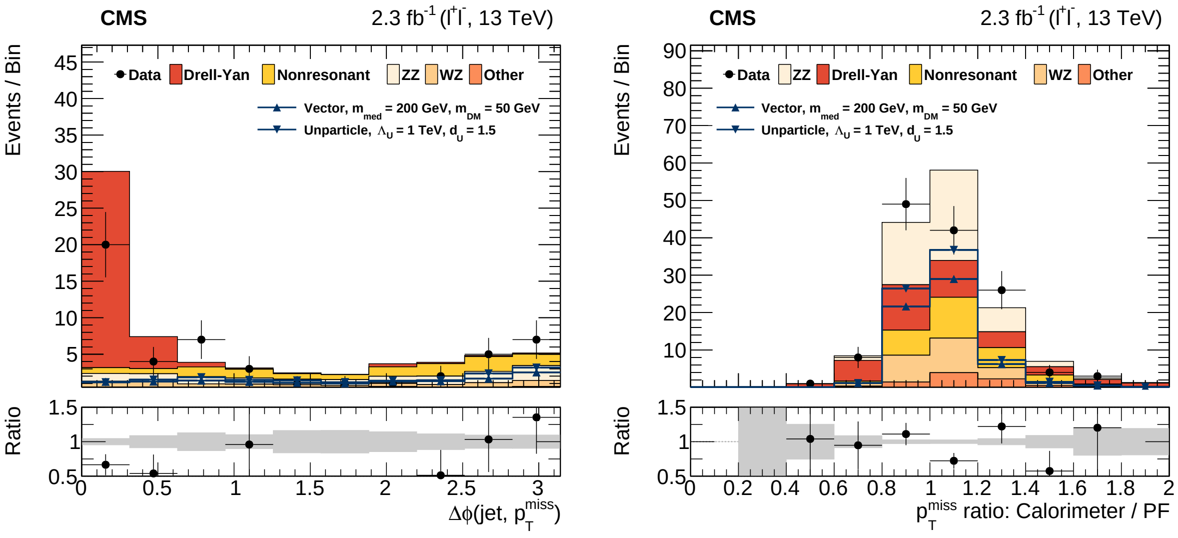

Figure 7.7.: Distributions of $\Delta\phi(jet, p_{\mathrm{T}}^{miss})$ (left) and $p_{\mathrm{T}}^{miss}$ (PF)/$p_{\mathrm{T}}^{miss}$ (Calo) (right) after requiring preselection, $p_{\mathrm{T}}^{miss} > 80$ GeV and $\Delta\phi(ll, p_{\mathrm{T}}^{miss}) > 2.7$. This region is referred to as “region 2” in the text.

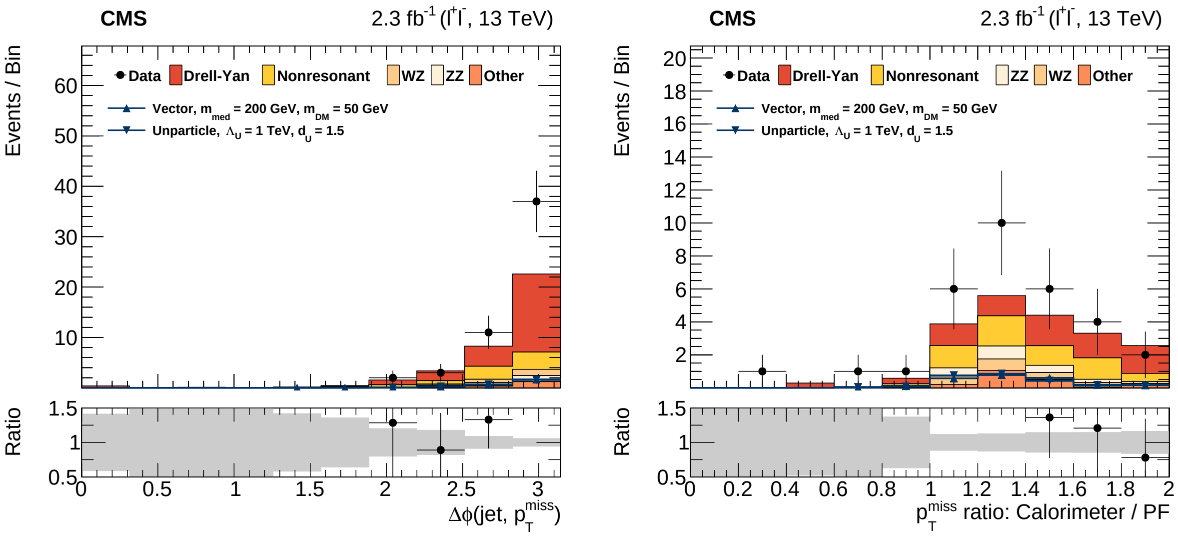

Figure 7.8.: Distributions of $\Delta\phi(jet, p_{\mathrm{T}}^{miss})$ (left) and $p_{\mathrm{T}}^{miss}$ (PF)/$p_{\mathrm{T}}^{miss}$ (Calo) (right) after requiring preselection, $p_{\mathrm{T}}^{miss} > 80$ GeV, $|p_{\mathrm{T}}^{miss} - p_{\mathrm{T}}^{\ell\ell}|/p_{\mathrm{T}}^{\ell\ell} > 0.4$ and $|u_{\parallel}/p_{\mathrm{T}}^{\ell\ell}| > 1$. This region is referred to as “region 3” in the text.

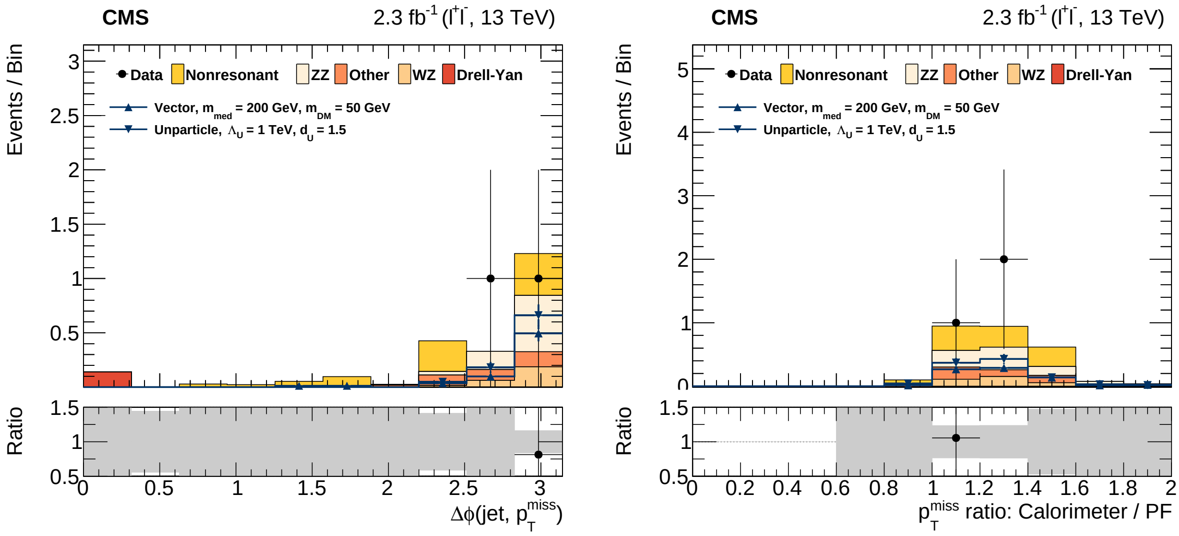

Figure 7.9.: Distributions of $\Delta\phi(jet, p_{\mathrm{T}}^{miss})$ (left) and $p_{\mathrm{T}}^{miss}$ (PF)/$p_{\mathrm{T}}^{miss}$ (Calo) (right) after requiring preselection, $p_{\mathrm{T}}^{miss} > 80$ GeV, $|p_{\mathrm{T}}^{miss} - p_{\mathrm{T}}^{\ell\ell}|/p_{\mathrm{T}}^{\ell\ell} > 0.4$ and $|u_{\parallel}/p_{\mathrm{T}}^{\ell\ell}| > 1$ and $\Delta\phi(ll, p_{\mathrm{T}}^{miss}) > 2.7$. This region is referred to as "region 4" in the text.

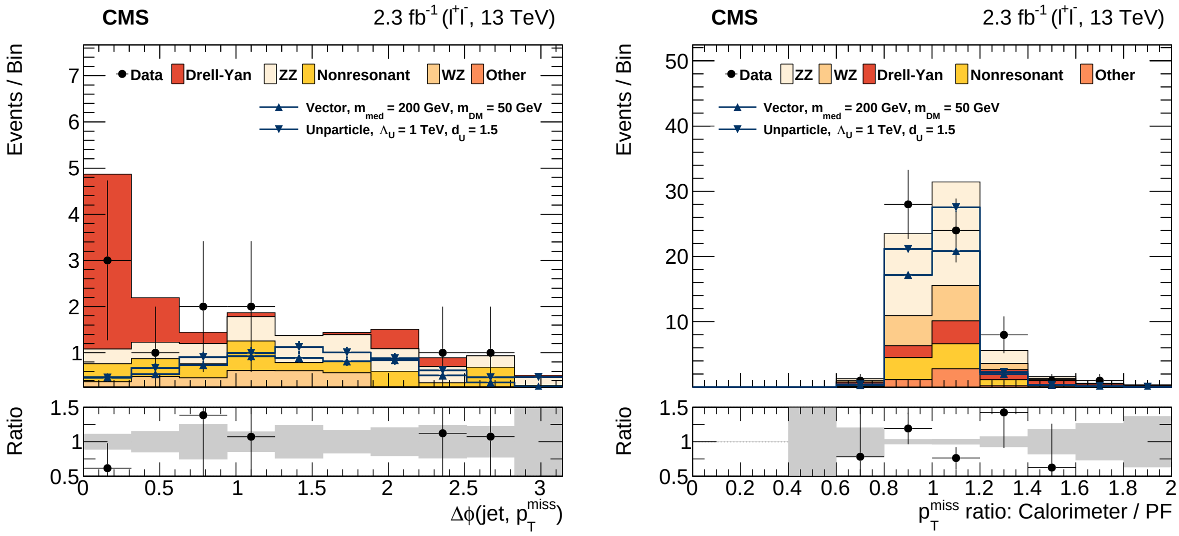

Figure 7.10.: Distributions of $\Delta\phi(jet, p_{\mathrm{T}}^{miss})$ (left) and $p_{\mathrm{T}}^{miss}$ (PF)/$p_{\mathrm{T}}^{miss}$ (Calo) (right) after final selection. This region is referred to as "region 5" in the text.

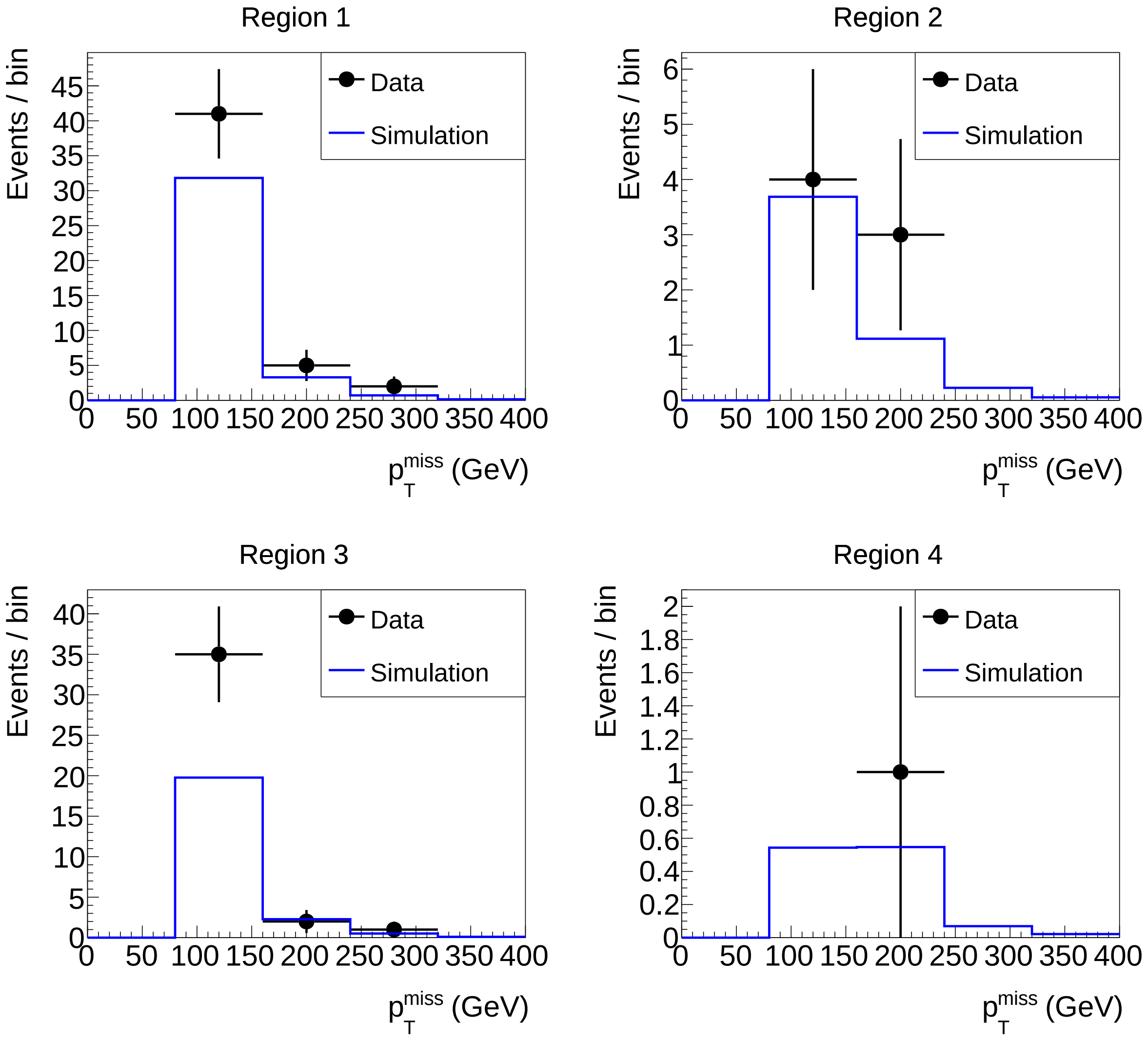

Figure 7.11.: $p_{\mathrm{T}}^{miss}$ distributions for regions 1 (top left), 2 (bottom left), 3 (top right) and 4 (bottom right). The shapes are shown for the events in the right-most bins of the $\Delta\phi(jet, p_{\mathrm{T}}^{miss})$ distributions shown above, i.e. at $\Delta\phi(jet, p_{\mathrm{T}}^{miss}) > 0.9 \times \pi$.

$$k_{\mathrm{ee}} = \frac{1}{2}\sqrt{\frac{N_{\mathrm{ee}}}{N_{\mu\mu}}}$$

$$k_{\mu\mu} = \frac{1}{2}\sqrt{\frac{N_{\mu\mu}}{N_{\mathrm{ee}}}}$$

The expected yield in each signal region is then calculated as the product of the respective transfer factor and the event yield in the control region $N_{\mathrm{e}\mu}$. The simulated estimate of contributions to the control region yield originating from other processes than the nonresonant ones are subtracted. This contribution is approximately 0.25 events compared to approximately 20 total expected events and thus negligible. A closure test is performed by using the simulated event yields as stand-ins for the observed values, deriving the transfer factors and the final yields. The simulated yields and the yields calculated with the closure test method are found to agree within 5% for the electron channel and 9% for the muon channel. These residual differences are assigned as relative systematic uncertainties to the final event yield prediction. However, the dominant uncertainty contribution lies in the limited statistical power of the control region: 20 eμ events passing the final selection are observed in data, resulting in an effective statistical uncertainty of approximately 20%, which is applied to the prediction.

### 7.3.4. Higher-order corrections for the VV processes

The calculation precision available in the theoretical literature is typically far ahead of what is implemented in commonly used matrix element and event generators. To profit from this available knowledge, higher-order corrections from fixed-order calculations are applied to the prediction for the leading ZZ background.

In the case of higher-order QCD corrections, simulated samples are available at one-loop level and an NLO→ NNLO k factor is applied as a function of the invariant mass of the two Z bosons on the generator level. The value of this k factor was obtained by the authors of Ref. [134] and communicated privately to members of the CMS collaboration. The correction ranges between 10 and 20%, and is shown in Fig. 7.12.

An additional correction is applied to account for the effect of higher-level electroweak corrections [135–137]. This correction, dubbed $k^{NLO}_{EWK}$ is available as a function of the $p_{\mathrm{T}}$ of the trailing Z boson (i. e. $min(p_{\mathrm{T}}(\mathrm{Z}_1), p_{\mathrm{T}}(\mathrm{Z}_2))$, and is shown in Fig. 7.12. The correction is dominated by the virtual component, which leads to an overall negative effect between −5% at low $p_{\mathrm{T}}(\mathrm{Z})$ and −25% at higher values. The correction is approximately 3% for the WZ background [137], which is only applied as an uncertainty, rather than as a correction to the central value.

No reliable estimate is available for higher-order mixed QCD-electroweak contributions. Therefore, they are naively estimated as the product of the difference induced by the separate QCD and EW LO→NLO k factors, and applied as an uncertainty on the central value of the background prediction, without correcting the central value itself:

$$\sigma_{EWK-QCD} = |(k^{NLO}_{QCD} - 1) \times (k^{NLO}_{EWK} - 1)| \;, \tag{7.1}$$

The QCD NLO correction $k^{NLO}_{QCD} = 1.6$ is taken from Ref. [146]. In cases where there is strong hadronic activity, as quantified by $\rho = \frac{|\sum_{\text{leptons}} \vec{p}_T|}{\sum_{\text{leptons}} |p_{\mathrm{T}}|} > 0.3$, the uncertainty is increased to the size of the full electroweak correction in order to take into account that the electroweak correction estimate is not fully accurate here. Fewer than 1% of ZZ events is affected by this increased uncertainty.

### 7.3.5. Experimental efficiencies

The efficiencies for the trigger-based event selection, as well as the subsequent offline reconstruction and identification of leptons are well modelled in simulation. To correct for residual differences, scale factors $w_{eff}$ based on the ratio of the efficiencies in data and simulation are used as weights for simulated events.

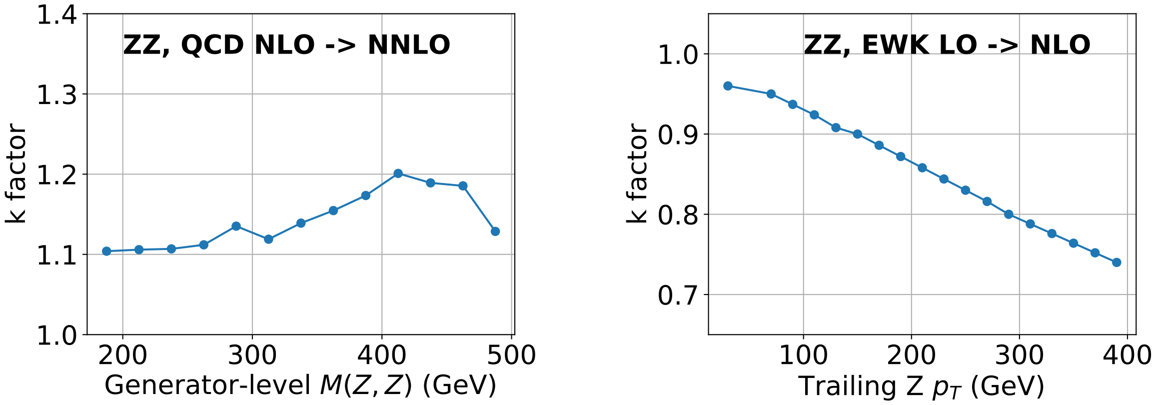

Figure 7.12.: Higher order correction factors for the ZZ process. The prediction is corrected from one-loop to two-loop level in QCD as a function of the generator-level invariant mass of the ZZ pair (left). The one-loop electroweak correction is applied as a function of the trailing generator-level $p_{\mathrm{T}}(\mathrm{Z})$ (right).

$$w_{eff} = \frac{\epsilon_{Data}}{\epsilon MC} \tag{7.2}$$

The trigger efficiencies are obtained using the reference trigger method [147]. An event sample is collected using a trigger path of known efficiency that is more inclusive than the trigger path under study, i.e. all events that would pass the trigger path of interest must also pass the reference trigger. Then, the efficiency $\epsilon_{trg}$ of the trigger of interest can be calculated as the product of the efficiency of the reference trigger $\epsilon_{trg}$ and the ratio of the numbers of events passing both triggers and the number of events passing only the reference trigger. The signal and reference trigger paths are listed in Tab. 6.5. The efficiency for the muon triggers is approximately 99% for central muons ($|\eta| < 1.5$ for both muons) with a minimal value around 95% if both muons are forward ($|\eta| > 2$). The electron trigger efficiency ranges between 94 and 100% depending on electron $p_{\mathrm{T}}$. Trigger scale factors are shown in Fig. 7.13.

$$\epsilon_{trg} = \epsilon_{ref} \times \frac{\text{Events passing both triggers}}{\text{Events passing the reference trigger.}} \tag{7.3}$$

The identification and reconstruction efficiencies are provided by the central CMS reconstruction groups. They are derived using the “tag-and-probe” method, in which events with leptonic Z boson decays are selected. By choosing events with a very-well identified *tag* lepton, and a *probe* lepton with a more inclusive selection, the probability for the probe muon to also pass the tag selection can be studied. By requiring that the tag and probe leptons form a dilepton candidate with an invariant mass close to the nominal Z boson mass it is possible to ensure that the selected event sample is dominated by real leptons. Therefore, the measured probability corresponds to the identification efficiency relative to the loose probe selection. The efficiency of reconstructing an electron candidate from an existing super cluster is approximately 95%. The subsequent combined efficiency for the identification and isolation criteria is approximately 65% at low electron $p_{\mathrm{T}} \approx 20$ GeV, and increases to 85% for $p_{\mathrm{T}} > 50$ GeV. For muons, the track reconstruction efficiency is better

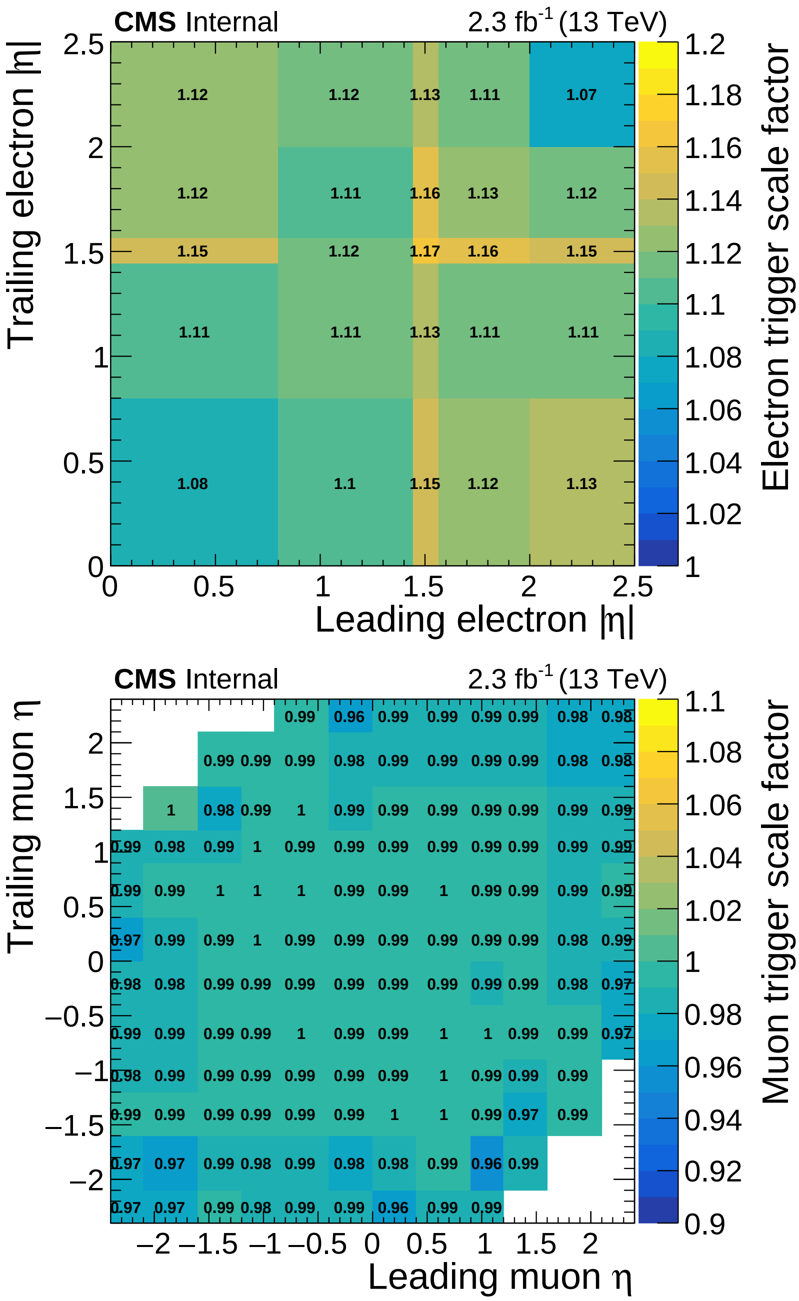

Figure 7.13.: Trigger efficiency scale factors for the electron (left) and muon triggers (right) as a function of the leading and trailing lepton $|\eta|$ (left) and $\eta$ (right).

than 99%, and the signal-like identification criteria applied here have an efficiency of $> 98\%$. The efficiency of the muon isolation criteria ranges from 88% at low $p_{\mathrm{T}} \approx 20$ GeV to more than 99% for $p_{\mathrm{T}} > 50$ GeV. The scaling factors for each of these efficiencies are shown in Figs. 7.14 and 7.15.

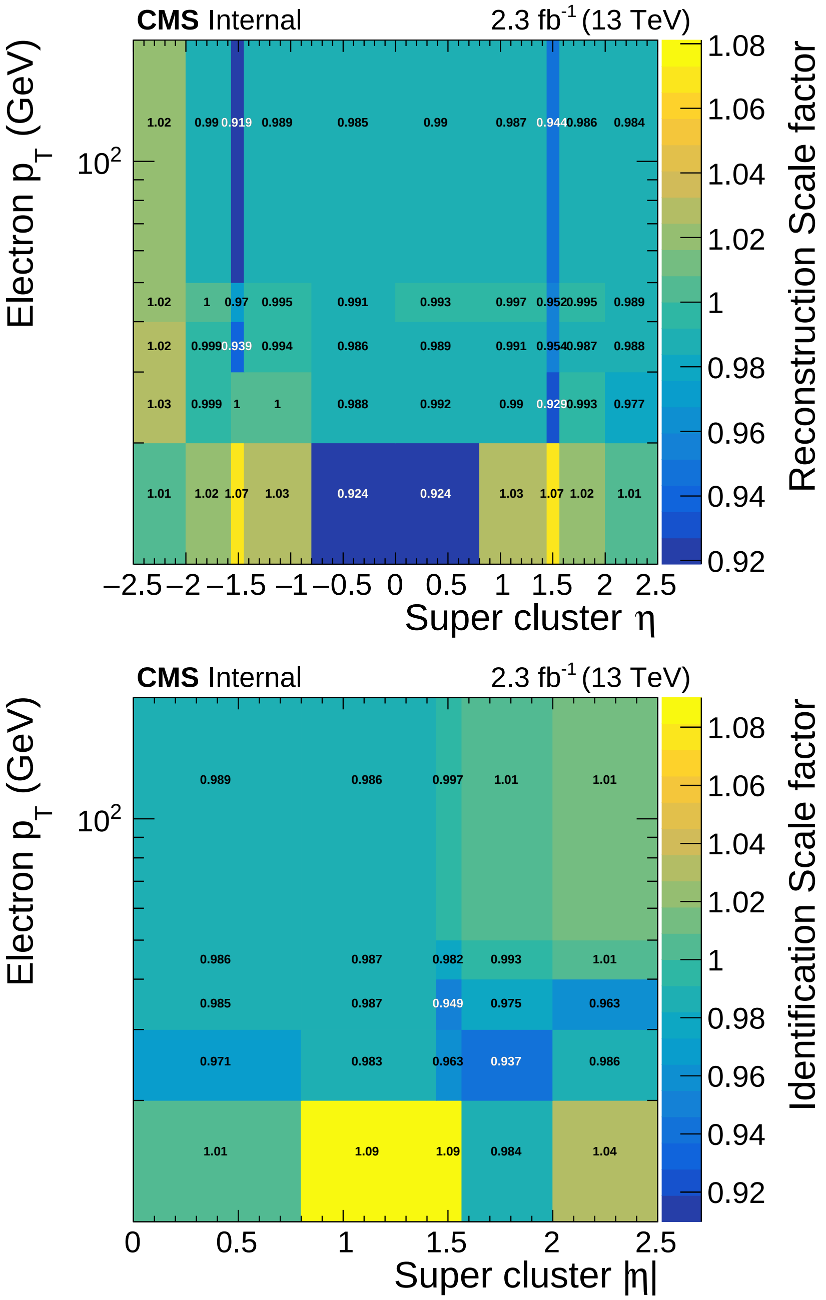

Figure 7.14.: Efficiency scale factors for the track reconstruction (left) and identification (right) of electron candidates as a function of super cluster $\eta$ and electron $p_\mathrm{T}$. The identification scale factor includes isolation.

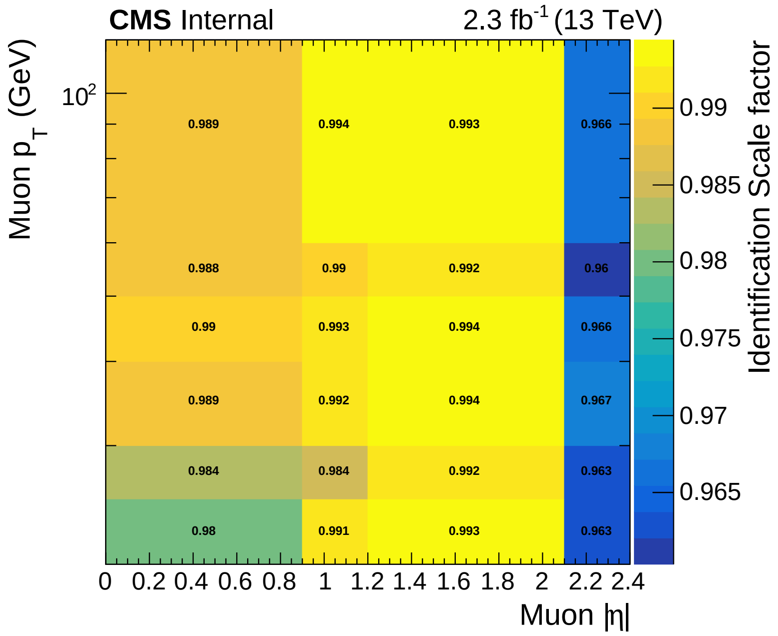

Figure 7.15.: Efficiency scale factors for the identification of muon candidates as a function of the muon $p_{\mathrm{T}}$ and $\eta$.

## 7.3.6. Pileup reweighting

The distribution of the number of PU events in simulated samples is corrected to more closely represent that observed in the data. Event weights based on the distribution of the number of *true* number of PU interactions in each events are used. The distribution is directly available for simulated events, and is calculated from the measured instantaneous luminosity and total inelastic cross section of 69 mb [148]. As a verification of the procedure, the distribution of the number of reconstructed primary vertices before and after reweighting is shown in Fig. 7.16. Good agreement is observed in the peak region of the distribution, with residual disagreements in the tails, which is likely caused by modeling differences in the vertex reconstruction efficiency. To estimate the uncertainty related to this reweighting method, alternative weights are calculated with the inelastic cross section shifted by 5% up and down.

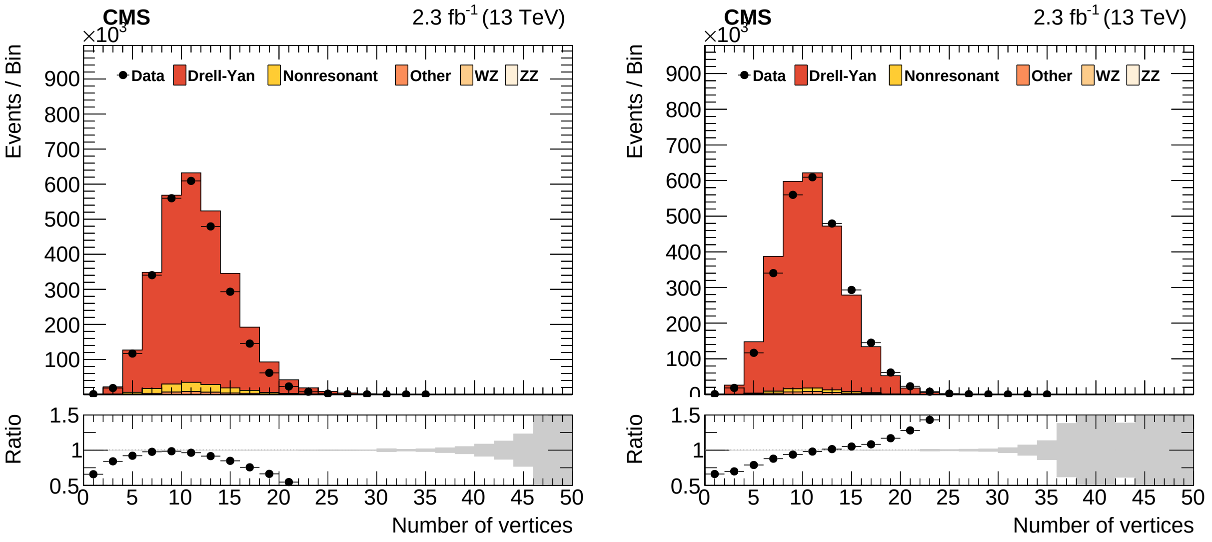

Figure 7.16.: Distribution of the number of primary vertices before (left) and after (right) PU reweighting.

## 7.4. Statistical method

The main results of this analysis are derived by considering the shape of the $p_{\mathrm{T}}^{miss}$ distribution to determine whether or not a signal is present. This determination is performed using a maximum-likelihood (ML) approach, which is explained in more detail in the following sections. The statistical method is directly taken from Ref. [149], which represents the conventions agreed upon between the CMS and ATLAS collaborations for the combination of searches for the SM Higgs boson at the LHC. An implementation of the method in the CMS `HiggsCombine` framework is used [150].

### 7.4.1. Likelihood and test statistic

The likelihood function $\mathcal{L}$ is defined with reference to a model of the expected yields given the background-only hypothesis plus a signal of strength $\mu = \sigma_{\text{signal}}/\sigma_{\text{theory}}$. Systematic uncertainties are incorporated into the model as *nuisance parameters*, which parameterize the dependence of the signal and background on a given source of systematic uncertainties.

$$\mathcal{L}(\text{data}\,|\,\mu,\theta) = \prod_{i\,\in\,\text{bins}} \frac{(\mu \times s_i(\theta) + b_i(\theta))^{n_i}}{n_i!} \exp\left(-\mu \times s_i(\theta) - b_i(\theta)\right) \tag{7.4}$$

$$\times \prod_{j\,\in\,\text{nuisances}} p_j\left(\tilde{\theta}_j|\theta_j\right) \tag{7.5}$$

In this equation, the term on the first line corresponds to the products of the probabilities to find a number of observed events $n_i$ in each of the bins $i$, if the total expected yield in that bin is the sum of background and scaled signal contributions $b_i + \mu \times s_i$. The background and signal yields depend on the values of the nuisance parameters $\theta$. Separate nuisance parameters will be used for each uncorrelated source of uncertainty, so one parameter will represent the uncertainty in the luminosity measurement, another parameter will represent the uncertainty in the electron reconstruction efficiency, and so on. The term on the second line incorporates our degree of belief as to what value of the nuisance parameters are possible, with $p_j$ representing our degree of belief that a value $\theta_j$ is compatible with our input value $\tilde{\theta}_j$. In the following, we will always define nuisance parameters so that $\tilde{\theta}_j = 0$. The function $p_j$ can be chosen arbitrarily, but the choice of a Gaussian distribution is favorable for its mathematical properties.

$$p_j\left(\tilde{\theta}_j|\theta_j\right) = \frac{1}{\sqrt{2\pi}} \exp\left(-\frac{(\tilde{\theta}_j - \theta_j)^2}{2}\right) \tag{7.6}$$

Different choices can additionally be made for the translation from the nuisance parameter value to the event yield. A linear translation, i.e. $\text{Yield}(\theta) = \text{Yield}(\tilde{\theta}) \times (1 + \sigma \times \theta)$, where $\sigma$ is the size of the uncertainty relative to the yield[1], results in yields that follow a Gaussian distribution with relative width $\sigma$ around the nominal yield. This behavior is well suited for uncertainties which are small relative to the nominal yield, but may cause issues when the uncertainty is so large as to give a non-negligible probability for negative yields. In this case, the Gaussian distribution would have to be truncated to enforce non-negative event yields. To avoid this issue, the effect of the nuisance parameters on the yields is instead calculated such that the yields follow a log-normal distribution.

$$Y(\theta) = Y(\tilde{\theta}) \times \kappa^{\theta} \tag{7.7}$$

The uncertainty measure $\kappa$ is related to the Gaussian $\sigma$ as $\kappa = 1 + \sigma$ for small uncertainties $\sigma \ll 1$. In this limiting case, the two distribution types are almost identical. However, the log-normal case leads to uncertainties that are symmetric in logarithmic space rather than linear space.[2].

A profile likelihood ratio is used as a test statistic $\tilde{q}_\mu$.

$$\tilde{q}_\mu = -2\,\ln\left(\frac{\mathcal{L}(\text{data}|\mu, \hat{\theta}_\mu)}{\mathcal{L}(\text{data}|\hat{\mu}, \hat{\theta}_{\hat{\mu}})}\right) \tag{7.8}$$

In this equation $\hat{\theta}_\mu$ is the set of nuisance parameter values that maximizes the likelihood for a given value of the signal strength $\mu$. The signal strength value that globally maximizes the likelihood is denoted as $\hat{\mu}$, with the corresponding set of optimal nuisance parameters being referred to as $\hat{\theta}_{\hat{\mu}}$. *Profiling* refers to the use of the optimized values $\hat{\mu}$ and $\hat{\theta}_{\hat{\mu}}$, in contrast to other conventions, in which the likelihood in the denominator would e.g. always be evaluated with $\mu = 0$.

### 7.4.2. Setting of exclusion limits

Exclusion limits are derived using the $CL_s$ method [149, 151]. The calculation of the $CL_s$ variable is based on the p-values $p_\mu$ and $p_b$, which represent the probabilities to encounter

---

[1] Example: If $Y = 50 \pm 5$, then $\sigma = 5/50 = 0.1$.

[2] So $|Y(\theta = +1) - Y(\theta = 0)| \neq |Y(\theta = 0) - Y(\theta = -1)|$, but $|\ln(Y(\theta = +1)) - \ln(Y(\theta = 0)|)| = |\ln(Y(\theta = 0)) - \ln(Y(\theta = -1))|$.

a value of the test statistic $\tilde{q}_\mu$ larger (i. e. representing a larger disagreement) than the observed value, if one assumes a non-zero signal strength $\mu \neq 0$ ($p_\mu$), or the background only hypothesis $\mu = 0$ ($p_b$).

$$CL_s(\mu) = \frac{P(\tilde{q}_\mu \geq \tilde{q}_\mu^{\mathrm{obs}}|\text{ signal + background})}{P(\tilde{q}_\mu \geq \tilde{q}_\mu^{\mathrm{obs}}|\text{ background only})}$$

A given signal parameter point is then said to be excluded at a confidence level of $\alpha$ if $CL_s(\mu) < 1 - \alpha$. The value of $\mu$ for which $CL_s(\mu) = 1 - \alpha$ is found by calculating $CL_s$ for a number of values of $\mu$ and then using a quadratic fit function to derive the threshold point.

The calculation of the $CL_s$ variable requires knowledge of the distribution of the test statistic assuming different values for the signal strength. In the *exact* version of the $CL_s$ method, these distributions are obtained by performing pseudo-experiments. The nuisance parameters are randomized according to the distribution functions described above. Subsequently, the central values for a given set of nuisance parameters are used to define a Poisson distribution, which is used to derive randomized bin contents for all relevant bins. These pseudo-data are then used in the same way as the real data to derive a value of the test statistic, which is histogrammed to find the distribution of the test statistic. Depending on how sensitive an analysis is to a given signal, it may be necessary to perform a large number of pseudo experiments to achieve a precise estimate of the $\mu$ value corresponding to the desired value of $CL_s$. In order to derive the results in this analysis, up to $50 \times 10^3$ pseudo-experiments are generated for each signal parameter point. The application of the full pseudo-experiment based method is necessary in this case as the discriminant $p_\mathrm{T}^{miss}$ distribution is sparsely populated in the signal region. In cases where there are sufficiently large expected event yields in the discriminant distribution, the asymptotic approximation of the method can be used [152], in which the distribution of the test statistic, and correspondingly the excluded $\mu$ value can be determined analytically.

## 7.5. Systematic Uncertainties

### 7.5.1. Experimental uncertainties

To account for differences in the lepton reconstruction performance in data and simulation, uncertainties are applied for lepton efficiencies and the lepton momentum scale determination. The relative uncertainty estimates are defined universally per lepton, i.e. they are independent of the lepton properties such as $p_\mathrm{T}$ and $\eta$. The effect of the lepton efficiencies is considered to affect only the normalization of the background prediction, i.e. its effect is correlated among the $p_\mathrm{T}^{miss}$ bins and has the same magnitude everywhere. The efficiency uncertainties for triggering, reconstructing and identifying each lepton are combined and are estimated to be 3% per lepton. The lepton momentum scale uncertainties are assumed to be 2% (5%) for electrons in the barrel (endcap) and 1% for muons. Their effect on the final discriminant is estimated by shifting the lepton momenta up and down in a correlated manner (all leptons are shifted at the same time in the same direction), propagating this effect to $p_\mathrm{T}^{miss}$ and re-evaluating the analysis acceptance. The resulting shifted $p_\mathrm{T}^{miss}$ distributions are used to define a shape-based uncertainty. The same approach is used for the uncertainty in the calibration of the jet energy scale and resolution [116]. An uncertainty of 2.7% is assigned to the luminosity determination and is applied to all background contributions which do not have their normalization derived from data [153]. Additional uncertainties related to the PU reweighting (cf. sec. 7.3.6) and b tagging efficiency are also evaluated, but found to be negligible. All experimental uncertainties are applied to both signals and backgrounds in a correlated manner. For example, the uncertainty assigned to the luminosity measurement will be represented by the same nuisance parameter for both signal and background processes, and can therefore only be varied up or down for both types of processes at once, but not up for one and down for the other, or vice versa.

### 7.5.2. Theoretical uncertainties

Simulation of hard scattering events is dependent on two - essentially arbitrary - choices: The choice of renormalization and factorization scales $\mu_R$ and $\mu_F$, as well as the choice of parton distribution function (cf. secs. 3.2 and 3.3). The central values for the two scales are chosen to be equal, with the exact choice depending on the software used to generate a given sample, as well as the used settings. For example, in the samples generated with Madgraph5_aMC@NLO, the scales are set to the transverse mass of the colorless system (e.g. the $\ell^+\ell^-$ system in the case of DY+jets production). In Powheg, the scales are instead set to the transverse momentum of the colorless system. The uncertainty associated to $\mu_R$ and $\mu_F$ is evaluated by generating alternative event-by-event weights independent assuming up- and downward variations of the two scales by factors of two and then using the maximal resulting variation of the considered distribution shape as the uncertainty. The standard “7-point” variation scheme is used, i. e. all possible combinations are considered except for the extreme ones where $\mu_F = 4 \times \mu_R$ or vice versa [154, 155].

The uncertainties related to the choice of PDF are also incorporated as alternative event-by-event weights. The groups who derive PDF fits provide not just one PDF, but PDF sets consisting of many members. The distribution of the values of the member PDFs are meant to reflect the uncertainties from the underlying experimental measurements, as well as from the extraction methods used to derive the PDF values. Two methods are commonly used: “MC replicas” and “Hessian eigensets”, which can be shown to give consistent results and methods exist to convert from one to the other [156]. In both cases, one calculates a PDF weight corresponding to each of the set members for each simulated event. The physical distribution of interest is derived once for each set of weights, and the distribution of the contents $c_i$ of a given bin is then used to derive an uncertainty on the central value. The two methods differ in the formula used to calculate the uncertainty. In the case of the MC replicas, the uncertainty is calculated as:

$$\sigma = \sqrt{\frac{1}{N-1}\sum_{i=1}^{N}(c_i - \bar{c})}\,, \tag{7.9}$$

where and $\bar{c}$ is the average of all $c_i$. In the case of Hessian PDF sets, the uncertainty is instead calculated as:

$$\sigma = \sqrt{\sum_{i=1}^{N}(c_i - c_0)}\,. \tag{7.10}$$

For both the scale choice and PDF uncertainties, only the effect on the acceptance of the signal selection is considered for signals, while the (typically much larger) effect on the total cross section is neglected. This convention is widely used in searches for new physics at ATLAS and CMS, and follows the notion that the theoretical cross section uncertainties are subject to change over time, and will likely improve in the future. A future physicist may therefore easily re-calculate the cross section and its associated theory uncertainties, and re-estimate the effect on the result by simple rescaling of the excluded cross section. This treatment only makes sense in the case where no signal is observed, and is therefore not applied in cases where a signal is observed, e.g. in case of a measurement of a known process. Consequently, both the acceptance and overall normalization components are considered for background processes, since a mis-estimation of the overall background rates would clearly bias the results in the here and now.

### 7.5.3. Summary of uncertainties

The total relative uncertainty in each bin of the $p_{\mathrm{T}}^{miss}$ distribution in the signal region is shown in Fig. 7.17. For the ZZ process, which is the dominant source of background events, the overall uncertainty is dominated by the theoretical components, with smaller contributions from the lepton scale uncertainties. For most of the spectrum, the size of simulated event samples gives a sub-dominant contribution. For the signals, only the acceptance component of PDF and QCD scale uncertainties is used in the limit setting and the theoretical uncertainties thus only have a small overall relevance. Leading uncertainty contributions arise from the lepton scale uncertainties, which are comparable to the sample size uncertainties.

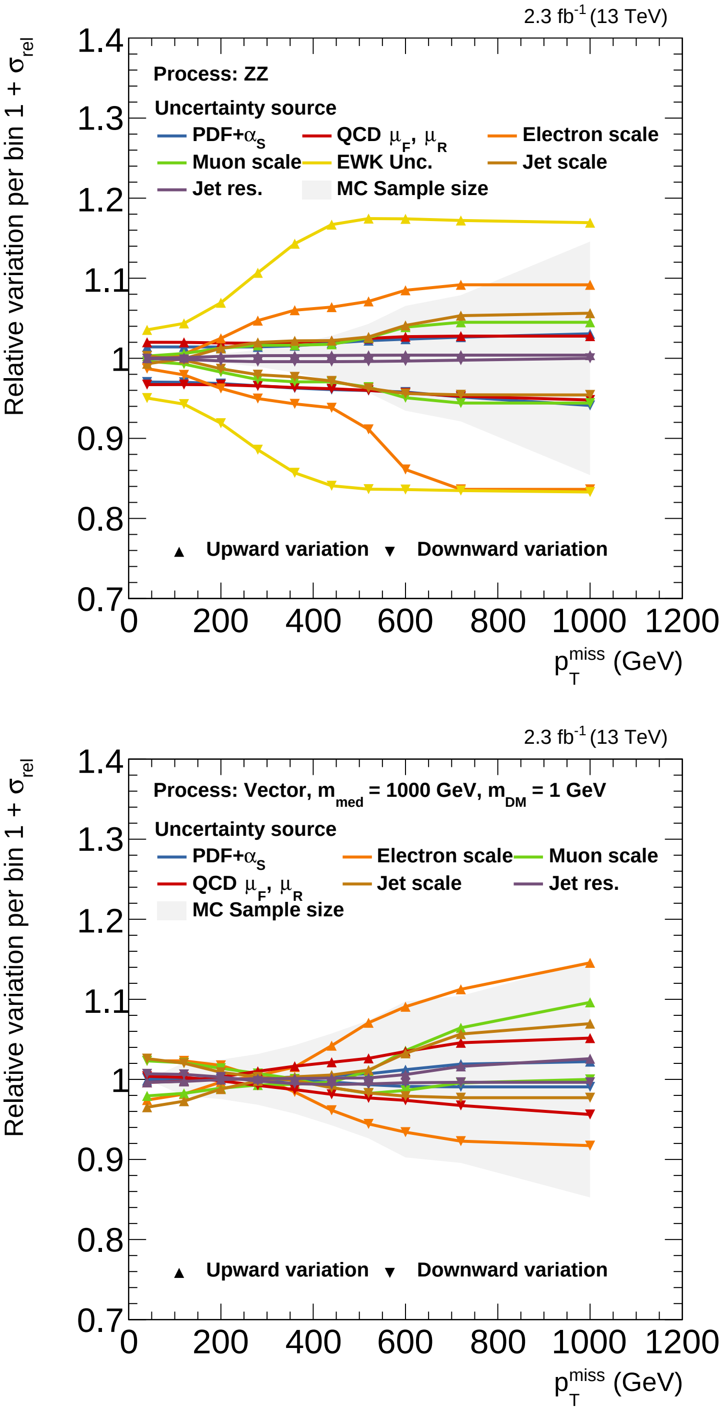

Figure 7.17.: Systematic uncertainty as a function of $p_T^{miss}$ for the leading background ZZ (upper panel) and a simplified model signal with a vector mediator and $m_{DM} = 1$ GeV, $m_{med} = 1$ TeV (lower panel). The entry labeled “EWK” in the top panel refers to the higher-order uncertainty on the ZZ background discussed in sec. 7.3.4. With the exception of the uncertainty related to the finite size of simulated samples, all uncertainties are treated as correlated among the bins. The size of the systematic uncertainty is shown relative to the sum of the expected event yield for the given process in the electron and muon channels.

## 7.6. Results

The distribution of $p_{\mathrm{T}}^{miss}$ in the signal region is shown in Fig. 7.18 after applying the background-only ML fit. No statistically significant excess of data events over the SM background expectation is observed. In the following, this null result is used to derive exclusion limits in the parameter space of simplified dark matter models and a model of unparticles. Additionally, model independent cross section limits are derived. Unless stated otherwise, 95% CL limits are used.

### 7.6.1. Dark matter

The 95% CL exclusion limits in the $m_{med}$-$m_{DM}$ plane are shown for axial and vector mediators in Fig. 7.19 for $g_q = 0.25$ and in Fig. 7.19 for $g_q = 1.0$. Independent of the coupling structure of the mediator, the largest excluded values of $m_{med}$ are observed for $m_{DM} \approx 1$ GeV. In this region, mediator masses of $280 - 300$ GeV (480 GeV) can be excluded for $g_\chi = 1.0$ and $g_q = 0.25$ (1.0). A difference between the axial-vector and vector mediators arises for larger values of $m_{DM}/m_{med}$. Here, the excluded value of $m_{med}$ is almost independent of $m_{DM}$ up to $m_{DM}/m_{med} \approx 2$, which is the kinematic boundary of the process. For the axial vector mediator, the excluded value of $m_{med}$ quickly reduces with increasing $m_{DM}$. This behavior is a direct result of different dependences of the partial width $\Gamma_\chi$ on $m_{DM}$ (cf. sec. 4.1). As $m_{DM}$ increases, the branching fraction for mediator decays to DM particles deteriorates quickly for the axial vector mediator, but stays approximately constant for the vector mediator. The highest excluded values of $m_{DM}$ are 110 GeV (140 GeV) for the vector mediator case and $g_q = 0.25$ (1.0). In the axial vector case, the highest excluded values is 65 GeV (80 GeV). For both mediators, sensitivity is sharply limited by the $m_{DM} = m_{med}/2$ line for $g_q = 0.25$. Due to the significantly increased relative mediator width, some off-shell sensitivity is possible for $g_q = 1.0$.

Formulating exclusion limits in the parameter space of simplified models is useful because it allows for benchmarking and straightforward comparisons between different analysis channels. However, the existence of DM particles has already been constrained not only by collider based experiments, which may use the simplified model language, but also direct and indirect detection experiments. These experiments formulate their results not in the context of a simplified model, but quote exclusion limits on the DM-nucleon scattering cross section for a given value of the DM mass. At the low momentum transfers ($\lesssim$ keV) relevant to direct detection experiments, the total DM-nucleus scattering amplitude is calculated as the coherent sum of the individual nucleon-DM amplitudes[3]. The behavior of the DM-nucleon scattering is assumed to be fully defined by the coupling type, which may be *spin dependent* or *spin independent*. For a spin independent coupling, the terms of the amplitude sum have the same sign, leading to an overall cross section enhancement proportional to the square of the number of nucleons of the target material. For spin dependent couplings, the sum terms take into account the nucleon spin direction, which leads to a partial cancellation, and therefore to a reduced signal rate. One way to obtain the theory used to interpret the direct searches is to consider the low-energy limit of the simplified models discussed here. The axial-vector (vector) mediated interactions correspond to the spin dependent (spin-independent)

---

[3] The discussion in this section focuses on direct detection experiments. Results from indirect detection experiments are less relevant for the quantitative comparison with collider searches.

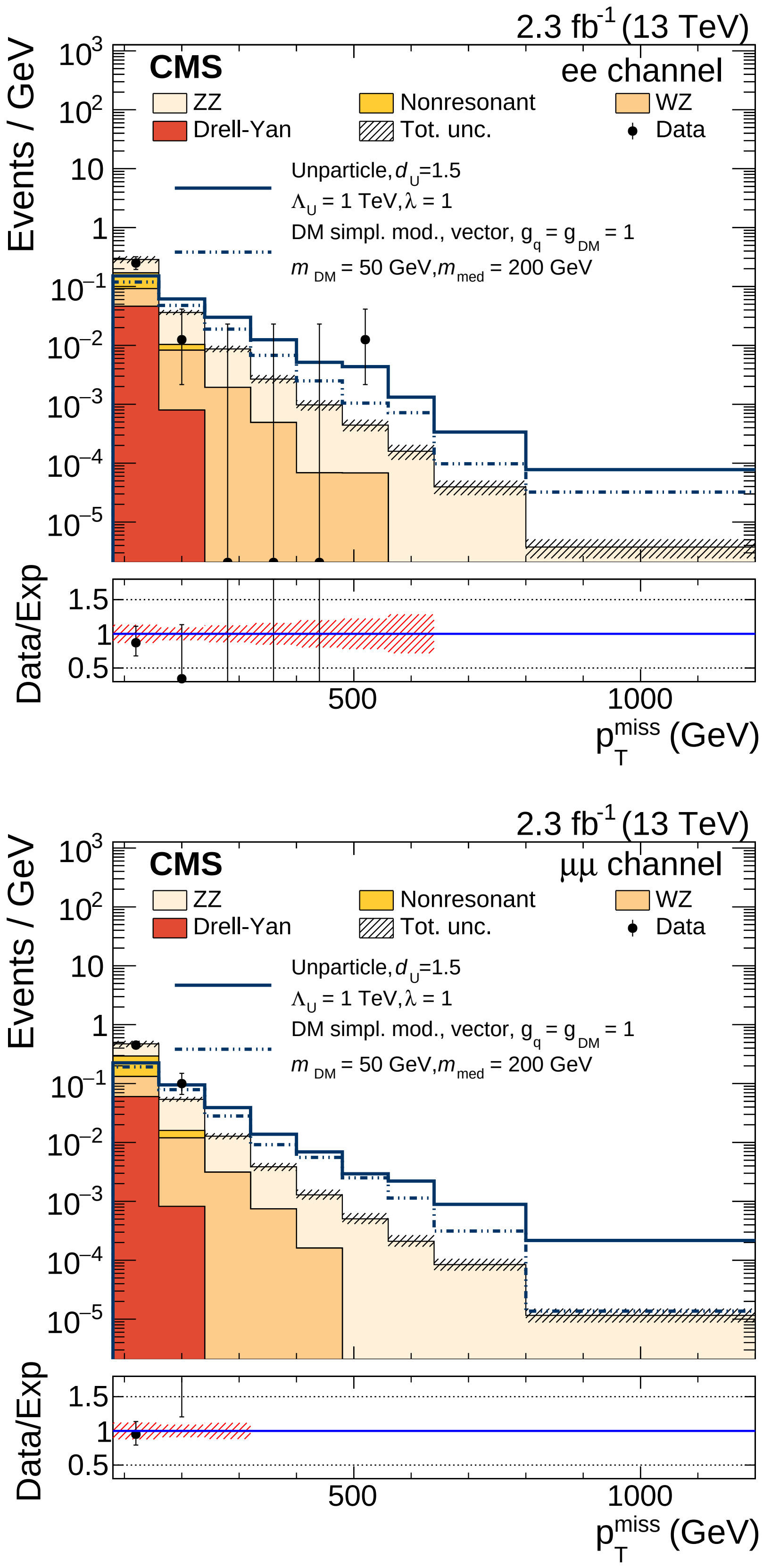

Figure 7.18.: Distribution of $p_T^{miss}$ after final selection for electron (top) and muon events (bottom). The result is shown after applying the maximum-likelihood fit (“postfit”).

low-energy interactions. A fully defined parameter point of the simplified model ($g_q$, $g_{DM}$, $m_{med}$, $m_{DM}$) can then be translated analytically into the plane of DM particle mass and DM-nucleon cross section, which then allows for a comparison between collider and direct searches [69]. The result of this procedure for the case of $g_q = 0.25$ and $g_{DM} = 1.0$ is shown in Fig. 7.21. The collider based exclusion curve follows the triangular shape already observed in the $m_{med}$-$m_{DM}$ plane. The minimal excluded DM-nucleon cross section is defined by the maximal excluded value of the mediator mass, with a minor dependence on the DM mass parameter. Compared to the direct searches, the collider search provides additional constraints especially in the case of spin dependent couplings and low values of the DM mass. While the former is a result of the aforementioned suppression, the latter effect is due to dependence of the energy deposited by a DM particle when scattering with a nucleon in a direct detection experiment. The deposited energy is reduced at low values of $m_{DM}$, leading to decreased signal acceptance because signal events may fall below the detection thresholds, or become obscured by increased background contributions. For spin-independent couplings, the collider sensitivity is very similar in terms of the simplified model parameter space, especially the maximally probed value of $m_{med}$. The direct detection experiments, however, profit from enhanced signal rates and can therefore provide much more stringent constraints. Only at the very lowest DM masses of a few GeV can collider searches contribute. It is worth noting explicitly that the translation from the $p_{\mathrm{T}}^{miss}$ based search to a direct detection cross section is model dependent, and should be understood as a qualitative way of comparing different experiments. The different dependences of the signatures at different experiments highlight the complementarity between the different approaches. The best case for discovery of a DM particle would certainly be made by the observation of consistent signals in both types of experiments. A comparison of the signal properties could then be used to further constrain the properties of a DM particle and its interactions.

### 7.6.2. Unparticles

For the unparticle model, exclusion limits are set on the scale of new physics $\Lambda_U$ as a function of the scaling dimension $d_U$. The result is shown in Fig. 7.22. For a large range of $d_U$, the exclusion limits are more stringent than previous bounds from searches performed at the LEP collider, as well as the CDF experiment at the Tevatron [100]. Over the full range of $d_U$, they coincide with those obtained in Ref. [97], which are based on the same event topology. For $1.5 \leq d_U \leq 1.9$, previous bounds from a CMS monojet search [165] are more stringent than the ones obtained here.

### 7.6.3. Model-independent cross section limits

Model independent exclusion limits are derived as a single-bin counting experiment with a lower $p_{\mathrm{T}}^{miss}$ threshold. For a given value of the threshold, the $p_{\mathrm{T}}^{miss}$ distribution above that threshold is integrated to derive the yields from each of the background contributions, as well as the events observed in data. Using the same CLs procedure as for the other signals, a signal strength limit is derived for a hypothetical signal with exactly one predicted event above the threshold. The value of the signal strength limit then corresponds to an exclusion limit on the number of signal events, which - when divided by the luminosity of 2.3 fb$^{-1}$ - finally yields a limit on signal cross section times branching fraction and efficiency. The

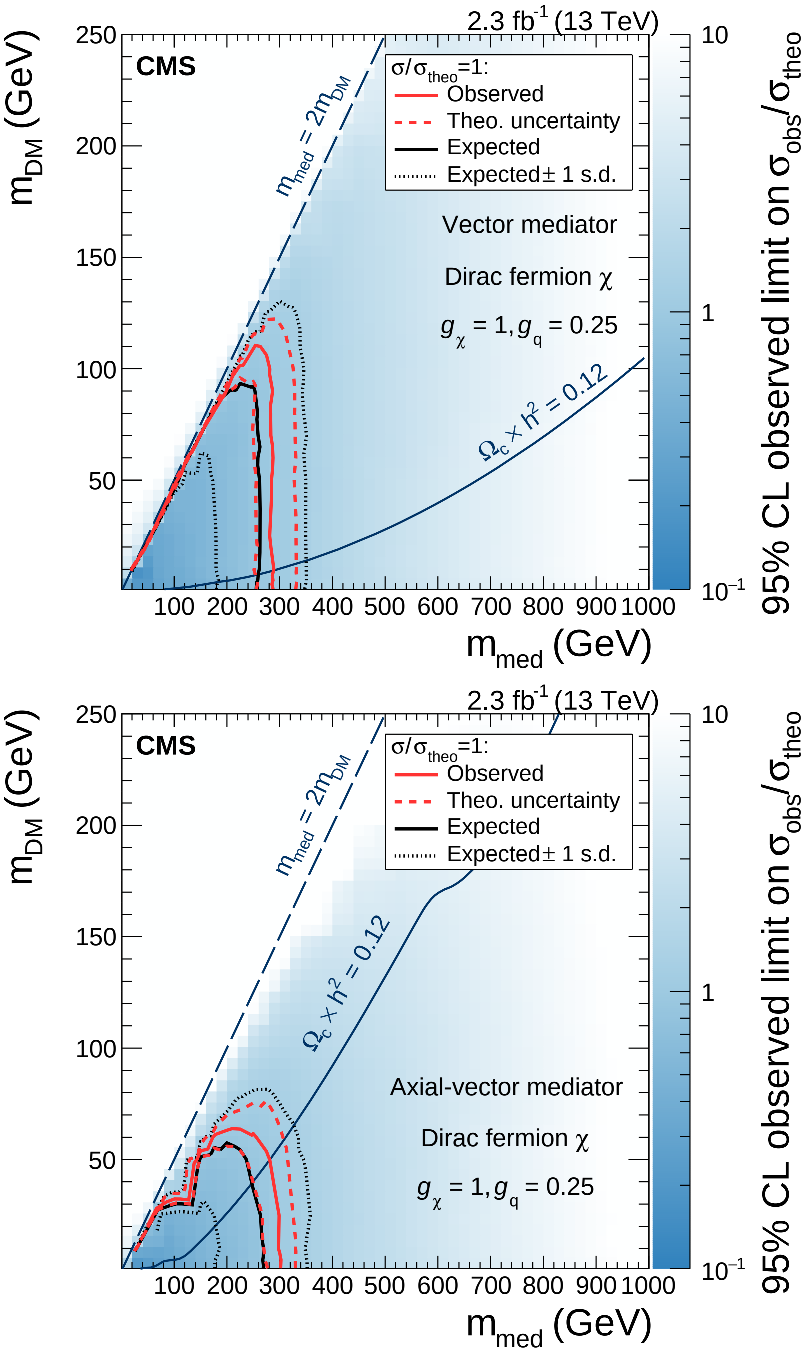

Figure 7.19.: Exclusion limits on the signal strength in the simplified model with a spin-1 mediator at 95% CL. The limits are shown in the $m_{med}$-$m_{DM}$ plane for $g_{DM} = 1$ and $g_q = 0.25$. The upper (lower) panel shows the results for a vector (axial-vector) mediator. The red solid line shows the observed exclusion, with the red dashed line reflecting the theoretical uncertainties from PDF and QCD scale variations on the signal cross-section. The black solid line indicates the median expected exclusion, with the black dashed lines corresponding to the 1 standard deviation (s.d.) variation around the median. Parameter points under and left of the shown curves are excluded.

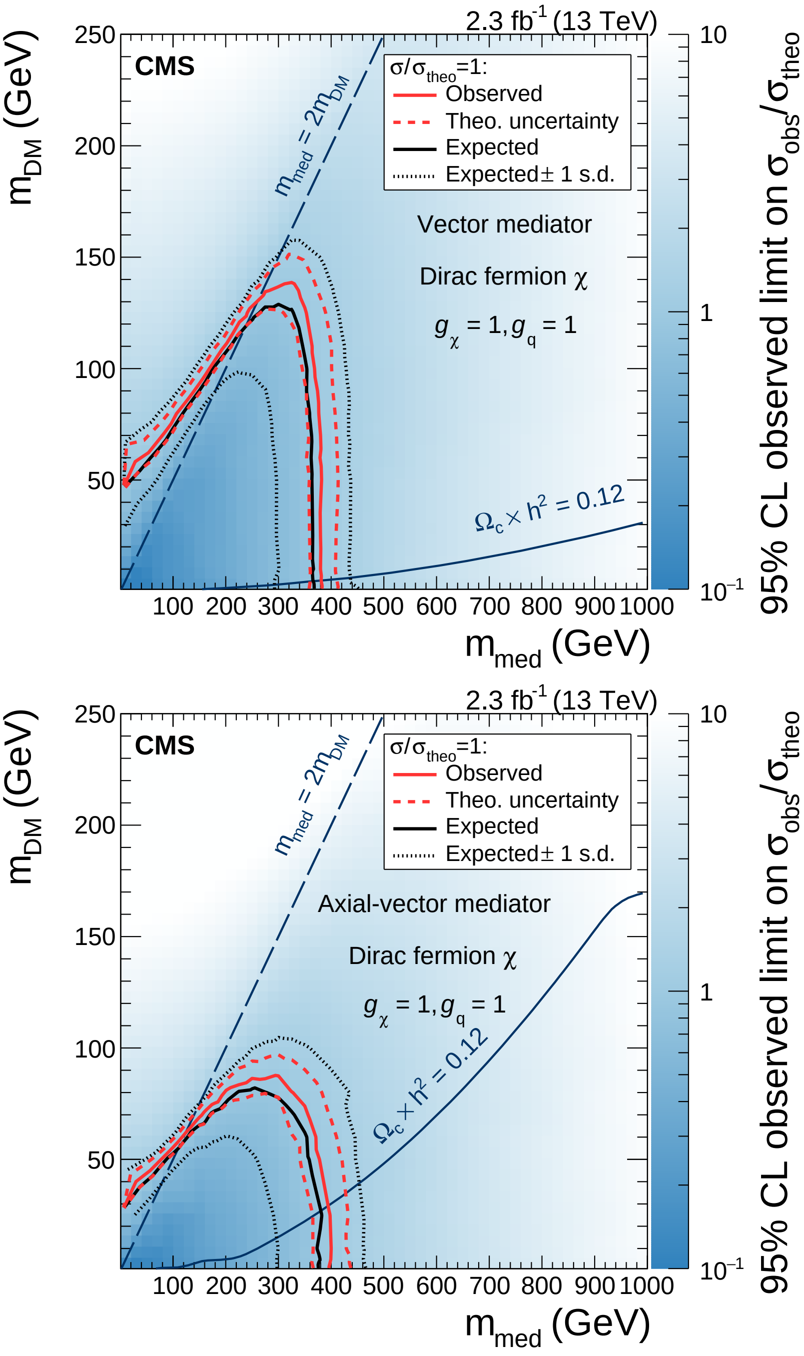

Figure 7.20.: Same as Fig. 7.19, but now for coupling values of $g_{DM} = g_q = 1.0$.

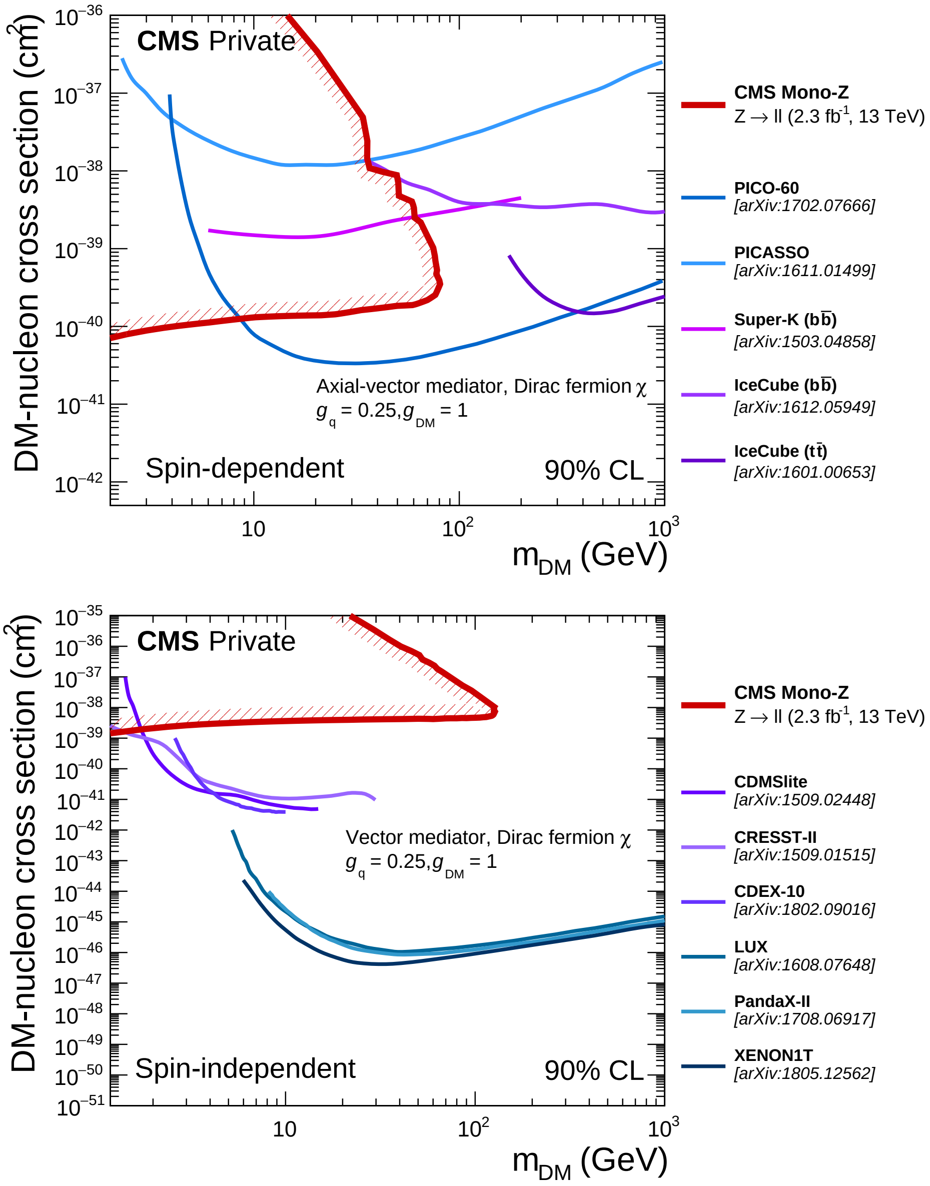

Figure 7.21.: Exclusion limits at 90% CL in the simplified model with a spin-1 mediator translated into the plane of DM mass and DM-nucleon cross section. The limits are shown for spin-dependent interactions (corresponding to an axial vector mediator) in the top panel, and for spin-independent interactions (vector mediator) in the bottom panel. For comparison, the results of direct and indirect detection experiments are shown: PICO-60 [157], PICASSO [158], Super-Kamiokande [159] and IceCube [160, 161] are shown for the spin-dependent case, while CDMSlite [162], CRESST-II [163], CDEX-10 [164], LUX [18], PandaX-II [19] and XENON1T [16] are relevant for spin-independent interactions.

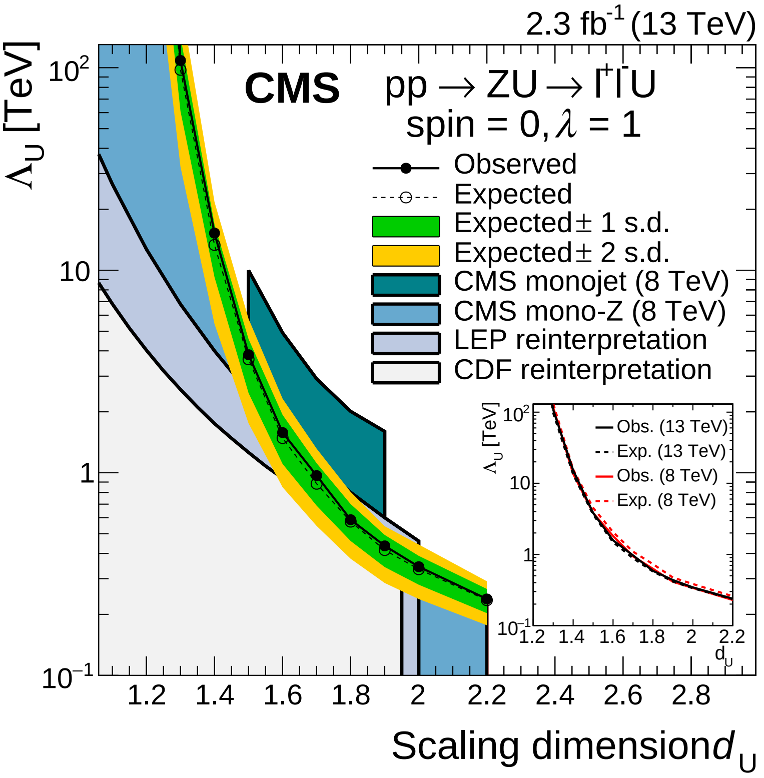

Figure 7.22.: Exclusion limits on the scale of new physics $\Lambda_U$ in the unparticle model as a function of the scaling dimension $d_U$. For comparison, results from previous CMS searches [97, 165] as well as constraints from LEP and the Tevatron are shown [100]. Parameter points below the shown curves are excluded. The LEP results assume a coupling of unparticles to Z bosons and photons. The CDF (CMS) monojet result is based on a gluon-unparticle coupling operator (gluon- and quark-unparticle coupling operators). The inset shows a more detailed comparison of this result with the previous result derived in events with the same topology in the 2012 data set, which coincidentally overlaps. Note that all results that are not obtained from the CMS mono-Z channel use different unparticle operators, which do not necessarily have the same values of $\Lambda_U$ and $\lambda$. Therefore, only a qualitative comparison is possible.

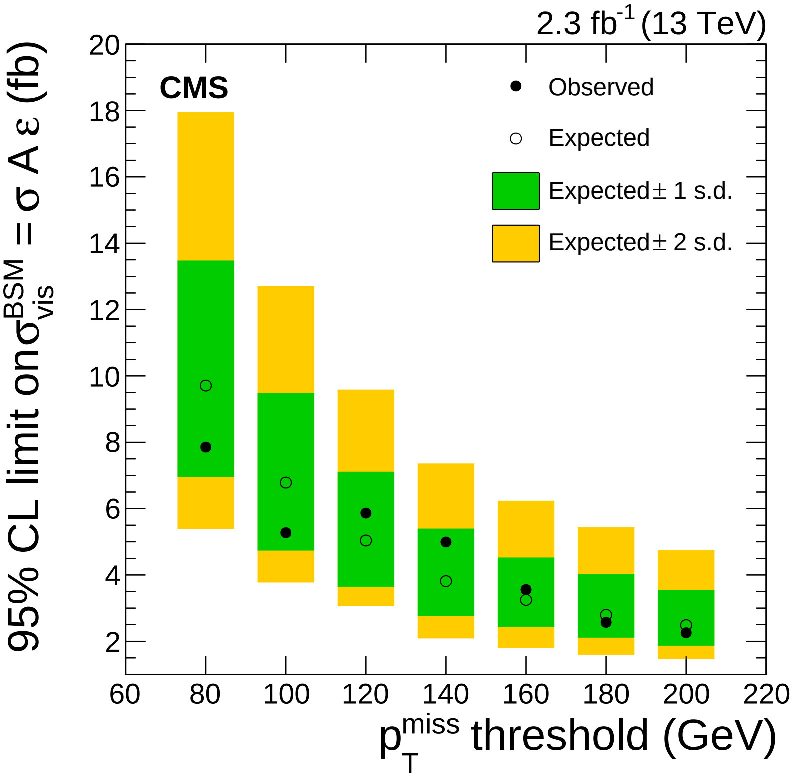

Figure 7.23.: Model independent 95% CL exclusion limits on the product of cross section, branching fraction and efficiency for a generic $Z + p_T^{miss}$ signature. Signals with larger cross sections than the shown points are excluded.

result is shown in Fig. 7.23. For all considered $p_T^{miss}$ thresholds between 80 and 200 GeV the observed and expected excluded cross sections agree within one standard deviation. For lower thresholds ($<$ 120 GeV), there is a small overall deficit observed in data, leading to more stringent observed than expected limits. For higher thresholds ($\geq$ 120 GeV), a slight excess is observed and this behavior is reversed. By using generator-level simulation and possibly a fast detector simulation program such as Delphes, one can derive the cross section, acceptance and efficiency for any signal model. The resulting yield can then be compared to the values provided here to determine whether a signal is excluded.

# 8. Analysis of the 2016 data set

In 2016, the CMS collaboration recorded a physics-grade data set of 35.9 $\mathrm{fb}^{-1}$ of proton-proton collisions at $\sqrt{s} = 13$ TeV. Compared to the 2015 data set, the increased sample size allows for a better statistical precision and better control of backgrounds, partially by using control regions in data. The overall analyzed topology and strategy remain the same: Events with well-reconstructed leptonic Z boson candidates are selected and the tail of the $p_{\mathrm{T}}^{miss}$ distribution is scrutinized for signs of the production of new invisible particles.

The technical implementation of the analysis in Ref. [166] is used in this chapter to derive interpretations in a number of scenarios of new physics. In the following section, a brief overview of the analysis and experimental result for the $p_{\mathrm{T}}^{miss}$ distribution in Z+$p_{\mathrm{T}}^{miss}$ events in the 2016 data set is given. Subsequent sections focus on the derivation of interpretations of the search in results in terms of DM production, as well as the unparticle and ADD scenarios. An additional study is performed to explore the analysis sensitivity for cases in which an unstable dark sector particle is produced.

A subset of the results shown here has been published by the CMS collaboration in Ref. [167].

## 8.1. Analysis summary

The analysis follows the main ideas outlined in sec. 7. The largest change relative to the strategy described there is the addition of a control-region scheme to constrain the WZ and ZZ backgrounds. The control region method closely follows the method of Ref. [168], which documents a search for new invisible particles in events with jets and $p_{\mathrm{T}}^{miss}$ at CMS. The control regions are constructed by selecting events with one or two additional leptons beyond the two that are required for the construction of the Z candidate. The three-lepton (four-lepton) region is enhanced in WZ (ZZ) events, in which the charged leptons from both bosons are reconstructed. Since the $p_{\mathrm{T}}^{miss}$ variable in the signal region closely corresponds to the generator-level boson $p_{\mathrm{T}}$ of the W (in WZ events) or Z boson (in ZZ events), respectively, the *emulated* $p_{\mathrm{T}}^{miss}$ is constructed as an equivalent variable in the control regions. Emulated $p_{\mathrm{T}}^{miss}$ is calculated by excluding from the $p_{\mathrm{T}}^{miss}$ calculation the one or two additional leptons that do not belong to the Z candidate that has its mass closest to the nominal Z boson mass. The control regions are included in the combined ML fit described in sec. 7.4 and allow for a greater ability to constrain the theoretical uncertainties of the ZZ and WZ backgrounds. A freely floating parameter is used to constrain the normalization of the WZ and ZZ contributions in a correlated way across all bins and regions. The (emulated) $p_{\mathrm{T}}^{miss}$ distributions in the signal and control regions are shown in Fig. 8.1. By correlating the normalization of the two processes, only the ratio of their predicted yields is still obtained from normalization and left to vary with the systematic uncertainties. The method is validated by considering the ZZ/WZ ratio in the predicted and observed spectra, which is shown in Fig. 8.2.

While the distributions of the emulated $p_{\mathrm{T}}^{miss}$ show a slight deficit towards higher values, there is no statistically significant deviation. Good agreement is observed in the behavior of the ratio. The signal region selection has been re-optimized for the increased size of the available data set. A summary of the selection is given in Tab. 8.1. Notable changes are the increase of the $p_{\mathrm{T}}^{miss}$ requirement from 80 to 100 GeV, which follows an increase in the average PU multiplicity in the 2016 data set, and a corresponding increase in the fake $p_{\mathrm{T}}^{miss}$ contribution in DY events. Additionally, a requirement on the angular separation $\Delta R(\ell\ell)$ of the two leptons forming the Z boson candidate has been introduced to slightly improve the signal-to-background ratio, and an additional requirement on the angular separation in the transverse plane of jets and $p_{\mathrm{T}}^{miss}$ has been imposed to avoid contamination from fake $p_{\mathrm{T}}^{miss}$ through jet mismeasurement (cf. sec. 7.3.2).

Table 8.1.: Requirements for the signal region selection in the analysis of the 2016 data set. The requirements fall in three categories: Lepton selection, vetoes based on the multiplicities of hadronic objects, dilepton candidate selection, and high-$p_{\mathrm{T}}^{miss}$ back-to-back topology requirements. The overall selection strategy is similar to that pursued in 2015, but the values of each variable have been re-optimized [166, 167].

| Quantity | Requirement |
|---|---|
| Number of charged leptons | = 2, with opposite charge, same flavour |
| Muon $p_{\mathrm{T}}$ | $> 20$ GeV |
| Leading (trailing) electron $p_{\mathrm{T}}$ | $> 25(20)$ GeV |
| | |
| Dilepton mass | $\lvert M(\ell\ell) - m_{\mathrm{Z}}\rvert < 15$ GeV |
| Dilepton $p_{\mathrm{T}}$ | $> 60$ GeV |
| Dilepton $\Delta R$ | $< 1.8$ |
| | |
| Jet multiplicity | $\leq 1$ jet with $p_{\mathrm{T}} > 30$ GeV |
| b jet multiplicity | No b jet with $p_{\mathrm{T}} > 20$ GeV |
| Hadronic $\tau$ multiplicity | No $\tau$ with $p_{\mathrm{T}} > 18$ GeV |
| | |
| $p_{\mathrm{T}}^{miss}$ | $> 100$ GeV |
| $\Delta\phi(\vec{p}_{\mathrm{T}}^{\,\ell\ell}, \vec{p}_{\mathrm{T}}^{\,miss})$ | $> 2.6$ |
| $\lvert p_{\mathrm{T}}^{miss} - p_{\mathrm{T}}^{\ell\ell}\rvert / p_{\mathrm{T}}^{\ell\ell}$ | $< 0.4$ |
| $\Delta\phi(\vec{p}_{\mathrm{T}}^{\,j}, \vec{p}_{\mathrm{T}}^{\,miss})$ | $> 0.5$ rad |

## 8.2. Results

No statistically significant excess of events is observed in the signal region. In the following sections, the absence of a signal is interpreted in terms of exclusion limits in simplified models of DM production with spin-1 or spin-0 mediators, unparticles, extra dimensions (ADD) and the a+2HDM model.

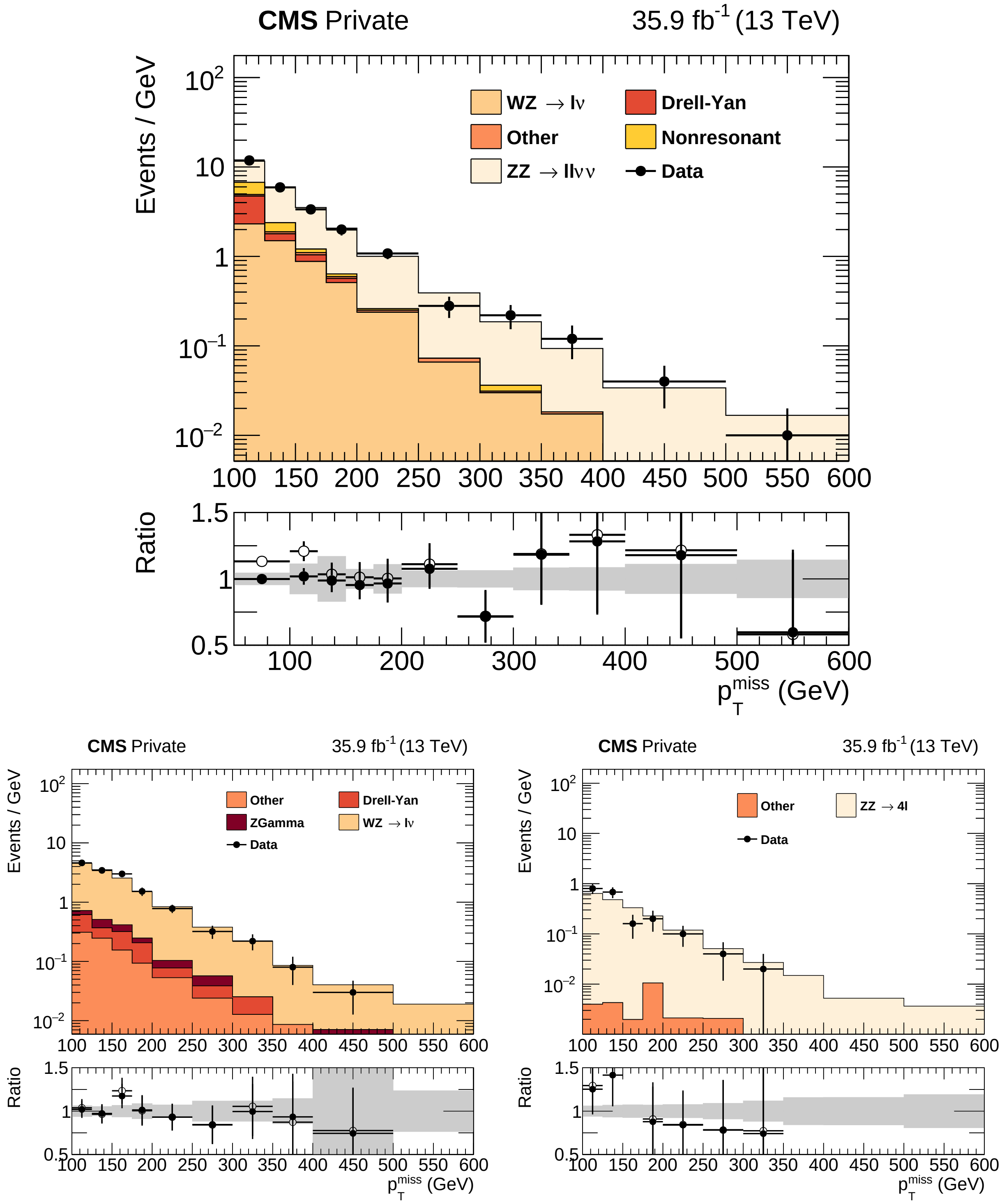

Figure 8.1.: Distributions of $p_{\mathrm{T}}^{miss}$ in the signal region (top) and emulated $p_{\mathrm{T}}^{miss}$ in the three-lepton (bottom left) and four-lepton control regions (bottom right). In the lower panel, the ratio of data over the background prediction is shown for the pre-fit background estimate (hollow markers) and for the post-fit estimate (solid markers).

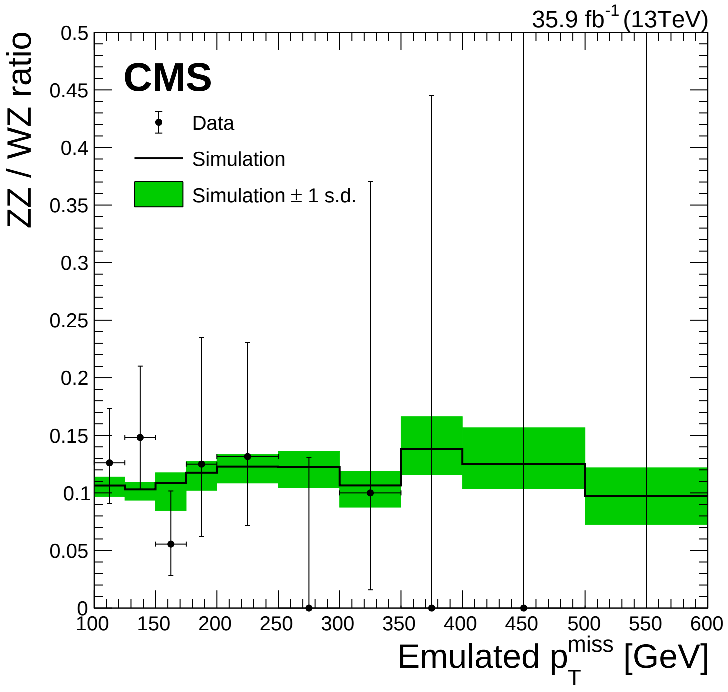

Figure 8.2.: Observed and simulated ratios of the distributions of the emulated $p_T^{miss}$ in the ZZ and WZ contributions in the three- and four-lepton control regions. Taken from Ref. [166].

## 8.2.1. Dark matter with a spin-1 mediator

In the spin-1 mediator scenario, exclusion limits are placed in the $m_{med}$-$m_{DM}$ plane for fixed couplings $g_q = 0.25$, $g_{DM} = 1.0$. The limits for both axial vector and vector mediators are shown in Fig. 8.3. Signal samples generated with Madgraph5_aMC@NLO at NLO in QCD are used, which provides a slight enhancement of the sensitivity. Mediator masses up to $m_{med} = 700$ GeV (720 GeV) can be excluded for the vector (axial vector) case. The maximal probed DM candidate masses are $m_{DM} = 290$ GeV (190 GeV) for vector (axial vector) mediators. In addition to the fixed-coupling case, exclusion limits are also placed on the couplings $g_q$ and $g_{DM}$ as a function of $m_{med}$. A fixed value of $m_{DM} = 1$ GeV is used, and the method discussed in sec. 4.1.1.1 is employed. The resulting exclusion limits are shown in Fig. 8.4. For a fixed value of $g_q = 0.25$, the DM coupling $g_{DM}$ can be tested down to values of 0.18 (0.24) for the axial (vector) case at low values of $m_{med} = 50$ GeV. At higher values of $m_{med} = 500$ GeV, coupling values larger than 0.55 (0.5) are excluded. The quark coupling $g_q$ can generally be probed down to lower values than $g_\chi$, as a reduction in $g_q$ partially self-corrects due to reverse effects on the mediator production cross section (which increases with $g_q$) and invisible branching fraction (which decreases with $g_q$). Here, values down to 0.04 (0.06) are tested at low $m_{med}$, while values larger than 0.14 (0.15) are excluded for higher masses. The formulation of exclusion limits on couplings rather than masses opens a complementary view of the power of this search to constrain new physics. While a given mass combination may be excluded for a pre-defined set of couplings, it can be argued that a lower coupling would effectively hide a signal. This relationship is studied quantitatively here for the first time for a mono-Z search.

### 8.2.2. Dark matter with a spin-0 mediator

For the spin-0 mediators, exclusion limits are placed on the signal strength $\mu$ as a function of $m_{med}$ for fixed $g_q = g_{DM} = 1$ and $m_{DM} = 1$ GeV. The results are shown in Fig. 8.5. The exclusion power for both scalar and pseudoscalar coupling structures are very similar, with slightly enhanced sensitivity in the pseudoscalar case. The most stringent limits can be obtained for low values of $m_{med} \approx 10$ GeV, where $\mu$ between 1.9 and 2 can be probed. Towards higher values of $m_{med}$, sensitivity is reduced continually, with a pronounced threshold behavior beginning at $m_{med} = 350$ GeV, at which point decays of the mediator into top quarks become possible, and the invisible branching fraction is reduced. The main results are obtained using signal simulation with 0- and 1-jet matrix elements matched to the parton shower using the MLM scheme. A comparison of the expected exclusion limits to the case where only the 0-jet matrix element is used is shown in Fig. 8.6.

### 8.2.3. a+2HDM

For the case of the a+2HDM model, exclusion limits are derived in the plane of the light pseudoscalar mass $m_{\mathrm{a}}$ and the common heavy boson mass $m_{\mathrm{H}} = m_{\mathrm{A}} = m_{\mathrm{H}^{\pm}}$. All other parameters are set to their default values as described in sec. 4.2. The maximal observed (expected) value of $m_{\mathrm{a}}$ that can be excluded is 340 GeV (320 GeV), while $m_{\mathrm{H}}$ values up to 1.05 TeV (1.03 TeV) can be excluded in low-$m_{\mathrm{a}}$ limit. The sensitive region is bounded for low $m_{\mathrm{H}}$ because of the kinematic threshold of the $H \rightarrow \mathrm{a} + Z$ decay. The exclusion derived here tests a previously unconstrained region of parameter space. During the preparation of this thesis, first constraints on the a+2HDM benchmark scenario considered here have also been released by the ATLAS collaboration [169]. The ATLAS results are derived by reinterpreting previously published results of DM searches in the $Z(\ell\ell)+p_{\mathrm{T}}^{miss}$ [170] (mono-Z) and $H(bb)+p_{\mathrm{T}}^{miss}$ topologies [171] (mono-H), as well as constraints for the invisible branching fraction of the Higgs boson with mass 125 GeV [172]. The ATLAS mono-Z search uses a similar strategy and equivalent data set to this result and consequently shows a comparable exclusion reach in the $m_{\mathrm{a}} - m_{\mathrm{H}}$ plane. There are small regions of parameter space excluded independently by only one of the experiments, which is a result of statistical fluctuations in the independent data samples. The mono-H result is derived from hadronic decays of the SM Higgs boson, which have a large branching fraction ($\mathrm{BR}(\mathrm{h} \rightarrow \mathrm{bb}) \approx 60\%$), but suffer from large backgrounds at low values of $p_{\mathrm{T}}^{miss}$, and correspondingly rely on higher $p_{\mathrm{T}}^{miss}$ thresholds. Accordingly, the sensitivity for a search in this topology is shifted towards higher $m_{\mathrm{H}} = m_{\mathrm{A}}$ than for the mono-Z topology. Finally, constraints from invisible decays of the SM Higgs are relevant for low values of $m_{\mathrm{a}} < 125$ GeV, where decays $\mathrm{h} \rightarrow \mathrm{aa}$ begin to contribute.

### 8.2.4. Unparticles

Exclusion limits in the parameter space of the unparticle model are shown in Fig. 8.9. The constraints are formulated on the Wilson coefficient $\lambda \times (1 \text{ TeV}/\Lambda_U)^{d_U - 1}$ as a function of the scaling dimension $d_U$. Using this parameter is advantageous compared to the use of

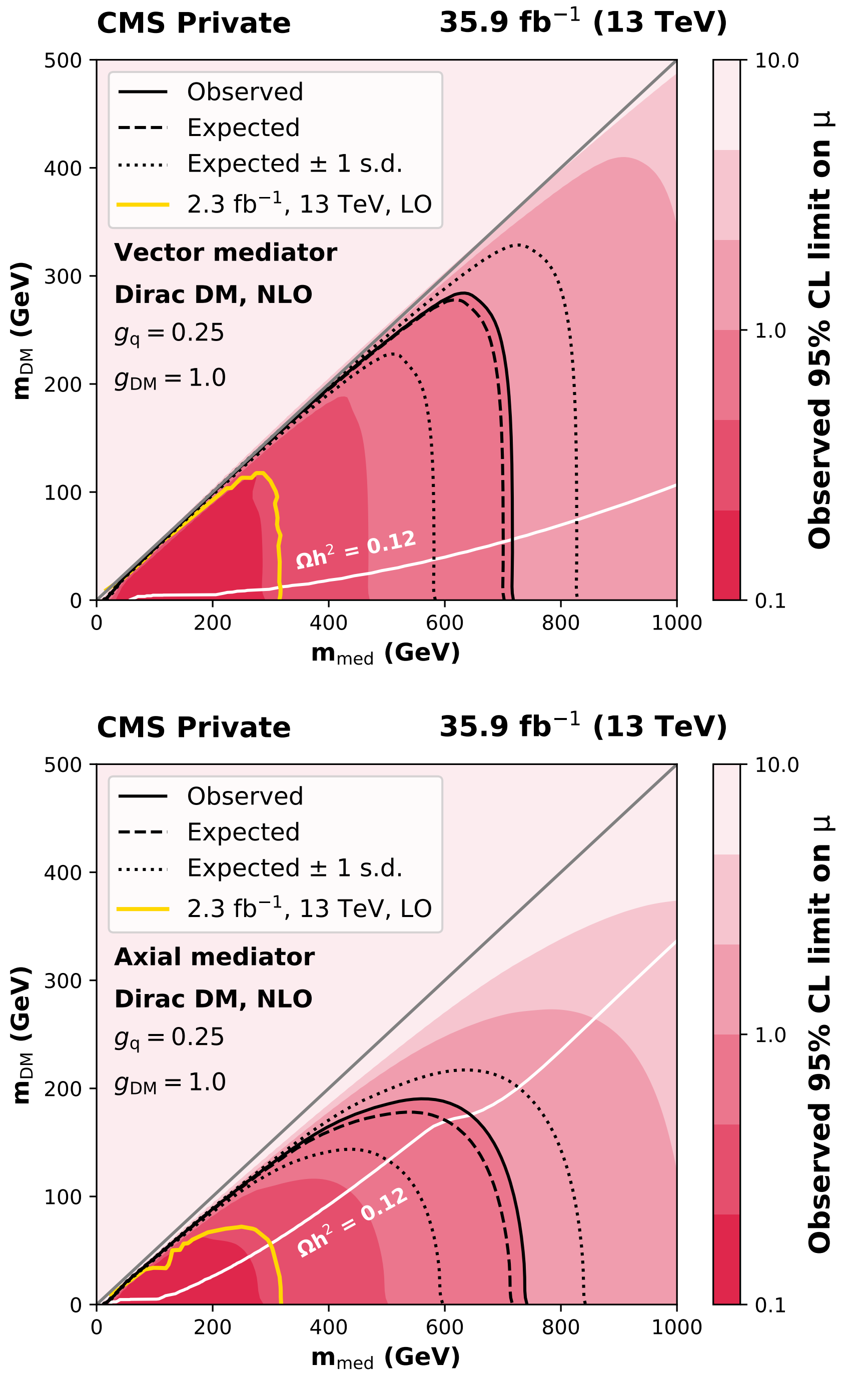

Figure 8.3.: Exclusion limits in the plane of mediator and DM candidate mass in the simplified model with a vector (upper panel) and axial-vector mediator (lower panel). Parameter combinations that give a DM relic density consistent with the observed value are indicated by the white line, with all parameter combinations below it resulting in an overabundance of DM in the universe. The yellow curve represents the results derived from the analysis of the 2015 data set (cf. sec. 7).

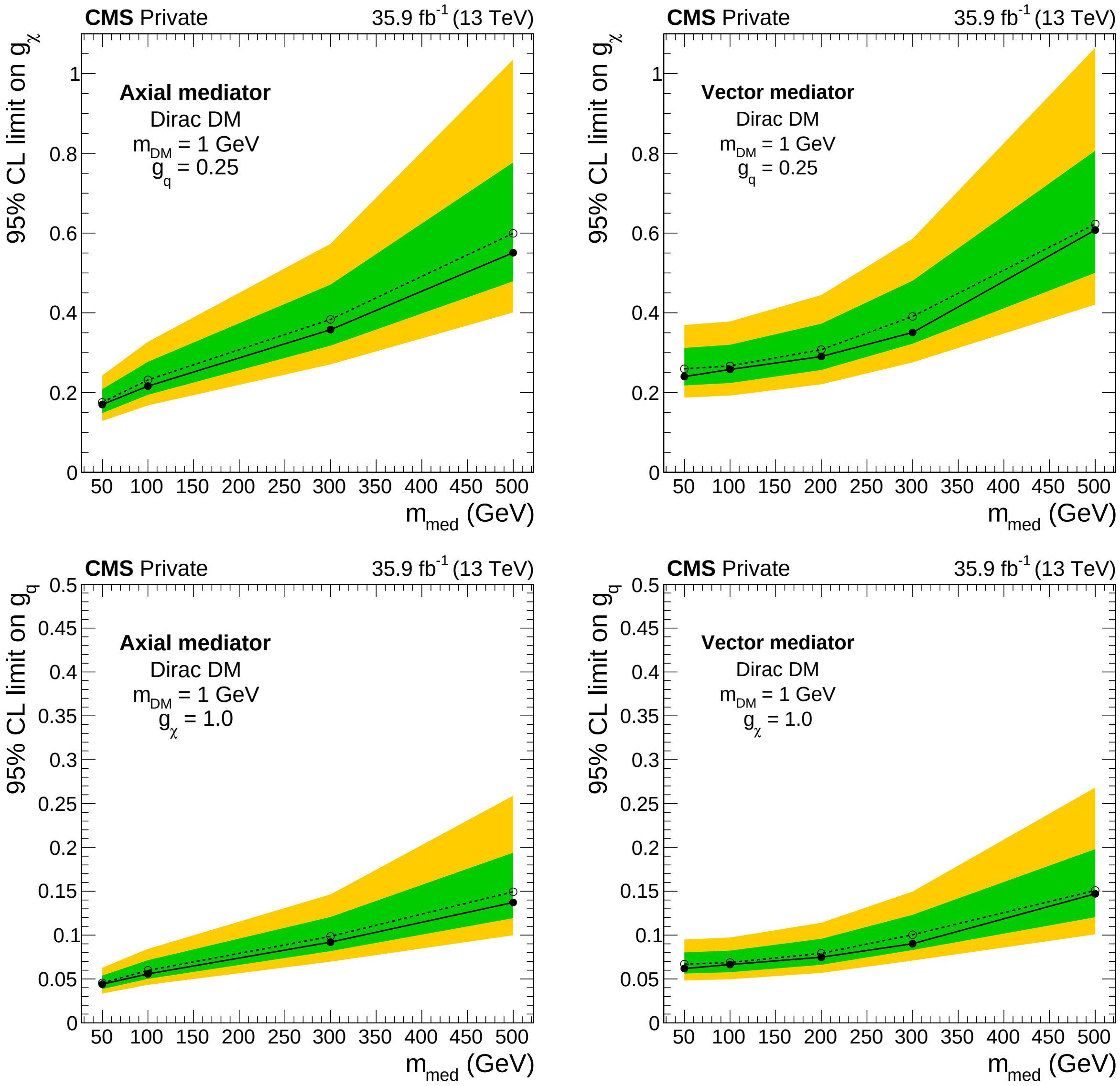

Figure 8.4.: Exclusion limits on the mediator couplings as a function of mediator mass for axial vector (left panels) and vector mediators (right panels). Separate bounds are derived for $g_q$ (bottom panels) and $g_\chi$ (top panels), with the respective other coupling being held constant at its default value indicated in the plots.

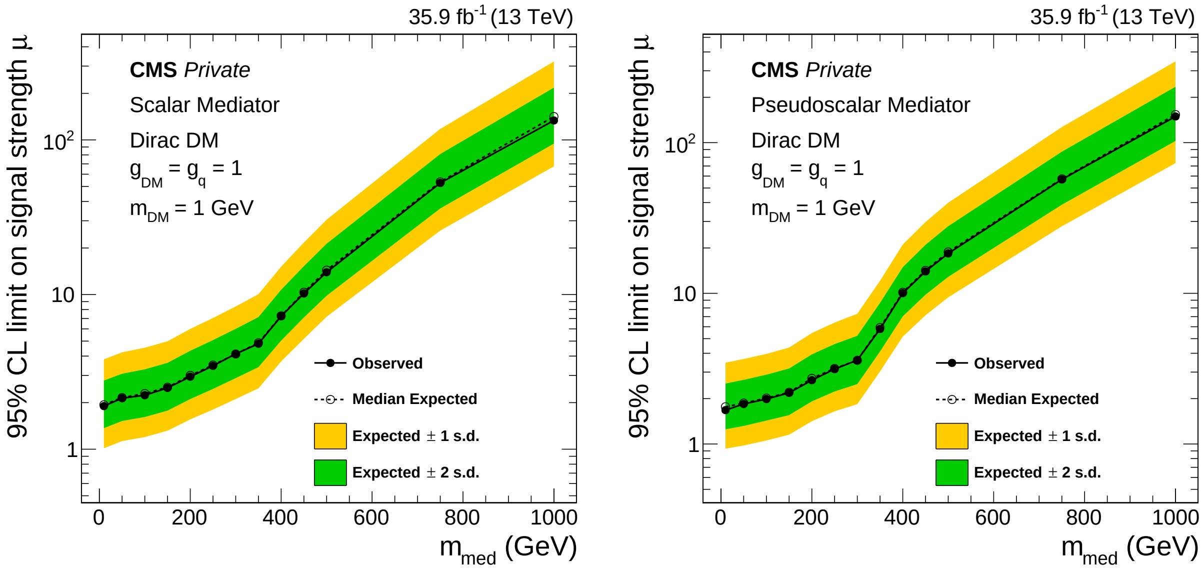

Figure 8.5.: Exclusion limits on the signal strength $\mu$ as a function of $m_{med}$ in the scalar (left) and pseudoscalar (right) coupling scenarios. The default coupling choices $g_q = g_{DM} = 1$ are used, and the mass of the DM candidate is fixed to $m_{DM} = 1$ GeV.

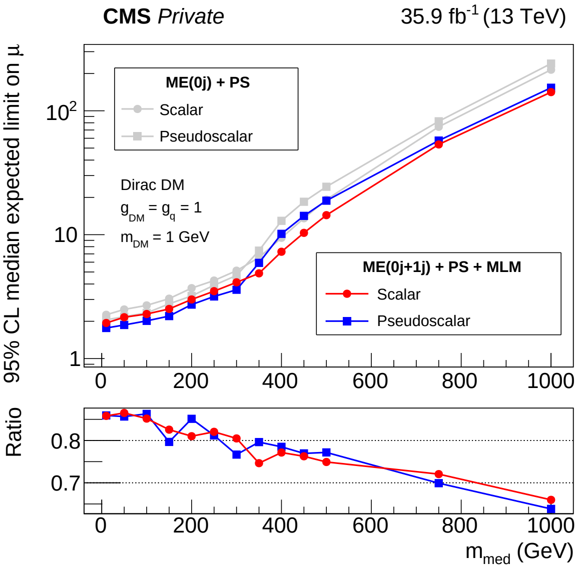

Figure 8.6.: Comparison of the expected signal strength limits in the scalar and pseudoscalar cases for the two sets of signal generation parameters. The gray solid lines show the expected limits for signal samples generated with no additional partons at the matrix-element level, while the colored lines represent signal samples where both the 0- and 1-jet matrix elements are combined using the MLM method.

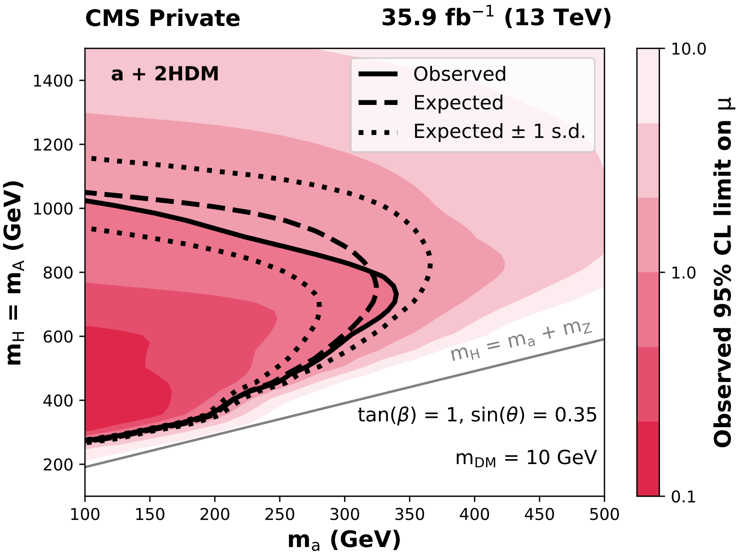

Figure 8.7.: Exclusion limits at 95% CL in the a+2HDM model. The limits are shown in the $m_\mathrm{a}$-$m_\mathrm{H}$ plane, with the default parameter choices described in the text. The expected and observed limits are shown as dashed and solid lines, respectively. The thin grey solid line indicates the kinematic threshold for the $H \to \mathrm{a} + \mathrm{Z}$ decay. Note that the $m_\mathrm{a}$ axis is truncated below 100 GeV, as that region of the parameter space would lead to significant distortions in the properties of the SM Higgs boson and is therefore not considered here.

$\Lambda_U$, as it explicitly avoids the ambiguity of the scale and coupling parameters, and already incorporates the behavior of the exponent $d_U - 1$, which otherwise leads to a divergence in the $\Lambda_U$ exclusion for $d_U \to 1$. The exclusion from the present analysis improves on the previous results from sec. 7 and Ref. [97] for all considered values of $d_U$ between 1.01 and 2.2. The relative improvement over previous constraints improves with increasing values of $d_U$ from a factor $\approx 1.5$ at $d_U = 1.05$ up to a factor of $\approx 2$ at $d_U = 2.2$, owing to the increase in center-of-mass energy as well as data set size. The comparison to other sources of constraints made in sec. 7 is explicitly not performed here, as there is no reason to assume that the $\Lambda_U$ and $\lambda$ parameters are identical for the different EFT operators employed in different analyses. If this assumption was made, the results presented here would present the most stringent limits on scalar unparticles over a wide range of $d_U$. Additional exclusion limits on the signal cross section, as well as the $\Lambda_U$ scale are given for reference in Fig. 8.10.

### 8.2.5. Extra dimensions

For the scenario of large extra dimensions in the ADD model, exclusion limits are formulated for values of the number of extra dimensions $n$ between 2 and 7, as well as values of the bulk mass $M_D$ between one and three TeV. The excluded cross sections for signal hypotheses with $p_\mathrm{T}(G) > 50$ GeV are shown in Fig. 8.11. In both the measured and predicted cross section values, the truncation procedure described in sec. 4.4 has been applied. Exclusion limits on $M_D$ as a function of $n$ are determined by considering the crossing of the predicted LO cross

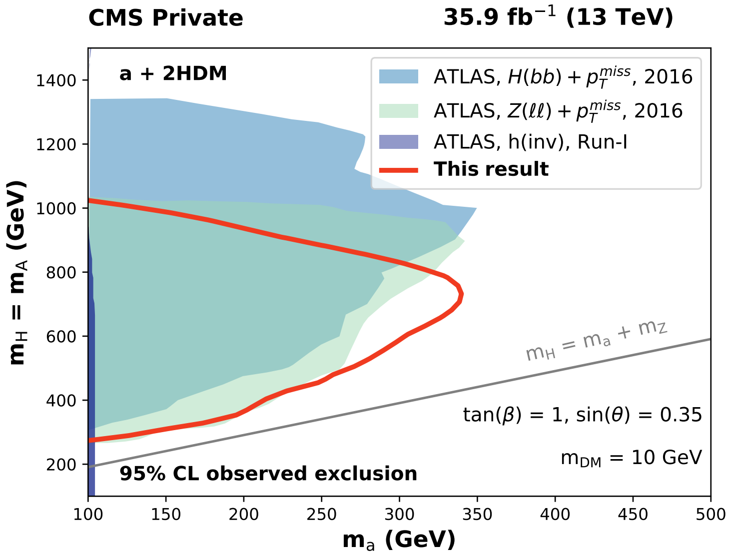

Figure 8.8.: Comparison of the result presented here with results obtained by the ATLAS collaboration [169–172]. Only observed exclusions are shown. The results labelled “2016” use a data set corresponding to 36.1 fb$^{-1}$ of proton-proton collisions at $\sqrt{s} = 13$ TeV. The result labelled “H(inv.)” is derived from constraints on the branching fraction of the Higgs boson with a mass of 125 GeV, which are based on the Run-I data sets of 4.7 fb$^{-1}$ at $\sqrt{s} = 7$ TeV and 20.3 fb$^{-1}$ at $\sqrt{s} = 8$ TeV. Note that the mono-Z results probe the diagrams with H → Za, while the mono-H result is only sensitive to reactions with A → ha. Both cases are comparable here due to the choice of $m_{\mathrm{H}} = m_{\mathrm{A}}$.

section and the observed cross section limits. These limits are shown in Fig. 8.12. Values of $M_D$ between 2.3 TeV (for $n = 2$) and 2.5 TeV (for $n = 7$) can be excluded. These exclusion limits are generally weaker than those from searches for virtual exchange of a graviton with a decay to lepton pairs, which can probe $M_D$ between 5 and 8 TeV [173], but provide critical additional information to determine the origin of a possible signal: While many different types of new physics phenomena could cause a signal in either channel, an observation of the presence or absence of a signal in both channels would allow to determine whether the putative signal is compatible with the graviton hypothesis.

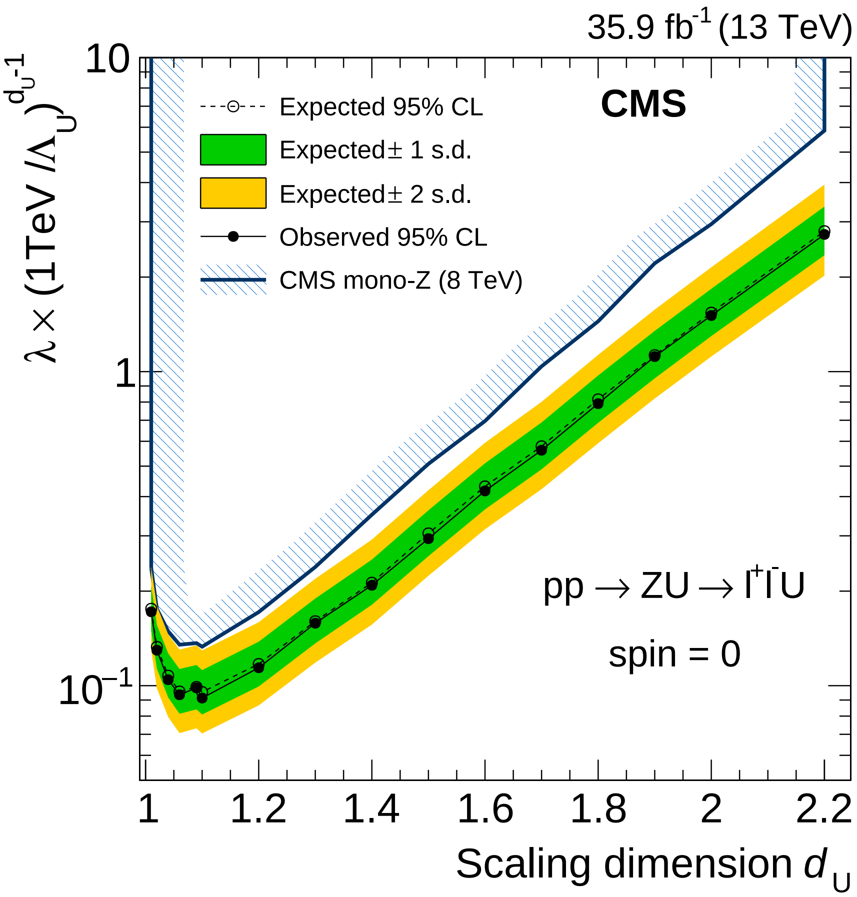

Figure 8.9.: Exclusion limit for the unparticle Wilson coefficient $\lambda \times (1\ \text{TeV}/\Lambda_U)^{d_U-1}$ as a function of $d_U$. For comparison, the results of a CMS analysis of the $Z + p_{\mathrm{T}}^{miss}$ topology in a data set with $\sqrt{s} = 8$ TeV [97] are also shown (blue hatched area).

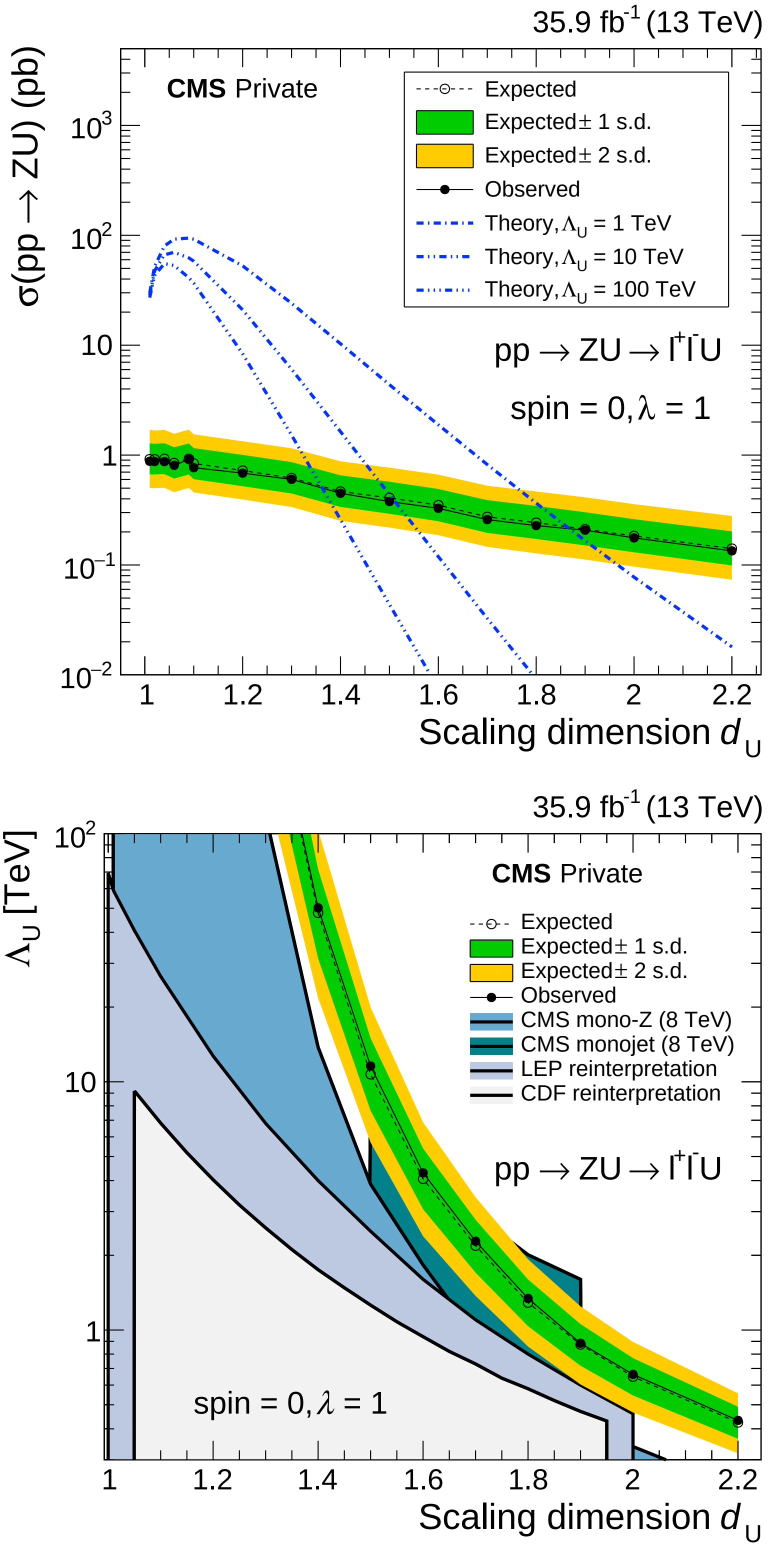

Figure 8.10.: Exclusion limit for the unparticle production cross section (top), and EFT scale $\Lambda_U$ (bottom) as a function of $d_U$. The shown references are the same as in Fig. 7.22. The cross section limits are independent of $\Lambda_U$ and $\lambda$, which only affect the total cross section. Cross section curves are shown assuming $\lambda = 1$ and $\Lambda_U$ values of 1, 10, and 100 GeV.

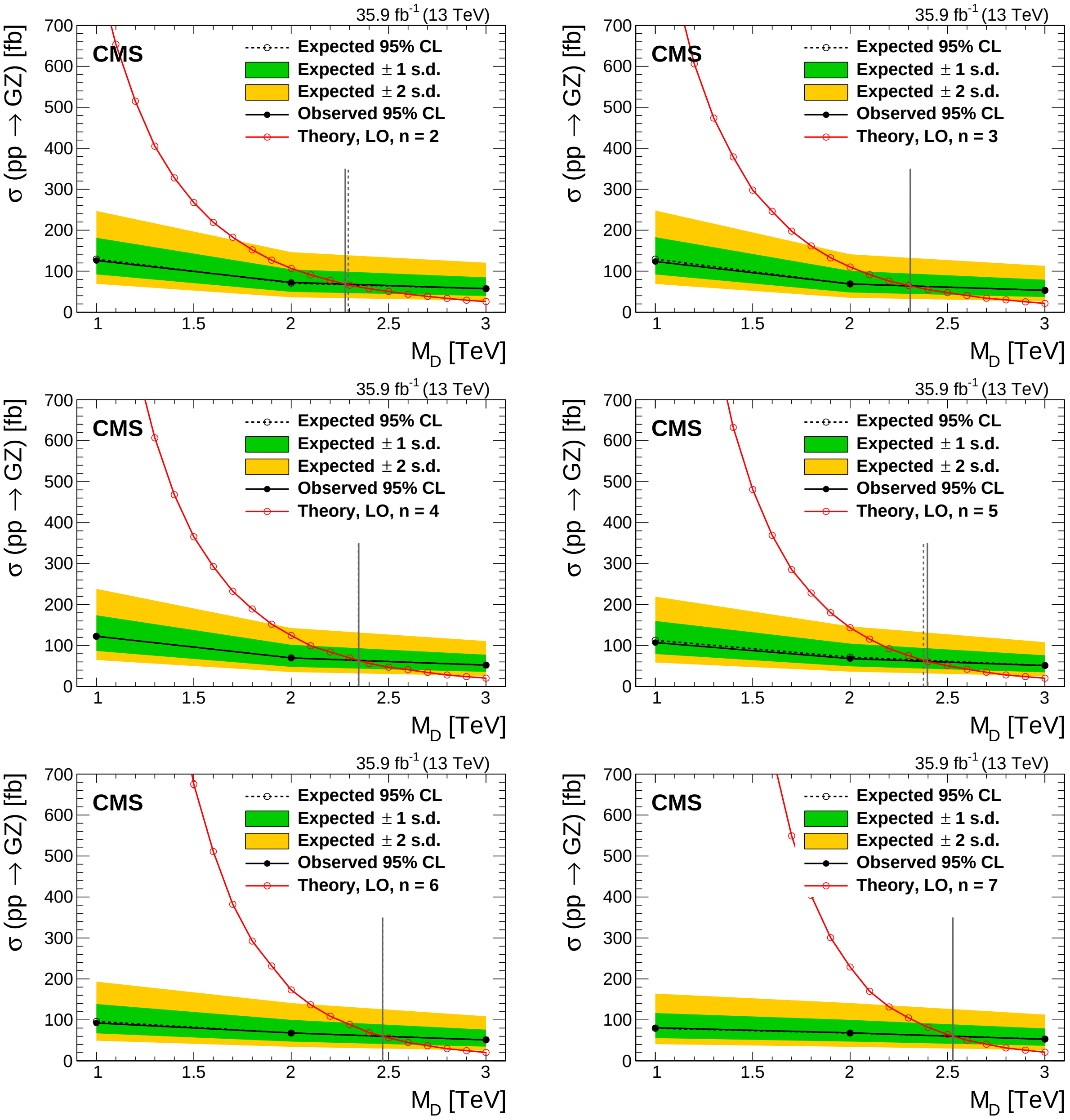

Figure 8.11.: Exclusion limit on the cross section for production of a graviton and Z a boson in the fiducial parameter space $p_T(G) > 50$ GeV as a function of $M_D$. Each of the panels shows a different value of the number of extra dimensions $n$ between 2 and 7. The red solid line indicates the cross section as predicted by Pythia8. The exclusion limit for $M_D$ is defined as the crossing point of the red and black lines, and is indicated by the vertical gray lines, which are given separately for the expected (dashed lines) and observed exclusion (solid lines). Values of $M_D$ to the left of the gray lines are excluded. The truncation method described in sec. 4.4 is applied.

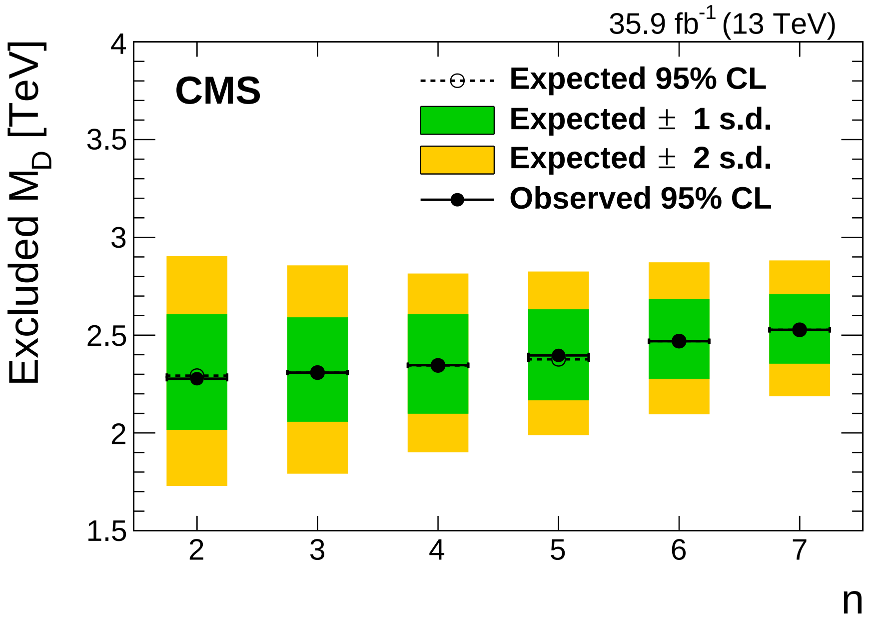

Figure 8.12.: Exclusion limit for $M_D$ as a function of the number of extra dimensions $n$.

## 8.3. Sensitivity to unstable new particles

Throughout this thesis, it is assumed that the targeted new particles do not leave a signature in the detector. While this assumption is valid for direct production of dark matter candidates, it is possible that a more complex dark sector could lead to deviations from this scenario. An example of a more complex interaction would be the initial production of heavier dark sector states, with subsequent decays of the heavy particles into lighter particles. If all decay products are invisible and stable, this additional mechanism is not observable experimentally. A more interesting case would be that of at least partially visible decay products, which is discussed in detail in Ref. [174]. Following the example cases given in that work, the sensitivity to the production of electrically neutral particles $\chi_2$ from the decay of a spin-1 vector mediator is studied here. The $\chi_2$ particle subsequently decays into the real DM candidate $\chi_1$ and a pair of either jets or photons. A graphical representation of this signature is given in Fig. 8.13. The generation of two additional SM particles and one dark sector particle in the decay allows to keep the dark and SM sectors largely separate. The decay could proceed e.g. via a heavy intermediate particle that couples to both DM and SM particles, which effectively avoids the addition of SM charges for the dark sector particles.

The sensitivity to this scenario is studied using an identical analysis strategy and implementation to before. Events with a prompt $e^+e^-$ or $\mu^+\mu^-$ pair and large $p_\mathrm{T}^{miss}$ are selected using the criteria defined in Tab. 8.1, and signal extraction is performed via an ML fit to the (emulated) $p_\mathrm{T}^{miss}$ distributions in the signal and control regions. The search strategy is not adapted to take into account any of the signal properties induced by the additional decay mechanism. Proper lifetimes of the $\chi_2$ particle between $c\tau = 1$ mm and $c\tau = 10$ m are considered. By evaluating the sensitivity of the prompt search strategy to this signal topology, it is possible to test what part of the parameter space of an extended model can already excluded, and allows to clearly define the parameter regions where dedicated searches optimized for the topology are necessary.

The decay signatures considered here ($\chi_2 \rightarrow \chi_1 jj$ or $\chi_2 \rightarrow \chi_1 \gamma\gamma$) give rise to two distinct effects on the sensitivity: The jets and photons from the $\chi_2$ decay will absorb some of the $\chi_2$ momentum, and therefore lead to an overall reduction in the expected values of $p_\mathrm{T}^{miss}$ compared to the case where the $\chi_2$ is stable. Furthermore, the additional final state particles may spoil the event selection efficiency, as many of the selection criteria are designed for the case where there are no intrinsic further particles in the final state in addition to the Z boson and DM candidates (not counting radiated partons, PU contributions, etc.). The strength of these effects will depend in a different way on the lifetime of the $\chi_2$ particle, as well as the mass splitting between the two $\chi$ particles. Additionally, they of course also depend on the parameters of the mediator, just as the non-displaced signature does. This combination of independent parameters and physical effects opens a large range of kinematic behaviors to be explored. In this section, the effects of a number of relevant parameters will be studied and the sensitivity of the existing analysis strategy to displaced signatures will be evaluated.

### 8.3.1. Technical implementation

The scenario described in the previous section is easily implemented based on the configuration used for the case of the spin-1 mediator with vector couplings. As the full parameter

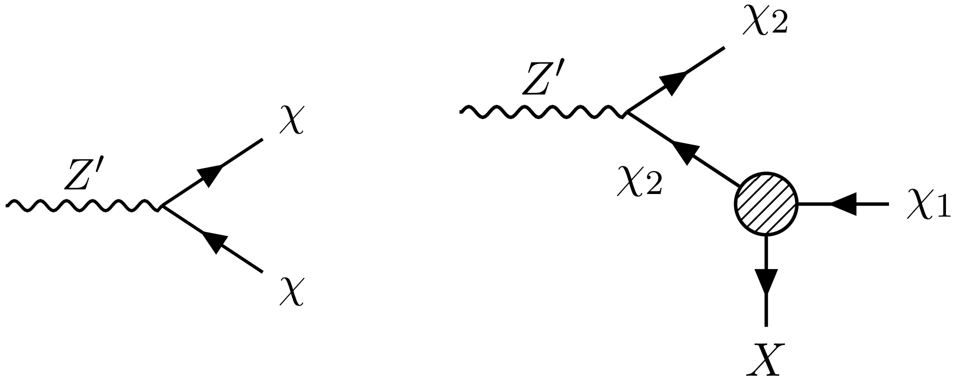

Figure 8.13.: Illustration of the mediator decay chain. In the "standard" simplified model case (left), the mediator $Z'$ decays to a pair of DM candidates $\chi$, which are stable and leave the detector without further interaction. In the alternative scenario discussed in this section, the mediator instead decays into a pair of dark sector particles $\chi_2$, which are unstable and further decay into the stable neutral fermion $\chi_1$ and an additional set of particles $X$. Here, the $X$ system is considered to be either a pair of photons or jets. The hatched circle represents an effective three-body decay of the $\chi_2$ particle. Note that the decay of the upper $\chi_2$ particle in the diagram is omitted in the graphic, but is always assumed to occur.

space of $m_{med}$, $m_{\chi_2}$, $m_{\chi_1}$, $g_q$, and $g_\chi$ is too complicated to be covered immediately, a single parameter point of the vector mediator scenario with $m_{med} = 500$ GeV and $m_{DM} = 150$ GeV is used. This point is chosen because it is relatively close to the exclusion boundary, has a sufficient mass splitting between the mediator and DM candidate, and a sizeable DM mass. The choice of DM mass allows us to explore different scenario for the mass splitting between the $\chi$ particles. Using the same MADGRAPH configuration as for the samples with direct production of stable DM candidates, particle-level events are generated. Usually, the parton shower generator PYTHIA8 would then simply ignore the DM candidates, as they do not decay or participate in any parton shower activity, and pass them through to the fully simulated samples. For this study, the PYTHIA8 configuration is changed to assign a finite life time to the neutral particle previously considered the DM candidate, which is now referred to as $\chi_2$. Furthermore, a custom decay mode is inserted manually into the PYTHIA8 configuration to govern how the $\chi_2$ particle is meant to decay. Based on this information, PYTHIA8 detects the presence of the $\chi_2$ particle, generates the decay, and takes into account any decay products for the parton showering. Of the example cases given in Ref [174], two decay scenarios are considered in this study: $\chi_2 \rightarrow \chi_1 u\bar{u}$ and $\chi_2 \rightarrow \chi_1\gamma\gamma$, where $\chi_1$ is the new, stable DM candidate. Four simplifying assumptions are made to allow for a simple parameterization of this decay:

1. A direct three-body decay without resolved intermediate particles is assumed.

2. The decay matrix element is assumed to be isotropic.

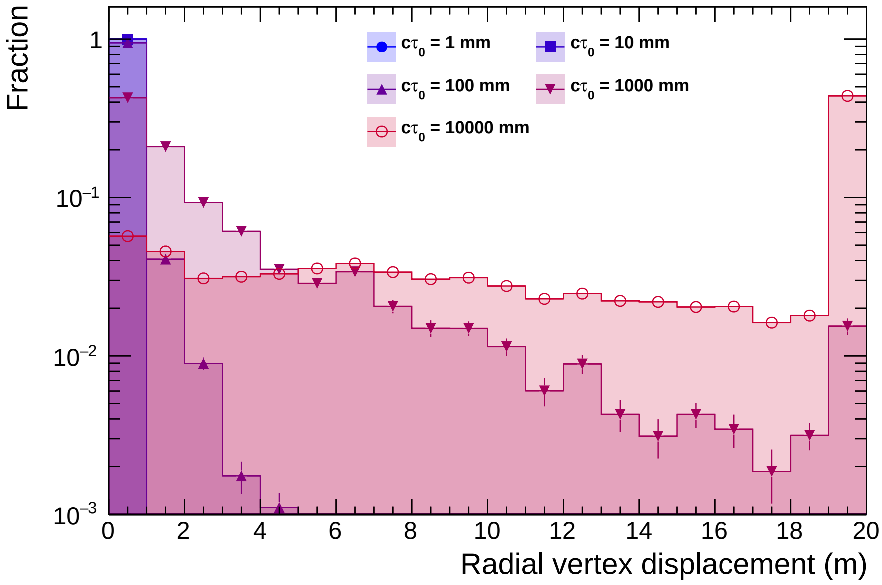

Figure 8.14.: Distribution of the radial distance of the $\chi_2$ decay vertex from the beam spot as a function of its proper lifetime $c\tau$. Lifetimes between $c\tau = 1$ mm and $c\tau = 10$ m are considered. The rightmost bin includes all events with a displacement of more than 20 m ("overflow").

3. The lifetime of the $\chi_2$ state is not generated dynamically from other parameters such as coupling strengths, mass splittings, etc., but set to predefined values.
4. The branching fraction of the $\chi_2 \to \chi_1 + X$ decay is assumed to be 100%.

These choices leave two free parameters, namely the proper lifetime of the $\chi_2$ state, and the mass of the $\chi_1$ particle, which are scanned in multiple steps.

$$c\tau/\mathrm{mm} \in \{1, 10, 100, 1000, 10000\}$$

$$m(\chi_1)/\mathrm{GeV} \in \{1, 50, 130, 145\}$$

The resulting displacement of the decay vertices from the primary vertex is shown in Fig. 8.14. Note that the displacement is further enhanced by the partially sizeable Lorentz $\gamma$ factors of the $\chi_2$ particles.

## 8.3.2. Efficiency of $p_\mathrm{T}^{miss}$ filtering

As described in sec. 6.1.5, it is vital for any $p_\mathrm{T}^{miss}$-based analyses at the LHC to employ a filtering of events to avoid being overwhelmed by events with spurious $p_\mathrm{T}^{miss}$ from detector noise, beam-induced backgrounds, etc. The main way in which events with spurious $p_\mathrm{T}^{miss}$ are detected is by applying criteria motivated by the kinematics of prompt particle production: The final state particles are expected to travel outward from the interaction point in the radial direction, and leave consistent deposits in different detector submodules. In the case of displaced decays, some of these assumptions are not applicable anymore: Depending on the momentum of the decaying particle, its decay products may or may not travel in the expected direction, may or may not interact in all detector submodules. Therefore, a first hurdle for the displaced signatures is to pass the noise filters designed for prompt events. The filter efficiency for signal events is shown in Fig. 8.15. While signals without displaced decays, as well as with those with relatively low lifetimes, show almost perfect efficiencies, a significant inefficiency can be observed at a lifetime of around $c\tau \approx 1$ m, which then recovers again towards higher lifetimes. The total inefficiency is to at least two thirds due to the `HBHE(Iso)NoiseFilter`, which is designed to reject events where the HCAL reports suspicious isolated energy deposits, with smaller contributions from the beam halo filter. A comparison of photon and jet samples with $m_{\chi_1} = 1$ GeV shows that the inefficiency is less pronounced in the case of the jet events. This is due to the presence of an intrinsic charged component, which results in reconstructed tracks if the decay happens inside the tracker volume, and makes the events less likely to pass the selection criteria for isolated calorimeter noise. Photons on the other hand will only produce tracks through electron conversion, which happens less frequently than charged particle creation in hadronic jets, and has overall smaller track multiplicities. The filtering efficiency also illustrates the effect of the $m_{\chi_2}$ variable: With increasing values of $m_{\chi_2}$, the mass difference to the $\chi_1$ parent particle is reduced, and the SM particles produced in the decay are left with ever smaller energies. Without the extra momentum obtained from larger mass splittings, it becomes less likely for them to trigger the noise rejection filters. the available energies are simply smaller than those of typical noise contributions. However, to trigger this mechanism, relatively large values of $m_{\chi_2}$ are necessary: There is virtually no difference in filter efficiency between the $m_{\chi_2} = 1$ GeV and 50 GeV cases. Significant improvements are only visible for $m_{\chi_2} \gtrapprox 100$ GeV. For sufficiently large lifetimes $c\tau > 1$ m, the filter efficiency recovers because the $\chi 2$ decays begin to happen outside the calorimeters, and will therefore not leave any energy deposits that could trigger the filtering.

Overall, the limited size of the inefficiency is good news: Although the filters are mainly designed for prompt phenomena, at least 75 % of signal events with signal events pass them. This indicates that the performance of the $p_{\mathrm{T}}^{miss}$ filters should be optimized for a dedicated search for these events. However, it also indicates that the current performance is no insurmountable obstacle: While there are cases where a 25 % decrease in expected signal yields will make the difference between making or missing a discovery, the $p_{\mathrm{T}}^{miss}$ filters will not be the dominating factor in the resulting sensitivity.

### 8.3.3. Acceptance of kinematic selection

The main hurdle the signals with a displaced decay will have to pass is the kinematic and topological event selection of the analysis. The kinematic selection is centered on the approximately symmetrical topology of high $p_{\mathrm{T}}^{miss}$ and $p_{\mathrm{T}}(\ell\ell)$. The most relevant impact of the secondary decays on this selection is the reduction of $p_{\mathrm{T}}^{miss}$, as some of it is absorbed by the production of the additional SM particles. This effect can easily be demonstrated in the inclusive distributions of the reconstructed $p_{\mathrm{T}}^{miss}$, which are shown in Fig. 8.16 for photonic decays and a number of parameter choices. A similar dependence on $m_{\chi_1}$ can be observed: For low values of $m_{\chi}$, such as 1 GeV, the mass of the parent $\chi_2$ particle will give democratic momentum contributions for all daughter particles. As a result, the $p_{\mathrm{T}}^{miss}$ distribution becomes much softer. This behavior is naturally enhanced for low lifetimes, and

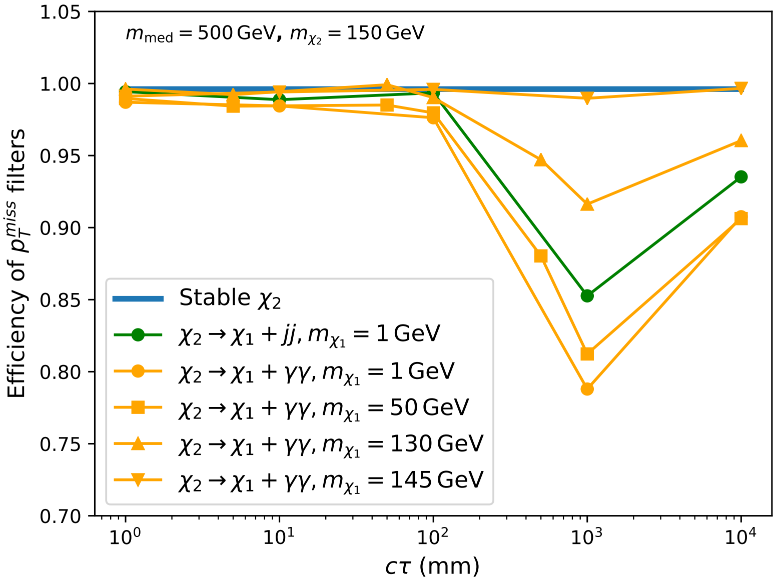

Figure 8.15.: Efficiency of the $p_{\mathrm{T}}^{miss}$ filters for signal events as a function of the $\chi_2$ proper lifetime $c\tau$. The blue solid line indicates the value for a signal sample with a stable $\chi_2$ particle, and serves as a reference.

recovers almost completely at $c\tau \approx 10$ m, when a significant portion of the decays happen outside of the sensitive detector volume. As $m_{\chi_1}$ is increased, the effect is overall reduced, and the dependence of $c\tau$ reduces with it. For $m_{\chi_1} = 145$ GeV, almost no momentum can be carried away by the SM decay products.

The acceptance of the full selection is shown after each selection step in Fig. 8.17 for jet and photon samples with $m_{\chi_1} = 1$ GeV. In both decay topologies, the acceptance is affected by the reduced values of $p_{\mathrm{T}}^{miss}$. In addition to this reduction, which reduces the acceptance of the kinematic selection in the right half of the plot, significant reductions in acceptance arise from the topological criteria meant to suppress background with additional objects, such as $\mathrm{t\bar{t}}$. Many signal events are rejected by the requirement that no more than one jet be present, which in the worst cases reduces the acceptance by factors as large between 20 and 100. This effect also appears for the photonic decays because the PF reconstruction also delivers jets obtained from reconstructed photons. However, the efficiency of the jet reconstruction is significantly reduced as the lifetime reaches $c\tau \approx 1$ m and decays occur predominantly outside of the tracker volume. Interestingly, the jet rejection influences the acceptance even at high values of $c\tau = 10$ m. This is simply a result of the exponential decay time distribution, which means that for this value of $c\tau$, a fraction of $1 - \exp(1/10) \approx 10\%$ of events will still decay within a distance of 1 m around the interaction point.

For decays with jets, an additional topological selection comes into play. The identification of b and $\tau$ jets is largely based on the displacement of tracks inside a given jet. For small life time values $c\tau \leq 10$ mm, the jet displacements will look like those from B meson and $\tau$ lepton decays. Accordingly, they are identified as such and the corresponding events are rejected.

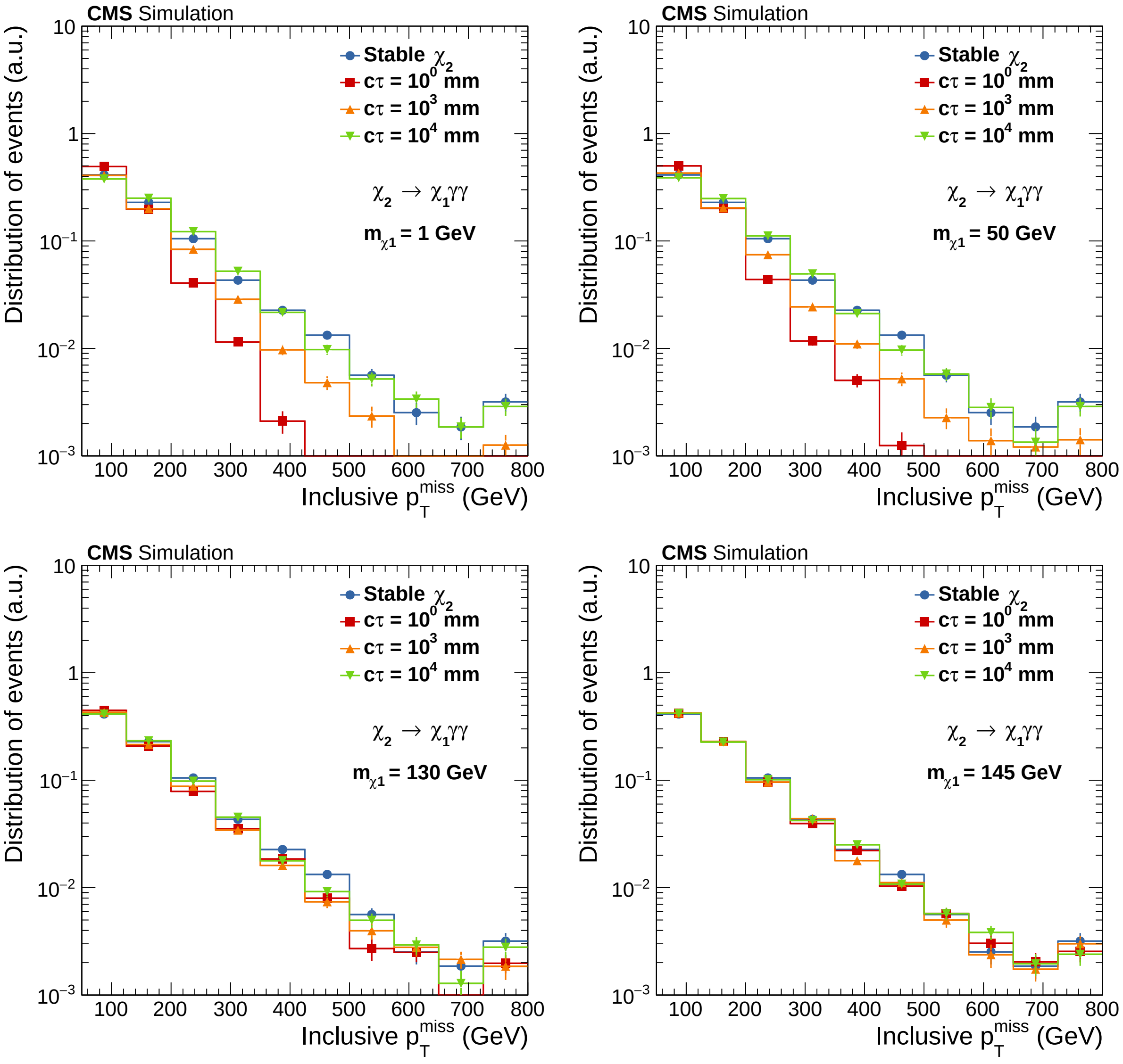

Figure 8.16.: Distribution of reconstructed $p_{\mathrm{T}}^{miss}$ in all events in a sample. Distributions are shown for different values of $c\tau$ for $\chi_2 \rightarrow \chi_1\gamma\gamma$ and $m_{\chi_1}$ values of 1 GeV (top left), 50 GeV (top right), 130 GeV (bottom left) and 145 GeV (bottom right).

The same cumulative acceptance representation is shown in Fig. 8.18 for higher values of $m_{\chi_1}$ and photonic decays. The smaller mass splittings implied by larger $m_{\chi_1}$ again recover significant portions of the acceptance. While there are still reductions to be feared from the jet requirements, they are less pronounced than for larger mass splitting. At $m_{\chi_1} \approx 145$ GeV, almost no loss of acceptance is observed.

### 8.3.4. Exclusion sensitivity

Exclusion limits are calculated for the more promising case of photonic decays. They are shown in Fig. 8.19 for all considered values of $m_{\chi_1}$. As already evident from the previous

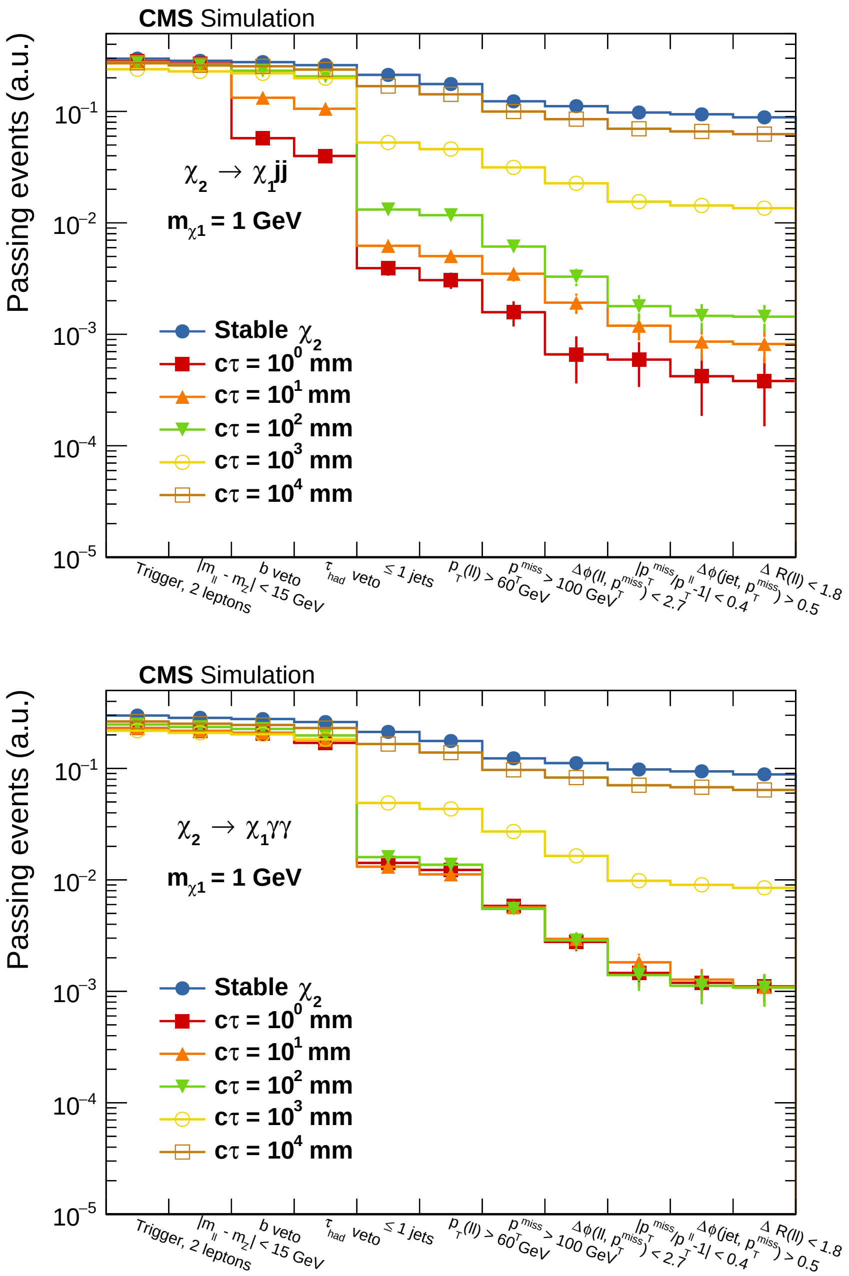

Figure 8.17.: Signal yield after the application of the consecutive selection requirements for $m_{\chi_1} = 1$ GeV, with decays $\chi_2 \to \chi_1 jj$ (top) and $\chi_2 \to \chi_1 \gamma\gamma$ (bottom) . The y-axis is scaled so that ratios between different signal samples are represented correctly. Note that all bins already have the $p_{\mathrm{T}}^{miss}$ filtering selection applied, which results in the different numbers of events in the first bin.

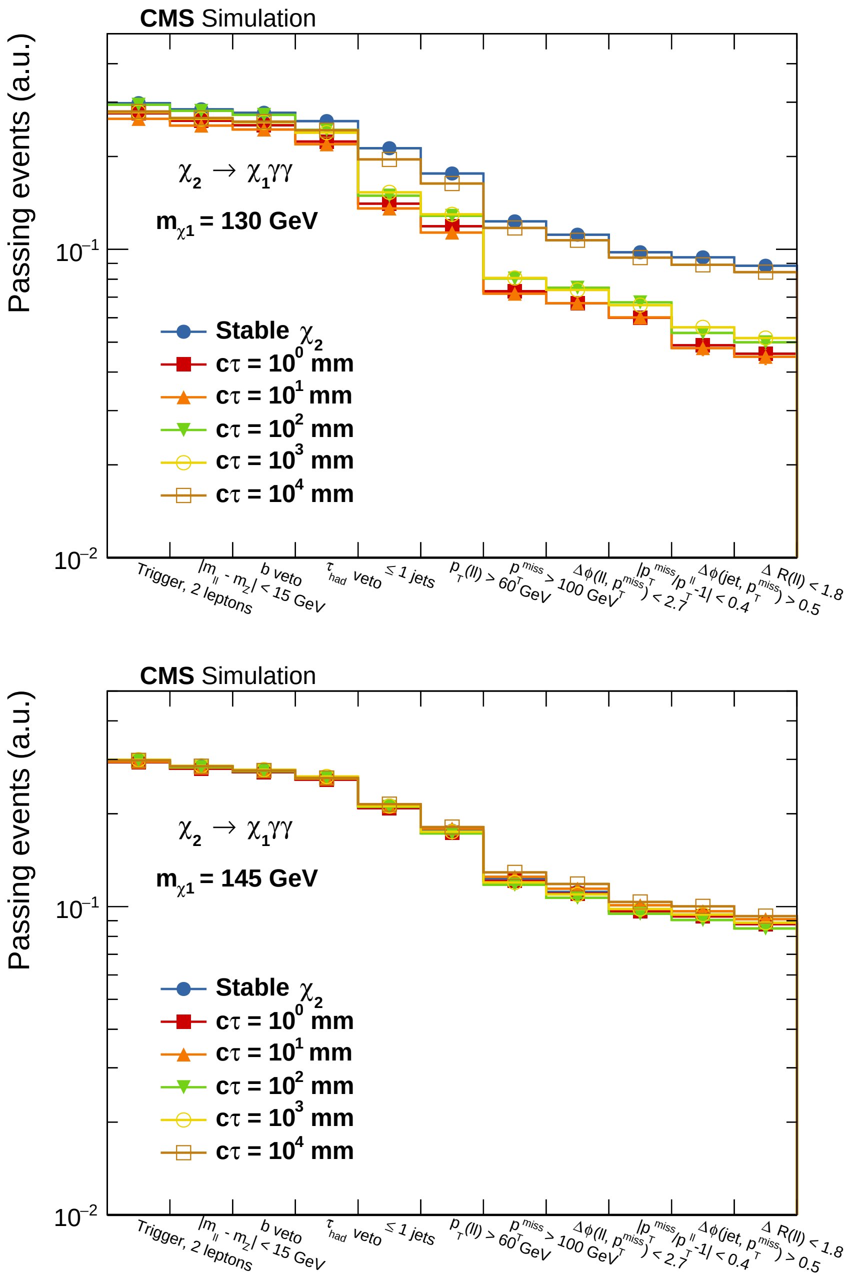

Figure 8.18.: Signal yield after the application of the consecutive selection requirements for $m_{\chi_1} = 130$ GeV (top) and 145 GeV (bottom). In both cases, decays $\chi_2 \rightarrow \chi_1\gamma\gamma$ are considered. The y-axis is scaled so that ratios between different signal samples are represented correctly. Note that all bins already have the $p_{\mathrm{T}}^{miss}$ filtering selection applied, which results in the different numbers of events in the first bin.

Table 8.2.: Minimal excluded values of $c\tau$ for displaced decays with production of photons. The default base scenario of a vector mediator with $m_{med} = 500$ GeV and $g_q = 0.25$, $g_{DM} = 1.0$ is used. The intermediate fermion mass is set to $m_{\chi_2} = 1$ GeV.

| $m_{\chi_1}$ (GeV) | Excluded $c\tau$ (m) |
|---:|---:|
| 1 | 7.5 |
| 50 | 5 |
| 130 | 2.5 |
| 145 | all |

section, the most strongest results can be obtained from scenarios with small mass splitting $m_{\chi_1} \approx m_{\chi_2}$. Assuming $m_{\chi_2} = 150$ GeV, all signal hypotheses with $m_{\chi_1} = 145$ GeV can be excluded, independent of the assumed lifetime. However, already for the slightly lower mass value of $m_{\chi_1} = 130$ GeV, only lifetimes of $c\tau \gtrapprox 2.5$ m can be excluded. However, the signal strength limit for this point does not diverge towards lower lifetimes, but stays constant around $\mu = 2$, indicating that it is not far from the exclusion threshold. A different behavior appears for the cases of $m_{\chi_1} = 50$ and 1 GeV, which can be excluded for $c\tau > 5$ and 7.5 m, respectively. For these signals, there is however little hope to reach smaller lifetimes with this analysis, which is optimized for the prompt topology. The excluded lifetimes are summarized in Tab. 8.2.

This result provides excellent complementarity to searches optimized for a direct detection of displaced particle signatures. Such searches obtain optimal sensitivity if displaced vertices can be reconstructed from particle tracks, which restricts the sensitive region to the physical tracker volume. The resulting sensitivity is optimal up to $c\tau \approx 100$ m, and mostly lost by $c\tau = 1$ m [175]. Searches relying on reconstructed jets, rather than individual vertices, can extend the sensitive range to $c\tau \leq 10$ m [176]. To cover the full range of $c\tau$, it is therefore imperative to combine results from all three search types.

### 8.3.5. Conclusion

The sensitivity of the analysis based on the $Z(\ell\ell) + p_{\mathrm{T}}^{miss}$ topology to signatures with a displaced decay of an intermediate dark sector particle has been studied. The extension of the standard simplified model scenario in this manner offers a large parameter space with qualitatively different phenomenological behaviors. Without adapting the analysis strategy to the partially displaced signature, it has been found that significant sensitivity is achieved either for relatively small mass splittings of the intermediate and final dark sector particles, or relatively long lifetimes of the order of a few meters. This knowledge is essential to enable an efficient matching of the results from dedicated prompt and displaced analyses. For future analyses, the signal hypotheses between these two sets of analyses should be coordinated to ensure their consistency, which is a prerequisite for a robust coverage of the full parameter space. A practical challenge will arise from the larger number of free parameters in the still relatively simple scenario considered here. Since dedicated signal samples are needed for each of the parameter combinations, it is essential to find well-defined overlapping parameter regions for all searches. For an analysis like this one, the focus should be put on the regions of small mass splitting and longer lifetimes. Dedicated search strategies should be employed for other regions.

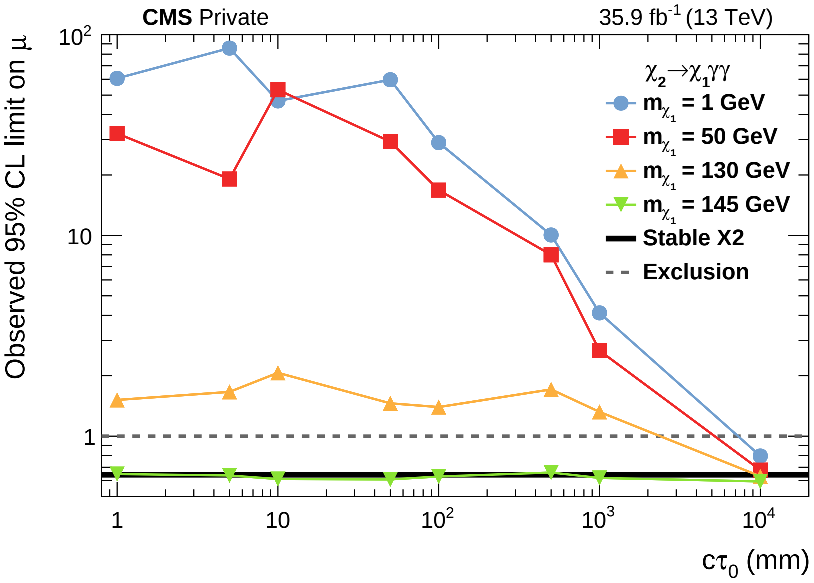

Figure 8.19.: Observed 95% CL signal strength exclusion limits as a function of $c\tau$. The limits are shown for decays $\chi_2 \rightarrow \chi_1\gamma\gamma$, with different values of $m_{\chi_1}$ (colored solid lines and markers). For reference, the signal strength limit for the corresponding sample with a stable $\chi_2$ is shown (thick black solid line). Cases for which $\mu < 1$ are excluded.

# 9. Extrapolation of results to the HL-LHC

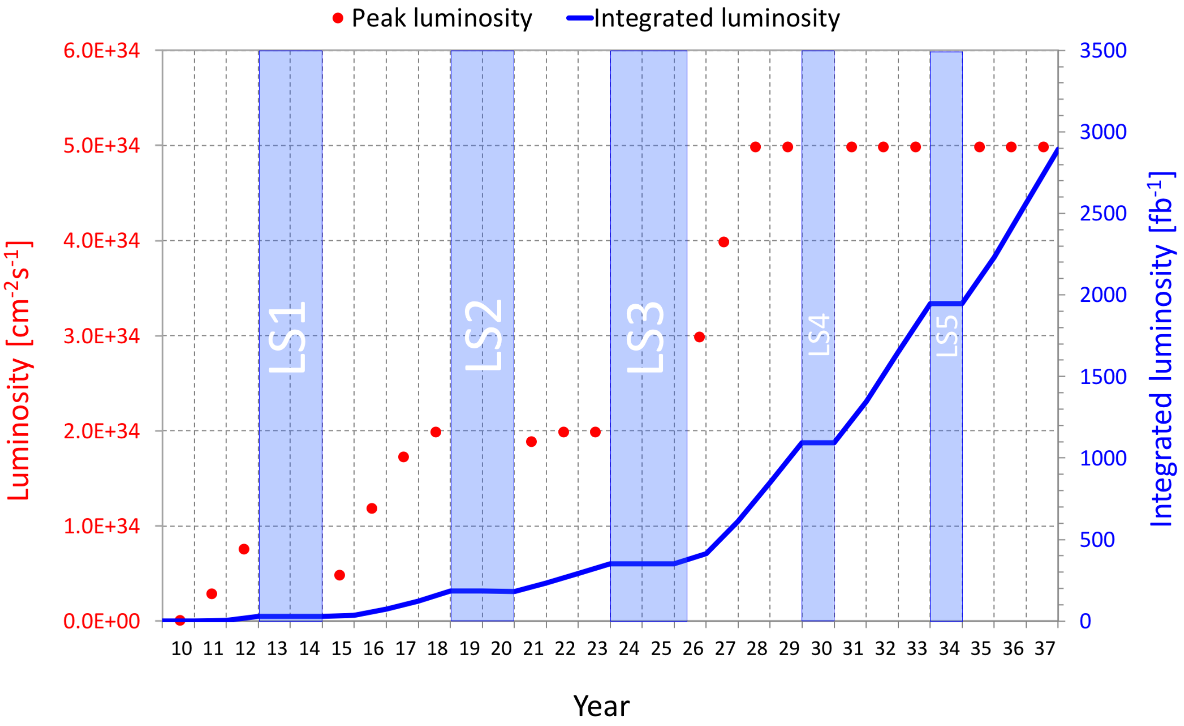

Figure 9.1.: Long-term projected performance of the LHC. The expected instantaneous (red markers) and integrated luminosity values (blue solid line) are shown as a function of time. Shaded time periods marked "LS" represent long shutdown periods. Image taken from Ref. [177].

At the end of 2018, the LHC has successfully completed its second running period, having delivered more than 150 $\text{fb}^{-1}$ of proton-proton collisions at $\sqrt{s} = 13$ TeV. At the time of writing, this combination of center-of-mass energy and data set size makes the LHC the unchallenged high-energy discovery machine. In the coming years up to 2026, the LHC and its experiments will undergo two long shutdown periods used for maintenance and hardware upgrades, with a three-year data-taking period in between. The goals of this period are the achievement of the final increase in collision energy to $\sqrt{s} = 14$ TeV, which marks the arrival of the LHC at its design energy after more than a decade of delay, as well as the preparation for the upgrade to the *high-luminosity LHC* (HL-LHC) [178]. The HL-LHC period is the last third of the life-cycle of the LHC and is meant to drastically increase the total integrated luminosity provided to the experiments, resulting in a final data set corresponding to 3 $\mathrm{ab}^{-1}$ at the end of 2037 (cf. Fig. 9.1). This feat is to be accomplished through a combination of an increase in the instantaneous luminosity from today's record of $\mathcal{L} \approx 2 \times 10^{34}\mathrm{cm}^{-2}\mathrm{s}^{-1}$ to $5 \times 10^{34}\mathrm{cm}^{-2}\mathrm{s}^{-1}$, and luminosity levelling. Luminosity levelling refers to a technique where the particle beams in the collider are adjusted during a run in order to mitigate the loss of integrated luminosity induced through the continuous particle collisions. Clearly, this plan poses a significant technical challenge to the operators of the collider as well as the experimental collaborations, which have prepared by tailoring their Phase-II upgrades around the parameters of the HL-LHC [179–181].

With this future in view, it is important to understand how this large data set will change our ability to find signs of BSM physics. To answer this question, experimentalists from the ATLAS, CMS and LHCb collaborations, as well as theoretical physicists, have collaborated to create a CERN *yellow report* (YR)[1], which collects and combines studies of the experimental sensitivity of a wide range of measurements and searches with the expected HL-LHC data set [182]. In this section, a study of the sensitivity of the mono-Z analysis at the HL-LHC is presented. The results of the study were published by the CMS collaboration as a physics analysis summary [183] and included in the BSM chapter of the YR [182, 184].

## 9.1. Study of $p_{\mathrm{T}}^{miss}$ resolution

The main variable used in this analysis is $p_{\mathrm{T}}^{miss}$, which is calculated using the information from all reconstructed particles in any event. Therefore, it is uniquely sensitive to the performance of the full detector. At the HL-LHC, the high expected luminosity will go hand-in-hand with an increase in the number of PU interactions per bunch crossing, which is expected to be around 200 and may induce a performance degradation of the $p_{\mathrm{T}}^{miss}$ reconstruction. Already during Run-II, algorithms have been developed to mitigate the influence of PU on measured quantities of interest. For the HL-LHC studies, the CMS collaboration has chosen the *pile-up per particle identification* (PUPPI) algorithm as the default method of reconstructing $p_{\mathrm{T}}^{miss}$ [185]. PUPPI derives a one-dimensional score for each particle, which is used to rescale the particle's momentum according to whether it is believed to originate from PU or the hard event. Particles from PU have their momenta rescaled by a factor $< 1$ and their effect on the resulting $p_{\mathrm{T}}^{miss}$ value is therefore minimized. The method is already used today, although the default choice for most CMS analysis is PF-based $p_{\mathrm{T}}^{miss}$ [2], as it performs well at the relatively low PU multiplicities of approximately 25 observed in Run-II [125, 186]. In this section, the performance of the CMS implementation of PUPPI $p_{\mathrm{T}}^{miss}$ is studied and a scaling method is derived that can be applied to events simulated with the 2016 running conditions to mimic the performance expected at the HL-LHC.

### 9.1.1. Comparison of $p_{\mathrm{T}}^{miss}$ performance in fully simulated events

To understand the change in $p_{\mathrm{T}}^{miss}$ performance between Run-II and Phase-II, two samples of $ZZ \to \ell\ell\nu\nu$ events are generated with Madgraph5_aMC@NLO at leading order (LO) in QCD with $\sqrt{s} = 14$ TeV and no outgoing partons at the matrix-element level. The two

---

[1] This type of CERN report historically used to be printed with a yellow cover, thus resulting in the establishment of "yellow report" as a brand name.

[2] PF-based $p_{\mathrm{T}}^{miss}$ is always understood to include Type-1 corrections (cf. sec. 6).

samples have identical generator configurations, and are processed through the full CMS detector simulation as implemented in GEANT4. The difference between the two samples consists of the experimental conditions, which encompass the value of the average number of PU events and the configuration of the physical detector hardware: one sample is processed using `RunIISummer16` conditions, while the other one uses the `PhaseIIUpgradeHGCAlPu200` conditions. The former represents the conditions observed during the data taking in 2016, and the latter those expected for the HL-LHC with an average number of PU interactions per bunch crossing of $\approx 200$. In both samples, the relevant high-$p_\mathrm{T}^{miss}$ regime is enriched by employing a matrix-element-level requirement of $p_\mathrm{T}^{miss} > 80$ GeV. Different random seeds are used for each step of the generation and simulation processes, leading to non-identical generated events in the two samples. Parton showering is applied with Pythia8 8.2.

The inclusive $p_\mathrm{T}^{miss}$ distributions in the two event samples are shown in Fig. 9.2 for both reconstruction algorithms, as well as on the generator-level. The $p_\mathrm{T}^{miss}(\mathrm{gen})$ variable is calculated by summing up the four-momenta of all final state neutrinos in the event and serves as a measure of the "true" $p_\mathrm{T}^{miss}$. A turn-on feature is visible in the generator-level distribution for $p_\mathrm{T}^{miss} \lessapprox 100$ GeV, which is a result of the requirement of $p_\mathrm{T}^{miss} > 80$ GeV mentioned above. The turn-on is smeared out relative to the value of 80 GeV due to parton showering, which is applied only after the requirement has been enforced. For both reconstruction algorithms, the reconstructed $p_\mathrm{T}^{miss}$ distribution in the Summer16 sample is almost identical to the generator-level distribution, which is the desired behavior. In the Phase-II sample, the reconstructed distributions deviate significantly from the generated one. This effect is especially pronounced in the low-$p_\mathrm{T}^{miss}$ region. At higher values of $p_\mathrm{T}^{miss}$, the agreement improves again, which is the expected behavior if the discrepancy is caused by PU contributions. Since PU has lower average particle momenta than the hard $pp \to ZZ$ interaction, PU will have a reduced effect at high $p_\mathrm{T}^{miss}$. Furthermore, the degradation is significantly more pronounced for the PF-based reconstruction. PUPPI shows a smaller overall broadening of the distribution with increased PU.

The reconstruction performance can more effectively be studied by considering the event-by-event $p_\mathrm{T}^{miss}$ resolution rather than the inclusive $p_\mathrm{T}^{miss}$ distributions. The $p_\mathrm{T}^{miss}$ resolution is extracted by studying the distribution of $\frac{p_\mathrm{T}^{miss}(\mathrm{reco})}{p_\mathrm{T}^{miss}(\mathrm{gen})} - 1$ in all events, where $p_\mathrm{T}^{miss}(\mathrm{reco})$ can be either PUPPI or PF reconstructed $p_\mathrm{T}^{miss}$ [125]. The distributions are evaluated separately for the components of the reconstructed $p_\mathrm{T}^{miss}$ that are parallel and orthogonal to the $p_\mathrm{T}^{miss}(\mathrm{gen})$ vector, respectively, as they may exhibit a different behavior. Example distributions for the Summer16 samples and the orthogonal component of PF $p_\mathrm{T}^{miss}$ are shown in Fig. 9.3 for different bins of $p_\mathrm{T}^{miss}(\mathrm{gen})$. The distributions are centered around mean values with magnitudes of less than half a percent, which indicates that there is no overall bias the reconstruction. The distributions are approximately Gaussian and their standard deviation is used as a measure of the resolution. The extracted resolution values as a function of $p_\mathrm{T}^{miss}(\mathrm{gen})$ are shown in Figs. 9.4 and 9.5. Generally, the $p_\mathrm{T}^{miss}$ resolution improves as a function of the generator-level $p_\mathrm{T}^{miss}$ as events become dominated by real $p_\mathrm{T}^{miss}$ rather than instrumental and pile-up induced components. While PUPPI and PF $p_\mathrm{T}^{miss}$ perform similarly in Run-II conditions, PUPPI $p_\mathrm{T}^{miss}$ clearly performs more favorably in Phase-II conditions, owing to a significant degradation of PF $p_\mathrm{T}^{miss}$ performance.

The real figure of merit for this study is the change in performance when shifting from PF $p_\mathrm{T}^{miss}$ in Run-II conditions (i.e. what is used in the analysis of 2016 data) to PUPPI

$p_{\mathrm{T}}^{miss}$ in Phase-II conditions (i.e. what will be used in Phase-II analysis). The ratios of the corresponding resolution curves are shown in Fig. 9.6. The ratios range between one and two for both components and $200 < p_{\mathrm{T}}^{miss}(\mathrm{gen}) < 600$ GeV. For larger values of $p_{\mathrm{T}}^{miss}(\mathrm{gen})$ the ratio evolves towards unity, and even goes below one for a number of bins. The reduction with increasing intrinsic boost is more pronounced for the parallel component. A ratio below one would indicate that the PUPPI algorithm can fully make up for the effect of higher PU, and performs better than today's PF reconstruction. However, the statistical accuracy of the available samples prevents a conclusive determination at the highest values of $p_{\mathrm{T}}^{miss}(\mathrm{gen})$. Note that the decreasing trend towards low $p_{\mathrm{T}}^{miss}(\mathrm{gen})$ is significantly shaped by the generator-level $p_{\mathrm{T}}^{miss}$ requirement and does not necessarily reflect the real physical behavior. The region with low $p_{\mathrm{T}}^{miss}(\mathrm{gen})$ has however already been studied in Ref. [187], which has found resolution ratios between 1.5 and 2.0 in DY events without intrinsic $p_{\mathrm{T}}^{miss}$, which is consistent with the values derived here.

Since both the actual running conditions, as well as the detector configuration and reconstruction software are not final at this time, the simulated behavior is the best available estimate, but may still change significantly. To understand the possible range of outcomes, one can therefore study the optimistic case of assuming Phase-II $p_{\mathrm{T}}^{miss}$ performance to be identical to Summer16, and the pessimistic scenario of a factor of two degradation in the resolution. The rest of this section is devoted to understanding the difference between the two scenarios.

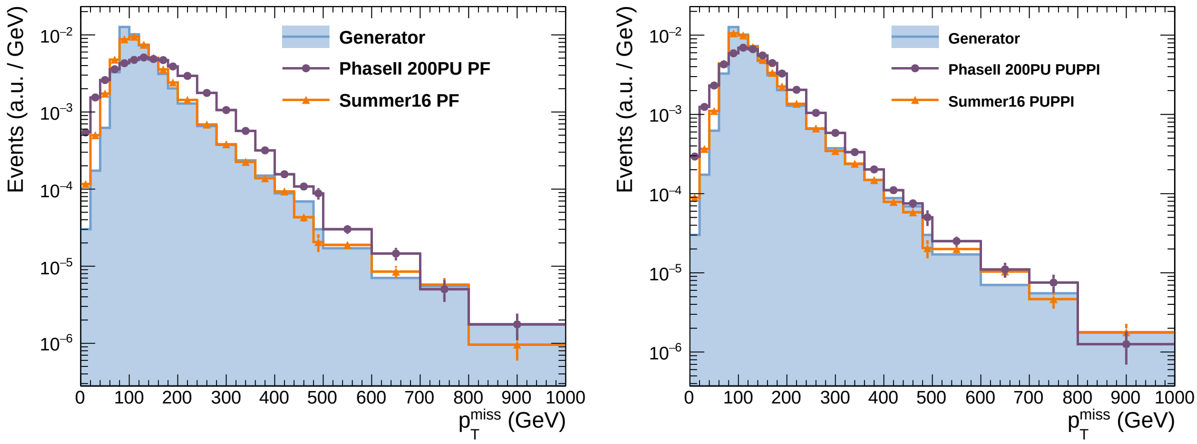

Figure 9.2.: Distribution of $p_{\mathrm{T}}^{miss}$ in $ZZ \to \ell\ell\nu\nu$ events as reconstructed by the PF (left) and PUPPI algorithms (right). The distributions are shown for the 2016 experimental conditions ("Summer16") and those expected for the HL-LHC ("Phase-II"). Additionally, the generator-level $p_{\mathrm{T}}^{miss}$ distribution is shown for comparison.

### 9.1.2. Scaling procedure and effect on results

In order to estimate the effect on the final results caused by a degradation of the $p_{\mathrm{T}}^{miss}$ performance, a resolution scale factor is applied to Run-II simulation. For each simulated event, the difference between generated and reconstructed $p_{\mathrm{T}}^{miss}$ is artificially increased by the multiplicative scale factor SF=2.

$$p_{\mathrm{T}}^{miss}(reco) \rightarrow p_{\mathrm{T}}^{miss}(reco) + \mathrm{SF} \times (p_{\mathrm{T}}^{miss}(reco) - p_{\mathrm{T}}^{miss}(gen)) \tag{9.1}$$

The procedure is validated by studying the distributions of $\Delta p_{\mathrm{T}}^{miss}$ before and after applying the scale factor, and good performance is observed.

The effect of the scaling procedure on the $p_{\mathrm{T}}^{miss}$ distribution in the signal region is demonstrated for the ZZ and DY processes in Fig. 9.7. For the ZZ process, significantly fewer low-$p_{\mathrm{T}}^{miss}$ events pass the final selection after the rescaling procedure is applied. This deficit reaches up to 40% in the $125 - 150$ GeV bin and is a result of the selection requirements on the orientation and magnitude of the $\vec{p}_{\mathrm{T}}^{miss}$ and $p_{\mathrm{T}}(\ell\ell)$ vectors. The scaling procedure leads to a net increase in the mismatch between these two, and therefore leads to a loss of acceptance. At higher $p_{\mathrm{T}}^{miss}$, however, the initial acceptance is recovered and the overall effect of the rescaling is reduced. This behavior is due to the nonresonant nature of the distribution and the relatively wide bins. For example, at $p_{\mathrm{T}}^{miss}(\mathrm{gen}) \approx 500$ GeV, the resolution under Summer16 conditions is approximately 10%, and an increase by a factor two will yield an absolute resolution of $2 \times 10\% \times 500$ GeV $= 100$ GeV, which is comparable to the bin size in this region. Additionally, since the resolution is derived from the standard deviation of the distribution, approximately 68% of events will have $\Delta p_{\mathrm{T}}^{miss}$ value smaller than the nominal value of the resolution, which further limits bin-to-bin migration effects. For the DY process, the situation is radically different. Before the rescaling, approximately 20 DY events are expected in the signal region with $p_{\mathrm{T}}^{miss} > 100$ GeV, with an almost immediate cutoff towards higher values of $p_{\mathrm{T}}^{miss}$. After application of the scaling, the DY contribution balloons to $\approx 10^3$ events, which are still distributed in a rapidly falling way, but still give significant yields in the bins up to 200 GeV. The behavior of the total background, as well as the signal contributions for a spin-1 vector mediator are shown in Fig. 9.8. The overall background behavior is split into a low-$p_{\mathrm{T}}^{miss}$ region, which is driven by the increase in DY events, and a high-$p_{\mathrm{T}}^{miss}$ regime where the VV processes dominate, and the spectrum is accordingly almost unaffected. Independently of the value of $m_{med}$, the signals follow the general behavior of the ZZ background: Reduced acceptance at low $p_{\mathrm{T}}^{miss}$, no significant changes at high $p_{\mathrm{T}}^{miss}$.

The effect of the rescaling on the expected limits for the vector mediator is shown in Fig. 9.9. The effect of the change in resolution is largest for lower mediator masses of $\approx 200$ GeV, where DY contamination and a degradation in signal acceptance lead to an increase of the signal strength of limit of $\approx 25\%$. For higher mediator masses, the effect is less pronounced as most of the signal is situated in the high-$p_{\mathrm{T}}^{miss}$ region that is less affected by a change in resolution. Here, the impact is $\approx 10\%$. In all cases, the nonresonant shape of the signal distributions mitigates the negative effects of the DY contamination. Since the higher $p_{\mathrm{T}}^{miss}$ regions provide significant sensitivity contributions for all values of $m_{med}$, they act as a safeguard against the sensitivity loss in the lower regions. Consequently, the minimal $p_{\mathrm{T}}^{miss}$ requirement for the signal region is increased from 100 GeV in the Run-II analysis to 200 GeV for this projection study. The removal of bins with $p_{\mathrm{T}}^{miss} < 200$ GeV has almost no effect on the resulting sensitivity.

### 9.1.3. Conclusion

The study of the impact of the $p_{\mathrm{T}}^{miss}$ resolution on this analysis shows that a $p_{\mathrm{T}}^{miss}$ independent resolution degradation of a factor two has a limited impact on the analysis result. Based on today's reconstruction software, this case can already be understood to be pessimistic, and future developments in the event reconstruction algorithms will likely lead to improved performance by the time the HL-LHC data taking begins. Further development of machine learning techniques for event reconstruction seems especially promising for improved PU rejection [188]. For the purposes of this study, the constant resolution scale factor SF $= 2$ is applied to the Run-II simulation in order to derive the final results. The application of this scale factor increases the contribution of DY events to the signal region, which is mitigated by raising the $p_{\mathrm{T}}^{miss}$ requirement from 100 to 200 GeV. The combination of both measures reduces the expected signal strength sensitivity by between 10 and 30%.

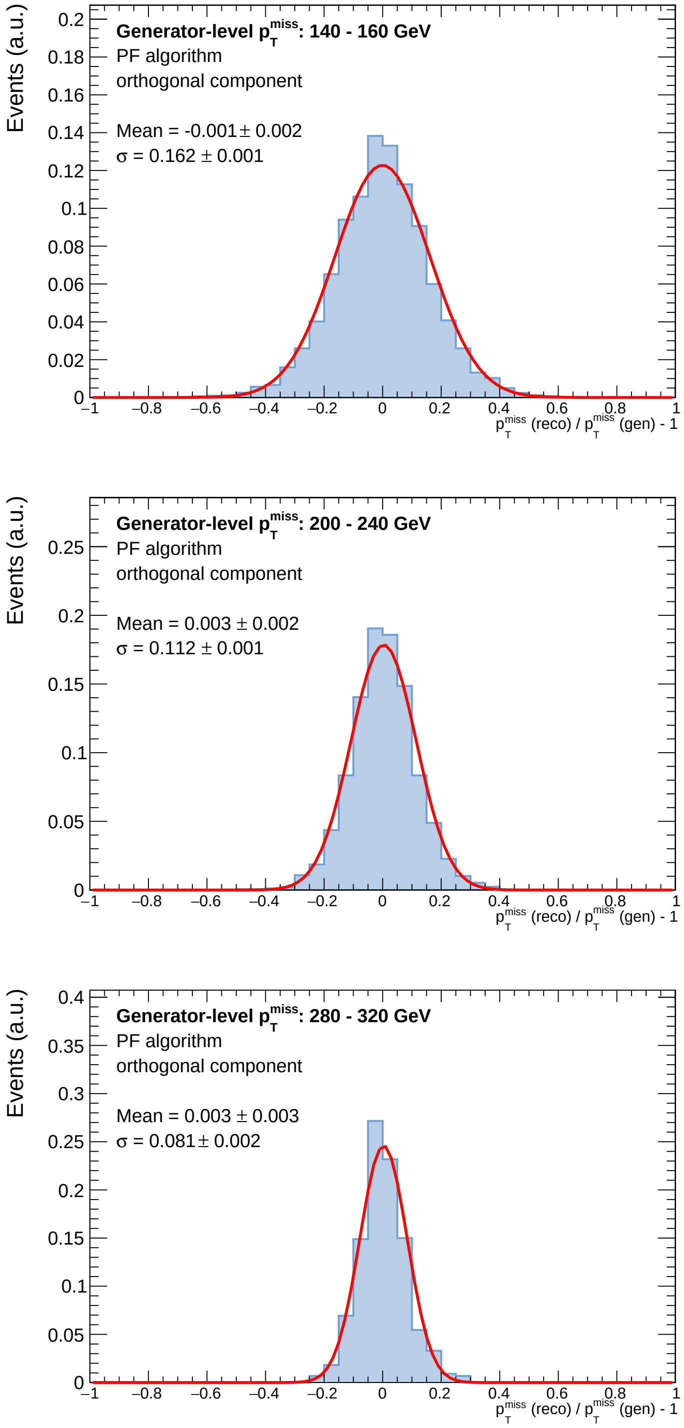

Figure 9.3.: Distribution of $p_{\mathrm{T}}^{miss}(\mathrm{reco})/p_{\mathrm{T}}^{miss}(\mathrm{gen}) - 1$ for the orthogonal component of Run-II PF $p_{\mathrm{T}}^{miss}$. Each of the panels shows the distribution in a different bin of $p_{\mathrm{T}}^{miss}(\mathrm{gen})$ (cf. the labels in the plots). To quote a single resolution value, the standard deviation of the histogram is calculated. The overlaid red Gaussian function is not obtained from a fit, but represents the mean and standard deviation of the histogram to validate that the distribution is approximately Gaussian with the given parameters. The red curve is normalized to the same integral as the histogram.

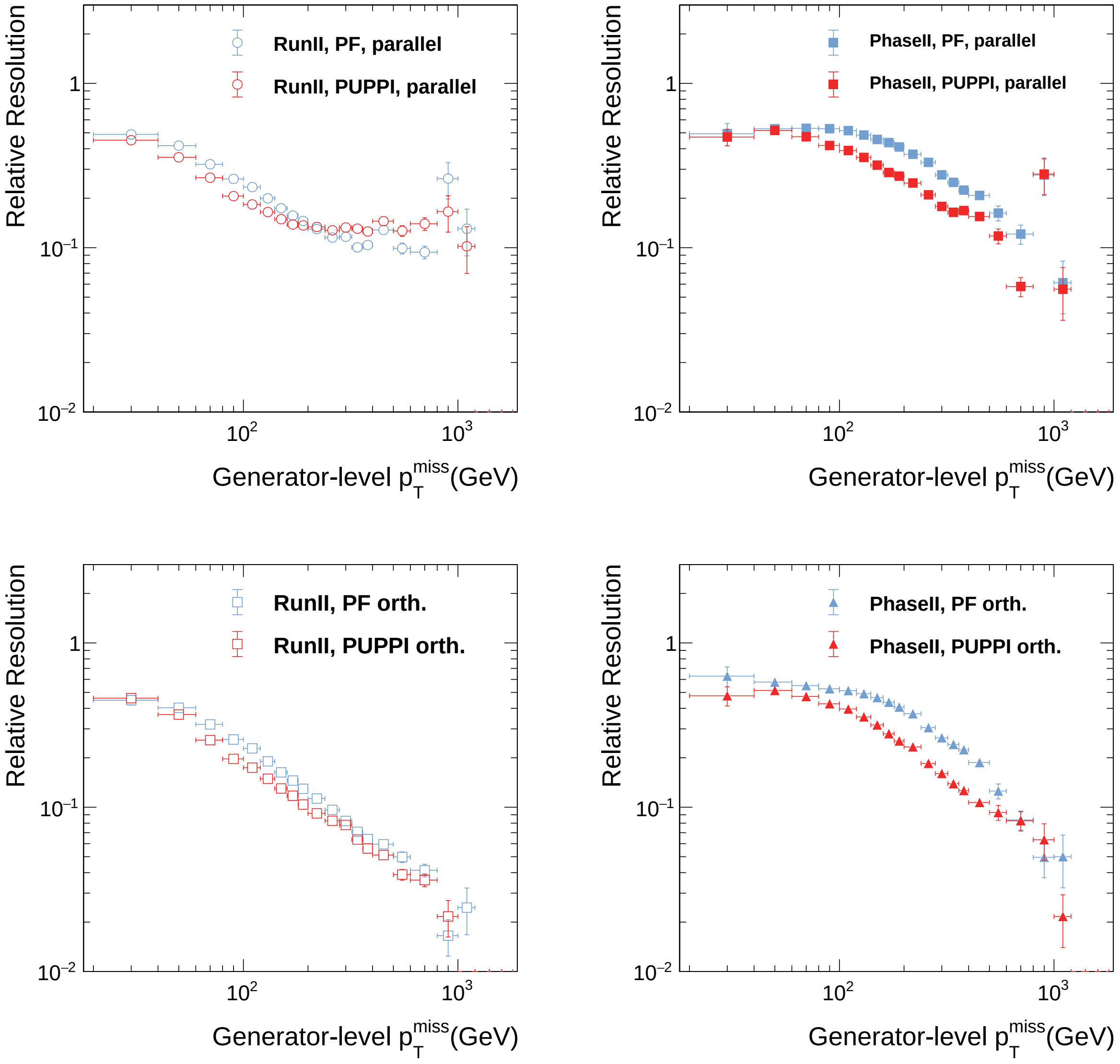

Figure 9.4.: Relative $p_{\mathrm{T}}^{miss}$ resolution as a function of generator-level $p_{\mathrm{T}}^{miss}$ for the parallel (top panels) and orthogonal components (bottom panels). The two left panels show Run-II conditions, the right panels show Phase-II conditions.

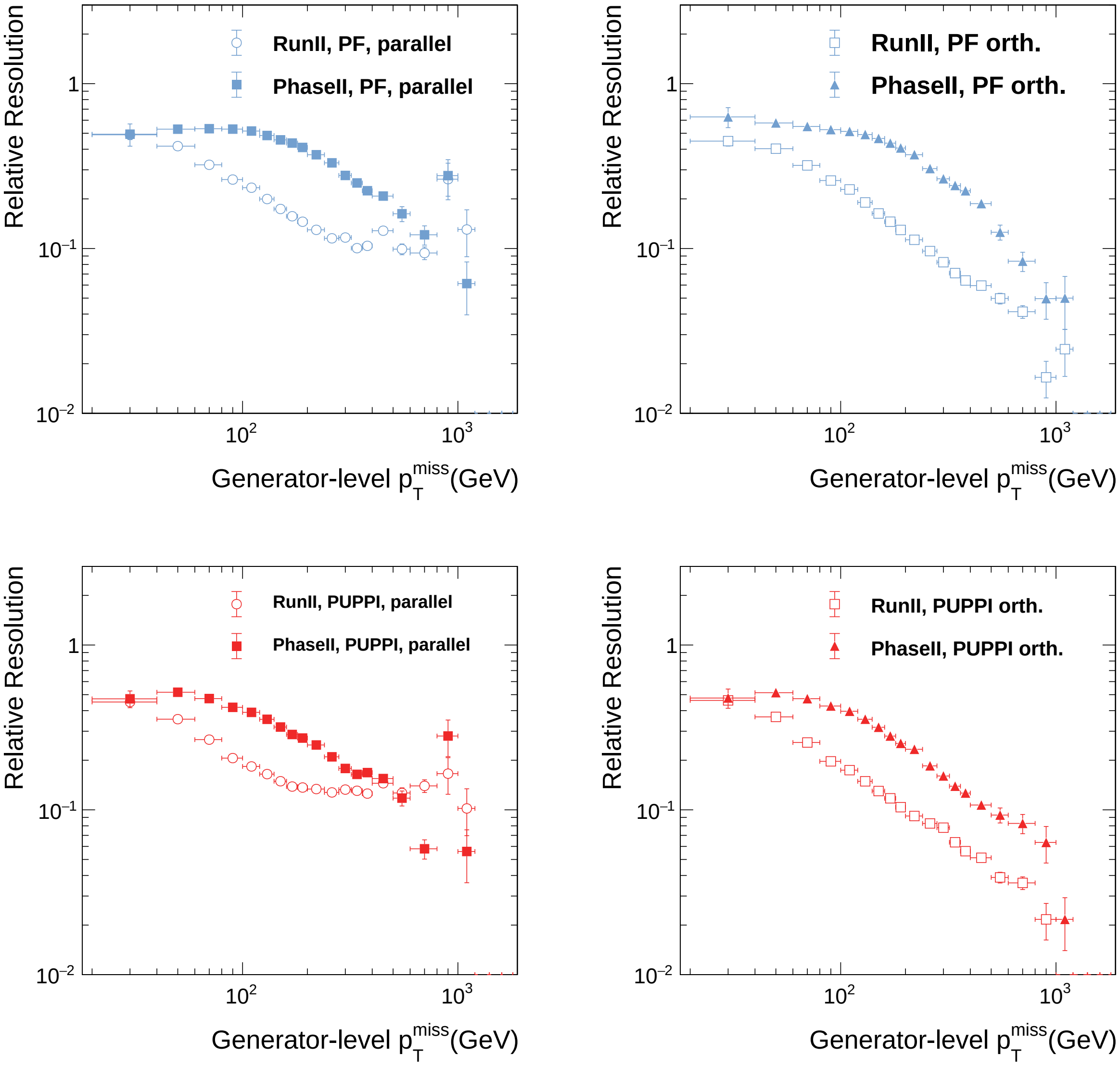

Figure 9.5.: Same as Fig. 9.4, but now grouped by MET algorithm with PF (PUPPI) in the top (bottom) row. The left (right) plots show the resolution for the parallel (orthogonal) components.

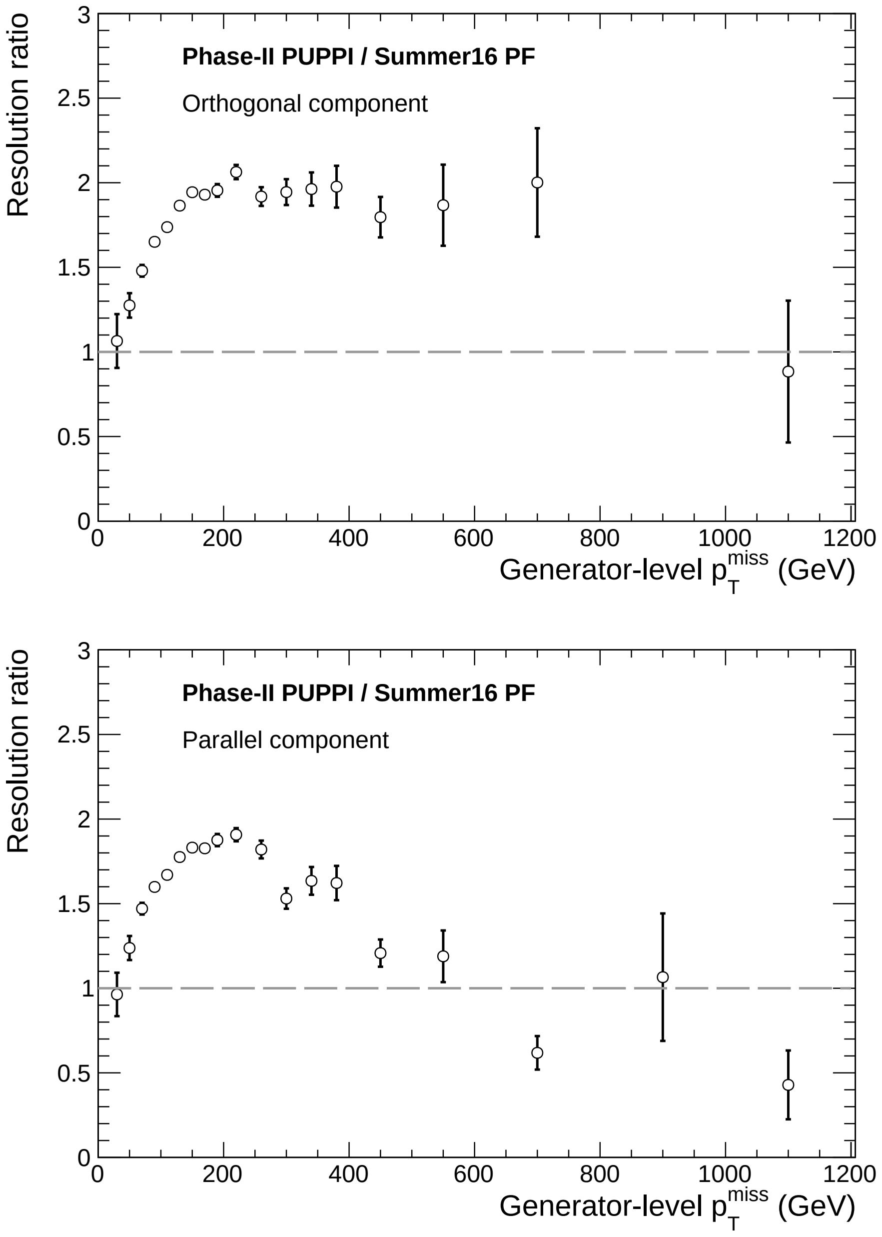

Figure 9.6.: Ratio of the resolution of PUPPI $p_{\mathrm{T}}^{miss}$ in Phase-II conditions over the resolution of PF $p_{\mathrm{T}}^{miss}$ in Run-II conditions. The upper panel shows the ratio for the orthogonal $p_{\mathrm{T}}^{miss}$ component, while the lower panel shows the parallel component. This ratio can effectively be used as a scale factor to simulate the effect of Phase-II conditions in Run-II MC.

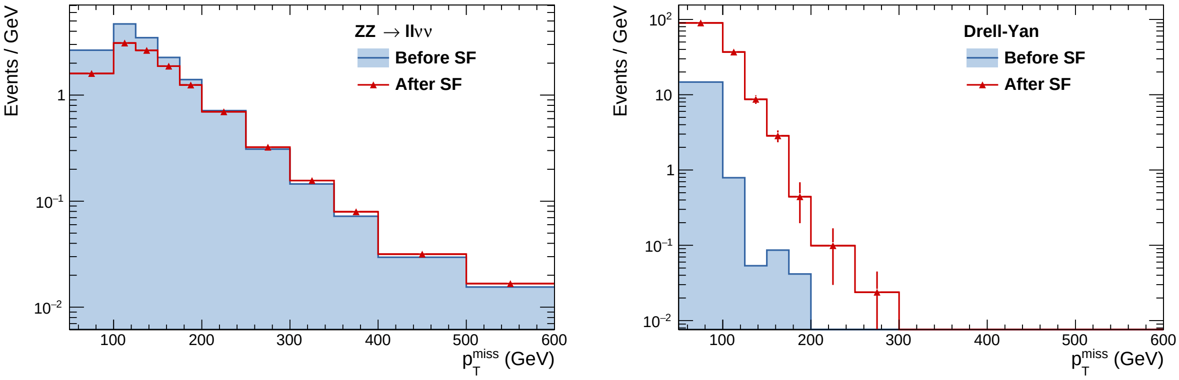

Figure 9.7.: Distribution of $p_{\mathrm{T}}^{miss}$ in the signal region before and after applying the scaling procedure for the $ZZ \rightarrow \ell\ell\nu\nu$ (left) and DY processes (right). All histograms are normalized to an integrated luminosity of 36 fb$^{-1}$.

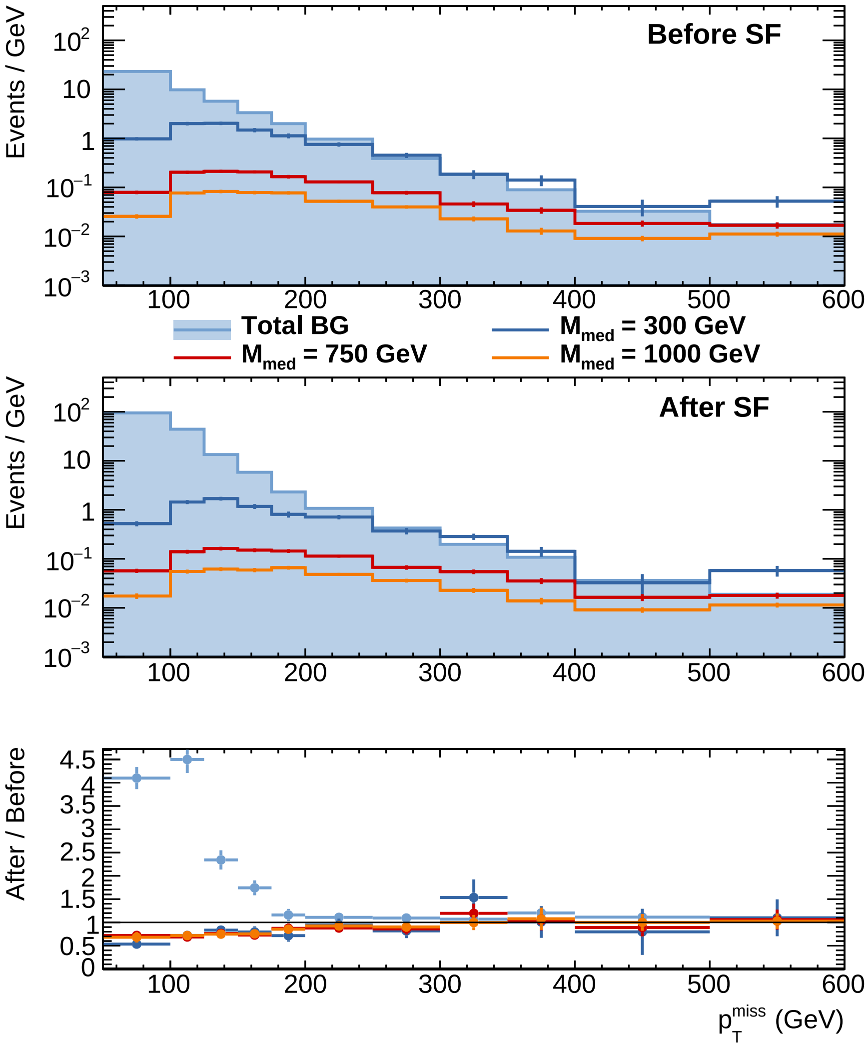

Figure 9.8.: Distribution of $p_{\mathrm{T}}^{miss}$ in the signal region before applying the scale factor (top panel), after applying the scale factor (middle panel) and the ratio of the two (bottom panel). Note that the signal region requires $p_{\mathrm{T}}^{miss} > 200$ GeV, and the $50 < p_{\mathrm{T}}^{miss} < 200$ GeV bin is used to derive a normalization factor for the DY process. Graphs are shown for the full summed-up background (solid grey/blue), as well as three signal hypotheses. Note that bin contents have been divided by the bin width. All histograms are normalized to an integrated luminosity of 36 fb$^{-1}$.

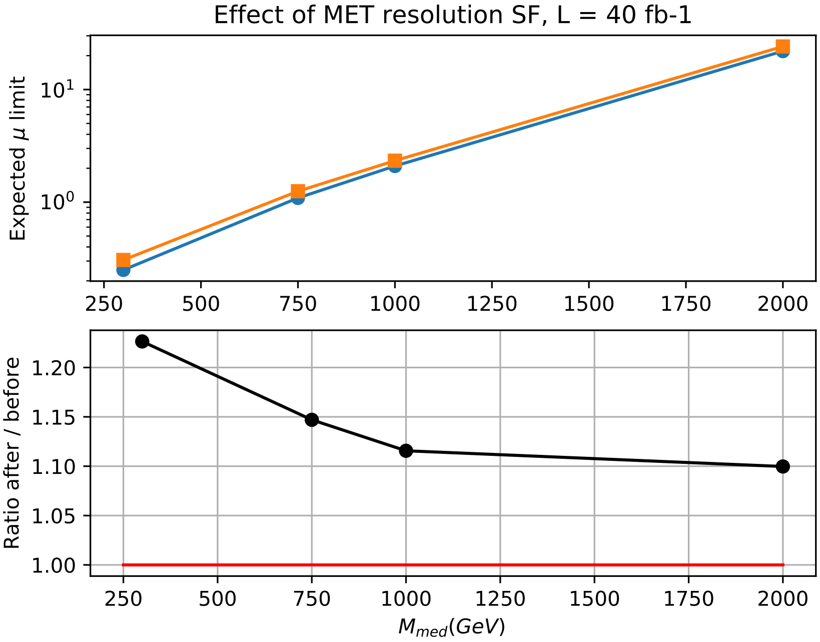

Figure 9.9.: Expected limits on the signal strength $\mu$ as a function of the mediator mass $M_{med}$ with and without application of the $p_{\mathrm{T}}^{miss}$ resolution scale factor SF=2 (top panel) and the ratio of the two (bottom panel).

## 9.2. Study of the effect of the center-of-mass energy

The HL-LHC is planned to operate at a center-of-mass energy of 14 TeV. In this section, a reweighting method is designed and tested that allows to mimic the effect of a change in $\sqrt{s}$ from 13 TeV to 14 TeV on the fly.

### 9.2.1. Reweighting procedure

An important feature of hadron colliders is their intrinsic scanning of the collision energy. Machines that collide elementary particles, e.g. electrons, will only ever observe collisions in which the total center-of-mass energy of the interaction is identical to that of the two-lepton system. Therefore, a fine-grained tuning of the beam energy is necessary to achieve a desired collision energy. This behavior allows for detailed study of resonances, such as the Z resonance at LEP [49], or the $\Upsilon(4S)$ at KEKB. However, the fixed energy is disadvantageous if one is interested in a range of center-of-mass energies, as a machine-based scanning method is necessary. At a composite-particle collider such as the LHC, on the other hand, the substructure of the colliding particles intrinsically results in a scan of the hard scatter energy scale without any need for outside action. In every proton-proton collision, the momentum fraction carried by the participating partons is randomly distributed according to its PDF. Different beam energies result in a shift of these underlying distributions. For values of the beam c.o.m. energy that are not too far apart, the sampled parameter space will be similar and an existing sample with a given value of $\sqrt{s}$ can be reweighted to reproduce the behavior of a target sample with a different energy $\sqrt{s'}$.

The reweighting is implemented on an event-by-event basis. For each event, the transition $\sqrt{s} \rightarrow \sqrt{s'}$ causes a shift in the Bjorken x variables, while leaving the factorization scale Q and the c.o.m. energy of the hard scattering unchanged [3].

$$\hat{s} = x_1 x_2 s = x'_1 x'_2 s' \tag{9.2}$$

The residual ambiguity in the choice of rescaling function is resolved by considering the symmetry argument: $x_1$ and $x_2$ should be changed in the same way in order to preserve the symmetry of the system and the independence of the two.

$$x_{1/2} \rightarrow x'_{1/2} = \frac{\sqrt{s}}{\sqrt{s'}} x_{1/2} \tag{9.3}$$

The new weight $w$ is then calculated as the ratio of PDF weights evaluated with the primed and unprimed Bjorken variables.

$$w = \frac{x'_1 f(x'_1, Q, f_1) \times x'_2 f(x'_2, Q, f_2)}{x_1 f(x_1, Q, f_1) \times x_2 f(x_2, Q, f_2)} \tag{9.4}$$

In this equation, $xf$ is the PDF value for a given set of input values, and $f_{1/2}$ represents the flavors of the incoming partons.

---

[3] Depending on the event generator used to produce the event sample, the scales are chosen according to different algorithms. For Pythia8, $Q = \sqrt{\hat{s}}$ is chosen, which is not generally true for other programs.

### 9.2.2. Validation

To demonstrate the effect of the reweighting and to validate the procedure, samples of ZZ → $\ell\ell\nu\nu$ events are generated for both values of $\sqrt{s}$.

The samples are generated using Madgraph5_aMC@NLO at LO in QCD without additional partons and are analyzed at parton level, i.e. without applying parton showering. Consequently $p_{\mathrm{T}}(\mathrm{Z}_1) = p_{\mathrm{T}}(\mathrm{Z}_2)$ by construction. A requirement of $p_{\mathrm{T}}(\mathrm{Z}) > 100$ GeV is applied to ensure that the phase space relevant for the analysis is represented by a sufficiently large number of simulated events. The distributions $p_{\mathrm{T}}$ (Z) for these samples, as well as a reweighted version of the 13 TeV sample, are shown in Fig. 9.10. Three aspects can be observed:

- The change in $\sqrt{s}$ leads to an overall increase in the ZZ cross section of approximately 10%.
- The ratio between the two scenarios exhibits a slope, increasing towards higher $p_{\mathrm{T}}(\mathrm{Z})$. This aspect is important to note, as it could not be captured in a more naive reweighting method, where one would simply rescale the normalization of each process to account for the overall change in cross section. The kinematic dependence can only be captured through an event-by-event reweighting as performed here.
- The reweighted 13 TeV curve reproduces the behavior of the 14 TeV curve, which is the intended result.

This test shows that the method performs as intended and can be used for the study at hand.

### 9.2.3. Application of reweighting

While it is simple to apply the event-by-event reweighting in the analysis, it is cumbersome to deal with the multitude of different choices of PDF sets in all analyzed simulation samples. To understand whether a dedicated treatment for each sample is necessary, the dependence of the resulting scale factor on the choice of PDF set is studied. For this purpose, events generated at $\sqrt{s} = 13$ TeV with the default PDF set `NNPDF23_lo_as_0130_qed` are reweighted multiple times using weights derived from different PDF sets. The resulting scale factors as a function of the Z boson transverse momentum are shown in Fig. 9.11. Compared to a reweighting using the default PDF set that was used to generate the events, alternative choices of the set used for reweighting yield difference of less than 2%. There are bins which show significantly larger variations of up to 6% in one bin each, but these can likely be attributed to statistical fluctuation. Note that it is not trivial to quote statistical uncertainty values on this ratio. In each of the reweighted histograms, the events entering a given bin are identical, but given a different weight. Therefore, the statistical uncertainty in each bin is correlated between the different curves and nearly cancels in the ratio. However, there is a second, more difficult to estimate component: The events in each bin follow a three-dimensional probability density in $\vec{X} = (x_1, x_2, Q)$ space, which – due to the limited number of simulated events – is only known to finite accuracy. The statistical uncertainties of this distribution primarily govern the statistical uncertainty of the ratio. To determine the exact contribution from this source, it would be necessary to generate random samples of

$\vec{X}$ vectors according to the underlying nominal probability density, as well as its variations within its statistical uncertainties. A propagation to the bin contents of the $p_{\mathrm{T}}^{miss}$ distribution would then yield the corresponding uncertainty on the ratio. However, for the purposes of this projection study, it is sufficient to know that the bias introduced by using an arbitrary PDF set for reweighting of a simulated sample rather than the original PDF set used in the generation of said sample is at most a few percent, which is certainly within the margin of error of any extrapolation that reaches years into the technological future. Consequently, all simulated samples are reweighted with one common PDF set and the small bias is neglected.

### 9.2.4. Effect on final discriminant

The effect of applying this reweighting technique in the analysis of fully simulated and reconstructed events is shown in Fig. 9.12. As in the closure test discussed above, the impact of the correction increases with boson $p_{\mathrm{T}}$ for both signals and background. In addition, for signals, the impact increases with $m_{med}$ as higher PDF scales are probed on average. This effect is to be compared with the inclusive signal cross section as a function of the mediator mass shown in Fig. 9.13. The cross sections have been directly calculated for both values of $\sqrt{s}$ and thus provide an independent estimate. For values of the mediator mass up to $m_{med} \approx 4$ TeV, the cross section gain due to the increases in $\sqrt{s}$ becomes more pronounced with increasing $m_{med}$. For larger values of $m_{med}$, the gain plateaus and begins to decrease again, which is a result of the PDF suppression of the on-shell mediator production. In this regime, the mediators are so heavy that DM production will predominantly occur through an off-shell mediator, creating events with $M(\chi\chi) \ll m_{med}$. Consequently, the $\sqrt{s}$-related gain approaches the values observed at lower $m_{med}$, where the mediator can still be produced on-shell.

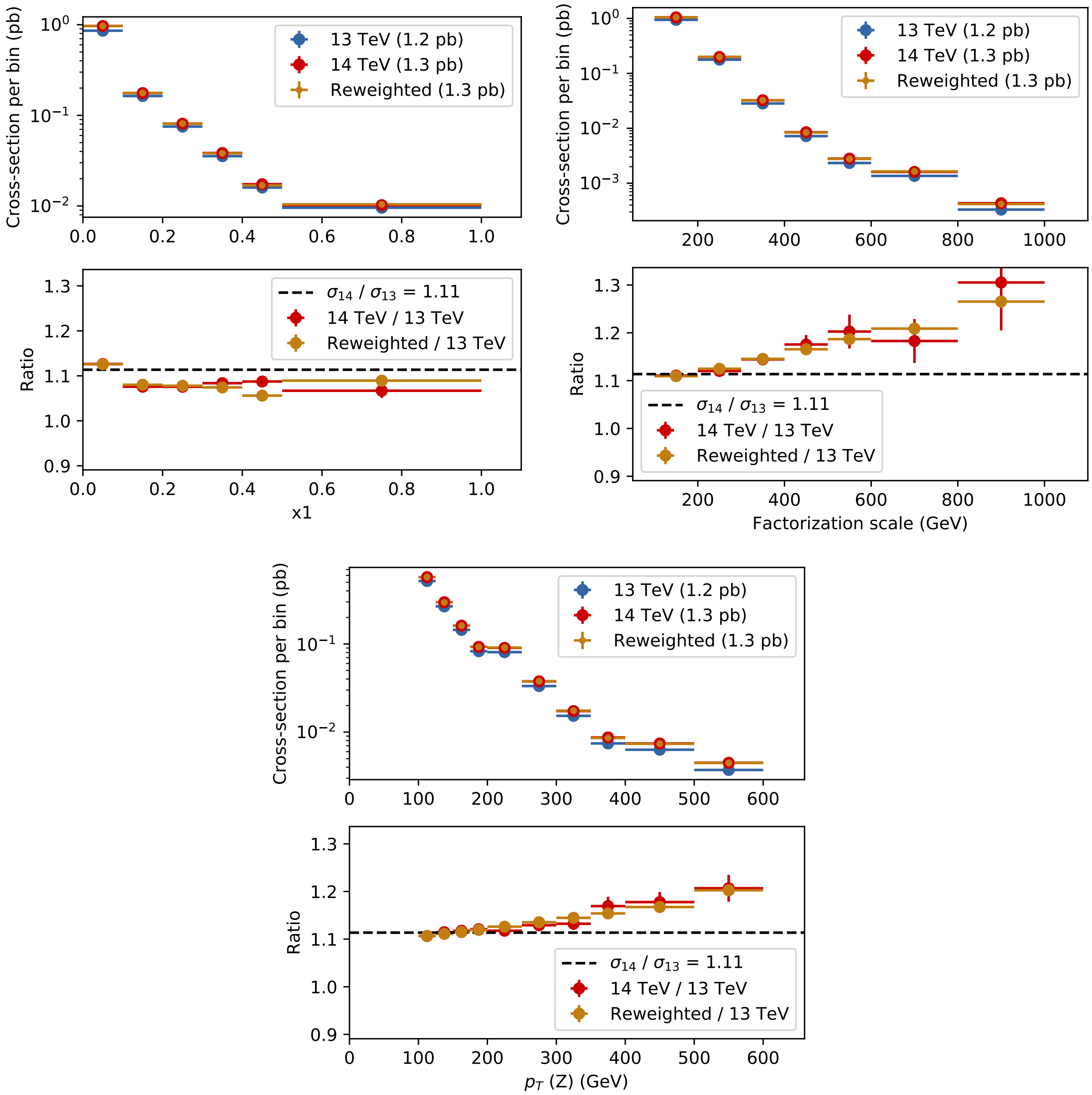

Figure 9.10.: Distributions of the Bjorken variable $x_1$ (top left), factorization scale (top right), and Z boson transverse momentum $p_{\mathrm{T}}(Z)$ (bottom) at parton level for ZZ events at $\sqrt{s} = 13$ and 14 TeV. The curves for the two values of $\sqrt{s}$ (red and blue markers) are derived from separate simulated samples. The curve labelled "reweighted" (golden markers) shows the result of applying the reweighting method described in the text to the 13 TeV sample. The black dashed line indicates the ratio of the cross sections of the 14 and 13 TeV samples.

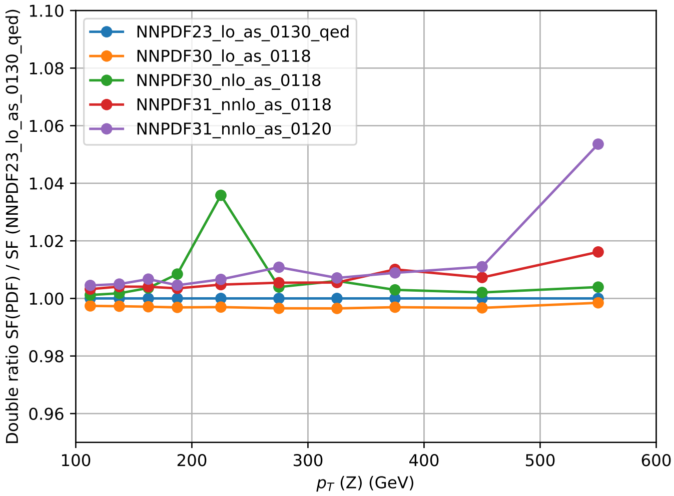

Figure 9.11.: Effect of the choice of PDF set used for reweighting on the scale factor. The y axis shows the ratio of the scale factor derived for a given PDF set divided by the scale factor derived with the `NNPDF23_lo_as_0130_qed` PDF set, i.e. a value of unity means that the PDF sets yield the same scale factor value as the reference set.

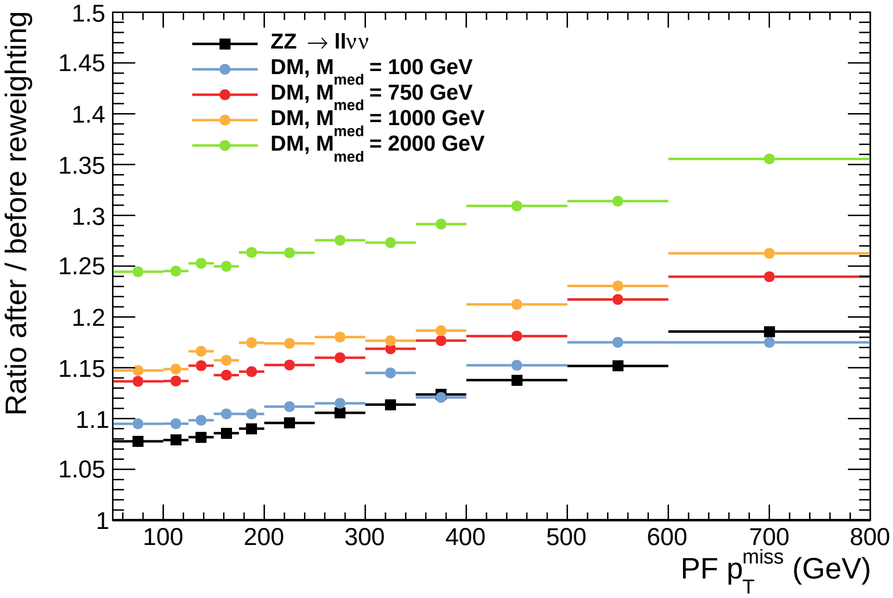

Figure 9.12.: Effect of the PDF reweighting on the reconstructed $p_T^{miss}$ distribution in the signal region. The curves are shown separately for the leading background from ZZ production, as well as signal hypotheses of light DM production with a vector mediator and different values of $m_{med}$.

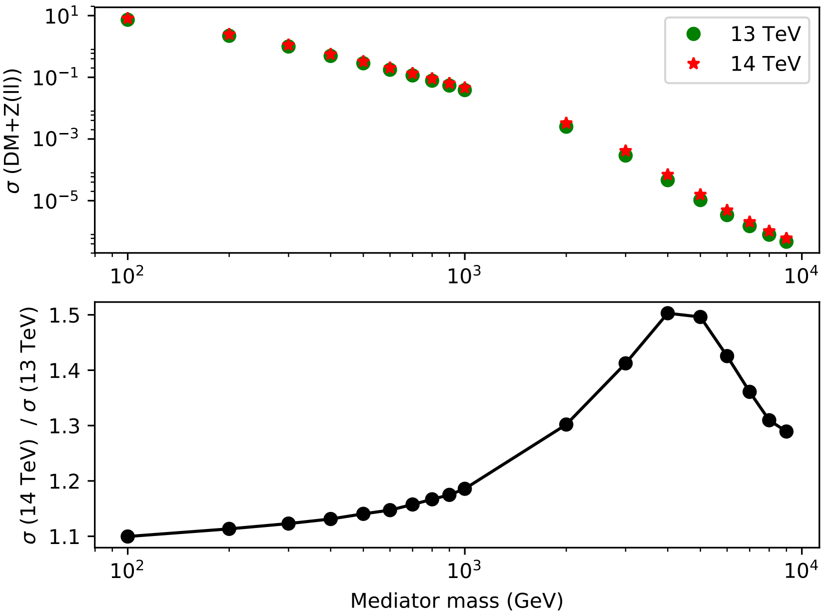

Figure 9.13.: Signal cross section as a function of $m_{med}$ for $\sqrt{s} = 13$ and 14 TeV.

## 9.3. Signal extraction

In this section, the signal extraction method is discussed. As in the Run-II analysis, a simultaneous ML fit to the (emulated) $p_{\mathrm{T}}^{miss}$ distributions in the signal and control regions is used to determine the signal contribution. The method used here differs in the parameterization model used to describe the leading background processes, which is described in sec. 9.4. Additionally, an alternative fit to the $M_T$ distribution is explored to improve the sensitivity for the a+2HDM model, which is described in sec. 9.4.1.

## 9.4. Fit model

In the Run-II analysis, a single floating parameter is used to constrain the overall of the VV backgrounds in a correlated way. At high luminosities, individual bins have large statistical power and may impose conflicting constraints on the normalization parameter, which will typically fail to correctly reproduce the behavior in the distribution tails. To combat this effect, a bin-by-bin normalization scheme is adopted. Instead of using a single floating parameter, one parameter is used per bin. The effect of each parameter is correlated among the WZ and ZZ processes in the signal region as well as the control regions, thus allowing the shape of the VV backgrounds to be determined from data rather than just the normalization. This procedure leaves the ratio between the WZ and ZZ contributions as the only quantity determined from simulation. The ratio is allowed to fluctuate within the ranges given by the theory uncertainties. This method has successfully been used in a number of analyses which encountered large event yields already in the Run-II data sets (for example cases, see Refs. [168, 189, 190]). The nuisance parameter impacts resulting from this method are shown in Fig. 9.14. The impacts are defined as the change in the best-fit signal strength when a given nuisance parameter is varied within its uncertainty. It serves as a measure of correlation between the signal strength and the value of a given nuisance. Fig. 9.14 also shows the reduction in uncertainty on the value of each nuisance parameter achieved by the ML fit. The statistical power of the expected data is sufficient to significantly constrain the nuisance parameters, but no pathological behavior is observed.

### 9.4.1. $M_T$ distribution

The analysis of the $p_{\mathrm{T}}^{miss}$ spectrum is optimal for nonresonant signals. As demonstrated in sec. 4.2, the a+2HDM signals show a Jacobian peak in the distribution of the transverse mass $M_T$. For the nonresonant processes like the leading VV backgrounds, $M_T$ and $p_{\mathrm{T}}^{miss}$ are very closely correlated after applying the signal selection. Since the $\vec{p}_{\mathrm{T}}^{miss}$ and Z momentum vectors are required to be back-to-back in the transverse plane, and have similar absolute values, the $M_T$ variable is directly related to $p_{\mathrm{T}}^{miss}$: $M_T \approx 2 \times p_{\mathrm{T}}^{miss}$. The consequence of this feature is that the distribution of $M_T$ can be used for signal extraction without having to adapt the background or systematic uncertainty estimation techniques. Fig. 9.15 shows a comparison of the $p_{\mathrm{T}}^{miss}$- and $M_T$ based expected exclusion limits obtained for the a+2HDM scenario in the $m_{\mathrm{a}}$-$m_{\mathrm{H}}$ plane. Compared to the default choice of using the $p_{\mathrm{T}}^{miss}$ distribution in the binning described in the previous section, an improvement of the sensitivity is observed when switching to the $M_T$ distribution. Two binning variants for the $M_T$ distribution are tested: In the first, labeled “400-1000 GeV”, the bin edges from the $p_{\mathrm{T}}^{miss}$ distribution are

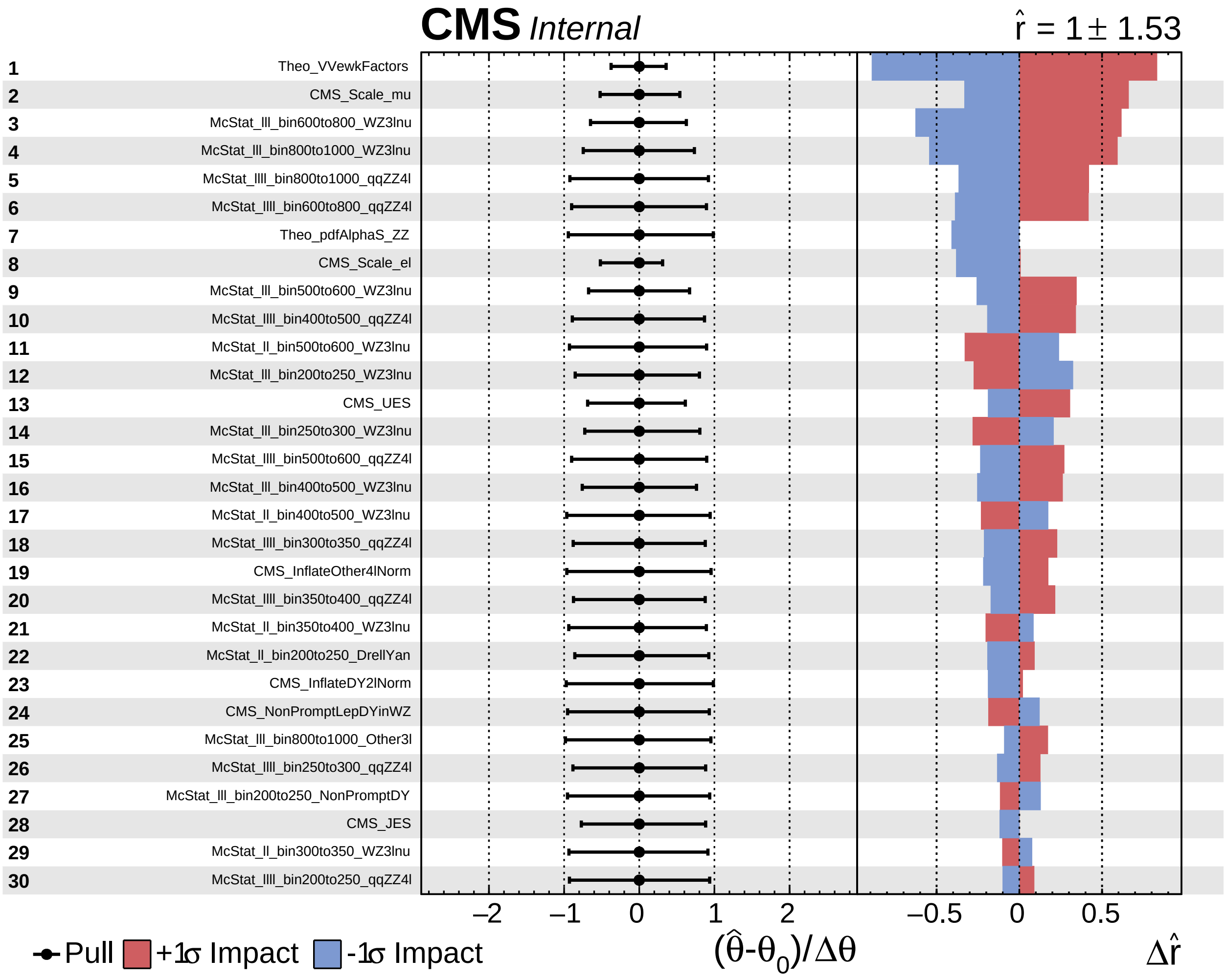

Figure 9.14.: Nuisance parameter impacts for $m_{med} = 2$ TeV and $\mathcal{L}_{\text{int}} = 3\ \text{ab}^{-1}$ and unity signal strength. Each line corresponds to one nuisance parameter. In the middle column, the best fit nuisance parameter values and their uncertainties are shown. Since no real data is involved, all parameters are fit to their prefit central values of zero, albeit with reduced uncertainty (an error bar ranging from -1 to +1 would indicate a postfit uncertainty of the same size as the prefit uncertainty). In the rightmost column, the effect on the best-fit signal strength of a change in the given nuisance parameter by its uncertainty is shown. The nuisance parameters are named as follows: `Theo_VVewkFactors` is uncertainty on the VV contributions related to higher-order EWK corrections, `CMS_scale_*` corresponds to the energy scale of a given object, `McStat_*` refers to the MC sample size uncertainty for a given bin, and `Theo_pdfAlphaS_ZZ` represents the PDF uncertainty of the ZZ process.

simply multiplied by a factor of two. Using this choice, the maximal reach is increased by 25 GeV in $m_{\mathrm{a}}$ and 35 GeV in $m_{\mathrm{H}}$. However, there is almost no improvement at the low-$m_{\mathrm{H}}$ edge, close to the kinematic border. Here, the low-$p_{\mathrm{T}}^{miss}$ and consequently low-$M_T$ region is relevant. Therefore, the second shown binning choice adds two equal size bins between $M_T = 200$ and 400 GeV. This addition leads to a reach increase of a further 4 GeV in $m_{\mathrm{a}}$ and 10 GeV in $m_{\mathrm{H}}$, but most importantly helps to establish sensitivity closer to the kinematic border.

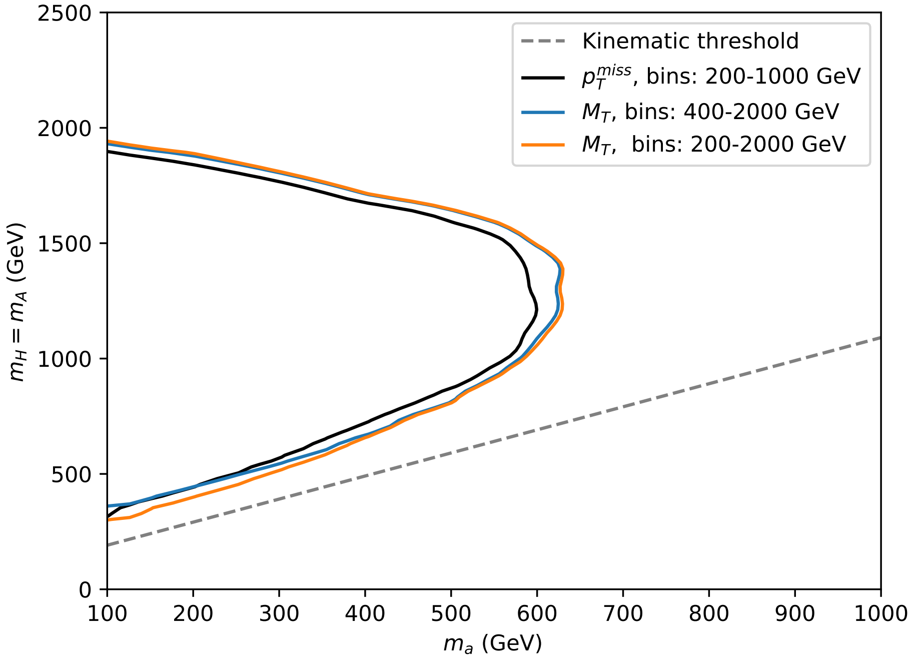

Figure 9.15.: Comparison of the expected exclusion limits in the a+2HDM when using either the $p_{\mathrm{T}}^{miss}$ distribution (solid black line) or $M_T$ distribution (solid colored lines) for signal extraction. The lines relying on $M_T$ use a different binning: The result shown in blue is obtained using the bin edges from the $p_{\mathrm{T}}^{miss}$ distribution multiplied by two, while for the result shown in orange, two additional low-$M_T$ bins are added with edges 200, 300, 400 GeV.

## 9.5. Systematic uncertainties

In addition to the vast improvements planned for the LHC luminosity performance, an important aspect of projections for future performance is the question of systematic uncertainties. Naturally, the two are intertwined, with many experimental uncertainties depending on the number of PU interactions in each event and thereby also the instantaneous luminosity. In addition to this experimental perspective, the continuous development of theoretical techniques must be taken into account. Many of the external inputs used for data analysis such as cross section calculations, MC event generators, and PDF predictions, have undergone rapid increases in precision over the last 20 years, and further improvements are likely to occur over the running period of the HL-LHC.

To better understand the effect of systematic uncertainties on the sensitivity of this analysis, all projection results are derived for three separate uncertainty scenarios that are designed to represent the likely range of possible improvements. The scenarios follow the definitions agreed upon between the CMS and ATLAS collaborations in the preparation of the YR [182]:

- **Run 2 syst. uncert.**: The relative systematic uncertainties are estimated to be of the same size as the Run-II analysis (cf. sec. 8.1). This scenario does not consider any possible future improvements or deteriorations to the systematic uncertainties.

- **YR18 syst. uncert.**: The effect of expected future improvements in the control of systematic uncertainties is included according to the conventions of the 2018 CERN yellow report (YR18) [182]. Theoretical and experimental uncertainties are reduced by 50%, and the statistical uncertainties due to the finite size of the simulation samples are neglected. This scenario is the current best estimate of what can be achieved at the HL-LHC.

- **Stat. uncert. only**: Only the expected statistical fluctuations of the data are considered. This scenario demonstrates the maximal reach of the analysis strategy if systematic uncertainties are negligible.

The effects of removing each of the different uncertainty components separately is shown in Fig. 9.16. While the theory uncertainties have a dominant effect at $\mathcal{L}_{\text{int}} \approx 300~\text{fb}^{-1}$, the most significant component at 3 $\text{ab}^{-1}$ are the statistical uncertainties related to the finite size of simulated samples. This is a result of the different correlation schemes: the theory uncertainties are correlated between bins and are thus more easily constrained in the case of large event numbers. The sample size uncertainties are not correlated between bins and are therefore less easily constrained at large $\mathcal{L}_{\text{int}}$. The difference in the fully defined uncertainty scenarios (Run-II, YR18, and stat. uncert. only) are shown in Fig. 9.17. The stat. uncert. only scenario improves on the Run-II scenario by between 20% and 40% at $\mathcal{L}_{\text{int}} = 300\text{fb}^{-1}$, and between 40% and 60% at $\mathcal{L}_{\text{int}} = 3\text{ab}^{-1}$. The YR18 scenario is close to half way between the two extreme scenarios.

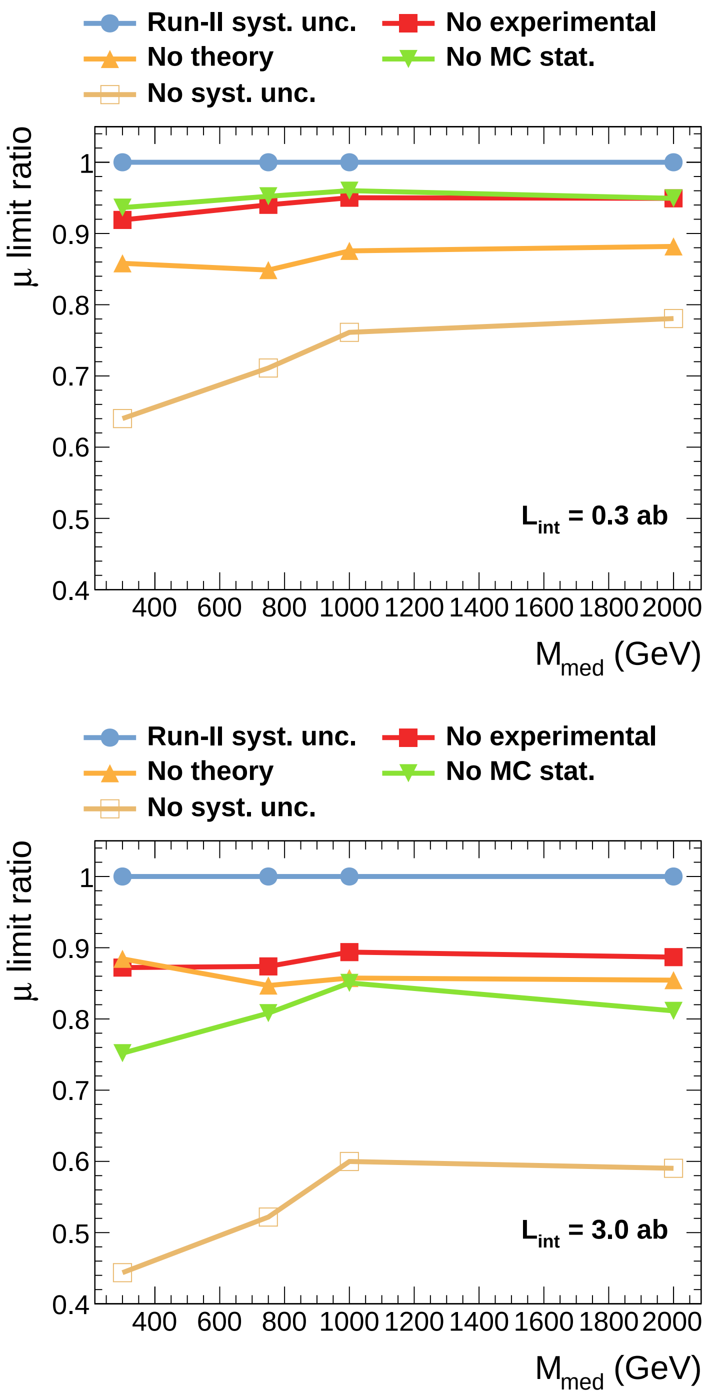

Figure 9.16.: The change in expected signal strength limits as a function of $m_{med}$ for different scenarios of systematic uncertainties for $\mathcal{L}_{\text{int}} = 300\ \text{fb}^{-1}$ (upper panel) and $\mathcal{L}_{\text{int}} = 3\ \text{ab}^{-1}$ (lower panel). A y-value of 1 means "no change compared to Run-II systematic uncertainties", 0.75 means "the expected limit improved by 25% relative to Run-II uncertainties", etc. Scenarios at a constant integrated luminosity are compared, with no changes due to increased luminosity being taken into account. The sensitivity increase from 0.3 to 3.0 $\text{ab}^{-1}$ corresponds to an approximate factor of 2.5 in the signal strength, i.e. the blue line in the bottom panel corresponds to a signal strength 2.5 times smaller than the blue line in the top panel.

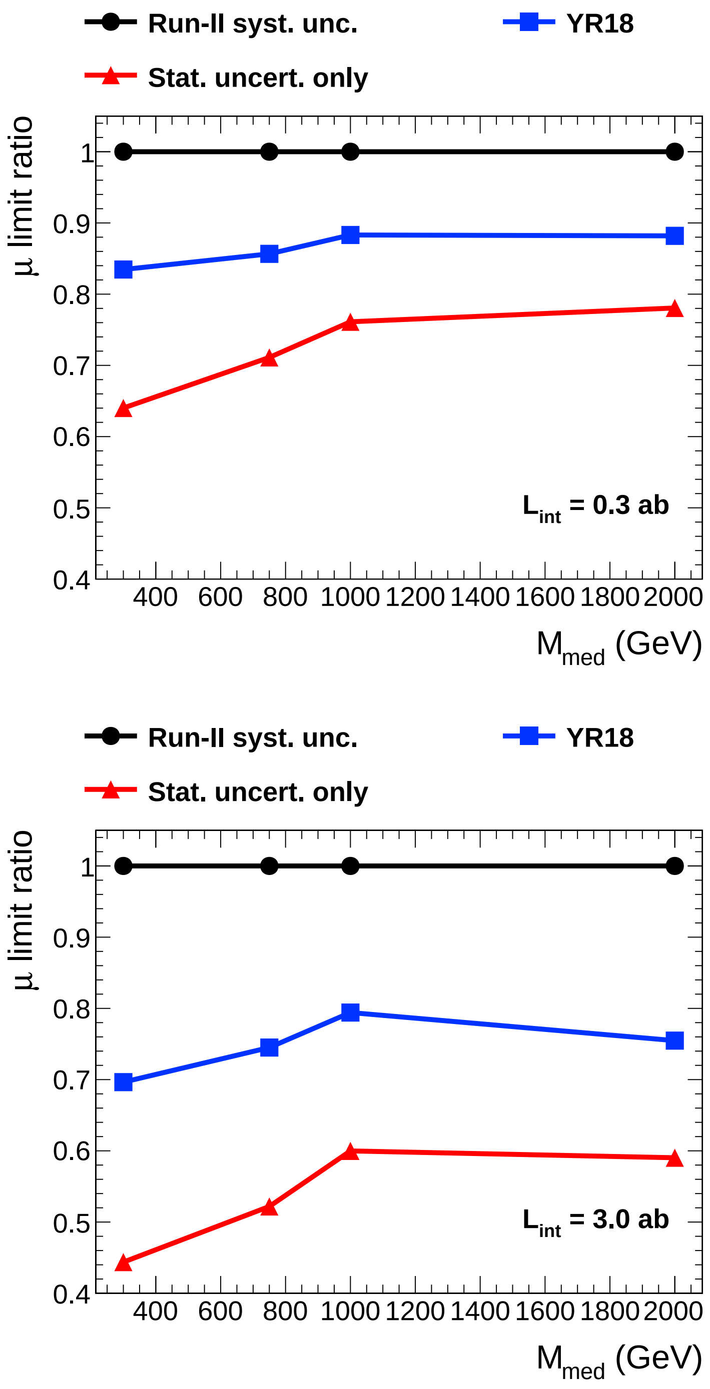

Figure 9.17.: Same as Fig. 9.16, but now showing the three scenarios defined in the text, rather than individual uncertainty components.

## 9.6. Results

The expected distribution of $p_{\mathrm{T}}^{miss}$ in the signal region is shown in Fig. 9.18.

Signal significances and exclusion limits are calculated with the asymptotic approximation of the CLs method [149, 151, 152, 191]. The significance is calculated as the quantile of a two-sided Gaussian distribution corresponding to the probability that an observed excess caused by a signal of unit signal strength could be the result of a statistical fluctuation of the standard model backgrounds. It is given in units of the standard deviation of the Gaussian distribution.

The discovery significance and 95% CL signal strength exclusion limits for a signal in the vector mediated simplified model are shown in Fig. 9.19. The sensitivity to a signal in this scenario does not depend strongly on the value of the DM candidate mass $m_{DM}$ as long as $m_{med} < m_{med}/2$ and the results are thus shown for the representative case $m_{DM} = 1$ GeV. At the lowest considered integrated luminosity $\mathcal{L}_{\mathrm{int}} = 300\ \mathrm{fb}^{-1}$, the search is statistically limited, and the result shows only a limited dependence on the choice of the systematic uncertainty scenario. Depending on the choice of mediator mass, the signal overlaps with different regions of the standard model $p_{\mathrm{T}}^{miss}$ background spectrum. Accordingly, the effect of systematic uncertainties is largest for lower values of the mediator masses ($\approx 300$ GeV), where there is significant overlap of the signal and background distributions. With increasing mediator mass, the effect subsides, as the signal moves towards the tails of the background $p_{\mathrm{T}}^{miss}$ distribution. Depending on the mass of the mediator, different values of $\mathcal{L}_{\mathrm{int}}$ are required to achieve a discovery. For the intermediate masses between 750 and 1000 GeV, a signal could have been small enough in Run-II not to be detected, while still achieving discovery sensitivity over the run time of the HL-LHC. The case of $m_{med} = 1$ TeV highlights the need for improved systematic uncertainties: Depending on the assumed scenario for systematic uncertainties, the signal may either already be discovered with an integrated luminosity of 1 $\mathrm{ab}^{-1}$, or it may remain below the discovery threshold even with 3 $\mathrm{ab}^{-1}$. In addition to the discovery sensitivity, Fig. 9.20 shows the expected limits on the couplings in the vector-mediated DM scenario. The general dependence on luminosity and systematic uncertainty scenarios is similar to the case of the discovery significance. For the case of the quark coupling $g_q$, values of approximately $0.04 - 0.10$ will be testable at the end of the HL-LHC run. For the DM coupling $g_{DM}$, values between 0.15 and 0.45 will be accessible, depending on the mediator mass. The difference in exclusion reach in the two couplings is due to their different effects on the product of signal cross section and branching fraction: While a reduction of $g_q$ decreases the mediator production cross section, it increases the branching fraction of the mediator to DM particles and thus partly counteracts the first effect. In the case of the DM coupling, there is no effect compensating the reduction it induces in the branching fraction of the mediator to DM particles.

The exclusion in the two-dimensional $m_{med}$-$m_{DM}$ plane for $\mathcal{L}_{\mathrm{int}} = 3\ \mathrm{ab}^{-1}$ is shown in Fig. 9.21. Assuming the YR18 systematic uncertainty scenario, mediator masses up to approximately 1.5 TeV can be probed, which is an improvement over the Run-II result by a factor of approximately 2.3. In the “stat. only” and “Run-II syst. unc.” scenarios, the exclusion is improved, respectively weakened, by slightly more than 100 GeV.

For the a+2HDM model, results are presented in terms of the two-dimensional exclusion reach with $\mathcal{L}_{\mathrm{int}} = 3\ \mathrm{ab}^{-1}$ in the plane of $m_{\mathrm{a}}$ and $m_{\mathrm{H}} = m_{\mathrm{A}}$, which is shown in Fig. 9.22. The results are derived using both the $M_T$ and $p_{\mathrm{T}}^{miss}$ distributions, with the $M_T$ based result being slightly more sensitive, as discussed in sec. 9.4.1. Note that for the parameter space covered in this analysis, the width of the heavy scalar H ranges between 5% of $m_{\mathrm{H}}$ at $m_{\mathrm{H}} = 500$ GeV and 30% of $m_{\mathrm{H}}$ at $m_{\mathrm{H}} = 2$ TeV. Due to the large relative width at large $m_{\mathrm{H}}$, the H boson is dominantly produced off-shell with a mass much lower than the $m_{\mathrm{H}}$ parameter. This ensures that even at high values of $m_{\mathrm{H}}$, the Z boson is not overly boosted and the leptons from its decay are well separated, which avoids any need for a dedicated treatment of overlapping leptons.

In the YR18 scenario, the light pseudoscalar can be probed up to masses of approximately 630 GeV, with the maximum reach being achieved around $m_{\mathrm{H}} = m_{\mathrm{A}} = 1.3$ TeV. Again, the range of outcomes defined by the “stat. only” and “Run-II syst. unc.” scenarios spans $100 - 150$ GeV in the pseudoscalar mass. The maximal exclusion reach in the mass of the heavy bosons is approximately 1.94 TeV for low values of $m_{\mathrm{a}} \approx 100$ GeV with a corresponding range of $100 - 200$ GeV for the different uncertainty scenarios. The mass reach is improved by at least a factor of two with respect to the result obtained from the analysis of the 2016 data set. Close to the kinematic boundary, the sensitivity is reduced in the HL-LHC case due to the increased backgrounds at low $p_{\mathrm{T}}^{miss}$. However, the loss in sensitivity at low masses can almost entirely be recovered by the use of $M_T$ for signal extraction.

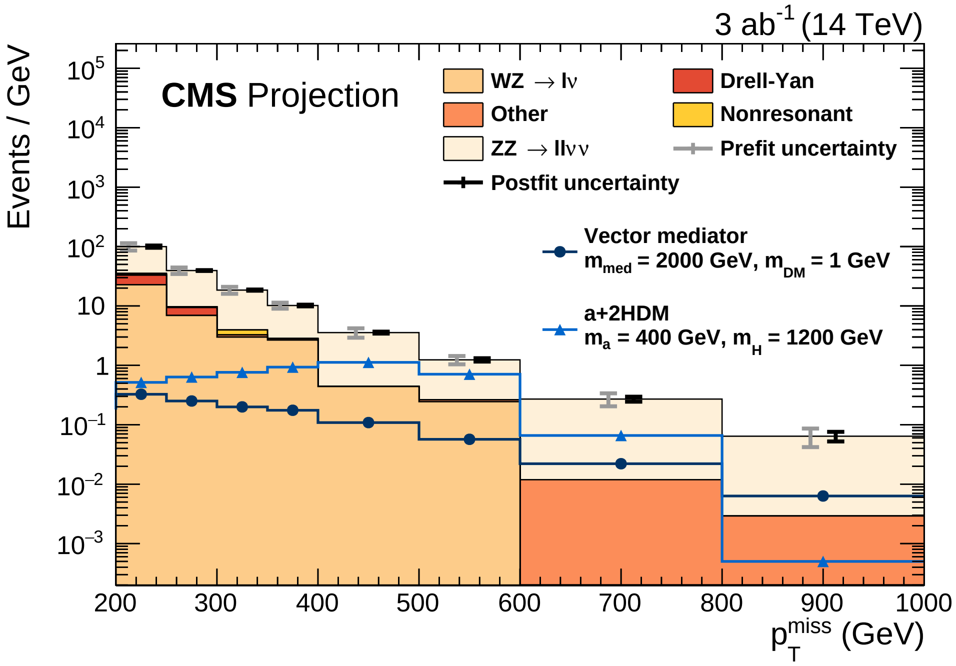

Figure 9.18.: Expected spectrum of $p_{\mathrm{T}}^{miss}$ in the signal region. The summed background spectrum is overlaid with the spectra for two signal hypotheses. The uncertainty bands for the background prediction correspond to the YR18 uncertainty scenario described in the text and are shown both before and after applying a background-only maximum-likelihood fit in signal and control regions (“prefit” and “postfit”, respectively). The fit is performed assuming that the observed data exactly agree with the prediction.

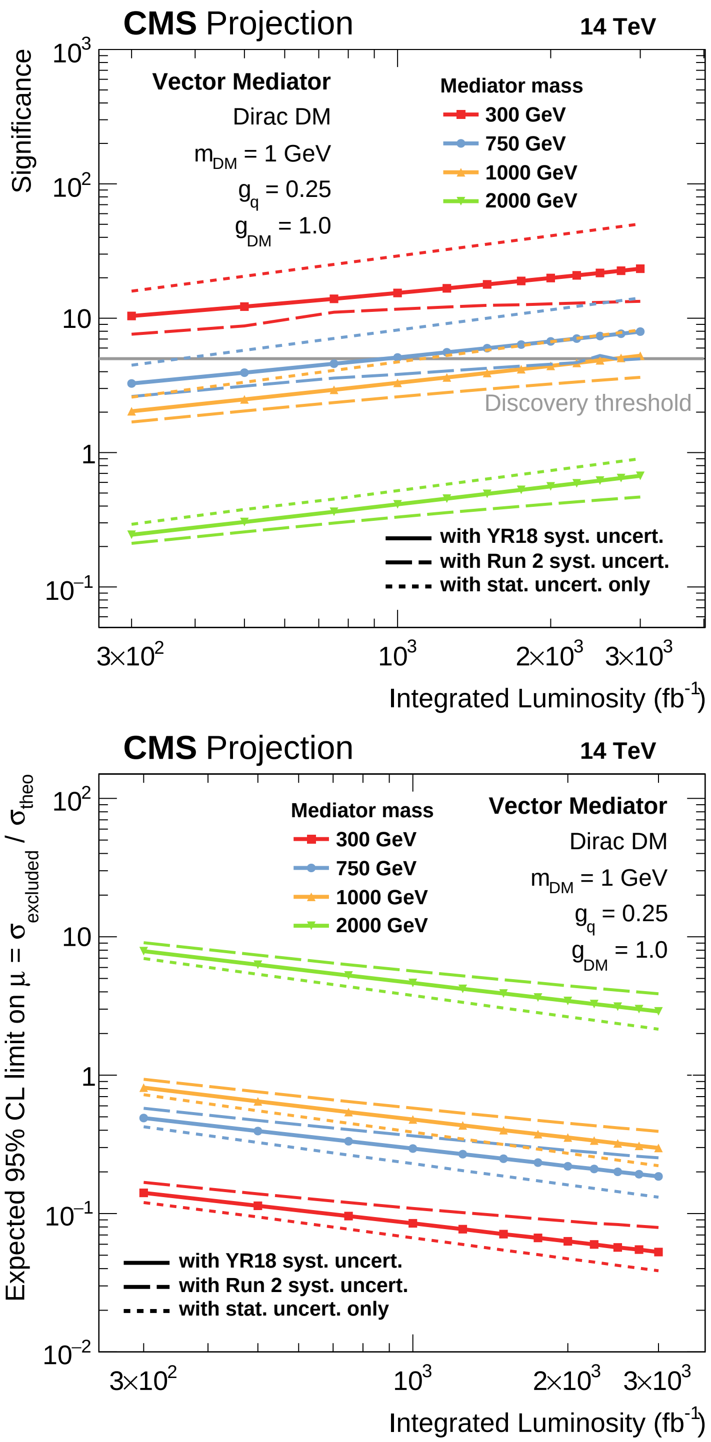

Figure 9.19.: Expected discovery significance (left) and signal strength exclusion limits (right) for the vector-mediated DM signal as a function of $\mathcal{L}_{\text{int}}$ and for different values of the mediator mass. The results are shown for the three systematic uncertainty scenarios described in the text, with the scenario labeled as “Run 2” corresponding to the systematic uncertainties estimates used in the analysis of the 2016 data set. The significance is calculated for unity signal strength, and the line marked “discovery threshold” indicates the “$5\sigma$” significance.

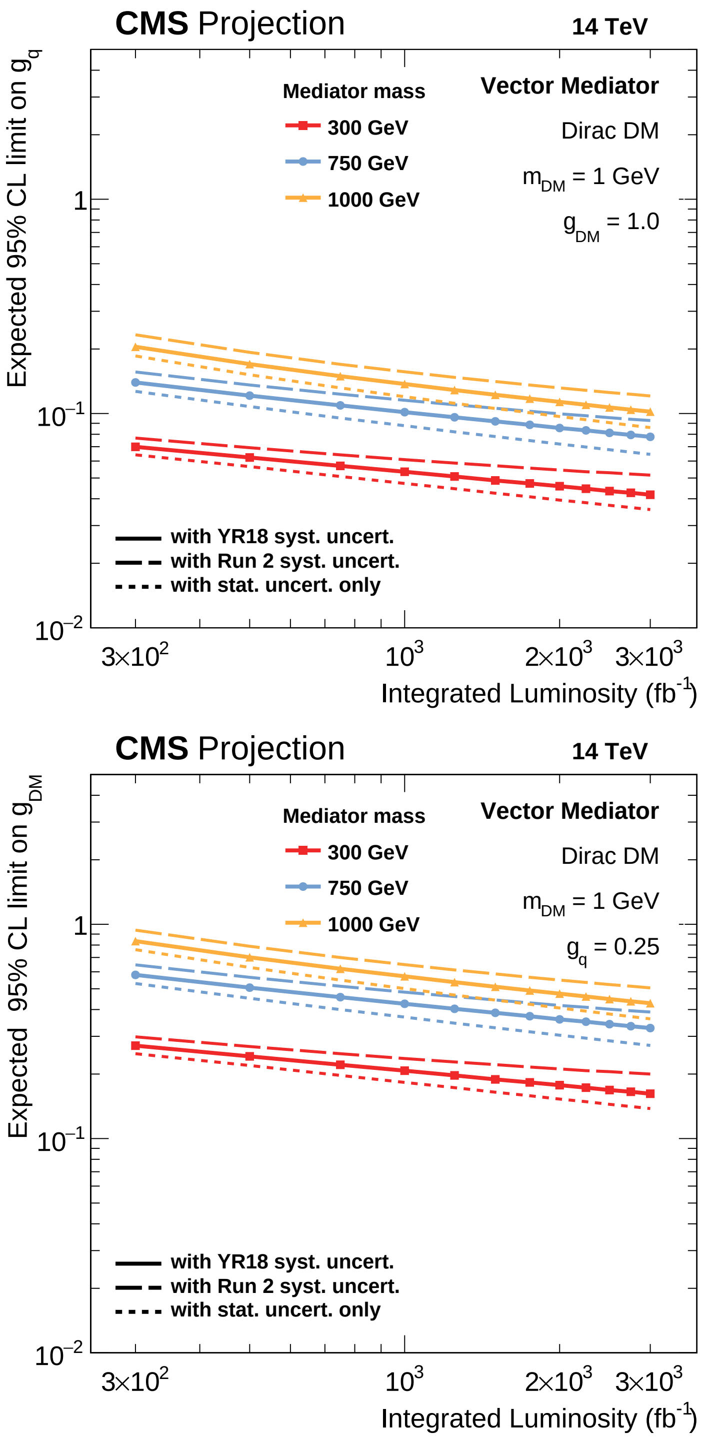

Figure 9.20.: Exclusion sensitivity for the couplings $g_q$ (left) and $g_{DM}$ (right) in the vector-mediated DM scenario as a function of $\mathcal{L}_{\text{int}}$ and for different values of the mediator mass. The results are shown for the three systematic uncertainty scenarios described in the text, with the scenario labeled as “Run 2” corresponding to to sec. 8. Note that no limit can be set if the sensitivity for a given point is too low. For increasing values of $g_q$ and $g_{DM}$, the product of cross section and branching fraction eventually reaches a plateau and does not increase further with an increase in one of the couplings. Due to this effect, no coupling limits can be set for $m_{med} = 2$ TeV.

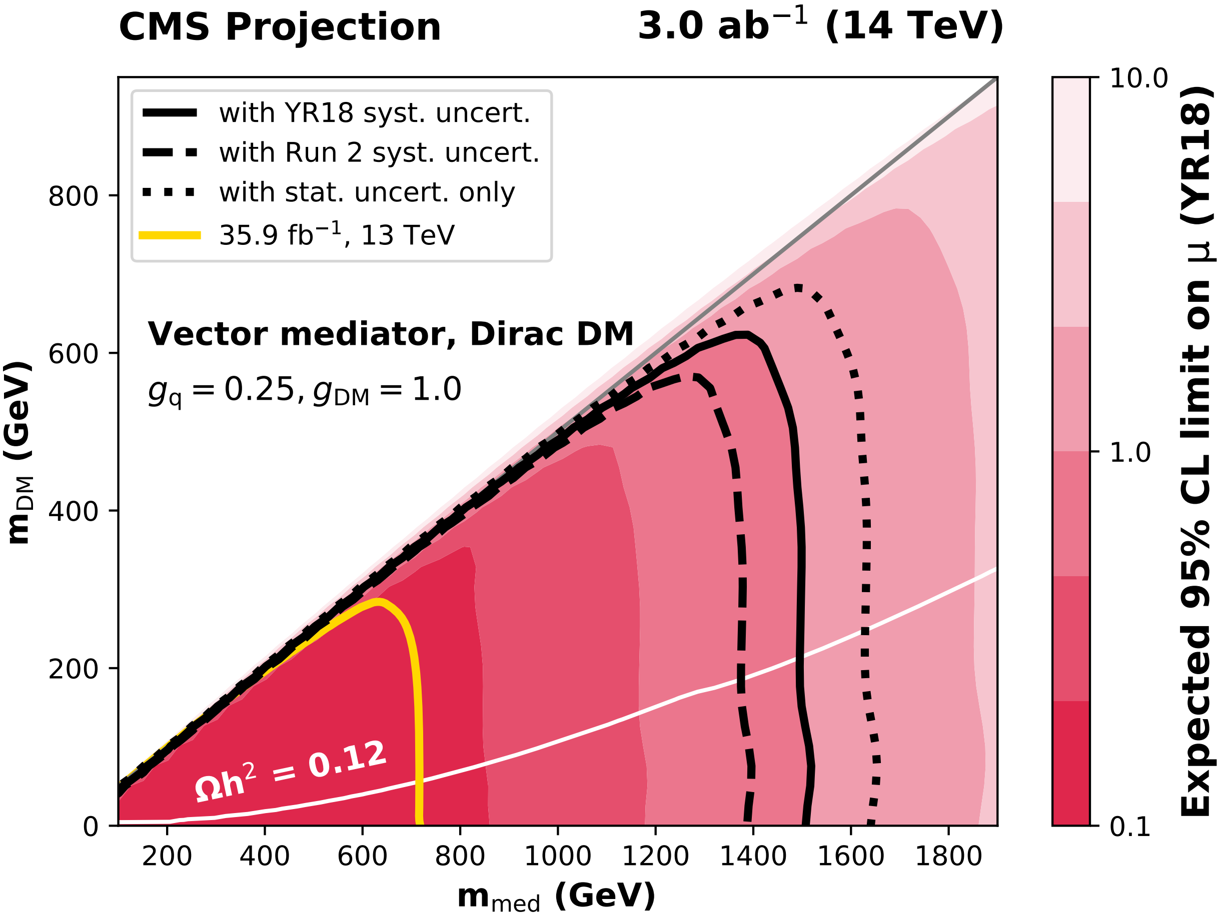

Figure 9.21.: Expected 95% CL exclusion limits on the signal strength of vector-mediated DM production in the plane of mediator and dark matter masses, assuming that no signal is found at the HL-LHC. The results are shown for the three systematic uncertainty scenarios described in the text, with the scenario labeled as “Run 2” corresponding to the systematic uncertainties estimates used in the analysis of the 2016 data set. The result of the analysis of the 2016 data set is shown as a yellow solid line. The $m_{med} = 2 \times m_{DM}$ diagonal, which is the kinematic boundary for decay of an on-shell mediator to DM particles, is indicated as a grey line. The white line indicates parameter combinations for which the observed DM relic density in the universe can be reproduced [70]. Points below (above) this line have relic densities that are larger (smaller) than the observed value of $\Omega h^2 = 0.12$ [10].

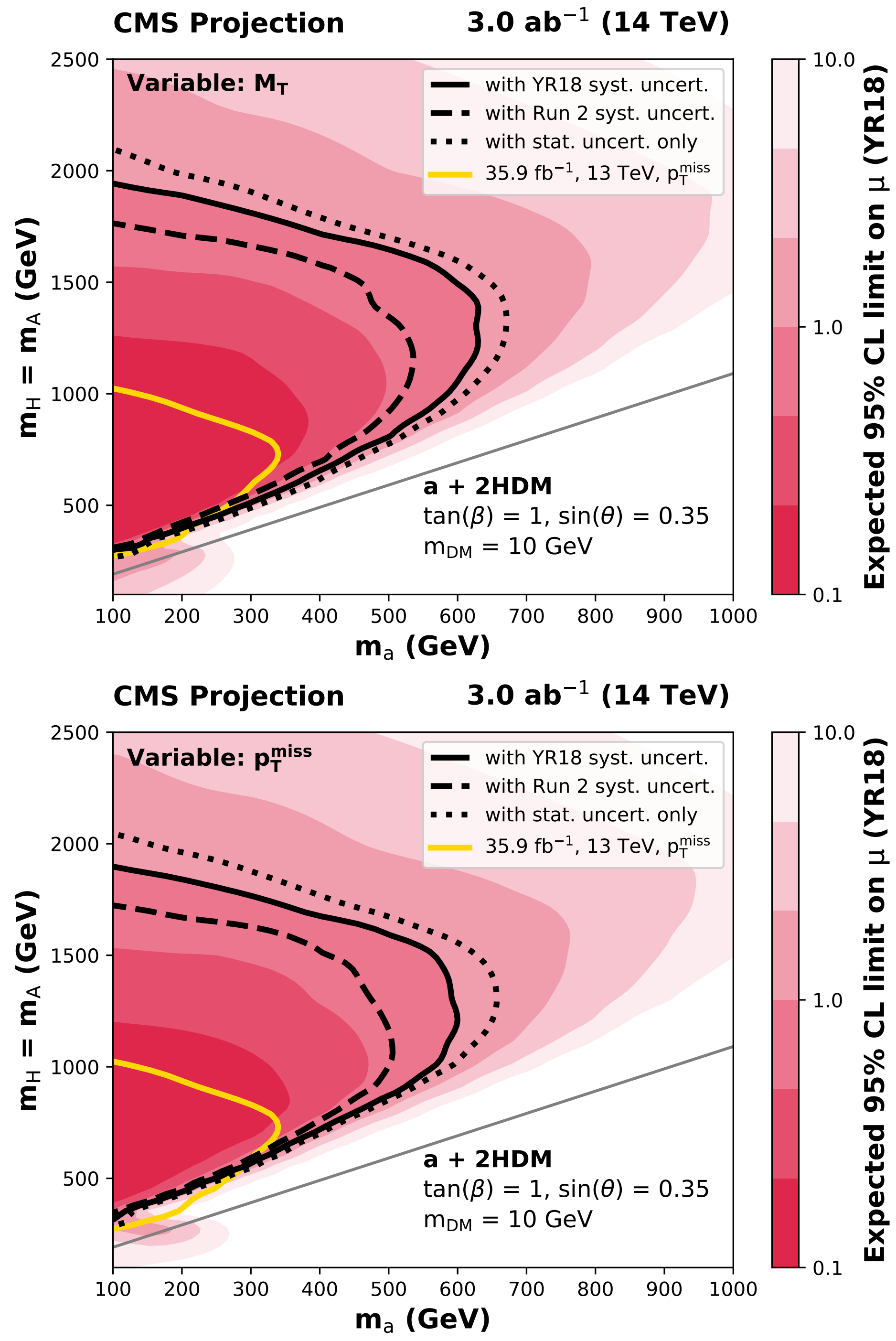

Figure 9.22.: Expected 95% CL exclusion limits on the signal strength in the a+2HDM scenario as a function of the mass of the main DM mediator a and the masses of the H and A bosons $m_{\mathrm{H}} = m_{\mathrm{A}}$, assuming that no signal is found at the HL-LHC. In the top (bottom) panel, the $M_T$ ($p_{\mathrm{T}}^{miss}$) variable is used for signal extraction. For each variable, the results are shown for the three systematic uncertainty scenarios described in the text, with the scenario labeled as “Run 2” corresponding to the systematic uncertainties estimates used in the analysis of the 2016 data set. The result of the analysis of the 2016 data set is shown as a yellow solid line. The grey line indicates the kinematic boundary $m_{\mathrm{H}} = m_{\mathrm{a}} + m_{\mathrm{Z}}$, below which the H → aZ decay is prohibited for an on-shell H and the sensitivity of this search is limited.

# 10. Summary

A search for new invisible particles produced in proton-proton collisions has been presented. By considering collision events with a Z boson and missing transverse momentum $p_{\mathrm{T}}^{miss}$ ("mono-Z" topology), it is possible to detect the production of new particles, even if the particles are not directly reconstructable. Z boson decays to pairs of electrons and muons are selected, and event selection is further based on topological requirements on the reconstructed Z boson candidate, as well as the missing transverse momentum vector. Leading background contributions are incurred from the irreducible ZZ and WZ processes, as well as reducible contributions from WW, $\mathrm{t}\bar{\mathrm{t}}$, and Drell-Yan processes. For smaller $p_{\mathrm{T}}^{miss}$ ($\lessapprox 80 - 100$ GeV), the analysis sensitivity is limited by large backgrounds from Drell-Yan production with $p_{\mathrm{T}}^{miss}$ originating from mismeasurement effects. The leading uncertainty in the determination of the standard model backgrounds originates from missing higher-order corrections to the shape of the $p_{\mathrm{T}}^{miss}$ spectrum in diboson events. The analysis method is applied to the early Run-II data sets recorded by the CMS collaboration at the LHC in 2015 and 2016. These two data sets correspond to 2.3 $\mathrm{fb}^{-1}$ and 35.9 $\mathrm{fb}^{-1}$ of proton-proton collisions at $\sqrt{s} = 13$ TeV, and their analyses reveal no evidence for new physics, and exclusion limits were formulated in a number of scenarios of new physics.

As a major improvement over dark matter (DM) constraints derived from LHC Run-I data, DM results are derived in terms of simplified models, which are more theoretically robust. In models of DM production with spin-1 mediators, mediator masses of up to 700 GeV, and DM masses of up to 280 GeV are excluded at 95% confidence level (CL). In models with spin-0 mediators and no additional new bosons, minimal signal strengths values $\mu \approx 2$ can be tested. It is found that frequently neglected modeling choices, such as the treatment of parton radiation, can have significant effects (up to 35%) on the final exclusion cross section sensitivity. In these *standard candle* simplified models, the sensitivity of a mono-Z search is limited by the initial state radiation based production of the Z boson. New ground is broken by interpreting the analysis results also in a simplified model of DM production with a second Higgs doublet and a pseudoscalar mediator. In this model, the production of the Z boson is an intrinsic part of the DM signature, and the mono-Z topology is therefore among the most sensitive signatures. In this model, the masses of the pseudoscalar mediator and heavy intermediate scalar can be excluded up to 340 GeV, and 1.01 TeV, respectively. This result provides competitive sensitivity and excludes these parameter ranges for the first time.

In addition to constraints on DM production, the results are also interpreted in terms of unparticle production. Before this work, the mono-Z signature was considered to be the most sensitive search channel for the production of unparticles. As discovered during the preparation of this thesis, this view was ultimately the result of a programming error and has been corrected in the literature. Even after this correction, the unparticle results derived here are the most stringent published to date for values of the unparticle scaling dimension of $d_U < 1.5$, as well as for $d_U > 1.9$.

The production of gravitons in association with a Z boson is considered in a scenario of large extra dimensions. The graviton would contribute to the missing momentum signature because it is not bound to the $3+1$-dimensional brane, and would likely escape into the additional dimensions after production, if such dimensions exist. The results in this scenario are formulated as 95% CL exclusion limits on the reduced Planck scale $M_D$ as a function of the number of extra dimensions $n$. The scenario is excluded for values of the reduced Planck scale between 2.3 ($n=2$) and 2.5 ($n=7$).

Finally, the sensitivity of the prompt analysis strategy to the production of unstable dark sector particles is explored. A signal model is considered in which a pair of prompt neutral particles $\chi_2$ is produced through a vector mediator, and each $\chi_2$ subsequently decays into the invisible DM candidate $\chi_1$ and a pair of displaced photons or jets. For $m_{med} = 500$ GeV and $m_{\chi_2} = 150$ GeV, scenarios with $\chi_2$ lifetimes $c\tau$ larger than 7.5 m are excluded for $m_{\chi_1} \ll m_{\chi_2}$. For smaller $\chi_2$-$\chi_1$ mass splittings, the sensitivity improves, and life times larger than 5 m ($m_{\chi_1} = 50$ GeV) and 2.5 m ($m_{\chi_1} = 130$ GeV) are excluded. In the case of a very small mass splitting of $m_{\chi_2} - m_{\chi_1} = 5$ GeV, the signal is excluded independently of the choice of $\chi_2$ lifetime. These results show that a significant portion of parameter space in models with displaced decays is already probed by prompt searches such as this one. For shorter lifetimes up to a few meters, these results motivate dedicated searches optimized for the detection of displaced objects.

The last part of this thesis is dedicated to the study of future prospects of the mono-Z search. Over the next two decades, the LHC is planned to be upgraded to run at significantly higher instantaneous luminosity, as well as an increased center-of-mass energy of $\sqrt{s} = 14$ TeV (high-luminosity LHC or HL-LHC). At the end of this running period, the LHC is expected to have delivered a data set corresponding to 3 ab$^{-1}$ of proton-proton collisions. The operation of a general-purpose experiment such as CMS will be a technological challenge in the environment of the HL-LHC, which will produce unprecedented numbers of simultaneous particle interactions per bunch crossing (pile-up or PU). A recurring worry is the performance of the reconstruction of missing transverse momentum, which relies on all signatures in all sub-detectors, and is vulnerable to contamination from PU contributions. The sensitivity of a mono-Z search under HL-LHC conditions is studied in detail. It is found that the sensitivity for the detection of the signatures discussed in this thesis is robust against a possible degradation of the $p_{\mathrm{T}}^{miss}$ resolution. Even in a pessimistic scenario, where the $p_{\mathrm{T}}^{miss}$ resolution is assumed to worsen by a factor of two, the mass reach of present-day results could be enhanced by an approximate factor of two by the end of the HL-LHC running period.

# Bibliography

[1] IceCube Collaboration, "Observation of High-Energy Astrophysical Neutrinos in Three Years of IceCube Data", *Phys. Rev. Lett.* **113** (2014) 101101, `arXiv:1405.5303`. `doi:10.1103/PhysRevLett.113.101101`. Cited on page 1.

[2] Super-Kamiokande Collaboration, "A Measurement of atmospheric neutrino oscillation parameters by SUPER-KAMIOKANDE I", *Phys. Rev. D* **71** (2005) 112005, `arXiv:hep-ex/0501064`. `doi:10.1103/PhysRevD.71.112005`. Cited on page 1.

[3] F. Zwicky, "Die Rotverschiebung von extragalaktischen Nebeln", *Helv. Phys. Acta* **6** (1933) 110, [Gen. Rel. Grav. 41, 207 (2009)]. `doi:10.1007/s10714-008-0707-4`. Cited on page 1.

[4] V. C. Rubin and W. K. Ford, Jr., "Rotation of the Andromeda Nebula from a Spectroscopic Survey of Emission Regions", *Astrophys. J.* **159** (1970) 379. `doi:10.1086/150317`. Cited on page 2.

[5] Y. Sofue and V. Rubin, "Rotation curves of spiral galaxies", *Ann. Rev. Astron. Astrophys.* **39** (2001) 137, `arXiv:astro-ph/0010594`. `doi:10.1146/annurev.astro.39.1.137`. Cited on page 2.

[6] D. Clowe, M. Bradac, A. H. Gonzalez et al., "A direct empirical proof of the existence of dark matter", *Astrophys. J.* **648** (2006) L109, `arXiv:astro-ph/0608407`. `doi:10.1086/508162`. Cited on page 2.

[7] S. W. Allen, R. W. Schmidt, and A. C. Fabian, "Cosmological constraints from the x-ray gas mass fraction in relaxed lensing clusters observed with Chandra", *Mon. Not. Roy. Astron. Soc.* **334** (2002) L11, `arXiv:astro-ph/0205007`. `doi:10.1046/j.1365-8711.2002.05601.x`. Cited on page 2.

[8] G. R. Blumenthal, S. M. Faber, J. R. Primack et al., "Formation of Galaxies and Large Scale Structure with Cold Dark Matter", *Nature* **311** (1984) 517, [,96(1984)]. `doi:10.1038/311517a0`. Cited on page 2.

[9] Planck Collaboration, Y. Akrami et al., "Planck 2018 results. I. Overview and the cosmological legacy of Planck". 2018. `arXiv:1807.06205`. Cited on pages 2 and 49.

[10] Planck Collaboration, N. Aghanim et al., "Planck 2018 results. VI. Cosmological parameters". 2018. `arXiv:1807.06209`. Cited on pages 2, 49, 53, and 160.

[11] M. Boylan-Kolchin, V. Springel, S. D. M. White et al., "Resolving Cosmic Structure Formation with the Millennium-II Simulation", *Mon. Not. Roy. Astron. Soc.* **398**

(2009) 1150, arXiv:0903.3041. doi:10.1111/j.1365-2966.2009.15191.x. Cited on page 2.

[12] D. H. Weinberg, J. S. Bullock, F. Governato et al., "Cold dark matter: controversies on small scales", *Proc. Nat. Acad. Sci.* **112** (2015) 12249, arXiv:1306.0913. doi:10.1073/pnas.1308716112. Cited on page 2.

[13] G. Jungman, M. Kamionkowski, and K. Griest, "Supersymmetric dark matter", *Phys. Rept.* **267** (1996) 195, arXiv:hep-ph/9506380. doi:10.1016/0370-1573(95)00058-5. Cited on page 2.

[14] P. Cushman et al., "Working Group Report: WIMP Dark Matter Direct Detection", in *Proceedings, 2013 Community Summer Study on the Future of U.S. Particle Physics: Snowmass on the Mississippi (CSS2013)*. Minneapolis, 2013. arXiv:1310.8327. Cited on page 2.

[15] XENON Collaboration, "The XENON1T Dark Matter Experiment", *Eur. Phys. J. C* **77** (2017) 881, arXiv:1708.07051. doi:10.1140/epjc/s10052-017-5326-3. Cited on page 3.

[16] XENON Collaboration, "Dark Matter Search Results from a One Ton-Year Exposure of XENON1T", *Phys. Rev. Lett.* **121** (2018) 111302, arXiv:1805.12562. doi:10.1103/PhysRevLett.121.111302. Cited on pages 3 and 103.

[17] G. Bertone and D. Hooper, "History of dark matter", *Rev. Mod. Phys.* **90** (2018) 045002, arXiv:1605.04909. doi:10.1103/RevModPhys.90.045002. Cited on page 3.

[18] LUX Collaboration, "Results from a search for dark matter in the complete LUX exposure", *Phys. Rev. Lett.* **118** (2017) 021303, arXiv:1608.07648. doi:10.1103/PhysRevLett.118.021303. Cited on pages 3 and 103.

[19] PandaX-II Collaboration, "Dark Matter Results From 54-Ton-Day Exposure of PandaX-II Experiment", *Phys. Rev. Lett.* **119** (2017) 181302, arXiv:1708.06917. doi:10.1103/PhysRevLett.119.181302. Cited on pages 3 and 103.

[20] J. Ellis, "TikZ-Feynman: Feynman diagrams with TikZ", *Comput. Phys. Commun.* **210** (2017) 103, arXiv:1601.05437. doi:10.1016/j.cpc.2016.08.019. Cited on page 5.

[21] L. Evans and P. Bryant, "LHC Machine", *JINST* **3** (2008) S08001. doi:10.1088/1748-0221/3/08/S08001. Cited on page 9.

[22] CMS Collaboration, "The CMS Experiment at the CERN LHC", *JINST* **3** (2008) S08004. doi:10.1088/1748-0221/3/08/S08004. Cited on pages 9, 10, 11, 12, 13, 14, 15, and 17.

[23] ATLAS Collaboration, "The ATLAS Experiment at the CERN Large Hadron Collider", *JINST* **3** (2008) S08003. doi:10.1088/1748-0221/3/08/S08003. Cited on page 9.

[24] CMS Collaboration, “Observation of a new boson at a mass of 125 GeV with the CMS experiment at the LHC”, *Phys. Lett. B* **716** (2012) 30, `arXiv:1207.7235`. `doi:10.1016/j.physletb.2012.08.021`. Cited on pages 9 and 19.

[25] ATLAS Collaboration, “Observation of a new particle in the search for the Standard Model Higgs boson with the ATLAS detector at the LHC”, *Phys. Lett. B* **716** (2012) 1, `arXiv:1207.7214`. `doi:10.1016/j.physletb.2012.08.020`. Cited on pages 9 and 19.

[26] CMS Collaboration, “Precise determination of the mass of the Higgs boson and tests of compatibility of its couplings with the standard model predictions using proton collisions at 7 and 8 TeV”, *Eur. Phys. J. C* **75** (2015) 212, `arXiv:1412.8662`. `doi:10.1140/epjc/s10052-015-3351-7`. Cited on pages 9 and 19.

[27] AC Team, “Diagram of an LHC dipole magnet. Schéma d’un aimant dipôle du LHC”, June, 1999. Accessed on Jan. 30th, 2019. `https://cds.cern.ch/record/40524`. Cited on page 10.

[28] CMS Collaboration, “Luminosity results web page”. Accessed on Dec 28th, 2018. `https://twiki.cern.ch/twiki/bin/view/CMSPublic/LumiPublicResults`. Cited on page 11.

[29] CMS Collaboration, “CMS detector design web page”. Accessed on Dec 28th, 2018. `https://cms.cern/news/cms-detector-design`. Cited on page 12.

[30] CMS Collaboration, “The CMS magnet project: Technical Design Report”. Technical Design Report CMS. CERN, Geneva, 1997. `https://cds.cern.ch/record/331056`. Cited on page 11.

[31] CMS Collaboration, V. Karimäki, M. Mannelli, P. Siegrist et al., “The CMS tracker system project: Technical Design Report”. Technical Design Report CMS. CERN, Geneva, 1997. `https://cds.cern.ch/record/368412`. Cited on page 12.

[32] CMS Collaboration, “The CMS electromagnetic calorimeter project: Technical Design Report”. Technical Design Report CMS. CERN, Geneva, 1997. `https://cds.cern.ch/record/349375`. Cited on page 13.

[33] CMS Collaboration, “The CMS hadron calorimeter project: Technical Design Report”. Technical Design Report CMS. CERN, Geneva, 1997. `https://cds.cern.ch/record/357153`. Cited on page 14.

[34] J. Mans, J. Anderson, B. Dahmes et al., “CMS Technical Design Report for the Phase 1 Upgrade of the Hadron Calorimeter”, Technical Report CMS-TDR-10, Sep, 2012. `https://cds.cern.ch/record/1481837`. Cited on page 14.

[35] M. Albrow, M. Arneodo, V. Avati et al., “CMS-TOTEM Precision Proton Spectrometer”, Technical Report TOTEM-TDR-003, Sep, 2014. `https://cds.cern.ch/record/1753795`. Cited on page 15.

[36] V. Andreev et al., “Performance studies of a full-length prototype for the CASTOR forward calorimeter at the CMS experiment”, *Eur. Phys. J. C* **67** (2010) 601. doi:10.1140/epjc/s10052-010-1316-4. Cited on page 15.

[37] CMS Collaboration, “The CMS muon project: Technical Design Report”. CERN, Geneva, 1997. https://cds.cern.ch/record/343814. Cited on page 15.

[38] A. Colaleo, A. Safonov, A. Sharma et al., “CMS Technical Design Report for the Muon Endcap GEM Upgrade”, Technical Report CMS-TDR-013, Jun, 2015. https://cds.cern.ch/record/2021453. Cited on page 15.

[39] CMS Collaboration, “The CMS trigger system”, *JINST* **12** (2017) P01020, arXiv:1609.02366. doi:10.1088/1748-0221/12/01/P01020. Cited on page 17.

[40] CMS Collaboration, G. L. Bayatyan, M. Della Negra, L. Foà et al., “CMS computing: Technical Design Report”. Technical Design Report CMS. CERN, Geneva, 2005. Submitted on 31 May 2005. https://cds.cern.ch/record/838359. Cited on page 17.

[41] CMS Collaboration, S. Cittolin, A. Rácz, and P. Sphicas, “The TriDAS Project: Technical Design Report, Volume 2: Data Acquisition and High-Level Trigger.”. Technical Design Report CMS. CERN, Geneva, 2002. http://cds.cern.ch/record/578006. Cited on page 18.

[42] T. Lancaster and S. J. Blundell, “Quantum Field Theory for the Gifted Amateur”. Oxford Univ. Press, Oxford, 2014. Cited on pages 19 and 21.

[43] A. Zee, “Quantum Field Theory in a Nutshell”. Princeton Univ. Press, Princeton, 2010. Cited on pages 19 and 21.

[44] M. E. Peskin and D. V. Schroeder, “An introduction to quantum field theory”. Addison-Wesley, Reading, Mass., 1995. Cited on pages 19 and 21.

[45] M. E. Peskin, “Lectures on the Theory of the Weak Interaction”, in *Proceedings, 2016 European School of High-Energy Physics (ESHEP2016): Skeikampen, Norway, June 15-28 2016*, p. 1. 2017. arXiv:1708.09043. Cited on page 19.

[46] C. S. Wu, E. Ambler, R. W. Hayward et al., “Experimental Test of Parity Conservation in Beta Decay”, *Phys. Rev.* **105** (1957) 1413. doi:10.1103/PhysRev.105.1413. Cited on page 19.

[47] M. Bardon, P. Norton, J. Peoples et al., “Measurement of the momentum spectrum of positrons from muon decay”, *Phys. Rev. Lett.* **14** (1965) 449. doi:10.1103/PhysRevLett.14.449. Cited on page 19.

[48] G. Czapek et al., “Branching ratio for the rare pion decay into positron and neutrino”, *Phys. Rev. Lett.* **70** (1993) 17. doi:10.1103/PhysRevLett.70.17. Cited on page 19.

[49] ALEPH, DELPHI, L3, OPAL, SLD, LEP Electroweak Working Group, SLD Electroweak Group, SLD Heavy Flavour Group Collaboration, “Precision electroweak measurements on the $Z$ resonance”, *Phys. Rept.* **427** (2006) 257, `arXiv:hep-ex/0509008`. `doi:10.1016/j.physrep.2005.12.006`. Cited on pages 19 and 144.

[50] ALEPH, DELPHI, L3, OPAL, LEP Electroweak Collaboration, “Electroweak Measurements in Electron-Positron Collisions at W-Boson-Pair Energies at LEP”, *Phys. Rept.* **532** (2013) 119, `arXiv:1302.3415`. `doi:10.1016/j.physrep.2013.07.004`. Cited on page 19.

[51] L. Susskind, “Dynamics of Spontaneous Symmetry Breaking in the Weinberg-Salam Theory”, *Phys. Rev. D* **20** (1979) 2619. `doi:10.1103/PhysRevD.20.2619`. Cited on page 20.

[52] G. t’Hooft, “Naturalness, chiral symmetry, and spontaneous chiral symmetry breaking”, *NATO Sci. Ser. B* **59** (1980) 135. `doi:10.1007/978-1-4684-7571-5_9`. Cited on page 20.

[53] S. Hossenfelder, “Screams for Explanation: Finetuning and Naturalness in the Foundations of Physics”. 2018. `arXiv:1801.02176`. Cited on page 20.

[54] Muon g-2 Collaboration, “Final Report of the Muon E821 Anomalous Magnetic Moment Measurement at BNL”, *Phys. Rev. D* **73** (2006) 072003, `arXiv:hep-ex/0602035`. `doi:10.1103/PhysRevD.73.072003`. Cited on page 20.

[55] LHCb Collaboration, “Test of lepton universality with $B^0 \to K^{*0}\ell^+\ell^-$ decays”, *JHEP* **08** (2017) 055, `arXiv:1705.05802`. `doi:10.1007/JHEP08(2017)055`. Cited on page 20.

[56] LHCb Collaboration, “Measurement of the ratio of branching fractions $\mathcal{B}(\bar{B}^0 \to D^{*+}\tau^-\bar{\nu}_\tau)/\mathcal{B}(\bar{B}^0 \to D^{*+}\mu^-\bar{\nu}_\mu)$”, *Phys. Rev. Lett.* **115** (2015) 111803, `arXiv:1506.08614`, [Erratum: Phys. Rev. Lett.115,no.15,159901(2015)]. `doi:10.1103/PhysRevLett.115.159901, 10.1103/PhysRevLett.115.111803`. Cited on page 20.

[57] LHCb Collaboration, “Angular analysis of the $B^0 \to K^{*0}\mu^+\mu^-$ decay using 3 fb$^{-1}$ of integrated luminosity”, *JHEP* **02** (2016) 104, `arXiv:1512.04442`. `doi:10.1007/JHEP02(2016)104`. Cited on page 20.

[58] SNO Collaboration, “Direct evidence for neutrino flavor transformation from neutral current interactions in the Sudbury Neutrino Observatory”, *Phys. Rev. Lett.* **89** (2002) 011301, `arXiv:nucl-ex/0204008`. `doi:10.1103/PhysRevLett.89.011301`. Cited on page 20.

[59] S. F. King, “Neutrino mass models”, *Rept. Prog. Phys.* **67** (2004) 107, `arXiv:hep-ph/0310204`. `doi:10.1088/0034-4885/67/2/R01`. Cited on page 20.

[60] J. C. Collins, D. E. Soper, and G. F. Sterman, “Factorization of Hard Processes in QCD”, *Adv. Ser. Direct. High Energy Phys.* **5** (1989) 1, arXiv:hep-ph/0409313. doi:10.1142/9789814503266_0001. Cited on page 22.

[61] A. Buckley et al., “General-purpose event generators for LHC physics”, *Phys. Rept.* **504** (2011) 145, arXiv:1101.2599. doi:10.1016/j.physrep.2011.03.005. Cited on page 22.

[62] H1, ZEUS Collaboration, “Combination of measurements of inclusive deep inelastic $e^{\pm}p$ scattering cross sections and QCD analysis of HERA data”, *Eur. Phys. J. C* **75** (2015) 580, arXiv:1506.06042. doi:10.1140/epjc/s10052-015-3710-4. Cited on page 23.

[63] NNPDF Collaboration, “Parton distributions for the LHC Run II”, *JHEP* **04** (2015) 040, arXiv:1410.8849. EDINBURGH-2014-15, IFUM-1034-FT, CERN-PH-TH-2013-253, OUTP-14-11P, CAVENDISH-HEP-14-11. doi:10.1007/JHEP04(2015)040. Cited on page 23.

[64] LHC New Physics Working Group Collaboration, “Simplified Models for LHC New Physics Searches”, *J. Phys. G* **39** (2012) 105005, arXiv:1105.2838. SLAC-PUB-15045, FERMILAB-PUB-11-842-A-PPD. doi:10.1088/0954-3899/39/10/105005. Cited on page 25.

[65] J. Abdallah et al., “Simplified Models for Dark Matter Searches at the LHC”, *Phys. Dark Univ.* **9-10** (2015) 8, arXiv:1506.03116. doi:10.1016/j.dark.2015.08.001. Cited on page 25.

[66] O. Mattelaer and E. Vryonidou, “Dark matter production through loop-induced processes at the LHC: the s-channel mediator case”, *Eur. Phys. J. C* **75** (2015) 436, arXiv:1508.00564. doi:10.1140/epjc/s10052-015-3665-5. Cited on page 25.

[67] M. Backović, M. Krämer, F. Maltoni et al., “Higher-order QCD predictions for dark matter production at the LHC in simplified models with s-channel mediators”, *Eur. Phys. J. C* **75** (2015) 482, arXiv:1508.05327. doi:10.1140/epjc/s10052-015-3700-6. Cited on page 25.

[68] M. Neubert, J. Wang, and C. Zhang, “Higher-Order QCD Predictions for Dark Matter Production in Mono-$Z$ Searches at the LHC”, *JHEP* **02** (2016) 082, arXiv:1509.05785. doi:10.1007/JHEP02(2016)082. Cited on page 25.

[69] G. Busoni et al., “Recommendations on presenting LHC searches for missing transverse energy signals using simplified $s$-channel models of dark matter”. 2016. arXiv:1603.04156. Cited on pages 25, 26, 31, and 100.

[70] A. Albert et al., “Recommendations of the LHC Dark Matter Working Group: Comparing LHC searches for heavy mediators of dark matter production in visible and invisible decay channels”. 2017. arXiv:1703.05703. Cited on pages 27, 49, 51, and 160.

[71] CMS Collaboration, "Jet Production Rates in Association with $W$ and $Z$ Bosons in $pp$ Collisions at $\sqrt{s} = 7$ TeV", *JHEP* **01** (2012) 010, `arXiv:1110.3226`. `doi:10.1007/JHEP01(2012)010`. Cited on pages 31 and 32.

[72] M. L. Mangano, M. Moretti, F. Piccinini et al., "Matching matrix elements and shower evolution for top-quark production in hadronic collisions", *JHEP* **01** (2007) 013, `arXiv:hep-ph/0611129`. `doi:10.1088/1126-6708/2007/01/013`. Cited on page 32.

[73] J. Alwall et al., "Comparative study of various algorithms for the merging of parton showers and matrix elements in hadronic collisions", *Eur. Phys. J. C* **53** (2008) 473, `arXiv:0706.2569`. `doi:10.1140/epjc/s10052-007-0490-5`. Cited on pages 32, 33, and 75.

[74] J. Alwall, S. de Visscher, and F. Maltoni, "QCD radiation in the production of heavy colored particles at the LHC", *JHEP* **02** (2009) 017, `arXiv:0810.5350`. `doi:10.1088/1126-6708/2009/02/017`. Cited on pages 32 and 75.

[75] J. Alwall, R. Frederix, S. Frixione et al., "The automated computation of tree-level and next-to-leading order differential cross sections, and their matching to parton shower simulations", *JHEP* **07** (2014) 079, `arXiv:1405.0301`. `doi:10.1007/JHEP07(2014)079`. Cited on page 32.

[76] T. Sjöstrand, S. Ask, J. R. Christiansen et al., "An Introduction to PYTHIA 8.2", *Comput. Phys. Commun.* **191** (2015) 159, `arXiv:1410.3012`. `doi:10.1016/j.cpc.2015.01.024`. Cited on pages 32 and 76.

[77] S. Catani, Y. L. Dokshitzer, M. H. Seymour et al., "Longitudinally invariant $K_t$ clustering algorithms for hadron hadron collisions", *Nucl. Phys. B* **406** (1993) 187. CERN-TH-6775-93, LU-TP-93-2. `doi:10.1016/0550-3213(93)90166-M`. Cited on page 32.

[78] S. D. Ellis and D. E. Soper, "Successive combination jet algorithm for hadron collisions", *Phys. Rev. D* **48** (1993) 3160, `arXiv:hep-ph/9305266`. CERN-TH-6860-93. `doi:10.1103/PhysRevD.48.3160`. Cited on page 32.

[79] CMS Collaboration, "Event generator tunes obtained from underlying event and multiparton scattering measurements", *Eur. Phys. J. C* **76** (2016) 155, `arXiv:1512.00815`. `doi:10.1140/epjc/s10052-016-3988-x`. Cited on pages 33 and 34.

[80] GEANT4 Collaboration, "GEANT4: A Simulation toolkit", *Nucl. Instrum. Meth. A* **506** (2003) 250. `doi:10.1016/S0168-9002(03)01368-8`. Cited on pages 33 and 76.

[81] P. Lenzi and J. M. Butterworth, "A Study on Matrix Element corrections in inclusive Z/ gamma* production at LHC as implemented in PYTHIA, HERWIG, ALPGEN and SHERPA". 2009. `arXiv:0903.3918`. Cited on page 33.

[82] R. Frederix and S. Frixione, "Merging meets matching in MC@NLO", *JHEP* **12** (2012) 061, `arXiv:1209.6215`. `doi:10.1007/JHEP12(2012)061`. Cited on pages 34 and 76.

[83] M. Bauer, U. Haisch, and F. Kahlhoefer, "Simplified dark matter models with two Higgs doublets: I. Pseudoscalar mediators", *JHEP* **05** (2017) 138, `arXiv:1701.07427`. `doi:10.1007/JHEP05(2017)138`. Cited on pages 36 and 37.

[84] T. Abe, A. Albert, et al., "LHC Dark Matter Working Group: Next-generation spin-0 dark matter models". 2018. `arXiv:1810.09420`. Cited on pages 37 and 49.

[85] Particle Data Group, "Review of Particle Physics", *Phys. Rev. D* **98** (2018) 030001. `doi:10.1103/PhysRevD.98.030001`. Cited on pages 39 and 49.

[86] H. Georgi, "Unparticle physics", *Phys. Rev. Lett.* **98** (2007) 221601, `arXiv:hep-ph/0703260`. `doi:10.1103/PhysRevLett.98.221601`. Cited on page 43.

[87] H. Georgi, "Another odd thing about unparticle physics", *Phys. Lett. B* **650** (2007) 275, `arXiv:0704.2457`. `doi:10.1016/j.physletb.2007.05.037`. Cited on page 43.

[88] K. Cheung, W.-Y. Keung, and T.-C. Yuan, "Collider Signals of Unparticle Physics", *Phys. Rev. Lett.* **99** (2007) 051803, `arXiv:0704.2588`. `doi:10.1103/PhysRevLett.99.051803`. Cited on page 43.

[89] K. Cheung, W.-Y. Keung, and T.-C. Yuan, "Collider phenomenology of unparticle physics", *Phys. Rev. D* **76** (2007) 055003, `arXiv:0706.3155`. `doi:10.1103/PhysRevD.76.055003`. Cited on page 43.

[90] T. M. Aliev, S. Bilmis, M. Solmaz et al., "Scalar Unparticle Signals at the LHC", *Phys. Rev. D* **95** (2017) 095005, `arXiv:1701.00498`. `doi:10.1103/PhysRevD.95.095005`. Cited on page 43.

[91] G. Alencar and C. R. Muniz, "Thermodynamic Properties of Static and Rotating Unparticle Black Holes", *JCAP* **1803** (2018) 040, `arXiv:1801.00483`. `doi:10.1088/1475-7516/2018/03/040`. Cited on page 43.

[92] Z. Leong, C. Setty, K. Limtragool et al., "Power-law liquid in cuprate superconductors from fermionic unparticles", *Phys. Rev. B* **96** (2017) 205101, `arXiv:1705.07130`. `doi:10.1103/PhysRevB.96.205101`. Cited on page 43.

[93] T. Banks and A. Zaks, "On the Phase Structure of Vector-Like Gauge Theories with Massless Fermions", *Nucl. Phys. B* **196** (1982) 189. `doi:10.1016/0550-3213(82)90035-9`. Cited on page 43.

[94] J. M. Maldacena, "The Large N limit of superconformal field theories and supergravity", *Int. J. Theor. Phys.* **38** (1999) 1113, `arXiv:hep-th/9711200`, [Adv. Theor. Math. Phys.2,231(1998)]. `doi:10.1023/A:1026654312961, 10.4310/ATMP.1998.v2.n2.a1`. Cited on page 43.

[95] Y. Liao, "Bounds on unparticles couplings to electrons: From electron g-2 to positronium decays", *Phys. Rev. D* **76** (2007) 056006, `arXiv:0705.0837`. `doi:10.1103/PhysRevD.76.056006`. Cited on page 43.

[96] S. Ask, I. V. Akin, L. Benucci et al., "Real Emission and Virtual Exchange of Gravitons and Unparticles in Pythia8", *Comput. Phys. Commun.* **181** (2010) 1593, `arXiv:0912.4233`. MAN-HEP-2009-20, MCNET-09-20, DESY-09-214. `doi:10.1016/j.cpc.2010.05.013`. Cited on page 44.

[97] CMS Collaboration, "Search for dark matter and unparticles produced in association with a Z boson in proton-proton collisions at $\sqrt{s} = 8$ TeV", *Phys. Rev. D* **93** (2016) 052011, `arXiv:1511.09375`, [Erratum: Phys. Rev.D97,no.9,099903(2018)]. `doi:10.1103/PhysRevD.97.099903, 10.1103/PhysRevD.93.052011`. Cited on pages 44, 45, 100, 104, 115, and 117.

[98] CMS Collaboration, "Search for dark matter and unparticles in events with a Z boson and missing transverse momentum in proton-proton collisions at $\sqrt{s} = 13$ TeV", *JHEP* **03** (2017) 061, `arXiv:1701.02042`, [Erratum: JHEP09,106(2017)]. `doi:10.1007/JHEP01(2018)056`. Cited on pages 44, 45, and 73.

[99] S. Ask, "Simulation of $Z$ plus Graviton/Unparticle Production at the LHC", *Eur. Phys. J. C* **60** (2009) 509, `arXiv:0809.4750`. MAN-HEP-2008-28. `doi:10.1140/epjc/s10052-009-0949-7`. Cited on page 44.

[100] S. Kathrein, S. Knapen, and M. J. Strassler, "Bounds from LEP on unparticle interactions with electroweak bosons", *Phys. Rev. D* **84** (2011) 015010, `arXiv:1012.3737`. `doi:10.1103/PhysRevD.84.015010`. Cited on pages 44, 100, and 104.

[101] T. Sjöstrand, S. Ask, J. R. Christiansen et al., "Pythia update history". Accessed on Dec. 27th, 2018. `http://home.thep.lu.se/Pythia/pythia82html/UpdateHistory.html`. Cited on page 45.

[102] N. Arkani-Hamed, S. Dimopoulos, and G. R. Dvali, "The Hierarchy problem and new dimensions at a millimeter", *Phys. Lett. B* **429** (1998) 263, `arXiv:hep-ph/9803315`. `doi:10.1016/S0370-2693(98)00466-3`. Cited on page 45.

[103] E. W. Kolb and M. S. Turner, "The Early Universe", volume 69 of *Frontiers in Physics*. Addison Wesley, 1990. Cited on pages 49 and 50.

[104] G. Bertone, D. Hooper, and J. Silk, "Particle dark matter: Evidence, candidates and constraints", *Phys. Rept.* **405** (2005) 279, `arXiv:hep-ph/0404175`. `doi:10.1016/j.physrep.2004.08.031`. Cited on page 49.

[105] T. du Pree, K. Hahn, P. Harris et al., "Cosmological constraints on Dark Matter models for collider searches". 2016. `arXiv:1603.08525`. Cited on page 49.

[106] M. Backovic, K. Kong, and M. McCaskey, “MadDM v.1.0: Computation of Dark Matter Relic Abundance Using MadGraph5”, *Physics of the Dark Universe* **5-6** (2014) 18, `arXiv:1308.4955`. `doi:10.1016/j.dark.2014.04.001`. Cited on page 50.

[107] M. Backovic, A. Martini, O. Mattelaer et al., “Direct Detection of Dark Matter with MadDM v.2.0”, *Phys. Dark Univ.* **9-10** (2015) 37, `arXiv:1505.04190`. `doi:10.1016/j.dark.2015.09.001`. Cited on page 50.

[108] C. Degrande, C. Duhr, B. Fuks et al., “UFO - The Universal FeynRules Output”, *Comput. Phys. Commun.* **183** (2012) 1201, `arXiv:1108.2040`. `doi:10.1016/j.cpc.2012.01.022`. Cited on page 51.

[109] CMS Collaboration, “Search for narrow and broad dijet resonances in proton-proton collisions at $\sqrt{s} = 13$ TeV and constraints on dark matter mediators and other new particles”, *JHEP* **08** (2018) 130, `arXiv:1806.00843`. `doi:10.1007/JHEP08(2018)130`. Cited on page 52.

[110] CMS Collaboration, “Search for high-mass resonances in dilepton final states in proton-proton collisions at $\sqrt{s} = 13$ TeV”, *JHEP* **06** (2018) 120, `arXiv:1803.06292`. `doi:10.1007/JHEP06(2018)120`. Cited on page 52.

[111] CMS Collaboration, “Search for new physics in dijet angular distributions using proton–proton collisions at $\sqrt{s} = 13$ TeV and constraints on dark matter and other models”, *Eur. Phys. J. C* **78** (2018) 789, `arXiv:1803.08030`. `doi:10.1140/epjc/s10052-018-6242-x`. Cited on page 52.

[112] CMS Collaboration, “Particle-flow reconstruction and global event description with the CMS detector”, *JINST* **12** (2017) P10003, `arXiv:1706.04965`. `doi:10.1088/1748-0221/12/10/P10003`. Cited on page 61.

[113] CMS Collaboration, “Description and performance of track and primary-vertex reconstruction with the CMS tracker”, *JINST* **9** (2014) P10009, `arXiv:1405.6569`. `doi:10.1088/1748-0221/9/10/P10009`. Cited on pages 61 and 63.

[114] CMS Collaboration, “Performance of the CMS muon detector and muon reconstruction with proton-proton collisions at $\sqrt{s} = 13$ TeV”, *JINST* **13** (2018) P06015, `arXiv:1804.04528`. `doi:10.1088/1748-0221/13/06/P06015`. Cited on pages 62 and 63.

[115] CMS Collaboration, “Performance of CMS Muon Reconstruction in Cosmic-Ray Events”, *JINST* **5** (2010) T03022, `arXiv:0911.4994`. `doi:10.1088/1748-0221/5/03/T03022`. Cited on page 62.

[116] CMS Collaboration, “Jet energy scale and resolution in the CMS experiment in pp collisions at 8 TeV”, *JINST* **12** (2017) P02014, `arXiv:1607.03663`. `doi:10.1088/1748-0221/12/02/P02014`. Cited on pages 63 and 94.

[117] CMS Collaboration, “Performance of Electron Reconstruction and Selection with the CMS Detector in Proton-Proton Collisions at $\sqrt{s} = 8$ TeV”, *JINST* **10** (2015) P06005, `arXiv:1502.02701`. `doi:10.1088/1748-0221/10/06/P06005`. Cited on page 63.

[118] W. Adam, R. Frühwirth, A. Strandlie et al., “Reconstruction of Electrons with the Gaussian-Sum Filter in the CMS Tracker at the LHC”, Technical Report CMS-NOTE-2005-001, CERN, Geneva, Jan, 2005. `http://cds.cern.ch/record/815410`. Cited on page 64.

[119] M. Cacciari, G. P. Salam, and G. Soyez, “The anti-$k_t$ jet clustering algorithm”, *JHEP* **04** (2008) 063, `arXiv:0802.1189`. `doi:10.1088/1126-6708/2008/04/063`. Cited on page 68.

[120] M. Cacciari, G. P. Salam, and G. Soyez, “FastJet User Manual”, *Eur. Phys. J. C* **72** (2012) 1896, `arXiv:1111.6097`. `doi:10.1140/epjc/s10052-012-1896-2`. Cited on page 68.

[121] CMS Collaboration, “Jet algorithms performance in 13 TeV data”, 2017. Physics Analysis Summary JME-16-003. `http://cds.cern.ch/record/2256875`. Cited on page 68.

[122] CMS Collaboration, “Identification of heavy-flavour jets with the CMS detector in pp collisions at 13 TeV”, *JINST* **13** (2018) P05011, `arXiv:1712.07158`. `doi:10.1088/1748-0221/13/05/P05011`. Cited on page 68.

[123] CMS Collaboration, “Reconstruction and identification of $\tau$ lepton decays to hadrons and $\nu_\tau$ at CMS”, *JINST* **11** (2016) P01019, `arXiv:1510.07488`. `doi:10.1088/1748-0221/11/01/P01019`. Cited on page 68.

[124] CMS Collaboration, “Performance of reconstruction and identification of $\tau$ leptons decaying to hadrons and $\nu_\tau$ in pp collisions at $\sqrt{s} = 13$ TeV”, *JINST* **13** (2018) P10005, `arXiv:1809.02816`. `doi:10.1088/1748-0221/13/10/P10005`. Cited on page 68.

[125] CMS Collaboration, “Performance of missing transverse momentum in pp collisions at $\sqrt{s} = 13$ TeV using the CMS detector”, 2018. Physics Analysis Summary JME-17-001. `http://cds.cern.ch/record/2628600`. Cited on pages 69, 132, and 133.

[126] P. Nason, “A New method for combining NLO QCD with shower Monte Carlo algorithms”, *JHEP* **11** (2004) 040, `arXiv:hep-ph/0409146`. `doi:10.1088/1126-6708/2004/11/040`. Cited on page 75.

[127] S. Frixione, P. Nason, and C. Oleari, “Matching NLO QCD computations with Parton Shower simulations: the POWHEG method”, *JHEP* **11** (2007) 070, `arXiv:0709.2092`. `doi:10.1088/1126-6708/2007/11/070`. Cited on page 75.

[128] S. Alioli, P. Nason, C. Oleari et al., “A general framework for implementing NLO calculations in shower Monte Carlo programs: the POWHEG BOX”, *JHEP* **06** (2010) 043, `arXiv:1002.2581`. `doi:10.1007/JHEP06(2010)043`. Cited on page 75.

[129] T. Melia, P. Nason, R. Rontsch et al., “W+W-, WZ and ZZ production in the POWHEG BOX”, *JHEP* **11** (2011) 078, `arXiv:1107.5051`. `doi:10.1007/JHEP11(2011)078`. Cited on page 75.

[130] P. Nason and G. Zanderighi, “$W^+W^-$ , $WZ$ and $ZZ$ production in the POWHEG-BOX-V2”, *Eur. Phys. J. C* **74** (2014) 2702, `arXiv:1311.1365`. `doi:10.1140/epjc/s10052-013-2702-5`. Cited on page 75.

[131] J. M. Campbell and R. K. Ellis, “MCFM for the Tevatron and the LHC”, *Nucl. Phys. Proc. Suppl.* **205** (2010) 10, `arXiv:1007.3492`. `doi:10.1016/j.nuclphysbps.2010.08.011`. Cited on page 75.

[132] R. Frederix, S. Frixione, F. Maltoni et al., “Automation of next-to-leading order computations in QCD: The FKS subtraction”, *JHEP* **10** (2009) 003, `arXiv:0908.4272`. `doi:10.1088/1126-6708/2009/10/003`. Cited on page 76.

[133] V. Hirschi, R. Frederix, S. Frixione et al., “Automation of one-loop QCD corrections”, *JHEP* **05** (2011) 044, `arXiv:1103.0621`. `doi:10.1007/JHEP05(2011)044`. Cited on page 76.

[134] M. Grazzini, S. Kallweit, and D. Rathlev, “ZZ production at the LHC: Fiducial cross sections and distributions in NNLO QCD”, *Phys. Lett. B* **750** (2015) 407, `arXiv:1507.06257`. `doi:10.1016/j.physletb.2015.09.055`. Cited on pages 81 and 87.

[135] S. Gieseke, T. Kasprzik, and J. H. Kühn, “Vector-boson pair production and electroweak corrections in HERWIG++”, *Eur. Phys. J. C* **74** (2014) 2988, `arXiv:1401.3964`. `doi:10.1140/epjc/s10052-014-2988-y`. Cited on pages 81 and 87.

[136] A. Bierweiler, T. Kasprzik, and J. H. Kühn, “Vector-boson pair production at the LHC to $\mathcal{O}(\alpha^3)$ accuracy”, *JHEP* **12** (2013) 071, `arXiv:1305.5402`. `doi:10.1007/JHEP12(2013)071`. Cited on pages 81 and 87.

[137] J. Baglio, L. D. Ninh, and M. M. Weber, “Massive gauge boson pair production at the LHC: a next-to-leading order story”, *Phys. Rev. D* **88** (2013) 113005, `arXiv:1307.4331`, [Erratum: 10.1103/PhysRevD.94.099902]. `doi:10.1103/PhysRevD.88.113005`. Cited on pages 81 and 87.

[138] R. Gavin, Y. Li, F. Petriello et al., “FEWZ 2.0: A code for hadronic Z production at next-to-next-to-leading order”, *Comput. Phys. Commun.* **182** (2011) 2388, `arXiv:1011.3540`. `doi:10.1016/j.cpc.2011.06.008`. Cited on pages 81 and 82.

[139] Y. Li and F. Petriello, “Combining QCD and electroweak corrections to dilepton production in the framework of the FEWZ simulation code”, *Phys. Rev. D* **86**

(2012) 094034, arXiv:1208.5967. doi:10.1103/PhysRevD.86.094034. Cited on pages 81 and 82.

[140] M. Beneke, P. Falgari, S. Klein et al., "Hadronic top-quark pair production with NNLL threshold resummation", *Nucl. Phys. B* **855** (2012) 695–741, arXiv:1109.1536. doi:10.1016/j.nuclphysb.2011.10.021. Cited on page 81.

[141] M. Cacciari, M. Czakon, M. Mangano et al., "Top-pair production at hadron colliders with next-to-next-to-leading logarithmic soft-gluon resummation", *Phys. Lett. B* **710** (2012) 612–622, arXiv:1111.5869. doi:10.1016/j.physletb.2012.03.013. Cited on page 81.

[142] P. Bärnreuther, M. Czakon, and A. Mitov, "Percent Level Precision Physics at the Tevatron: First Genuine NNLO QCD Corrections to $q\bar{q} \to t\bar{t} + X$", *Phys. Rev. Lett.* **109** (2012) 132001, arXiv:1204.5201. doi:10.1103/PhysRevLett.109.132001. Cited on page 81.

[143] M. Czakon and A. Mitov, "NNLO corrections to top-pair production at hadron colliders: the all-fermionic scattering channels", *JHEP* **12** (2012) 054, arXiv:1207.0236. doi:10.1007/JHEP12(2012)054. Cited on page 81.

[144] M. Czakon and A. Mitov, "NNLO corrections to top pair production at hadron colliders: the quark-gluon reaction", *JHEP* **01** (2013) 080, arXiv:1210.6832. doi:10.1007/JHEP01(2013)080. Cited on page 81.

[145] M. Czakon, P. Fiedler, and A. Mitov, "Total Top-Quark Pair-Production Cross Section at Hadron Colliders Through $\mathcal{O}(\alpha_S^4)$", *Phys. Rev. Lett.* **110** (2013) 252004, arXiv:1303.6254. doi:10.1103/PhysRevLett.110.252004. Cited on page 81.

[146] J. M. Campbell, R. K. Ellis, and C. Williams, "Vector boson pair production at the LHC", *JHEP* **07** (2011) 018, arXiv:1105.0020. doi:10.1007/JHEP07(2011)018. Cited on page 87.

[147] CMS Collaboration, "Search for dark matter, unparticle, and extra dimension in events with a Z boson and missing transverse momentum in pp collisions at $\sqrt{\mathrm{s}} = 13$ TeV", technical report. Internal analysis note AN-2015/285. Cited on page 88.

[148] CMS Collaboration, "Measurement of the inelastic proton-proton cross section at $\sqrt{s} = 13$ TeV", *JHEP* **07** (2018) 161, arXiv:1802.02613. doi:10.1007/JHEP07(2018)161. Cited on page 91.

[149] The ATLAS Collaboration, The CMS Collaboration, The LHC Higgs Combination Group Collaboration, "Procedure for the LHC Higgs boson search combination in Summer 2011", Technical Report CMS-NOTE-2011-005. ATL-PHYS-PUB-2011-11, CERN, Geneva, Aug, 2011. https://cds.cern.ch/record/1379837. Cited on pages 92, 93, and 156.

[150] "The HiggsCombine framework". https://github.com/cms-analysis/HiggsAnalysis-CombinedLimit. Cited on page 92.

[151] T. Junk, “Confidence level computation for combining searches with small statistics”, *Nucl. Instrum. Meth. A* **434** (1999) 435, `arXiv:hep-ex/9902006`. CARLETON-OPAL-PHYS-99-01, CERN-EP-99-041. `doi:10.1016/S0168-9002(99)00498-2`. Cited on pages 93 and 156.

[152] G. Cowan, K. Cranmer, E. Gross et al., “Asymptotic formulae for likelihood-based tests of new physics”, *Eur. Phys. J. C* **71** (2011) 1554, `arXiv:1007.1727`, [Erratum: Eur. Phys. J. C 73,2501(2013)]. `doi:10.1140/epjc/s10052-011-1554-0, 10.1140/epjc/s10052-013-2501-z`. Cited on pages 94 and 156.

[153] CMS Collaboration, “CMS luminosity measurement for the 2015 data-taking period”, 2017. Physics Analysis Summary LUM-15-001. `http://cds.cern.ch/record/2138682`. Cited on page 95.

[154] S. Catani, D. de Florian, M. Grazzini et al., “Soft gluon resummation for Higgs boson production at hadron colliders”, *JHEP* **07** (2003) 028, `arXiv:hep-ph/0306211`. `doi:10.1088/1126-6708/2003/07/028`. Cited on page 95.

[155] M. Cacciari, S. Frixione, M. L. Mangano et al., “The t anti-t cross-section at 1.8-TeV and 1.96-TeV: A Study of the systematics due to parton densities and scale dependence”, *JHEP* **04** (2004) 068, `arXiv:hep-ph/0303085`. `doi:10.1088/1126-6708/2004/04/068`. Cited on page 95.

[156] J. Butterworth et al., “PDF4LHC recommendations for LHC Run II”, *J. Phys. G* **43** (2016) 023001, `arXiv:1510.03865`. `doi:10.1088/0954-3899/43/2/023001`. Cited on page 95.

[157] PICO Collaboration, “Dark Matter Search Results from the PICO-60 $C_3F_8$ Bubble Chamber”, *Phys. Rev. Lett.* **118** (2017) 251301, `arXiv:1702.07666`. FERMILAB-PUB-17-058-AE-PPD. `doi:10.1103/PhysRevLett.118.251301`. Cited on page 103.

[158] E. Behnke et al., “Final Results of the PICASSO Dark Matter Search Experiment”, *Astropart. Phys.* **90** (2017) 85, `arXiv:1611.01499`. `doi:10.1016/j.astropartphys.2017.02.005`. Cited on page 103.

[159] Super-Kamiokande Collaboration, “Search for neutrinos from annihilation of captured low-mass dark matter particles in the Sun by Super-Kamiokande”, *Phys. Rev. Lett.* **114** (2015) 141301, `arXiv:1503.04858`. `doi:10.1103/PhysRevLett.114.141301`. Cited on page 103.

[160] IceCube Collaboration, “Search for annihilating dark matter in the Sun with 3 years of IceCube data”, *Eur. Phys. J. C* **77** (2017) 146, `arXiv:1612.05949`. `doi:10.1140/epjc/s10052-017-4689-9`. Cited on page 103.

[161] IceCube Collaboration, “Improved limits on dark matter annihilation in the Sun with the 79-string IceCube detector and implications for supersymmetry”, *JCAP* **1604** (2016) 022, `arXiv:1601.00653`. `doi:10.1088/1475-7516/2016/04/022`. Cited on page 103.

[162] SuperCDMS Collaboration, “New Results from the Search for Low-Mass Weakly Interacting Massive Particles with the CDMS Low Ionization Threshold Experiment”, *Phys. Rev. Lett.* **116** (2016) 071301, `arXiv:1509.02448`. `doi:10.1103/PhysRevLett.116.071301`. Cited on page 103.

[163] CRESST Collaboration, “Results on light dark matter particles with a low-threshold CRESST-II detector”, *Eur. Phys. J. C* **76** (2016) 25, `arXiv:1509.01515`. `doi:10.1140/epjc/s10052-016-3877-3`. Cited on page 103.

[164] CDEX Collaboration, “Limits on Light Weakly Interacting Massive Particles from the First 102.8 kg × day Data of the CDEX-10 Experiment”, *Phys. Rev. Lett.* **120** (2018) 241301, `arXiv:1802.09016`. `doi:10.1103/PhysRevLett.120.241301`. Cited on page 103.

[165] CMS Collaboration, “Search for dark matter, extra dimensions, and unparticles in monojet events in proton-proton collisions at $\sqrt{s} = 8$ TeV”, *Eur. Phys. J. C* **75** (2015) 235, `arXiv:1408.3583`. `doi:10.1140/epjc/s10052-015-3451-4`. Cited on pages 100 and 104.

[166] N. C. Smith, “A Search for new physics in events with a leptonically decaying Z boson and a large transverse momentum imbalance with the CMS Detector at the LHC”, 2018. `https://cds.cern.ch/record/2646356`. Cited on pages 107, 108, and 110.

[167] CMS Collaboration, “Search for new physics in events with a leptonically decaying Z boson and a large transverse momentum imbalance in proton-proton collisions at $\sqrt{s}$ = 13 TeV”, *Eur. Phys. J. C* **78** (2018) 291, `arXiv:1711.00431`. `doi:10.1140/epjc/s10052-018-5740-1`. Cited on pages 107 and 108.

[168] CMS Collaboration, “Search for new physics in final states with an energetic jet or a hadronically decaying $W$ or $Z$ boson and transverse momentum imbalance at $\sqrt{s} = 13$ TeV”, *Phys. Rev. D* **97** (2018) 092005, `arXiv:1712.02345`. `doi:10.1103/PhysRevD.97.092005`. Cited on pages 107 and 150.

[169] ATLAS Collaboration, “Constraints on mediator-based dark matter models using $\sqrt{s} = 13$ TeV $pp$ collisions at the LHC with the ATLAS detector”, Technical Report ATLAS-CONF-2018-051, CERN, Geneva, Nov, 2018. `https://cds.cern.ch/record/2646248`. Cited on pages 111 and 116.

[170] ATLAS Collaboration, “Search for an invisibly decaying Higgs boson or dark matter candidates produced in association with a $Z$ boson in $pp$ collisions at $\sqrt{s} = 13$ TeV with the ATLAS detector”, *Phys. Lett. B* **776** (2018) 318, `arXiv:1708.09624`. `doi:10.1016/j.physletb.2017.11.049`. Cited on pages 111 and 116.

[171] ATLAS Collaboration, “Search for Dark Matter Produced in Association with a Higgs Boson Decaying to $b\bar{b}$ using 36 fb$^{-1}$ of $pp$ collisions at $\sqrt{s} = 13$ TeV with the ATLAS Detector”, *Phys. Rev. Lett.* **119** (2017) 181804, `arXiv:1707.01302`. `doi:10.1103/PhysRevLett.119.181804`. Cited on pages 111 and 116.

[172] ATLAS Collaboration, “Constraints on new phenomena via Higgs boson couplings and invisible decays with the ATLAS detector”, *JHEP* **11** (2015) 206, arXiv:1509.00672. doi:10.1007/JHEP11(2015)206. Cited on pages 111 and 116.

[173] CMS Collaboration, “Search for contact interactions and large extra dimensions in the dilepton mass spectra from proton-proton collisions at $\sqrt{s} = 13$ TeV”, *Submitted to: JHEP* (2018) arXiv:1812.10443. Cited on page 116.

[174] O. Buchmueller, A. De Roeck, K. Hahn et al., “Simplified Models for Displaced Dark Matter Signatures”, *JHEP* **09** (2017) 076, arXiv:1704.06515. doi:10.1007/JHEP09(2017)076. Cited on pages 121 and 122.

[175] CMS Collaboration, “Search for long-lived particles with displaced vertices in multijet events in proton-proton collisions at $\sqrt{s}$ =13 TeV”, *Phys. Rev. D* **98** (2018) 092011, arXiv:1808.03078. doi:10.1103/PhysRevD.98.092011. Cited on page 129.

[176] CMS Collaboration, “Search for long-lived particles decaying into displaced jets in proton-proton collisions at $\sqrt{s} = 13$ TeV”, *Phys. Rev. D* **99** (2019) 032011, arXiv:1811.07991. doi:10.1103/PhysRevD.99.032011. Cited on page 129.

[177] LHC Coordination Group, “Nominal HL-LHC luminosity”. Accessed on Dec. 13th, 2018. https://lhc-commissioning.web.cern.ch/lhc-commissioning/schedule/images/Nom-to-2037.png. Cited on page 131.

[178] G. Apollinari, I. Béjar Alonso, O. Brüning et al., “High-Luminosity Large Hadron Collider (HL-LHC): Technical Design Report V. 0.1”. CERN Yellow Reports: Monographs. CERN, Geneva, 2017. http://cds.cern.ch/record/2284929. Cited on page 131.

[179] D. Contardo, M. Klute, J. Mans et al., “Technical Proposal for the Phase-II Upgrade of the CMS Detector”, Technical Report CERN-LHCC-2015-010, Geneva, Jun, 2015. https://cds.cern.ch/record/2020886. Cited on page 132.

[180] ATLAS Collaboration, “ATLAS Phase-II Upgrade Scoping Document”, Technical Report CERN-LHCC-2015-020, CERN, Geneva, Sep, 2015. https://cds.cern.ch/record/2055248. Cited on page 132.

[181] LHCb Collaboration, R. Aaij, B. Adeva, M. Adinolfi et al., “Expression of Interest for a Phase-II LHCb Upgrade: Opportunities in flavour physics, and beyond, in the HL-LHC era”, Technical Report CERN-LHCC-2017-003, CERN, Geneva, Feb, 2017. https://cds.cern.ch/record/2244311. Cited on page 132.

[182] CERN, “Yellow Report: HL/HE-LHC Physics Performance”. To be published, 2018. Cited on pages 132 and 153.

[183] CMS Collaboration, “Projection of the Mono-Z search for dark matter to the HL-LHC”, 2018. Physics Analysis Summary FTR-18-007. http://cds.cern.ch/record/2644529. Cited on page 132.

[184] X. Cid Vidal, A. Albert, et al., "Beyond the Standard Model Physics at the HL-LHC and HE-LHC". 2018. arXiv:1812.07831. Cited on page 132.

[185] D. Bertolini, P. Harris, M. Low et al., "Pileup Per Particle Identification", *JHEP* **10** (2014) 059, arXiv:1407.6013. doi:10.1007/JHEP10(2014)059. Cited on page 132.

[186] CMS Collaboration, "CMS Luminosity Measurements for the 2016 Data Taking Period", 2017. Physics Analysis Summary LUM-17-001. http://cds.cern.ch/record/2257069. Cited on page 132.

[187] CMS Collaboration, "The phase-2 upgrade of the CMS endcap calorimeter", Technical Report CMS-TDR-17-007, CERN, Geneva, 2017. Cited on page 134.

[188] J. Arjona Martínez, O. Cerri, M. Pierini et al., "Pileup mitigation at the Large Hadron Collider with Graph Neural Networks". 2018. arXiv:1810.07988. Cited on page 136.

[189] CMS Collaboration, "Search for new physics in final states with a single photon and missing transverse momentum in proton-proton collisions at $\sqrt{s} = 13$ TeV", *Submitted to: JHEP* (2018) arXiv:1810.00196. Cited on page 150.

[190] CMS Collaboration, "Search for dark matter produced in association with a Higgs boson decaying to a pair of bottom quarks in proton-proton collisions at $\sqrt{s} = 13$ TeV", *Submitted to: Eur. Phys. J.* (2018) arXiv:1811.06562. Cited on page 150.

[191] A. L. Read, "Presentation of search results: the $CL_s$ technique", *J. Phys. G* **28** (2002) 2693. doi:10.1088/0954-3899/28/10/313. Cited on page 156.

# Acknowledgements

The preparation of this thesis was supported by a number of colleagues without whom it would not have been possible. Here, I would like to express my thanks to them.

First, I would like to thank my advisor Thomas Hebbeker, who welcomed me into the Aachen 3A CMS group and thus allowed me to participate in bleeding edge particle physics research. As a student in this group, I was granted wide-ranging freedom in my research and choice of projects, which is not to be taken for granted. In the group, I further profited from the expertise of Arnd Meyer and Kerstin Hoepfner, who were always ready to offer guidance and to help me navigate life in a large scientific collaboration. As particle physics is computing intensive, my work relied heavily on the Aachen computing systems, which are managed expertly by Thomas Kress, Andreas Nowack and others. Similarly, this work has been supported administratively by Markus Merschmeyer, Melanie Roder, and Iris Rosewick. My thanks to you!

At CERN, I had the privilege of collaborating with numerous people who shaped my understanding of experimental particle physics and helped me succeed. Among them, I would like to thank the members of the CMS mono-Z group, especially Darien Wood, Daniele Trocino and Nicholas Smith. In the wider CMS Exotica community, I am particularly thankful for the support of Oliver Buchmüller, Ivan Mikulec and Adish Vartak. Tristan du Pree was one of my first collaborators at CERN and jump-started my involvement in the LHC dark matter working group.

I would further like to extend my thanks to Christopher Wiebusch, who agreed to serve as the second reviewer for this thesis.

Finally, I am indebted to the German people for providing the funding for the CMS program in Aachen.

# Eidesstattliche Erklärung

Andreas Albert erklärt hiermit, dass diese Dissertation und die darin dargelegten Inhalte die eigenen sind und selbstständig, als Ergebnis der eigenen originären Forschung, generiert wurden.

Hiermit erkläre ich an Eides statt:

1. Diese Arbeit wurde vollständig oder größtenteils in der Phase als Doktorand dieser Fakultät und Universität angefertigt;
2. Sofern irgendein Bestandteil dieser Dissertation zuvor für einen akademischen Abschluss oder eine andere Qualifikation an dieser oder einer anderen Institution verwendet wurde, wurde dies klar angezeigt;
3. Wenn immer andere eigene oder Veröffentlichungen Dritter herangezogen wurden, wurden diese klar benannt;
4. Wenn aus anderen eigenen oder Veröffentlichungen Dritter zitiert wurde, wurde stets die Quelle hierfür angegeben. Diese Dissertation ist vollständig meine eigene Arbeit, mit der Ausnahme solcher Zitate;
5. Alle wesentlichen Quellen von Unterstützung wurden benannt;
6. Wenn immer ein Teil dieser Dissertation auf der Zusammenarbeit mit anderen basiert, wurde von mir klar gekennzeichnet, was von anderen und was von mir selbst erarbeitet wurde;
7. Teile dieser Arbeit wurden zuvor veröffentlicht und zwar in:
    - CMS Collaboration, “Search for dark matter and unparticles in events with a Z boson and missing transverse momentum in proton-proton collisions at $\sqrt{s} = 13$ TeV”, *JHEP* **03** (2017) 061, `arXiv:1701.02042`, [Erratum: JHEP09,106(2017)]. `doi:10.1007/JHEP01(2018)056`
    - A. Albert et al., “Recommendations of the LHC Dark Matter Working Group: Comparing LHC searches for heavy mediators of dark matter production in visible and invisible decay channels”. 2017. `arXiv:1703.05703`
    - CMS Collaboration, “Search for new physics in events with a leptonically decaying Z boson and a large transverse momentum imbalance in proton-proton collisions at $\sqrt{s} = 13$ TeV”, *Eur. Phys. J. C* **78** (2018) 291, `arXiv:1711.00431`. `doi:10.1140/epjc/s10052-018-5740-1`
    - CMS Collaboration, “Projection of the Mono-Z search for dark matter to the HL-LHC”, 2018. Physics Analysis Summary FTR-18-007. `http://cds.cern.ch/record/2644529`
    - T. Abe, A. Albert, et al., “LHC Dark Matter Working Group: Next-generation spin-0 dark matter models”. 2018. `arXiv:1810.09420`
    - X. Cid Vidal, A. Albert, et al., “Beyond the Standard Model Physics at the HL-LHC and HE-LHC”. 2018. `arXiv:1812.07831`

Aachen, den 30.05.2019

Andreas Albert